Ph.D. Thesis

박사 학위 논문

Solar Light Activated Photocatalysts for Enhanced CO_2 Conversion to Hydrocarbon Fuels

Abdul Razzaq (압둘 라자크, 埃波杜勒-拉扎克)

Department of Energy Systems Engineering

DGIST

6th January 2017

Ph.D. Thesis

박사 학위 논문

Solar light activated photocatalysts for enhanced CO_2 conversion to hydrocarbon fuels

Abdul Razzaq (압둘 라자크)

Department of Energy Systems Engineering

DGIST

6th January 2017

Ph.D. Thesis

Solar light activated photocatalysts for enhanced CO_2 conversion to hydrocarbon fuels

Abdul Razzaq (압둘 라자크)

Department of Energy Systems Engineering

DGIST

6th January 2017

Solar light activated photocatalysts for enhanced CO_2 conversion to hydrocarbon fuels

Adviser: Professor Su-Il In

Co-Adviser: Dr. Soo-Keun Lee

by

Abdul Razzaq (압둘 라자크)

Department of Energy Systems Engineering

DGIST

A thesis submitted to the faculty of DGIST in partial fulfillment of the requirements for the degree of Doctor of Philosophy in the Department of Energy System Engineering. The study was conducted in accordance with Code of Research Ethics[1)].

01. 06. 2017

Approved by

Professor Su-Il In _____ (Signature)

(Adviser)

Dr. Soo-Keun Lee_____ (Signature)

(Co-Adviser)

1) Declaration of Ethical Conduct in Research**:** I, as a graduate student of DGIST, hereby declare that I have not committed any acts that may damage the credibility of my research. These include, but are not limited to: falsification, thesis written by someone else, and distortion of distortion of research findings or plagiarism. I affirm that my thesis contains honest conclusions based on my own careful research under the guidance of my thesis advisor.

Solar light activated photocatalysts for enhanced CO_2 conversion to hydrocarbon fuels

Abdul Razzaq (압둘 라자크)

Accepted in partial fulfillment of the requirements for the degree of
Doctor of Philosophy.

01. 06. 2017

Head of Committee_____(인)

Professor Jong-Sung Yu

Committee Member_____(인)

Professor Su-Il In

Committee Member_____(인)

Dr. Soo-Keun Lee

Committee Member_____(인)

Professor Sangaraju Shanmugam

Committee Member_____(인)

Professor Jinhee Park

Ph.D./ES 201334003	압둘 라자크. ABDUL RAZZAQ. **TITLE.** "Solar Light Activated Photocatalysts for Enhanced CO_2 conversion to Hydrocarbon Fuels" **Date.** 2017.01.06 **Pages.** 216 Professor Su-Il In, Dr. Soo-Keun Lee

Abstract

The enormous and continuous release of anthropogenic CO_2 into earth's atmosphere have excessively increased the atmospheric CO_2 level, resulting in natural carbon cycle disturbance and stemming the critical issues of global warming, climate change and environmental pollution. Amongst greenhouse gasses (GHG), CO_2 is a prominent gas responsible for proliferating the greenhouse effect. An effective approach to overcome such issue of elevated atmospheric CO_2 level is to capture CO_2 followed by its utilization in industrial processes and/or its conversion to useful chemicals/fuels. As revealed by thermodynamic studies, CO_2 is a very stable molecule, demanding additional energy to overcome the uphill barrier for its conversion to useful chemicals. In this regard, several approaches have been developed to overcome the overpotential in its conversion to useful chemicals. Various techniques include chemical conversion, thermal conversion, biological conversion, electrocatalytic conversion, photoelectrochemical conversion and photocatalytic conversion. Amongst these approaches, photocatalytic CO_2 conversion/CO_2 photoreduction via solar light to useful hydrocarbons and chemicals seems to be an appealing and compelling strategy, well-fitting to the objectives of renewable energy utilization and, environment and energy infrastructure in a sustainable manner. Despite of extensive research and development, the respective field still remain in its infancy and demand enormous amount of efforts for improved photocatalytic performance and product selectivity. A plenty of photocatalytic materials have been developed for improved CO_2 photoreduction, amongst which Titanium dioxide/Titania (TiO_2) and/or TiO_2 based photocatalysts are extensively studied within the scientific society. TiO_2 offers several advantages such as corrosion stability, abundant availability and low cost, though its performance is largely limited due to inadequate light absorption, mainly attributed to its wide

band gap (~3.2 eV) and low quantum yield in sunlight due to surface and bulk volume charge recombination. However, despite of such critical disadvantages, TiO_2 still remains a champion material in the field of photocatalysis due to its stable and commendable properties. A number of approaches have been developed to overcome the issues of limited light absorption and efficient charge separation, including doping with non-metal or noble metal co-catalysts, coupling with low band gap semiconductors, and the synthesis of carbon-based TiO_2 composites. Hence, with the aim of improving the photocatalytic performance of TiO_2 and TiO_2 based materials, the experimental works performed and investigated in this thesis consists of three key strategies leading to enhanced light absorption and improved charge separation for TiO_2 and TiO_2 based materials. Mainly three experimental works are done and investigated during Ph.D. research which include approaches such as (i) foreign element doped sodium titanate nanotubes (Na^+-TNT), (ii) synthesis of reduced graphene oxide (rGO) coupled TiO_2 nanotube arrays, a novel heterostructured photocatalyst and (iii) development of reduced TiO_2 by a newly developed approach.

During past few years, TiO_2 nanotubes (TNT), a one dimensional (1-D) TiO_2 nanostructures have attracted a great interest among the photocatalysis research community, offering more active sites and improved charge separation by its high surface area and directional charge transport. In the first experimental approach of the thesis, an attempt was made to enhance the photocatalytic performance of sodium titanate nanotubes (Na^+-TNT) by a co-doping strategy of foreign elements. Carbon and nitrogen co-doped sodium titanate nanotubes (C,N-TNT) are synthesized by designing a simple two-step process, comprising of an alkaline hydrothermal technique followed by calcining the well mixture of Na^+-TNT (obtained from alkaline hydrothermal method) with varied amounts of urea (as a nitrogen and carbon dopant source). The photocatalysts are characterized using numerous experimental techniques, and investigated under simulated solar light spectrum for the photocatalytic

conversion of CO_2 and water vapor to methane (CH_4). The C,N-TNT sample with optimum dopant concentration yields the maximum methane yield of 230.80 $ppm \cdot g^{-1} \cdot h^{-1}$, 2.63 times more than pure Na^+-TNT. The key factors contributing to enhanced photocatalytic performance include increased light absorption, surface area and Na^+ ions concentration in TNT which acts as a CO_2 adsorption site and photogenerated electrons recombination centers. It is observed that higher doping of the TNT, resulted in lower photocatalytic performance which might be due to decreased surface area or increased recombination centers. Our results suggest, co-doping of nanostructured photocatalysts is an excellent pathway for improving textural and photocatalytic properties for the respective application domain.

Graphene based TiO_2 nanostructures have also been found to offer improved photocatalytic/photoelectrochemical properties, with graphene contents enhancing light absorption as well as promoting rapid charge transfer. With the aim of improved photocatalytic performance via enhanced light absorption and efficient charge separation, an attempt is made in second experimental work of the thesis for the synthesis of novel heterostructure comprising of reduced graphene oxide (rGO) coupled with 1-D TiO_2 nanotube (TNT) arrays. A facile synthesis approach is designed resulting in a noble metal-free novel nanostructured photocatalytic material, comprising of one-dimensional arrays of TNT covered with reduced graphene oxide and TiO_2 nanoparticles termed as rGO-TNTNP. The probable mechanism which might be involved in the fabrication of such novel nanostructured photocatalyst is proposed on the basis of reported literature and experimental results specifically, Raman spectra, XPS data and SEM images. The novel nanostructure exhibits significantly improved photocurrent density and photochemical activity via photocatalytic conversion of CO_2 into CH_4 under simulated solar light irradiation. The rGO-TNTNP produces CH_4 with an evolution rate of 5.67 $ppm \cdot cm^2 \cdot h^{-1}$, 4.4 times more than pure TNT sample (1.28 $ppm \cdot cm^2 \cdot h^{-1}$). The improved

performance appears due to the combined effect of enhanced light absorption and effective charge separation promoted by the rGO content over photocatalyst surface.

The discovery of black or reduced TiO_2 materials with extended light absorption and suitable band structure has offered improved photocatalytic properties. Until now a variety of methods have been reported for the synthesis of reduced TiO_2 (RT), suggesting different material properties which can be manipulated by a number of process parameters. In the third and last experimental work of the thesis, the performance of RT for CO_2 photoreduction with water vapor to hydrocarbons mainly CH_4, is investigated under simulated solar light irradiation. The RT employed in this work is synthesized by a newly developed reduction process using dual reducing agents i.e. Mg in 5% H_2/Ar. Further, to improve the charge separation efficiency, platinum (Pt) nanoparticles as co-catalyst are loaded by a photodeposition method and Pt concentration is optimized on the RT surface. With optimally photodeposited Pt nanoparticles on RT, it exhibits a stable performance and a threefold increase in CH_4 production rate (1640.58 $ppm \cdot g^{-1} \cdot h^{-1}$ or 1.13 $\mu mol \cdot g^{-1} \cdot h^{-1}$) as compared to Pt photodeposited pure commercial nano-TiO_2 (546.98 $ppm \cdot g^{-1} \cdot h^{-1}$, 0.38 $\mu mol \cdot g^{-1} \cdot h^{-1}$). The improved photocatalytic performance is mainly attributed to the suitable band gap with enhanced light absorption, well-aligned position of band edges against CO_2/CH_4 redox potential and efficient photogenerated charge separation by well-dispersed Pt nanoparticles co-catalyst having optimum size, concentration and well dispersion.

Keywords: Solar light activated photocatalysts, Photocatalytic CO_2 conversion, TiO_2 nanotubes, Co-doping strategy, Reduced Graphene Oxide, Reduced TiO_2.

Contents

Chapter 2. Characterization and analysis tools

Chapter 4. TiO_2 Nanotube Arrays Covered with Reduced Graphene: A Facile Fabrication approach towards a Noble Metal-free photocatalyst and its application in Photocatalytic CO_2 conversion to methane

List of figures

List of Tables

List of Publications

Following is a list of publications resulting from the Ph.D. degree thesis

1 **Abdul Razzaq**, Sreenivasan Koliyat Parayil, Seung-Min Park, Hye-Rim Kim, Carig. A. Grimes and Su-Il In, "Photocatalytic Conversion of CO_2 to Hydrocarbon Fuel using Carbon and Nitrogen co-doped Sodium Titanate Nanotubes", *Applied Catalysis A: General*, 498 (2015) 205-213. [IF: 4.012, Q1 (Environmental Sciences, JIF Percentile 87.33 %)]

2 **Abdul Razzaq**, Craig. A. Grimes, and Su-Il In, "Facile Fabrication of Noble Metal-Free Photocatalyst: TiO_2 Nanotube Arrays Covered with Reduced Graphene Oxide", *Carbon*, 98 (2016) 537-544. [IF: 6.198, Q1 (Material Science, Multidisciplinary JIF Percentile 90.221 %)]

3 **Abdul Razzaq**, Apurba Sinhamahapatra, Jong-Pil Jeon, Craig A. Grimes, Jong-Sung Yu and Su-Il In "Efficient Solar Light CO_2 Photoreduction to Hydrocarbon Fuels via Reduced TiO_2 Photocatalyst", To be Submitted yet.

Following is a list of publications, published as a co-author during Ph.D. degree

1. Seung-min Park, **Abdul Razzaq,** Young Ho Park, Saurav Sorcar, Craig A. Grimes and Su-Il In, " Hybrid Cu_xO-TiO_2 Heterostructured composites for Photocatalytic CO_2 Reduction into Methane by Solar irradiation : Sunlight into Fuels, *ACS Omega*, Article in press (2016).
2. Saurav Sorcar, **Abdul Razzaq**, Haining Tian, Craig A. Grimes and Su-Il In, "Facile electrochemical synthesis of anatase nano-architectured titanium dioxide films with reversible superhydrophilic behaviour", *Journal of Industrial and Engineering Chemistry*, Article in press (2016) http://dx.doi.org/10.1016/j.jiec.2016.10.032. [IF: 4.179, Q1 (Engineering, Chemical, JIF Percentile 90.000 %)]

3. Su-ll In, Young S. Gwak, Hye Rim Kim, **Abdul Razzaq**, Kyeong-Seok Lee, Hee Young Kim, SuChan Chang, Bong Hyo Lee, Craig A. Grimes and Chae Ha Yang, "Hierarchical Micro/Nano-Porous Acupuncture Needles Offering Enhanced Therapeutic Properties", *Scientific Reports*, 6 (2016) 34061. [IF: 5.228, Q1 (Multidisciplinary sciences, JIF Percentile 89.683 %)]

4. Kidon Kim, **Abdul Razzaq**, Saurav Sorcar, Yiseul Park, Craig A. Grimes and Su-Il In, "Hybrid mesoporous Cu_2ZnSnS_4-TiO_2 photocatalyst for efficient photocatalytic conversion of CO_2 into CH_4 under solar irradiation", *RSC Advances*, 6 (2016) 38964. [IF: 3.289, Q2 (Chemistry, Multidisciplinary, JIF Percentile 70.245 %)]
5. Sreenivasan Koliyat Parayil, **Abdul Razzaq** and Su-Il In, "Formation of Titania-Silica Mixed Oxides in Solvent Mixtures and their Influences for the Photocatalytic CO_2 Conversion to Hydrocarbon", *Journal of Nanoscience and Nanotechnology*, 15 (2015) 7285-7292. [IF: 1.338, Q3 (Chemistry, Multidisciplinary, JIF Percentile 41.411 %)]
6. Minju Kim, **Abdul Razzaq**, Young Kwang Kim, Soonhyun Kim and Su-Il In, "Synthesis and characterization of platinum modified TiO_2 embedded carbon nanofibers for solar hydrogen generation", *RSC Advances*, 4 (2014) 51826. [IF: 3.289, Q2 (Chemistry, Multidisciplinary, 70.245 %)]
7. HyeRim Kim, **Abdul Razzaq**, Hyo Jung Heo and Su-Il In, "Photcatalytic conversion of CO_2 into hydrocarbon fuels with standard titania (Degussa P25) using newly installed experimental setup", *Rapid Communication in Photoscience*, 2 (2013) 64-66.

Chapter 1. Introduction

1.1 Impact of industrialization on environment

The industrial and technological uprising for economic growth, social modernization, technological development and comfortable human life have been propelling urbanization and industrialization in recent years [1]. However such benefits from industrialization are achieved at a cost of intensive amount of energy specifically in forms of heat and electricity. Until today, a major portion of the energy is generated from non-renewable resources like coal, fossil fuels oils and natural gas. With the passage of time, it is believed that world energy consumption will abruptly increase because of reasons of increased world population and higher energy demand for the account of better life. According to International Energy Agency (IEA), the final consumption of the energy had exceeded more than double in 2014 as that of 1974 with the industrial sector, the largest consuming sector as shown in Figure 1.1a [2]. Further, amongst the non-renewable, fossil fuels such as natural gas, crude oil and coal contributes major portion to provide energy with crude oil as a dominant primary energy supply fuel in 2014 (Figure 1.1b) [2]. The increased energy demand will lead to depletion of fossil fuels with severe and harmful effects on the environment and human health significantly by the emission of toxic byproducts during their refined production and usage. Hence, industrialization, transport and human activities for the technological development and social modernization promotes rapid consumption of fossil fuels with a variety of environmental disruptions such as greenhouse gas (GHG) emissions, noise pollution, air pollution and severe effect on the crops and living organism's ecology via toxic substance emissions [3,4]. As energy is consumed in all such activities (industrial, transport or residential activities), hence its usage and conversion to useable forms like heat, electricity and power is considered as a proxy for all such environmental impacts. The fossil fuels usage for energy generation provides high energy density with easy storage and transport, but their excessive usage has induced a serious and

severe issue of GHG emissions specifically carbon dioxide (CO_2), along with security and economic concerns related to depletion of limited and finite fossil fuels reserves.

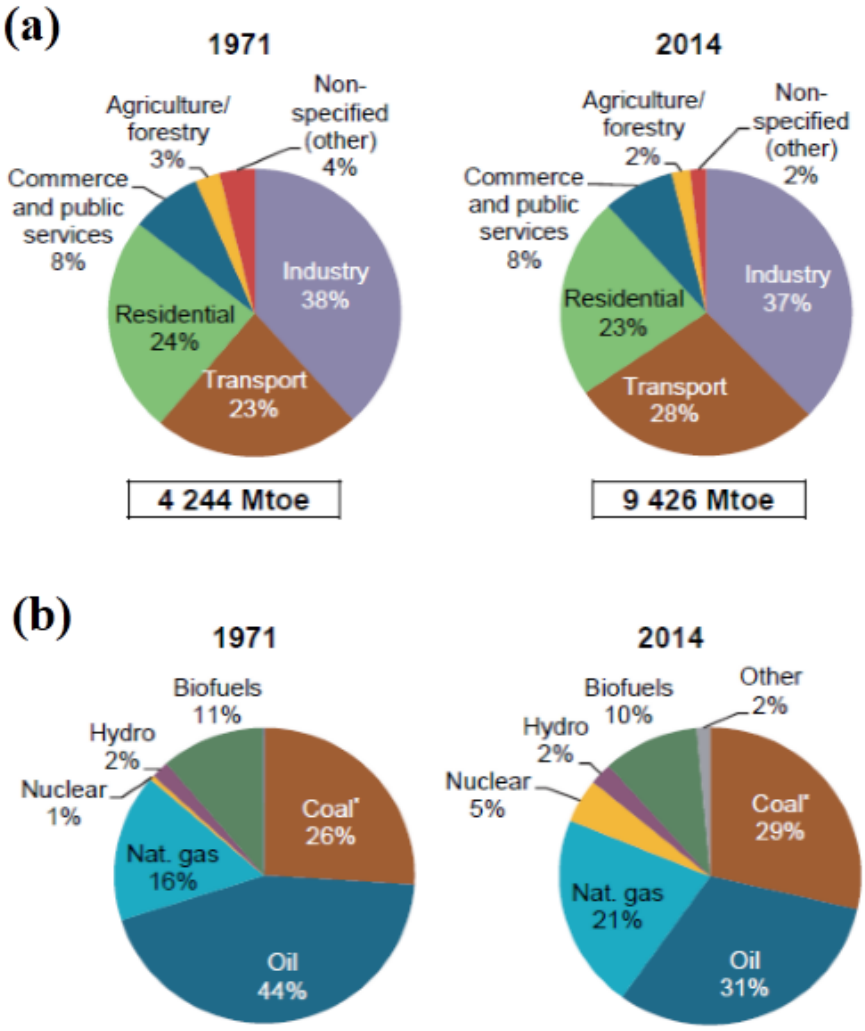

Figure 1.1 (a) Energy demand with respect to various consumer sectors. (b) Comparison of energy produced form various primary energy sources. (Taken from Ref. 2)

Such GHG emissions if are not dealt properly, then their increased concentration might amplify exponentially several challenging issues like climate change, sea level rise, environmental pollution and adverse effects on crop cultivation and human health. Numerous models forecasted an increase of 2-3 °C in temperature by the end of 21st century mainly

contributed by global warming induced by GHG emissions [3,5]. Further it is very crucial and strenuous to recover from such climate alteration as it requires a lot of efforts and long duration to retain the original environmental status, as an example, 50 to 100 years are needed for normalizing half of the anthropogenic CO_2 being spread in 4 to 8 years. Hence it is of extensive urgency to deal with such a substantial issue with a potential solution, well-fitting to the eradication of global warming and well-matching the energy infrastructure in a carbon neutral manner.

1.2 Carbon dioxide (CO_2): A potential greenhouse gas

Greenhouse gases (GHG) emissions as a result of fossil fuels utilization is a topic of extreme interest amongst the global scientific society specifically when it comes to global warming. The GHG promotes the greenhouse effect by trapping the sun's heat or heat emitted from earth's surface and radiating it back, hence amplifying the issues of climate change and global warming. The most significant GHG includes carbon dioxide (CO_2), methane (CH_4), ozone (O_3), nitrous oxide (N_2O), fluorinated gases (HFCs, PFCs) and water vapors. Amongst various GHG, CO_2 is the most prominent contributor to climate change over the past century as compared to the other gasses [6,7]. The CO_2 is mainly produced and released into atmosphere by human activities. According to IEA [8], CO_2 emissions via combustion of fuels for energy, industrial and transportation sectors dominates the total GHG emissions. One can clearly notice from Figure 1.2 that the energy sector releases the largest amount of GHG into atmosphere and contributes around 90 % of the GHG emissions. Thus the energy sector is considered mainly for CO_2 emissions with CO_2 a key and potential greenhouse gas and largest share amongst GHG emissions. As reported in year 2014, around 22 million tonnes of coal, 12 million tonnes of oil and 10 billion m^3 of natural gas are consumed each day which fulfills around 82 % of energy demand [9]. All such energy sources together release around 30 billion

tonnes of anthropogenic CO_2 thus increasing the atmospheric CO_2 concentration to 400 ppm which is about 40 % higher than mid-1800s, i.e. pre-industrial era [8,9].

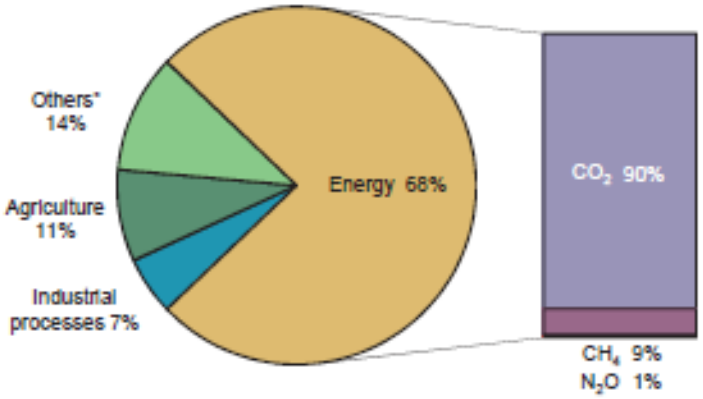

Figure 1.2 Share of the global GHG emissions with respect to various consumer sectors. (Taken from Ref. 8)

Due to this reason, CO_2 emission is considered as a primary cause for the global warming, bringing about adverse climate change and other irreversible effects on nature driven environment. The key and major adverse effects of global warming are explained below:

1.2.1 Climate change

One of the key issue which is globally of great importance is unusual change in climatic patterns of the earth [4,6]. This means disturbance of the natural variation in temperature due to global warming resulting in extreme, more frequent, widespread and intense weather events such as heat waves, floods, storms and droughts. Such a climate change is believed by the climate scientists due to increase in the earth's average temperature.

1.2.2 Increase in earth's average temperature

It is of common insight that the global warming induced by GHG emissions adds energy to the earth's biosphere resulting in heat, which acts as a fuel for earth's temperature rise [5]. Further the energy also drives the water cycle thus leading to extreme weather patterns. The International panel on climate change (IPCC) predicts that by the year 2100, the atmospheric

CO_2 concentration may rise to 570 ppm with a 1.9 °C rise in the earth's average temperature [10].

1.2.3 Rise in sea level

Another severe effect of global warming is the rise in the sea level [11]. As mentioned above the average temperature of the earth is increasing which will directly affect the polar ice caps by melting them. The melting of the polar ice caps will results in raising sea level, imbalance of global ecosystem, promoting the temperature rises and will change the landscapes of the glaciers.

1.2.4 Spreading of diseases

Increase in earth's temperature can lead to air pollution such as formation of photochemical smog and Ozone which causes a certain adverse respiratory effects like airway irritation, coughing, reducing lung functions, asthma, emphysema and bronchitis [4,12]. Further many airborne allergens are also significantly enhanced by climate change e.g. the rise in pollen counts with increase in temperature and increase in mold and fungal growth by flooding hence again associated to respiratory ill-health. On the other hand the rise in water level can provoke the major water-borne diseases such as cholera, cyclospora, cryptosporidiosis, campylobacter and leptospirosis.

1.2.5 Disturbing ecosystems

Such abrupt climate changes induced by global warming also effects the various ecosystems around the globe [4,13]. It is observed that uncounted valuable species will either face extinction or might shift their ranges. Such extinction or shifting will lead to numerous pests and tropical diseases specifically spreading in the warmer regions.

1.2.6 Crops cultivation

Moreover, all above mentioned issues will harm the crops natural biological systems and will pertain towards the imbalance of benefit *vs.* harm of plants and crops [7,13]. Due to increased temperature and water level some crops will be benefited while the others are harmed. Similarly, the increased CO_2 level will make the oceans more acidic, harmful for coral reefs and also effects fisheries and marine life.

Hence to overcome above mentioned issues and adverse effects of global warming, immense efforts are required on emergency basis to save the human planet i.e. earth from several disasters in near future. The issue of global warming should be handled in an engineered and realistic manner with the development and implication of various methodologies and approaches such as enhancing energy efficiencies, selecting non-emitting alternatives for energy production and reducing the GHG emissions via carbon tax policy. All such approaches should be aimed towards only one objective of "bringing back the CO_2 level where it was", thus solving all the issues associated with global warming.

1.3 The "Carbon Cycle" disturbance

Carbon cycle, like various other natural cycles is one of the key biogeochemical cycle with prominent influences on atmosphere and terrestrial biosphere [14,15]. The key step in the carbon cycle is the transformation of carbon containing compounds specifically atmospheric CO_2 into carbohydrates by plants photosynthetic process. Such carbohydrates are then consumed by herbivores which again releases the CO_2 (via respiration) into atmosphere. However beyond the terrestrial reservoir (including plants, animals, soil microbes and decomposed organic materials), oceans also contributes as a reservoir to absorb the atmospheric CO_2 at the water surface via simple diffusion. The CO_2 solubilized at the ocean surface can be converted to carbonates/bicarbonates which are fixed biologically by ocean and sea environment to $CaCO_3$. This material is helpful for body parts of various aquatic organisms. However, in case of excess CO_2 absorption by ocean and sea water, it can lead to formation of carbonic acid and can affect the aquatic life. The basic schematic of the carbon cycle is portrayed in Figure 1.3.

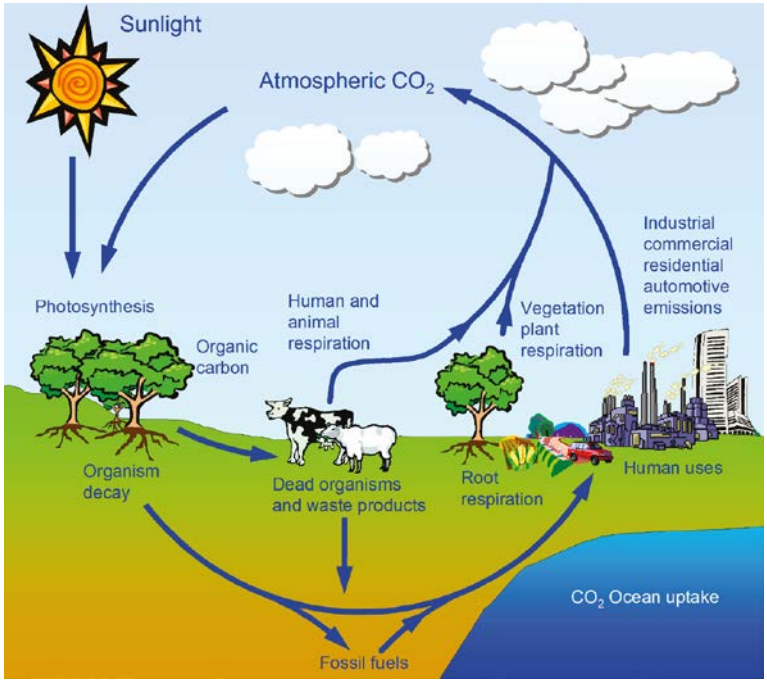

Figure 1.3. Schematic of the natural carbon cycle with demonstration of natural pathways and anthropogenic pathways influencing the carbon cycle. (Taken from Ref. 14)

Since the industrial revolution of 1800s, for better and comfortable lifestyle human beings have started the burning of fossil fuels (inorganic materials like coal, oil, shale and natural gas which is believed to be biomass of dead plants and animals stored in the earth crust over millions of years) in turn releasing the stored carbon in them into atmosphere mainly as CO_2 and CH_4 gases. Such burning of fossil fuels as a means to generate heat, electricity, for industrial processes and transportation etc., definitely makes the human life better and comfortable, but on the other hand had accelerated the CO_2 concentration in atmosphere which ultimately influences and disturbs the natural carbon cycle. As mentioned previously (section 1.2), anthropogenic CO_2 (CO_2 generated by human activities) has led the atmospheric CO_2 concentration increase to 400 ppm which is about 40 % higher than mid-1800s, i.e. pre-industrial era. Such a gigantic increase of atmospheric CO_2 is difficult to compensate by the natural carbon cycle, thus as a result the excess CO_2 remains in the atmosphere or absorbs into water sinks (oceans, seas, lakes etc.) influencing the terrestrial and aquatic life. The excess CO_2 in atmosphere is a very crucial and important issue to deal with as it is considered a prominent GHG, altering the earth's radiant energy balance resulting in global warming and climate change. Hence, human activities and industrialization have certainly played a primary role in disturbing the natural carbon cycle, booming the issues of climate change and global warming. To fix such issues, several researches are under investigation by global scientific community to minimize, prevent or inhibit the increased level of atmospheric CO_2.

1.4 Normalizing excess atmospheric CO_2 level

In order to overcome the issues of climate change and global warming, there is an intense need to minimize and normalize the increased atmospheric CO_2 level. In this regard the scientific research and development provides an effective and realistic pathway of "carbon capture and utilization (CCU)" technology to overcome the increased atmospheric CO_2 level [16]. CCU can be further subdivided into (i) CO_2 capture/separation via various technologies, followed by (ii) its utilization/conversion into useful chemicals and/or fuels.

1.4.1 CO_2 capture and separation

As mentioned previously CO_2 concentration in atmosphere currently is estimated to be around 400 ppm which has 40 % increased as compared to that in pre-industrial era. However, with respect to CO_2 capture/separation technology, such concentration is still low and hence requires expensive and sophisticated methods/processes to capture it. Thus it is more beneficial and advantageous to capture/separate the CO_2 from the stationary sources of flue gases rather than the atmosphere, such as electric power plants, coal fired plants and various industrial chimneys. The main CO_2 capture/separation technologies frequently used in industrial process are as follows [17]:

a) **Absorption:** In absorption technology, the flue gas is allowed to flow upward in a absorber column, while the liquid solvent acting as an absorbent is flowing down. On contact with the solvent, CO_2 gas gets absorbed in the solvent and the CO_2 rich solvent is collected at the bottom which is then taken to the stripper for steam regeneration of CO_2 gas. The commonly solvents used for CO_2 gas absorption includes, glycol ethers, methanol, and monoethanolamine (MEA) 20-30 % in water.

b) **Adsorption:** Adsorption technology use solid materials as CO_2 gas adsorbents to capture the CO_2 gas. In this method, flue gas is allowed to pass through the solid adsorbent in the form of packing and sieves, CO_2 gas gets physically or chemically adsorbed on the solid

adsorbent surfaces which is then desorbed using pressure swing or temperature swing systems. A variety of adsorbents used nowadays include metal-organic frameworks (MOFs), supported amines, polymers and zeolites.

c) **Membrane separation:** Another effective approach to capture/separate the CO_2 gas from flue gas is using the membrane technology. Various membranes such as polymeric membrane, matrix membranes and functionalized membranes can be utilized with the required selectivity for efficient capture/separation of CO_2 gas form flue gas.

d) **Cryogenic distillation:** The cryogenic technology also offers an effective approach to achieve the solid and liquid CO_2 via cooling down to -110 and -56 °C respectively. This process is comparatively reliable with CO_2 product in different phases but such technology requires multistep cryogenic distillation to remove other products and hence requires high capital and energy cost.

1.4.2 CO_2 utilization and conversion

Once the CO_2 gas is captured successfully, the next task is to effectively utilize/convert the CO_2 gas in order to harvest the maximum benefits form CO_2 capturing technology [16,17]. As CO_2 is a well-known stable molecule, hence extra energy is always required to convert or transform into useful chemical or fuel product (the detail explanation regarding the thermodynamics of CO_2 conversion is presented in the next section). At present several approaches are available for CO_2 gas conversion into useful products. Few of them are tabulated in table 1.1 and briefly explained as follow [17–19]:

a) **Chemical conversion:** Chemical conversion mainly involves the reaction of CO_2 gas at specified temperature and pressure conditions with other reactants to give useful products. Some of the examples are as follow: (i) synthesis of potassium or sodium salts of phenols by reaction of carboxylic acid with CO_2 gas, (ii) methanol synthesis also employing small

amount of CO_2 gas, (iii) DMC (dimethyl carbonate) an important reactant for synthesis of polycarbonate, polyurethane, is produced by reaction of methanol and CO_2.

b) **Thermal conversion:** This method involves a one-step direct chemical reduction process at very high temperatures with strong reducing metals/ metal oxides such as Mg, Na, Sn, CeO_2 etc. At elevated temperatures such metals chemically reduce the CO_2 gas to various products like C, CO etc. with their respective oxides or reduced metal oxides.

c) **Biological conversion:** Various biological microorganisms also provide an opportunity to transform the CO_2 into useful products photosynthetically or non-photosynthetically. Microalgae have 10 times greater ability to fix CO_2 using sunlight as compared to simple plants. The bacteria *Methanobacterium thermoautotophicum* can convert the CO_2 with H_2 stream into CH_4 with 80 % of theoretical yield.

d) **Electrocatalytic conversion:** This approach provides an electrocatalytic reduction of CO into fuels in similar manner as water electrolysis. The CO_2 reduction occurs at the cathode surface whereas the oxygen is evolved at the anode. The CO_2 reduction efficiency depends upon the catalytic material used as a cathode surface. The external electrical current is provided to overcome the uphill energy barrier to convert/reduce the CO_2 into useful products/fuels.

e) **Photoelectrochemical conversion:** The photoelectrochemical conversion proceeds in a similar manner as electrocatalytic method with the addition of sunlight as a bias along with external electricity. Thus herein, in addition to electrical bias, solar energy is also irradiated on the respective cathode to enhance the yield of the CO_2 conversion. In both the methods i.e. electorcatalytic and photoelectrochemical, the hydrogen evolution reaction at the anode surface competes with the CO_2 reduction process at the cathode surface which lowers the product selectivity, a key problem in the aqueous medium process. To improve the product

selectivity various attempts have been made with a non-aqueous medium as an alternate medium to overcome the generation of hydrogen.

f) Photocatalytic conversion: The photocatalytic conversion involves the transformation of CO_2 gas via its reduction by electrons provided by a semiconductor/photocatalyst exposed to sunlight. When sunlight is irradiated on a photocatalyst (placed in gaseous CO_2 medium or CO_2 rich aqueous/non-aqueous medium), the electron-hole (e^--h^+) pairs are photogenerated, electrons are given to surface adsorbed CO_2 species thus reducing the CO_2 into useful products like CO, HCOOH, HCHO, CH_4 and CH_3OH while the holes are filled by water oxidation reaction. The Photocatalytic CO_2 conversion/reduction requires sacrificial electron donor and hydrogen source such as water, methanol and isopropyl alcohol to regenerate the photocatalyst and improve the efficiency of the system.

Table1.1 Various approaches developed for conversion of CO_2 into useful chemicals/products.

Approach	Definition	Example
Chemical conversion	CO_2 conversion proceeded by a chemical reaction	$Mg + CO_2 \rightarrow MgO + CO$ $Na + CO_2 \rightarrow Na_2C_2O_4$
Thermal conversion	CO_2 conversion on a catalyst surface at high temperatures	$CO_2 + Ce^{4+} \rightarrow CO+1/2O_2$ T > 900 °C
Biological conversion	Chemical conversion of CO_2 into other products promoted by biological organisms	$CO_2 + 4H_2 \rightarrow CH_4 + H_2O$ Bacteria
Electrocatalytic conversion	CO_2 conversion on a catalyst surface by externally applied electric bias	$CO_2 + 2e^- + 2H^+ \rightarrow CO+ H_2O$ eV
Photoelectrochemical conversion	CO_2 conversion on a catalyst surface by applying a combination of electric current and light as an external bias	$CO_2 + 2e^- + 2H^+ \rightarrow CO+ H_2O$ hν +eV
Photocatalytic conversion	CO_2 conversion on a light active photocatalyst surface under light illumination only	$CO_2 + 2e^- + 2H^+ \rightarrow CO+ H_2O$ hν

1.5 Photocatalytic CO_2 conversion/reduction

1.5.1 Introduction

In 1972, Honda and Fujishima reported the generation of H_2 and O_2 from water splitting by a photoelectrochemical process i.e. illuminating a TiO_2 anode in an electrochemical system [20]. Since then an enormous amount of interests have been developed in the field of photo-electrochemistry for the development of highly efficient photoelectrochemical or photochemical systems. Such process of yielding photocatalytic H_2 or O_2 is conventionally termed as "artificial photosynthesis" (AP) and was focused mainly towards water splitting in the early days. Being motivated form AP, Halmann in 1978 attempted to yield formic acid, formaldehyde and methanol using an electrochemical cell bubbled with CO_2 employing a single crystal p-type GaP irradiated using an Hg lamp [21]. In 1979, just after an year of Halmann experiments, Inoue and co-workers demonstrated the production of formic acid, formaldehyde, methanol and methane via photoelectrocatalytic CO_2 reduction over a variety of single semiconductor materials which include TiO_2, ZnO, CdS, GaP, SiC, and WO_3 [22]. Since the breakthrough works by Halmann and Inoue, an excessive investigations have been done and are indulged for the development of AP technology for efficient CO_2 photoreduction, particularly pure photocatalytic systems, utilizing only sunlight as an energy source and free from any additional external bias.

Amongst various technologies as mentioned above, photocatalytic CO_2 conversion via reduction reactions into useful chemicals and fuels seems to be most appealing concept, as it can use a free source of energy i.e. sunlight to proceed the photocatalytic reduction reactions [17,23,24]. Such approach provides a ready-made mean to utilize a gigantic renewable energy source i.e. sunlight for conversion of CO_2 into useful chemicals or fuels, ultimately supporting the minimization or normalization of atmospheric CO_2 level with producing useful chemicals and fuels in a sustainable manner.

The photocatalytic CO_2 conversion/reduction is carried out on the surfaces of semiconductor materials, an attractive type of materials possessing a gap between the filled valence band (VB) and bottom of the conduction band (CB), well known as band gap. Unlike metals which possess a continuum of energy states, semiconductor materials have gap in between the fully filled electronic states (VB) and unfilled electronic states (CB), termed as band gap. When light is irradiated on them, the semiconductors absorb photon from the light whose energy is equal or greater than the band gap. Such light absorption can excite electrons from valence band to conduction band thus creating electron-hole (e^--h^+) pairs with the electrons exciting to the conduction band while the holes remaining in the valence band [25]. Once the electron-hole (e^--h^+) pairs are photogenerated by sunlight, they migrates toward the surface of semiconductor or photocatalyst following one of the below mentioned four pathways to proceed the fruitful reactions or generation of energy/heat [26]:

I. Donation of the photoexcited electrons to the acceptor species.
II. Donation of the photogenerated holes to the acceptor species.
III. Recombination of the photoexcited charge carriers (e^--h^+ pairs) within the volume of the semiconductor/photocatalyst material.
IV. Recombination of the photoexcited charge carriers (e^--h^+ pairs) at the surface of the semiconductor/photocatalyst material.

The first two paths (path (I) and (II)) proceeds leading to the required redox reactions and are more effective when the reactant to be reduced or oxidized is adsorbed on the surface. In contrary, the photogenerated charge carriers can also lead to the volume recombination or surface recombination if not separated efficiently i.e. path (iii) and path (iv) respectively.

In case of photocatalytic CO_2 reduction, CO_2 gas is reduced by accepting the photoexcited electrons and reacting with protons to give the desired products, whereas the holes are regenerated by hole scavengers or electron donor reagents such as water, methanol, isopropyl

alcohol etc [23,24]. The schematic demonstration of the basic mechanism involved in photocatalytic reactions for general photocatalysis and CO_2 photoreduction are depicted in the Figure 1.4.

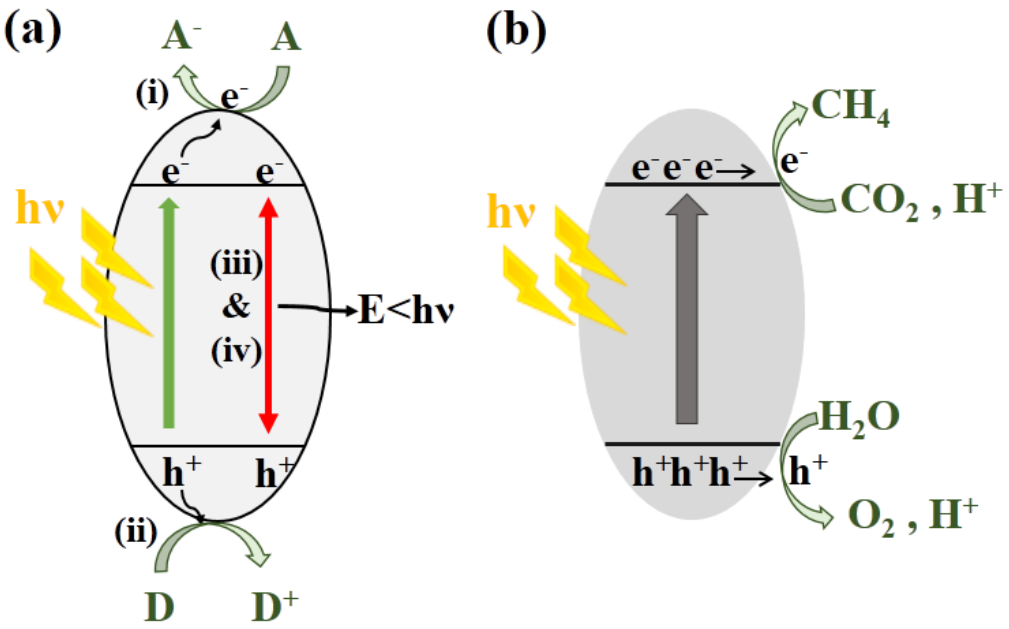

Figure 1.4 (a) General representation of photogeneration of electron-hole pair in a semiconductor material and possible pathways to proceed reactions and recombination (A= electron acceptor and D= electron donor). (b) Schematic presentation of reaction pathway for photocatalytic CO_2 conversion to useful products.

1.5.2 Thermodynamics

CO_2 is a well-known thermodynamically stable molecule with a standard Gibbs free energy of $\Delta G° = -394.4$ KJ·mole^{-1} in gaseous form [24]. Because of such a low relative energy, it is a very stable molecule and hence extra energy is needed to be given to the reaction mixture comprising of CO_2 reactant for its conversion/transformation to useable chemicals. According to Gibbs free energy equation (equation 1.1 and equation 1.2) [24], more negative potential is required than E° to overcome the overpotential and making the $\Delta G°$ negative enough to proceed the reduction reactions of CO_2 in a spontaneous manner.

$$\Delta G° = nFE° \quad (1.1)$$

Where, $\Delta G°$ = Standard Gibbs free energy, n= no of electrons involved in the reaction, F= Faradays constant (96465 $C \cdot mole^{-1}$) and E°= standard potential of the respective reaction.

$$\eta = E - E° \quad (1.2)$$

Where, η= overpotential, E= required potential and E°=standard potential

Such a potential in terms of extra energy can be applied by various means such as thermal energy, electrical energy, chemical energy and light energy. Ideally, renewable sources of energy such as light, wind, hydropower etc. should be utilized to overcome the overpotential, however, the reactants involved in the reaction can also be selected to avoid the overpotential and overcoming of activation barrier in order to achieve the desired products. *Peter et al.* suggested two different catalytic pathways for conversion of CO_2 feedstock into desired products [16]. First path follows the reaction of CO_2 with high energy reactants on catalyst surface transforming into low energy product, whereas the second path involves the reaction of CO_2 with medium or low energy reactants along with extra energy which is added to the reaction mixture resulting in high energy products. The schematic view represented by them is shown in Figure 1.5.

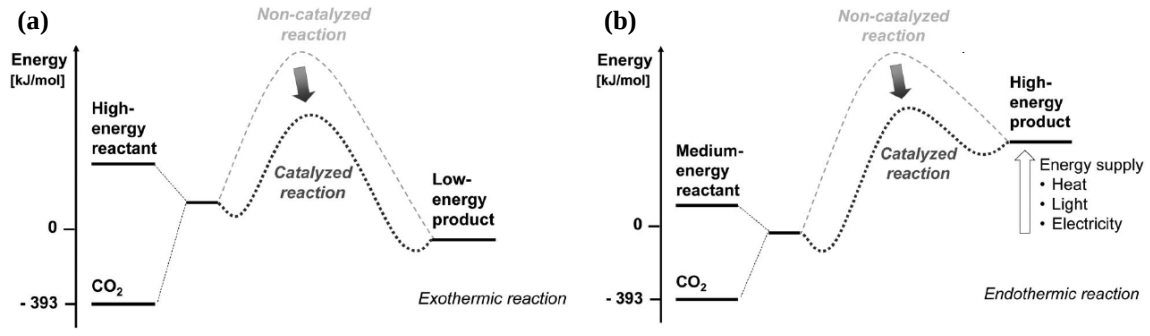

Figure 1.5 (a) Thermodynamic pathways displaying the activation barrier for CO_2 conversion into products with (a) high energy reactants and (b) low energy reactants. (Taken from Ref.16)

Therefore, in accordance with the respective redox potential, an optimal photocatalyst should harvest enough sunlight to allow the conversion or reduction of CO_2 to the desired products. Due to possessing high stability, it seems impossible for a photocatalyst alone to reduce CO_2 into products, therefore the CO_2 reduction is proceeded with the support of reducing agents such as H_2O, H_2 etc.[16,24]. The reducing agents regenerates the photocatalyst by readily providing the electrons in order to fill the holes, releasing protons in turn. Such released protons can react with the surface adsorbed CO_2 and electrons to give the desired product, a relative feasible and less energetic pathway. Such process is commonly known as proton assisted multi-electron photoreduction process and is generally accepted among the research society indulged in the respective field. Furthermore, the selectivity of the product can be manipulated by varying the properties of the photocatalytic materials such as aligning the conduction band and valence band edges with respect to the redox potentials of reduction reactions. The redox potentials for various CO_2 reduction reactions (at pH=7.0 and E *vs.* NHE) with water in vapor or in liquid form are obtained from reported data and summarized in Table 1.2 [27].

Based upon the redox potential information, one can selectively choose or develop the photocatalyst material with its conduction band edge position lying at more negative potential than the redox potential of the desired product, whereas the valence band edge at more positive potential then the redox potential of the reducing agents such as in case of water, it should lie below the water oxidation potential (+0.81 V *vs.* NHE, pH=7.0).

Table 1.2 Electrochemical Redox potentials (E° *vs.* NHE, pH=7.0) for CO_2 reduction into a variety of useful chemical products. (Obtained using data from Ref. 27)

No.	Reactions	E° *vs.* NHE (V)
1	$CO_2 + 2H^+ + 2e^- \rightarrow HCOOH$	-0.61 V
2	$CO_2 + 2H^+ + 2e^- \rightarrow CO + H_2O$	-0.53 V
3	$CO_2 + 4H^+ + 4e^- \rightarrow HCHO + H_2O$	-0.48 V
4	$CO_2 + 6H^+ + 6e^- \rightarrow CH_3OH + H_2O$	-0.38 V
5	$CO_2 + 8H^+ + 8e^- \rightarrow CH_4 + 2H_2O$	-0.24 V
6	$2H^+ + 2e^- \rightarrow H_2$	-0.41 V
Water oxidation reaction		
7	$2H_2O \rightarrow O_2 + 4H^+ + 4e^-$	+0.81V

1.5.3 Mechanism and reactions pathways

As mentioned above and is well known, CO_2 is the most thermodynamically stable compound of the carbon family, thus an enormous amount of effort is required to break up the C=O bond and forming the desired C-H bonds in the products. Because of the very stable and low Gibbs free energy, it is very difficult and challenging for a photocatalytic material itself to convert, transform or reduce the CO_2 into useful chemicals, hence the conversion or reduction of CO_2 is more feasible in the presence of reducing agents such as H_2O, H_2, and amines etc. H_2O as a reducing agent is the most preferable choice because of easy handling, less toxicity and cheaper reactant. Therefore a mixture of CO_2 and H_2O is commonly used for the photocatalytic conversion of CO_2 into desired products. As the light is illuminated upon the photocatalyst with adsorbed $CO_{2(g)}/H_2O_{(g/l)}$ mixture, the photoexcited electrons are rapidly transferred to the adsorbed CO_2 and in the presence of protons (H^+, which are provided by reducing agents) reacts to give the desired products. It is reported that CO_2 is generally

adsorbed in five possible configurations as reported by *Tu et al.* and portrayed in Figure 1.6 [23].

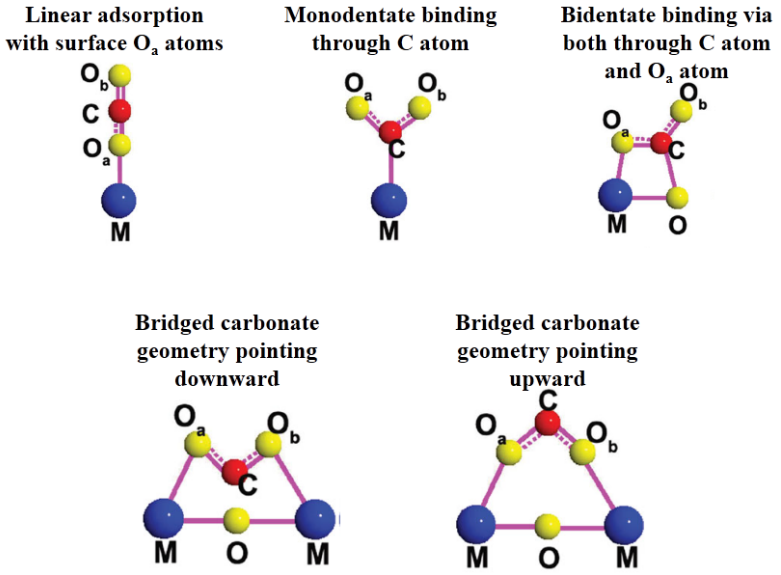

Figure 1.6 Possible adsorption configurations of CO_2 molecule on the photocatalyst surface (blue ball= M, metal of metal oxide, red ball= C, carbon atom of CO_2, yellow balls with **a** and **b** are O atoms for CO_2 and yellow ball without any indication is oxygen atom of metal oxide surface). (Taken from Ref. 23)

The exact pathway for the CO_2 photoreduction is still not clear but depending upon the binding and bridging mode of CO_2 with photocatalyst surface, two key accepted full pathways have been proposed in the literature. These pathways are explained as follow:

I. Carbene pathway [28–31]

In the carbene pathway, $CO_2^{\bullet -}$ radicals are believed to form very quickly by injection of single electron to the surface adsorbed CO_2. These $CO_2^{\bullet -}$ radicals bond to two metal atoms (e.g titanium atoms) in a bidentate mode through a carbon atom. These radicals can react with hydrogen radicals and electrons to form CO as an intermediate product which can remain adsorbed on the photocatalyst surface, further reacting with electrons

and hydrogen radicals to convert to carbon residue. The carbon residue can then reacts with number of electrons and hydrogen radicals in multi-steps to give CH• radical, carbene, methyl radical and finally methanol or methane as key products. The possible reactions reported in the literature for carbene pathway are given as follow:

I. $CO_2 + e^- \rightarrow CO_2^{\bullet -}$

II. $CO_2^{\bullet -} + e^- + H^+ \rightarrow CO + OH^-$

III. $CO + e^- \rightarrow {\bullet}CO^-$

IV. ${\bullet}CO + e^- + H^+ \rightarrow C + OH^-$

V. $C + e^- + H^+ \rightarrow CH{\bullet}$

VI. $CH{\bullet} + e^- + H^+ \rightarrow CH_2$

VII. $CH_2 + e^- + H^+ \rightarrow CH_3$

VIII. $CH_3 + e^- + H^+ \rightarrow CH_4$

IX. $CH_3 + OH^- \rightarrow CH_3OH$

II. Formaldehyde pathway [32,33]

In this pathway the formation of carboxyl radical (·COOH) is mainly favored due to monodentate configuration via binding of one oxygen atom to metal (titanium) atom or binding of materials surface oxygen atom to the carbon atom of the CO_2. The carboxyl radical (·COOH) can react with the hydrogen radical (H·), which is provided via reduction of H_2 or oxidation of water by photogenerated electrons and holes from the photocatalyst respectively, and forms the formic acid. The formic acid proceeds multi-steps of electrons accepting and dehydration reactions to give formaldehyde, methanol and methane. The proposed reactions involved in the formaldehyde pathway are given as follow:

I. $CO_2 + e^- \rightarrow CO_2^{\bullet -}$

II. $CO_2^{\bullet -} + H^+ \rightarrow {\bullet}COOH$

III. ${\bullet}COOH + e^- + H^+ \rightarrow HCOOH$

IV. $HCOOH + e^- + H^+ \rightarrow H_2OOC{\bullet}$

V. $HC{\bullet}OOH + e^- + H^+ \rightarrow HCOH + H_2O$

VI. $HCOH + e^- \rightarrow H_2C{\bullet}O^-$

VII. $H_2C{\bullet}O^- + H^+ \rightarrow H_2OHC{\bullet}$

VIII. $H_2OHC{\bullet} + e^- + H^+ \rightarrow CH_3OH$

IX. $CH_3OH + e^- + H^+ \rightarrow {\bullet}CH_3 + H_2O$

X. ${\bullet}CH_3 + e^- + H^+ \rightarrow CH_4$

1.6 Photocatalytic materials trend

Conventionally the photocatalytic CO_2 reduction or conversion is carried out on variety of inorganic semiconductor materials comprising of metal oxides such as TiO_2 [34], ZnO and NiO [35], metal chalcogenides like CdTe [36], CdS [37], ZnS [38], and various heterosturctured semiconductors [39]. However, apart from inorganic semiconductor materials, there are also several reports on utilizing the metal organic frameworks (MOFs) and organic semiconductors for photoreduction of CO_2 [40,41]. Amongst all materials, inorganic based semiconductor materials are still attractive and potential candidates to be employed and tested in photocatalytic CO_2 conversion and other photocatalytic domains because of their superior light harvesting capability, ease of manufacturing, less toxicity and superb stability. Until today, enormous amount of researches have been conducted to employ inorganic semiconductor materials in a variety of ways and approaches, starting from bare semiconductor photocatalysts to metal/non-metal doped and junctioned semiconductors, all aimed towards the performance and efficiency enhancement of the photocatalytic CO_2 reduction. The key for selecting and choosing a semiconductor material for CO_2 photoreduction is that thermodynamic redox potentials representing the conduction band edge and valence band edge of the respective semiconductor material should be well aligned and matched with the redox potentials of reactants to be reduced and oxidized respectively. Schematic for few renowned photocatalytic materials displaying their conduction band and valence band edges relative to the redox potential of different chemical species [42] is shown in Figure 1.7.

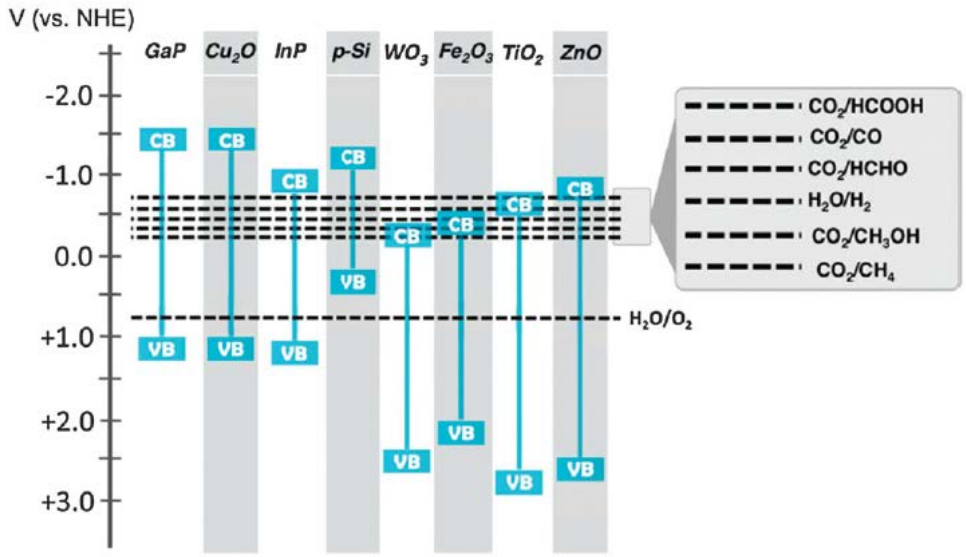

Figure 1.7 Band structures of selected photocatalytic materials *vs.* redox potential of CO_2 reduction reactions and water oxidation reaction (at pH = 0). (Taken from Ref. 42)

Few excerpts from the semiconductor materials trend as a photocatalytic materials for CO_2 photoreduction are selected from reported literature and briefly explained in the below sub-sections.

1.6.1 Single semiconductor photocatalysts

A large amount of various single or bare semiconductors have been employed for photocatalytic applications including CO_2 photoreduction. Over a single semiconductor which provides a simple photocatalytic system but due to very low efficiency, single semiconductors are not observed as an interesting or attractive domain to be investigated. The low efficiency in case of single semiconductor can be attributed to various factors. Firstly, many semiconductor materials possesses wider band gap e.g TiO_2, ZnO which is very good for chemical and environmental stability but on the other hand also limits the sunlight absorption mainly to the Ultra Violet (UV) region which comprises only 4-5 % of the solar spectrum. Hence because of very less light absorption, the performance of these photocatalysts are very

low and not suitable for practical or commercial applications. On the other hand narrow band gap materials like Cu_2O, CdS, CdTe etc. which can absorb a broader region of sunlight (mainly a greater portion of visible light) but exhibit poor performance because of poor charge separation and high charge recombination. Furthermore, for narrower band gap semiconductors another important parameter to consider is well alignment and matching of their conduction and valence band edges for smooth and spontaneous reduction and oxidation reactions, respectively. Second major issue faced in single semiconductor is absence of charge driving force within the bulk volume, thus leading to high volume recombination rate of photoexcited charge carriers. Thirdly as compared to metal surfaces, the semiconductor materials doesn't possess surfaces with high redox activation ability and in addition to volume recombination, the photoexcited electron-hole pairs also recombines at the surface thus limiting the photocatalytic efficiency. Despite of their poor photocatalytic performance, the single semiconductor are still intensively investigated to develop a high performance single semiconductor photocatalyst by various research approaches such as facet engineered semiconductor materials, self-doped semiconductor materials, nanostructured semiconductor materials, metal and non-metal doped semiconductor materials.

1.6.2 Doped semiconductor photocatalysts

Creating defects or vacancies in the semiconductors by self-doping and foreign impurities (external doping) is considered as one of the effective approach to improve their photocatalytic activity. The doping of semiconductor can manipulate and adjust the conduction band and valence band edges by creation of defects or vacancies thus introducing new energy levels around the conduction band and valence band edges or in between the original band gap. The creation of these energy levels can lower the conduction band minimum or rises the valence band maximum, narrowing the band gap of the bare or original semiconductor. As a

representative example, consider herein a well-known champion metal oxide semiconductor, titanium dioxide/TiO_2 for both self-doping, reduced (H-doped) and foreign elements doping. In case of self-doping, oxygen vacancies are created within TiO_2 by high vacuum treatment, knocking out the oxygen atoms and narrowing the band gap. A variety of reduction methods for TiO_2 are also employed using strong reducing agents (H_2 gas, $NaBH_4$, and Mg) leads to formation of several surface defects and high concentration of oxygen vacancies, thus increasing the number of Ti^{3+} ions [43–45]. Such created oxygen vacancies or Ti^{3+} ions lead to formation of localized energy states in form of a sub-band which can overlap the conduction band minimum thus narrowing down the wider band gap of TiO_2. The reduced TiO_2 (TiO_{2-x}) obtained after the self-doping phenomenon can then absorb a broad range of sunlight extending up to visible and near-infrared (NIR) regions.

On the other hand, foreign elements doping of TiO_2 creates impurity energy levels by getting doped into the lattice of TiO_2 or into oxygen vacancies in the TiO_2. For the case of metal doping, such as Cr, Ni, V and Mn, [46] they usually get doped into the TiO_2 lattice creating new energy levels within the band gap. However the metals doping are thermally unstable and usually acts as an electron-hole recombination centers, thus because of such reasons less attention have been given to metal doping of TiO_2. In contrary to metal doping, non-metal elements such as C, N, S and P [47] gets doped to the oxygen vacancies of the TiO_2 lattice. The non-metals usually shifts the valence band of the TiO_2 via creation of impurity energy levels above the valence band maximum. Such upward shift of the valence band maximum, narrows down the band gap and thus provide an opportunity for TiO_2 to harvest broader range of sunlight. Furthermore, the doping effect can be made more significant with more enhanced performance by a co-doping (bi, tri or quad doping of elements) strategy, i.e. doping two or more than two elements for the aim of improved photocatalytic performance. The schematic view for the self-doping and foreign elements doping is shown in Figure 1.8.

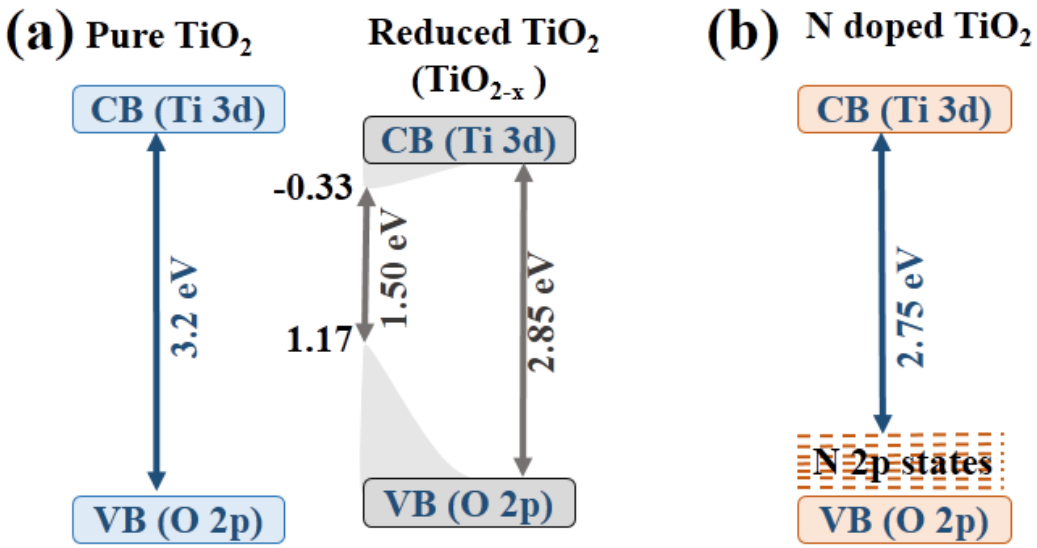

Figure 1.8 Schematic illustration of band structure for (a) self-doped and reduced TiO_2, and (b) foreign element i.e. N doped TiO_2.

1.6.3 Nanostructured semiconductor photocatalysts

Various nanostructures of semiconductors such as nanowires, nanosheets, nanobelts, nanotubes and nanorods are also an extensively studied domain in the field of photocatalytic CO_2 reduction. The key advantage provided by the nanostructured photocatalysts are less grain boundaries and defects as compared to conventional structured materials with higher possibility of single crystal phase thus minimizing the photoexcited electron-hole recombination. In addition, various nanostructures, specifically nanotubes and nanorods provides high surface to volume aspect ratio and a unidirectional pathway for photoexcited electrons to diffuse to surface of photocatalyst. Such pathway improves the separation of photoexcited electron-hole charge carriers thus exhibiting the enhanced performance for the nanostructured photocatalysts. Until now various nanostructured photocatalysts have been investigated in CO_2 photoreduction e.g. TiO_2 nanosheets [48], TiO_2 nanotubes [49], HNb_3O_8 nanoribons [50], $NaNbO_3$ nanowires [51], Zn_2GeO_4 nanowires [52] etc., all these nanostructured photocatalytic materials had shown an enhanced performance in comparison to respective bulk materials.

1.6.4 Graphene based photocatalysts

Since the discovery of Graphene, a breakthrough by Geim and Novoselov in 2004 [53], a great amount of attention and investigation have been involved for the development and application of graphene based materials in broad range of scientific and industrial applications. Graphene is a single layer, two dimensional (2D) carbon layer with hexagonally packed lattice providing some extraordinary and superb properties such as extremely high surface areas (2630 $m^2 \cdot g^{-1}$), excellent electrical conductivity (20000 $cm^2 \cdot V^{-1} \cdot s^{-1}$), high transparency and chemical stability [54]. Due to such extremely marvelous properties of graphene, it has directed the photocatalysis research field to develop graphene based photocatalytic materials for improving their activities and performance. In the field of CO_2 photoreduction, graphene or graphene related materials when coupled with photocatalysts can provide the following benefits, resulting in improved photocatalyst performance:

I. Efficient separation of photoexcited charge carriers, as graphene layers are highly electrical conductive and can provide a direct pathway for the photoexcited electrons to involve in photocatalytic reactions.

II. Improved CO_2 adsorption and activation via Pi-Pi interaction among CO_2 molecules and graphene layers thus leading to improved availability of adsorbed CO_2 on surface resulting in enhanced CO_2 photoreduction.

III. Graphene is also a chemical and light stable material so when wrapped on unstable photocatalytic materials it can provide a moderate to good photo corrosion or chemical stability to such materials.

IV. Graphene or graphene related materials such as graphene oxide, reduced graphene oxide can absorb a broad spectrum of light based on their respective band gap. Therefore the light absorption of the photocatalysts can be improved via coupling with

graphene or graphene related materials, which can help to improve their photocatalytic activities.

V. Lastly because graphene possess an extremely high surface area, also with many surface functional groups so various photocatalytic materials can be linked or grown on the surface of graphene sheets resulting in high surface area and well dispersed graphene coupled photocatalysts.

Until now, various investigations have been done for application of graphene coupled photocatalysts to improve the product yield of CO_2 photoreduction. Moreover to harvest the maximum advantage of 2D graphene sheets, various nanostructures of photocatalysts like nanorods and nanosheets have also been coupled with graphene exhibiting significantly improved performance. Some of the examples of graphene coupled photocatalysts for CO_2 photoreduction includes, rGO-CdS nanorods [55], G-TiO_2 [56], rGO-Cu_2O [57] and G-WO_3 [58]. An illustrative example of graphene based CdS nanorods is displayed in Figure 1.9 showing basic mechanism of CO_2 photoreduction into CH_4.

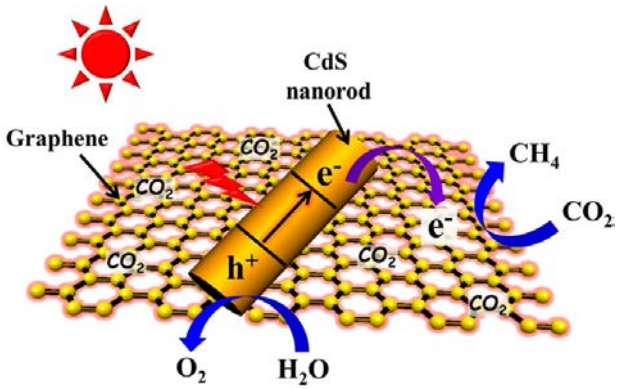

Figure 1.9 Schematic illustration of CdS-graphene composite material for CO_2 photoreduction into CH_4. (Taken from Ref. 55)

1.6.5 Metal loaded photocatalysts

As it is well documented, the volume or surface charge recombination for a photoexcited semiconductor material are the main pathways ceasing the effective charge separation and limiting the photocatalytic efficiency. In this regard, coupling of a metal (mainly noble) with semiconductor materials is a common practice to suppress the charge recombination for improving the charge separation and photocatalytic performance of the semiconductor materials. At present, abundant amount of reports are present for the utilization of metal loading as a co-catalysts on a variety of semiconductors and their application in CO_2 photoreduction such as Rh, Pd, Cu, Au, Ag, Pt etc [23].

The metal loaded on the semiconductor plays role in mainly two ways i.e. (i) Schottky junction and (ii) Plasmonic effect. There exits possibility that both effects can appear simultaneously or separately depending upon the nature of the metal and semiconductor (p-type or n-type) along with the properties of the incident light on the metal loaded photocatalysts.

In case of Schottky junction, an internal electric field is developed at the metal-semiconductor interface via charge transfer from semiconductor (electrons form n-type and holes from p-type semiconductor) due to difference in Fermi levels [26,59]. As an example for the case of n-type semiconductor, when light is irradiated on metal loaded photocatalyst, the electron-hole pairs are generated, the electrons get accumulated in the conduction band whereas the holes in the valence band of the semiconductor leading to charge accumulation. The electron accumulation in the conduction band makes them energetic enough to get transferred into the metal while the holes get filled in the semiconductor. Once the electrons are injected into the metal it is difficult for electron collected on the metal to go back to semiconductor and recombine with holes. Such phenomenon effectively separate the photoexcited electrons resulting in improved photocatalytic performance.

It is observed when light is irradiated on specific noble metals like Cu, Ag, or Au, the photon frequency of the incident light can match with the oscillation frequency of the surface free electrons, giving rise to intense localized electromagnetic field. This oscillation of all surface free electrons on the metals surface is collectively known as localized surface plasmon resonance (LSPR) with its effect commonly known as plasmonic effect [60]. The plasmonic effect induced by metals can be manipulated via tuning the shape and size of the metal nanoparticles. The plasmonic effect induced by metals loaded on semiconductors are categorized mainly in two ways:

I. Firstly, if a metal forms a Schottky junction with a semiconductor then upon light irradiation it can directly inject the electron form the plasmonic metal to the semiconductor conduction band while the hot holes remains on the metal surface to get filled via oxidation reactions.

II. Secondly, upon light absorption, the plasmonic metal can transfer the energy to the coupled semiconductor via the electromagnetic field induced due to collective oscillation. Such energy transfer can generate more electro-hole pairs in the adjacent semiconductor material thus speeding up the charge transfer and photocatalytic reactions.

The pictorial depiction in the reported literature for both Schottky junction and plasmonic effect induced by metals loading is portrayed in Figure 1.10.

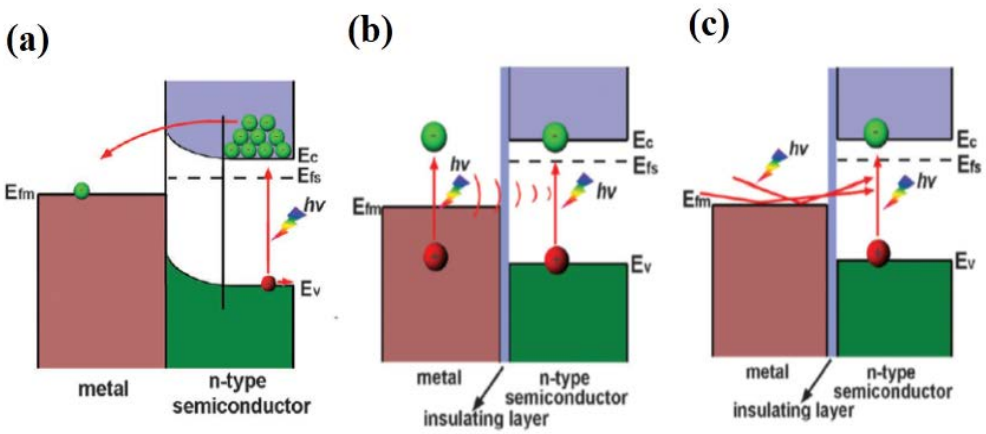

Figure 1.10 Schematic illustration of (a) Schottky junction between metal and n-type semiconductor. (b) & (c) possible two pathways for plasmonic effect between metal and n-type semiconductor. (Taken from Ref. 59)

1.6.6 Semiconductor–semiconductor junction photocatalysts

Another efficient and attractive approach to improve the performance of photocatalyst systems is fabricating a heterostructure of two different semiconductor materials via coupling them together. Such an approach provides three key advantages to a photocatalyst system.

I. Extending the light absorption of the photocatalyst system by making suitable junction between a narrow and a wider band gap semiconductors.

II. Improved photogenerated charge separation via built-in electric field induced at the semiconductor-semiconductor interface due to charge transfer between both the materials as a result of Fermi level difference. Such an effective charge separation can in turn speed up the transfer of photogenerated electrons or holes for reduction and oxidation reactions respectively.

III. The semiconductor-semiconductor junctioned photocatalyst also provide the opportunity of preventing a semiconductor material form photo-corrosion by coating another stable semiconductor material on an unstable material.

Again the important step for fabricating the semiconductor-semiconductor junction is selecting and choosing materials with suitable and well aligned band gaps amongst them, as well as one of them well matching with the redox potentials of reduction and oxidation reactions. The most commonly selected and fabricated semiconductor-semiconductor junction or heterostructured semiconductors in the field of CO_2 photoreduction are mainly categorized as

a) p-n junction photocatalysts.
b) Z-scheme photocatalysts.

a) p-n junction photocatalysts

p-n junction between two semiconductors is created when one the semiconductor material is p-type and another is n-type in nature. When both materials come in contact, because of difference in Fermi level the charge (electrons from n-type and holes from p-type) flows amongst each other to equilibrate the Fermi level with respective band shifting for each material (downward for n-type and upward for p-type). After short interval, an electric field is developed due to charge transfer at the semiconductor-semiconductor interface which acts as a barrier (depletion layer) for further charge to be interchanged. When the light is irradiated on such a heterostructured photocatalyst system, electrons generated in the p-type material are attracted towards n-type due to induced electric field resulting in the effective charge separation and accumulation of electrons in conduction band of n-type material whereas the holes gets accumulated in the valence band of p-type material. Such accumulations of electrons and holes can then foster the respective reduction and oxidation reactions. The pictorial depiction of the mechanism involved in the p-n junction photocatalytic system is depicted in Figure 1.11a. Some of the common examples of p-n junction photocatalysts employed for CO_2

photoreduction include GaP-TiO_2 [61], CuO-$TiO_{2-x}N_x$ [62], CZTS-TiO_2 [63], Cu_2O-ZnO [64] etc.

b) Z-scheme photocatalysts

Another commonly used heterostructured photocatalyst is Z-scheme photocatalyst with staggered alignment of band structures. Such alignment directs each semiconductor material to perform oxidation or reduction half reactions separately. Upon light illumination, the electron-hole (e^-/h^+) pairs are generated in both semiconductors, the electrons form the semiconductor 1 (SC1) with a higher conduction band will proceed the reduction reaction while the holes of SC1 are filled by the electrons coming from the semiconductor 2 (SC2) with lower conduction band. In turn the holes remaining in the SC2 can be filled by oxidation half reaction. The main benefits of Z-scheme photocatalysts is that they provide a very effective manner to separate the photogenerated charge carriers with keeping the stability of the photocatalytic system. The pictorial illustration for the Z-scheme photocatalytic system mechanism is depicted in Figure 1.11b. Few examples for the Z-scheme photocatalysts employed for CO_2 photoreduction includes Si-TiO_2 [65], BiOI-gC_3N_4 [66], Fe_2O_3-CuO [67]etc.

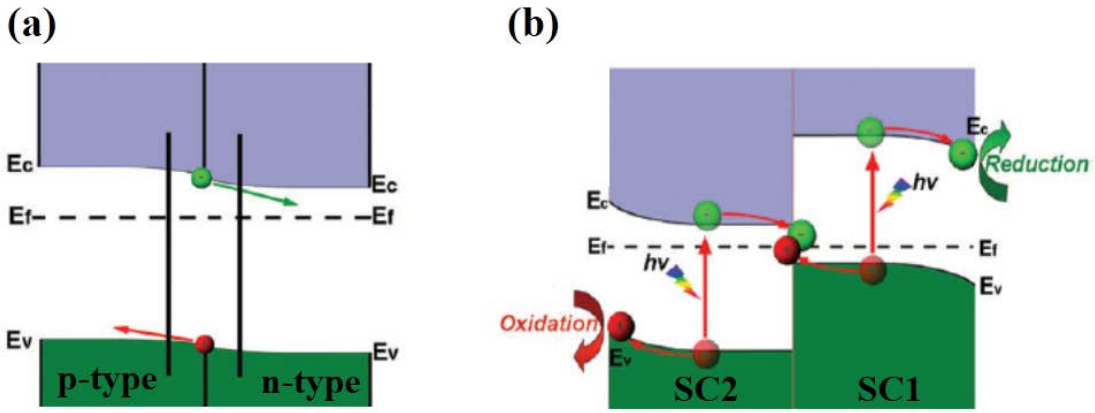

Figure 1.11. Schematic illustration (a) p-n junction photocatalyst (b) Z-scheme photocatalyst. (Take from Ref. 59)

1.7 Research objectives and approaches

The photocatalytic CO_2 conversion/CO_2 photoreduction into useful chemicals and fuels, unlike thermally or electrochemically activated catalysis, is activated in a sustainable manner by solar energy. After the pioneering work by Inoue et al. in 1979 for the photocatalytic conversion of CO_2 into organic compounds via various semiconductor powders such as TiO_2, WO_3, ZnO and CdS in aqueous solution [22], many researches have been reported on liquid based CO_2 conversion. However, for practical applications, gas phase CO_2 conversion is more desirable and an enormous amount of work has been demonstrated for the direct conversion of CO_2 gas to hydrocarbon fuels. As mentioned previously, CO_2 is a thermodynamically very stable compound and requires additional energy to get converted into useful products. However, in addition to the activation barrier offered by CO_2 thermodynamics, there is also an activation barrier in the charge-transfer process between photocatalysts and CO_2 molecules, necessitating photon energies greater than theoretically required. Therefore efforts are needed to develop an efficient photocatalyst system providing:

a) Improved light absorption to harvest the maximum sunlight which can in turn enhance the CO_2 photoreduction reactions. Various strategies employed in this regard, includes self-doped and foreign elements doped photocatalysts, coupled photocatalysts, plasmonic metals coupled photocatalysts, using light up-conversion and light scattering/trapping phenomena in photocatalysts.
b) Efficient separation of photogenerated charges for improved charge transfer resulting in accelerated redox reactions can potentially enhance the CO_2 photoreduction yields. It has been observed that the charge recombination is 2-3 times faster than the charge separation and transfer hence enormous investigation should focus on this critical issue to make CO_2 photoreduction process efficient. Several strategies aimed for improved charge separation

includes heterojunctioned semiconductors (p-n junction, n-n junction, Z-scheme), metal loaded photocatalysts, graphene based photocatalysts etc.

c) Photocatalysts with high surface areas, porosity and good affinity for CO_2 adsorption can also help in boosting the CO_2 photoreduction process via enhanced CO_2 adsorption and activation. Various strategies like surface functionalization with CO_2 adsorbent groups (e.g. amines), metal organic frameworks (MOFs), and creating oxygen vacancies have been employed to enhance the adsorption and activation of CO_2.

d) Lastly, with the development of most efficient systems, serious intentions should also be focused toward the development of low cost, non-toxic, industrially scalable, chemically and thermally stable photocatalyst systems to make the field commercially applicable in real sense.

Amongst various semiconductors, TiO_2 due to its advantages of excellent oxidation properties and stable behavior is considered to be one of the most appropriate material for photoreduction of CO_2 into fuels. However, photocatalytic reactions mediated by TiO_2 alone are limited due to its wide bandgap of 3.2 eV. The excited electrons available for chemical reactions by TiO_2 are generated by absorption of ultraviolet light and thus, TiO_2 itself does not contribute much to the photocatalytic production of hydrocarbon fuels. Until now various strategies like self and foreign elements doped semiconductors, nanostructured photocatalysts, graphene coupled semiconductors and metal loaded semiconductors are being executed for performance and productivity enhancement of the CO_2 photoreduction. Despite of extensive amount of research, still a plenty can be done to improve the performance and productivity in this research area with focused strategy. Hence aimed towards the performance enhancement of TiO_2 based photocatalysts with respect to its utility for CO_2 photoreduction, various attempts were made during the span of Ph.D. degree and are presented in the current research document.

In the first part of my research work, an attempt was made by employing foreign elements co-doped layered sodium titanate structures i.e. nanotubes (Na^+-TNT) for CO_2 photoreduction. The Na^+-TNT are synthesized using highly alkaline hydrothermal treatment of TiO_2 nanoparticles. Technically these layered titanate nanotubes can provide the higher surface area to volume ratio and vectorial charge transport as compared to the spherical nanoparticles. These two benefits can enhance the performance of the respective photocatalyst by providing more active sites and reduced charge recombination. Furthermore it is reported that the Na ions (Na^+) intercalated between the titanate interlayers can significantly enhance the CO_2 adsorption and thus can improve the CO_2 photoconversion rate. Being inspired form such interesting properties of Na^+-TNT and co-doping effect, we selected herein non-metals i.e. C and N form same source urea, as a co-dopants to improve the photocatalytic activity for Na^+-TNT. The strategy employed here was aimed to improve photocatalytic activity of Na^+-TNT by extending its light absorption via C,N co-doping. Therefore, Na^+-TNT with high surface area and intercalated Na^+ ions can improve the photocatalyst performance by improved light absorption and enhanced CO_2 adsorption.

In the second experimental approach, an attempt was made to develop a noble-metal free nanostructured photocatalyst and test its utility in CO_2 photoreduction. During the last few years, graphene and graphene related materials have received a great attention in photocatalysis specifically due to its high surface area and excellent electron mobility. Thus being motivated from it, we designed a specific experimental strategy resulting in a novel nanostructure i.e. reduced graphene oxide (rGO) with embedded TiO_2 nanoparticles on the surface of TiO_2 nanotubes arrays. Such a novel nanostructure improved the CO_2 photoreduction process mainly due to enhanced light absorption and efficient charge separation.

The third experimental approach is focused towards the investigation of reduced TiO_2 (RT) or TiO_{2-x} for CO_2 photoreduction process. RT was synthesized using a newly developed

synthesis approach, magnesiothermic reduction utilizing Mg in 5% H_2/Ar. The RT obtained using such method showed improved CO_2 photoreduction as compared to pristine TiO_2. It is believed that reduction of TiO_2 increases the number of defects i.e. Ti^{3+} ions and oxygen vacancies (V_o) which results in generation of new energy levels and band tailing effect. Due to creation of new energy levels, the light absorption is increased in RT and can absorb a broad range of sunlight as compared to pristine TiO_2 which only absorbs UV light. Furthermore it is also believed that oxygen vacancies also improves the CO_2 adsorption on the RT surfaces. Hence to investigate such an attractive properties of RT, we synthesized RT by a new approach and then tested its photochemical activity by employing RT samples in CO_2 photoreduction. Moreover to improve the charge separation, platinum (Pt) noble metal was also loaded onto catalyst which resulted in a superb CO_2 photoreduction performance.

1.8 References

[1] S.R. Mudakkar, K. Zaman, M.M. Khan, M. Ahmad, Energy for economic growth, industrialization, environment and natural resources: Living with just enough, Renew. Sustain. Energy Rev. 25 (2013) 580–595. doi:10.1016/j.rser.2013.05.024.

[2] Key World Energy Trends Excerpt from : World energy balances, Int. Energy Agency. (2016) 3–6. www.iea.org/statistics/topics/energybalances/.

[3] P. Poizot, F. Dolhem, Clean energy new deal for a sustainable world: from non-CO_2 generating energy sources to greener electrochemical storage devices, Energy Environ. Sci. 4 (2011) 2003. doi:10.1039/c0ee00731e.

[4] A.J. McMichael, J.W. Powles, C.D. Butler, R. Uauy, Food, livestock production, energy, climate change, and health, Lancet. 370 (2007) 1253–1263. doi:10.1016/S0140-6736(07)61256-2.

[5] M. Meinshausen, N. Meinshausen, W. Hare, S.C.B. Raper, K. Frieler, R. Knutti, D.J. Frame, M.R. Allen, Greenhouse-gas emission targets for limiting global warming to 2 degrees C., Nature. 458 (2009) 1158–1162. doi:10.1038/nature08017.

[6] A. Carlsson-Kanyama, Climate change and dietary choices - how can emissions of greenhouse gases from food consumption be reduced?, Food Policy. 23 (1998) 277–293. doi:10.1016/S0306-9192(98)00037-2.

[7] G.P. Robertson, E.A. Paul, R.R. Harwood, Greenhouse Gases in Intensive Agriculture: Contributions of Individual Gases to the Radiative Forcing of the Atmosphere, Science 289 (2000) 1922–1925. doi:10.1126/science.289.5486.1922.

[8] I. Statistics, CO_2 Emissions From Fuel Combustion Highlights, Int. Energy Agency. (2015) 7–17.

[9] A. Goeppert, M. Czaun, J.-P. Jones, G.K. Surya Prakash, G.A. Olah, Recycling of carbon dioxide to methanol and derived products-closing the loop, Chem. Soc. Rev. 43

(2014) 7995–8048. doi:10.1039/C4CS00122B.

[10] https://www.ipcc.ch/publications_and_data.

[11] G. A. Meehl, W.M. Washington, W.D. Collins, How Much More Global Warming and Sea Level Rise, Science. 1769 (2009) 1769–1773. doi:10.1126/science.1106663.

[12] A. Haines, A.J. McMichael, K.R. Smith, I. Roberts, J. Woodcock, A. Markandya, B.G. Armstrong, D. Campbell-Lendrum, A.D. Dangour, M. Davies, N. Bruce, C. Tonne, M. Barrett, P. Wilkinson, Public health benefits of strategies to reduce greenhouse-gas emissions: overview and implications for policy makers, Lancet. 374 (2009) 2104–2114. doi:10.1016/S0140-6736(09)61759-1.

[13] R. Darwin, Effects on greenhouse gas emissions on world agriculture, food consumption, and economic welfare, Clim. Change. 66 (2004) 191–238. doi:10.1023/B:CLIM.0000043138.67784.27.

[14] G.A. Olah, G.K.S. Prakash, A. Goeppert, Anthropogenic chemical carbon cycle for a sustainable future. J.Am. Chem. Soc. 133 (2011) 12881–12898. doi:10.1021/ja202642y.

[15] J.S. Landry, H.D. Matthews, Non-deforestation fire vs. fossil fuel combustion: The source of CO_2 emissions affects the global carbon cycle and climate responses, Biogeosciences. 13 (2016) 2137–2149. doi:10.5194/bg-13-2137-2016.

[16] P. Markewitz, W. Kuckshinrichs, W. Leitner, J. Linssen, P. Zapp, R. Bongartz, A. Schreiber, T.E. Müller, Worldwide innovations in the development of carbon capture technologies and the utilization of CO_2, Energy Environ. Sci. 5 (2012) 7281. doi:10.1039/c2ee03403d.

[17] J.A. Herron, J. Kim, A.A. Upadhye, G.W. Huber, C.T. Maravelias, A general framework for the assessment of solar fuel technologies, Energy Environ. Sci. 8 (2015) 126–157. doi:10.1039/C4EE01958J.

[18] M. Mikkelsen, M. Jørgensen, F.C. Krebs, The Teraton Challenge. A Review of Fixation

and Transformation of Carbon Dioxide, Energy Environ. Sci. 3 (2010) 43–81. doi:10.1039/B912904A.

[19] A. Scibioh, B. Viswanathan, Electrochemical reduction of carbon dioxide a status report, Proc. Natl. Acad. Sci. India Sect. A Phys. Sci. 70 (2004) 407.

[20] A. Fujishima, K. Honda, Electrochemical photolysis of water at a semiconductor electrode., Nature. 238 (1972) 37–38. doi:10.1038/238037a0.

[21] M. Halmann, Photoelectrochemical reduction of aqueous carbon dioxide on p-type gallium phosphide in liquid junction solar cells, Nature. 275 (1978) 115–116. doi:10.1038/275115a0.

[22] T. Inoue, A. Fujishima, S. Konishi, K. Honda, Photoelectrocatalytic reduction of carbon dioxide in aqueous suspensions of semiconductor powders, Nature. 277 (1979) 637–638. doi:10.1038/277637a0.

[23] W. Tu, Y. Zhou, Z. Zou, Photocatalytic conversion of CO_2 into renewable hydrocarbon fuels: State-of-the-art accomplishment, challenges, and prospects, Adv. Mater. 26 (2014) 4607–4626. doi:10.1002/adma.201400087.

[24] J.L. White, M.F. Baruch, J.E. Pander, Y. Hu, I.C. Fortmeyer, J.E. Park, T. Zhang, K. Liao, J. Gu, Y. Yan, T.W. Shaw, E. Abelev, A.B. Bocarsly, Light-Driven Heterogeneous Reduction of Carbon Dioxide: Photocatalysts and Photoelectrodes, Chem. Rev. 115 (2015) 12888–12935. doi:10.1021/acs.chemrev.5b00370.

[25] K. Kabra, R. Chaudhary, R.L. Sawhney, Treatment of Hazardous Organic and Inorganic Compounds through Aqueous-Phase Photocatalysis: A Review, Ind. Eng. Chem. Res. 43 (2004) 7683–7696. doi:10.1021/ie0498551.

[26] A.L. Linsebigler, A.L. Linsebigler, J.T. Yates Jr, G. Lu, G. Lu, J.T. Yates, Photocatalysis on TiO_2 Surfaces: Principles, Mechanisms, and Selected Results, Chem. Rev. 95 (1995) 735–758. doi:10.1021/cr00035a013.

[27] S.N. Habisreutinger, L. Schmidt-Mende, J.K. Stolarczyk, Photocatalytic reduction of CO_2 on TiO_2 and other semiconductors, Angew. Chemie - Int. Ed. 52 (2013) 7372–7408. doi:10.1002/anie.201207199.

[28] M. Anpo, H. Yamashita, Y. Ichihashi, S. Ehara, Photocatalytic reduction of CO_2 with H_2O on various titanium oxide catalysts, J. Electroanal. Chem. 396 (1995) 21–26. doi:10.1016/0022-0728(95)04141-A.

[29] I.A. Shkrob, N.M. Dimitrijevic, T.W. Marin, H. He, P. Zapol, Heteroatom-transfer coupled photoreduction and carbon dioxide fixation on metal oxides, J. Phys. Chem. C. 116 (2012) 9461–9471. doi:10.1021/jp300123z.

[30] S.S. Tan, L. Zou, E. Hu, Kinetic modelling for photosynthesis of hydrogen and methane through catalytic reduction of carbon dioxide with water vapour, Catal. Today. 131 (2008) 125–129. doi:10.1016/j.cattod.2007.10.011.

[31] H. He, P. Zapol, L.A. Curtiss, Computational screening of dopants for photocatalytic two-electron reduction of CO_2 on anatase (101) surfaces, Energy Environ. Sci. 5 (2012) 6196. doi:10.1039/c2ee02665a.

[32] M. Subrahmanyam, S. Kaneco, N. Alonso-Vante, A screening for the photo reduction of carbon dioxide supported on metal oxide catalysts for C1-C3 selectivity, Appl. Catal. B Environ. 23 (1999) 169–174. doi:10.1016/S0926-3373(99)00079-X.

[33] N. Sasirekha, S.J.S. Basha, K. Shanthi, Photocatalytic performance of Ru doped anatase mounted on silica for reduction of carbon dioxide, Appl. Catal. B Environ. 62 (2006) 169–180. doi:10.1016/j.apcatb.2005.07.009.

[34] A. Dhakshinamoorthy, S. Navalon, A. Corma, H. Garcia, Photocatalytic CO_2 reduction by TiO_2 and related titanium containing solids, Energy Environ. Sci. 5 (2012) 9217. doi:10.1039/c2ee21948d.

[35] A.H. Yahaya, M.A. Gondal, A. Hameed, Selective laser enhanced photocatalytic

conversion of CO_2 into methanol, Chem. Phys. Lett. 400 (2004) 206–212. doi:10.1016/j.cplett.2004.10.109.

[36] B. Aurian-Blajeni, M. Ahsan Habib, I. Taniguchi, J.O. Bockris, The study of adsorbed species during the photoassisted reduction of carbon dioxide at a p-CdTe electrode, J. Electroanal. Chem. Interfacial Electrochem. 157 (1983) 399–404. doi:10.1016/S0022-0728(83)80367-2.

[37] B.R. Eggins, J.T.S. Irvine, E.P. Murphy, J. Grimshaw, Formation of two-carbon acids from carbon dioxide by photoreduction on cadmium sulphide, J. Chem. Soc. Chem. Commun. (1988) 1123–1124. doi:10.1039/c39880001123.

[38] B.R. Eggins, P.K.J. Robertson, E.P. Murphy, E. Woods, J.T.S. Irvine, Factors affecting the photoelectrochemical fixation of carbon dioxide with semiconductor colloids, J. Photochem. Photobiol. A Chem.118 (1998) 31–40. doi:10.1016/S1010-6030(98)00356-6.

[39] Y.-P. Yuan, L.-W. Ruan, J. Barber, S.C. Joachim Loo, C. Xue, Hetero-nanostructured suspended photocatalysts for solar-to-fuel conversion, Energy Environ. Sci. 7 (2014) 3934–3951. doi:10.1039/C4EE02914C.

[40] S. Zhang, L. Li, S. Zhao, Z. Sun, J. Luo, Construction of Interpenetrated Ruthenium Metal-Organic Frameworks as Stable Photocatalysts for CO_2 Reduction, Inorg. Chem. 54 (2015) 8375–8379. doi:10.1021/acs.inorgchem.5b01045.

[41] Q. Liu, Z.-X. Low, L. Li, A. Razmjou, K. Wang, J. Yao, H. Wang, ZIF-8/Zn_2GeO_4 nanorods with an enhanced CO_2 adsorption property in an aqueous medium for photocatalytic synthesis of liquid fuel, J. Mater. Chem. A. 1 (2013) 11563. doi:10.1039/c3ta12433a.

[42] J. Rongé, T. Bosserez, D. Martel, C. Nervi, L. Boarino, F. Taulelle, G. Decher, S. Bordiga, J.A. Martens, Monolithic cells for solar fuels., Chem. Soc. Rev. 43 (2014)

7963–81. doi:10.1039/c3cs60424a.

[43] A. Naldoni, M. Allieta, S. Santangelo, M. Marelli, F. Fabbri, S. Cappelli, C.L. Bianchi, R. Psaro, V. Dal Santo, Effect of nature and location of defects on bandgap narrowing in black TiO_2 nanoparticles, J. Am. Chem. Soc. 134 (2012) 7600–7603. doi:10.1021/ja3012676.

[44] X. Xin, T. Xu, L. Wang, C. Wang, Ti^{3+}-self doped brookite TiO_2 single-crystalline nanosheets with high solar absorption and excellent photocatalytic CO_2 reduction., Sci. Rep. 6 (2016) 23684. doi:10.1038/srep23684.

[45] A. Sinhamahapatra, J.-P. Jeon, J. Kang, B. Han, J.-S. Yu, Oxygen-Deficient Zirconia (ZrO_{2-x}): A New Material for Solar Light Absorption, Sci. Rep. 6 (2016) 27218. doi:10.1038/srep27218.

[46] J.S. M. Fuerte, A.J. Maira, A. Martinez-Arias, M. Fernadez-Garcia, J.C. Conesa, Visible light-activated nanosized doped-TiO_2 photocatalysts, Chem. Commun. vol. 24 (2001) 2718–2719. doi:10.1039/b107314a.

[47] R. Asahi, Visible-Light Photocatalysis in Nitrogen-Doped Titanium Oxides, Science 293 (2001) 269–271. doi:10.1126/science.1061051.

[48] H. Xu, S. Ouyang, P. Li, T. Kako, J. Ye, High-active anatase TiO_2 nanosheets exposed with 95% {100} facets toward efficient H_2 evolution and CO_2 photoreduction, ACS Appl. Mater. Interfaces. 5 (2013) 1348–1354. doi:10.1021/am302631b.

[49] O.K. Varghese, M. Paulose, T.J. LaTempa, C.A. Grimes, High-Rate Solar Photocatalytic Conversion of CO_2 and Water Vapor to Hydrocarbon Fuels, Nano Lett. 9 (2009) 731–737. http://pubs.acs.org/doi/abs/10.1021/nl803258p.

[50] X. Li, H. Pan, W. Li, Z. Zhuang, Photocatalytic reduction of CO_2 to methane over HNb_3O_8 nanobelts, Appl. Catal. A Gen. 413-414 (2012) 103–108. doi:10.1016/j.apcata.2011.10.044.

[51] H. Shi, T. Wang, J. Chen, C. Zhu, J. Ye, Z. Zou, Photoreduction of carbon dioxide over $NaNbO_3$ nanostructured photocatalysts, Catal. Letters. 141 (2011) 525–530. doi:10.1007/s10562-010-0482-1.

[52] Q. Liu, Y. Zhou, J. Kou, X. Chen, Z. Tian, J. Gao, S. Yan, Z. Zou, High-yield synthesis of ultralong and ultrathin Zn_2GeO_4 nanoribbons toward improved photocatalytic reduction of CO_2 into renewable hydrocarbon fuel., J. Am. Chem. Soc. 132 (2010) 14385–14387. doi:10.1021/ja1068596.

[53] K. S. Novoselov, A.K. Geim, S. V. Morozov, D. Jiang, Y. Zhang, S. V. Dubonos, I. V. Grigorieva, A.A. Firsov, Electric Field Effect in Atomically Thin Carbon Films, Science. 306 (2004) 666–669.

[54] A.K. Geim, Graphene : Status and Prospects, Science. 320 (2009) 1530–1534. doi:10.1126/science.1158877.

[55] J. Yu, J. Jin, B. Cheng, M. Jaroniec, A noble metal-free reduced graphene oxide–CdS nanorod composite for the enhanced visible-light photocatalytic reduction of CO_2 to solar fuel, J. Mater. Chem. A. 2 (2014) 3407. doi:10.1039/c3ta14493c.

[56] W. Tu, Y. Zhou, Q. Liu, S. Yan, S. Bao, X. Wang, M. Xiao, Z. Zou, An in situ simultaneous reduction-hydrolysis technique for fabrication of TiO_2-graphene 2D sandwich-like hybrid nanosheets: Graphene-promoted selectivity of photocatalytic-driven hydrogenation and coupling of CO_2 into methane and ethane, Adv. Funct. Mater. 23 (2013) 1743–1749. doi:10.1002/adfm.201202349.

[57] X. An, K. Li, J. Tang, Cu_2O/reduced graphene oxide composites for the photocatalytic conversion of CO_2, ChemSusChem. 7 (2014) 1086–1093. doi:10.1002/cssc.201301194.

[58] P.Q. Wang, Y. Bai, P.Y. Luo, J.Y. Liu, Graphene-WO_3 nanobelt composite: Elevated conduction band toward photocatalytic reduction of CO_2 into hydrocarbon fuels, Catal. Commun. 38 (2013) 82–85. doi:10.1016/j.catcom.2013.04.020 Short Communication.

[59] S. Bai, J. Jiang, Q. Zhang, Y. Xiong, Steering charge kinetics in photocatalysis: intersection of materials syntheses, characterization techniques and theoretical simulations, Chem. Soc. Rev. 44 (2015) 2893–2939. doi:10.1039/C5CS00064E.

[60] S. Linic, P. Christopher, D.B. Ingram, Plasmonic-metal nanostructures for efficient conversion of solar to chemical energy, Nat. Mater. 10 (2011) 911–921. doi:10.1038/nmat3151.

[61] G. Zeng, J. Qiu, Z. Li, P. Pavaskar, S.B. Cronin, CO_2 Reduction to Methanol on TiO_2-Passivated GaP Photocatalysts, ACS Catal. 4 (2014) 3512–3516. doi:10.1021/cs500697w.

[62] S. Il In, D.D. Vaughn, R.E. Schaak, Hybrid CuO-$TiO_{2-x}N_x$ hollow nanocubes for photocatalytic conversion of CO_2 into methane under solar irradiation, Angew. Chemie - Int. Ed. 51 (2012) 3915–3918. doi:10.1002/anie.201108936.

[63] K. Kim, A. Razzaq, S. Sorcar, Y. Park, C.A. Grimes, S.-I. In, Hybrid mesoporous Cu_2ZnSnS_4 (CZTS)–TiO_2 photocatalyst for efficient photocatalytic conversion of CO_2 into CH_4 under solar irradiation, RSC Adv. 6 (2016) 38964–38971. doi:10.1039/C6RA02763F.

[64] W.N. Wang, F. Wu, Y. Myung, D.M. Niedzwiedzki, H.S. Im, J. Park, P. Banerjee, P. Biswas, Surface Engineered CuO Nanowires with ZnO Islands for CO_2 Photoreduction, ACS Appl. Mater. Interfaces. 7 (2015) 5685–5692. doi:10.1021/am508590j.

[65] Y. Liu, G. Ji, M.A. Dastageer, L. Zhu, J. Wang, B. Zhang, X. Chang, M.A. Gondal, Highly-active direct Z-scheme Si/TiO_2 photocatalyst for boosted CO_2 reduction into value-added methanol, RSC Adv. 4 (2014) 56961–56969. doi:10.1039/C4RA10670A.

[66] J.C. Wang, H.C. Yao, Z.Y. Fan, L. Zhang, J.S. Wang, S.Q. Zang, Z.J. Li, Indirect Z-Scheme BiOI/g-C_3N_4 Photocatalysts with Enhanced Photoreduction CO_2 Activity under Visible Light Irradiation, ACS Appl. Mater. Interfaces. 8 (2016) 3765–3775.

doi:10.1021/acsami.5b09901.

[67] J.-C. Wang, L. Zhang, W.-X. Fang, J. Ren, Y.-Y. Li, H.-C. Yao, J.-S. Wang, Z.-J. Li, Enhanced Photoreduction CO_2 Activity over Direct Z-Scheme α-Fe_2O_3/Cu_2O Heterostructures under Visible Light Irradiation, ACS Appl. Mater. Interfaces. 7 (2015) 8631–8639. doi:10.1021/acsami.5b00822.

Chapter 2. Characterization and analysis tools

2.1 Characterization tools

The photocatalysts developed during the research span were characterized to investigate their intrinsic and developed properties. Certain number of characterization tools were used and are appropriately explained in the below sub-sections.

2.1.1 X-ray diffraction (XRD)

X-ray diffraction (XRD) is a well-known and very common tool used in the field of materials science to determine and investigate the crystalline properties and phases of the materials and quantitative analysis regarding the relative composition of various phases in the respective sample [1]. Besides these, XRD information can also be used to determine the crystallite size of the materials synthesized (using Scherrer equation). As mostly XRD is employed for powder samples so sometimes it is also termed as powder XRD. There are certain XRD methods to determine the fine crystalline structure for thin films, polymer aggregates, fibers, single crystal substances like wide angle XRD (WAXD) and high resolution XRD (HRXRD).

As obvious form its name, XRD involves the X-rays in its measurement process. The X-rays are electromagnetic waves with high energy and very short wavelength (λ=0.5-2.5Å) discovered by a Noble prize winner German physicist, Roentgen in 1895. Later on in 1912, Max von Laue (German physicist, noble prize in 1914) invented that when such X-rays are incident onto the crystals, then these are diffracted in a specific manner and can give the information regarding the crystalline structure of the substance.

a) Theoretical background

The fundamental theory involved in the XRD is well defined by the basic law of diffraction i.e. Braggs law, a specific information for X-ray diffraction explained by William Henry Bragg in 1923. This law states that when two light waves having the same wavelength travels in one direction, they can either reinforce or cancel out each other upon interaction which depends upon the phase difference between them. If they have phase difference equals to nλ, where n is an integer, constructive interference occurs. On the other hand if the phase difference is nλ/2, the destructive interference occurs.

As atoms in a crystalline materials are well arranged in various oriented crystallographic planes. So when the X-rays of equal wavelength (beam 1 and 2) are incident on the crystalline material (Figure 2.1), the incident waves are reflected or diffracted back are in phase with each other as represented by beam 1′ and 2′, then the reflected beam will have increased intensity and the difference of path length between 1 to 1′ and 2 to 2′ should be an integral number n of wavelength. Based on this information, Bragg propose a law which is given as

$$2d \sin\theta = n\lambda \qquad (2.1)$$

Where θ= scattering angle, d= interplanar spacing, λ= wavelength of beam.

It is obvious form the figure that the incident beam makes an angle θ with the fixed crystal plane, however the deflected or diffracted beams make an angle 2θ with the incident beam. Thus the angle 2θ is needed to be determine at which the diffraction from certain crystallographic plane occurs giving the intrinsic phase information regarding the material. The possible 2θ values are determined by the dimensions of unit cell such as lattice parameter (a) and the Miller indices (hkl) of the respective planes. When the Bragg's law conditions are satisfied, the constructive interferences usually appears as light spots and represents the crystallographic planes (hkl). Combining all the spots of crystallographic planes from a material under investigation, a reciprocal crystal lattice can be formed which represents a three-

dimensional array of the crystal. Furthermore using the information and concept of reciprocal lattice, *Ewald sphere* can also be drawn to present the graphical expression of the crystal lattice, a separated sub-domain of XRD field.

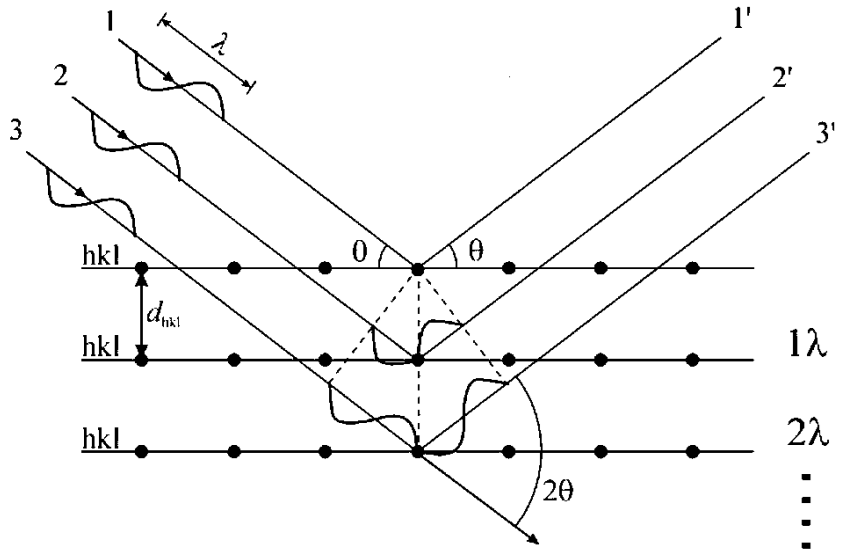

Figure 2.1 Illustration of X-rays diffraction by crystal planes satisfying the Braggs conditions. (Taken from Ref. 1)

b) Instrumentation

The basic instrumental arrangement for an XRD is demonstrated in Figure 2.2b. The key components of an XRD instrument includes an X-ray source, specimen holder and a detector. The x-rays beam generated by X-ray tube are allowed to pass through the solar slits, made of thin metal plates and prevents the divergence of the beam. The slight divergent X-rays from the solar slits then passes through the slit and strikes the sample placed on the holder (usually flat plate). The samples causes the diffraction of the X-rays and is detected by a detector after passing through a convergence and solar slits. Before coming to the detector the X-rays from sample are passed through a monochromatic filter which can suppress the source radiations and the noise background radiations originating within the sample. For the generation of the X-rays, X-rays tubes are used which consists of a source of electrons and two metal electrodes

in vacuum tube (figure 2.2a). When a high voltage is applied across the electrodes, the electrons are drawn towards the anode where they can strike with the anode material and can generate the X-rays in random directions. The commonly used X-ray source is Copper Kα.

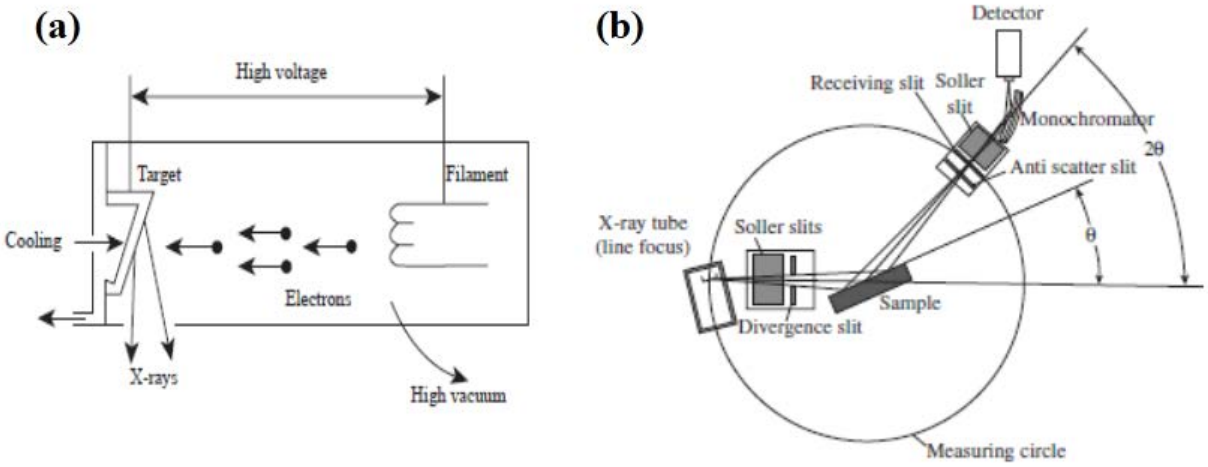

Figure 2.2 Demonstration of **(a)** X-rays generation and **(b)** key components of an X-ray diffraction instrument. (Taken from Ref. 1)

An example of the XRD data is shown in Figure 2.3 where one can see the various peaks appearing at 2θ values corresponding to various planes of the respective material. The data acquisition and conversion is mainly done by the computer linked to the XRD machine. The choice of 2θ angle range depends upon the sample analyzed, however for an un-known sample the range of 2θ is commonly set about 5-65° with a suitable value of scanning rate and step width in a stepwise XRD machine.

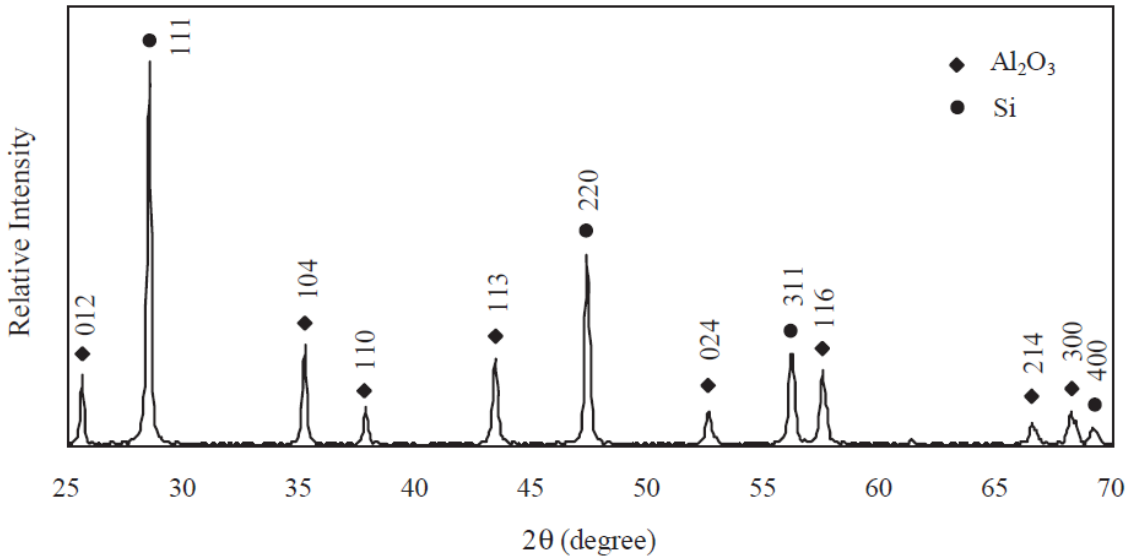

Figure 2.3 Demonstration of an example of XRD data obtained for silicon and alumina mixture showing the miller indices for corresponding crystal planes indicated by three digits. (Taken from Ref. 1)

2.1.2 Raman spectroscopy

The spectroscopy field is the study of electromagnetic waves interaction with the matter based upon the absorption, emission, fluorescence and scattering phenomena. As obvious form its name Raman spectroscopy, was invented by C.V. Raman (Noble prize 1930) and K. F. Krishnan in 1928, who discovered the inelastic scattering of the light from the samples and experimentally demonstrate such phenomenon [2]. In their original experiments they used a simple telescope through which a sunlight was focused to a sample and then detected the scattered light from the sample with an altered frequency when compared to that of incident light. During the 1960s, with the invention of lasers and a non-destructive analysis technique, a considerable interest was developed to study the Raman spectroscopy with first Fourier-transform (FT) Raman instrument developed in 1986.

a) Theoretical background

The basic theory of the Raman spectroscopy is based on simple principle that when light interacts with the sample, it may be absorbed, scattered or passed without any effect [2,3]. In case if the light is absorbed it is known as absorption whereas in the case if it is passed through the sample without any or minor effect its known as transmittance. In the case of absorbance, the light should have energy equal to the energy difference between the sample's ground state and excited state, so as the light strikes the molecules goes to excited state. However if the light waves doesn't have energy equal to that gap difference, it can also interacts with the atoms or molecules and is then scattered. Raman spectroscopy is based on such type of light scattering phenomenon due to interaction with the vibrational, rotational, and other low-frequency modes of molecules. Usually the scattering are of two types elastic and inelastic, Raman spectroscopy utilizes the information obtained from inelastic scattering for analysis and determination of various groups anchored within the molecules or compounds. For the Raman effect we can think of the light as a wave, when the light falls on the sample, it provides energy to the sample and can alter the vibrational mode of the structure (symmetric, asymmetric or bending mode) by exciting it to some virtual state. After some time when the molecule is relaxed the light is scattered back with a changed frequency (increased or decreased energy) as of its original frequency. This is also known as inelastic scattering, if however the frequency is not changed after interaction with the sample it is known as elastic or Rayleigh scattering. The illustration of these phenomena with respect to excitation of a molecule in terms of quantum energy diagram is shown in Figure 2.4.

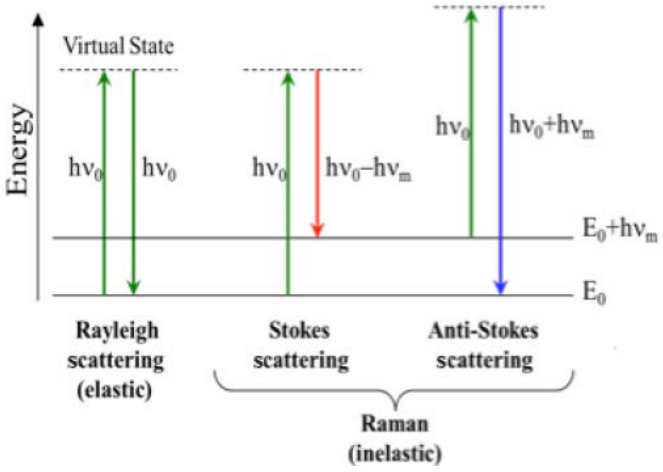

Figure 2.4 Illustration of elastic and inelastic scattering of light in forms of photons. Raman scattering is depicted by inelastic scatterings.

b) Instrumentation

The key components of a Raman spectrometer includes: (i) lasers as a light source, (ii) wavelength selector, (iii) sample illumination and collection system and (iv) detector with computer control system for processing the data. First of all the light of required wavelength is selected coming from the laser source before illuminating the sample. Commonly two different wavelengths of light used for illumination of sample includes 532 nm and 785 nm wavelengths. After that the sample region is properly selected using the fiber optic probe as Raman scattering are very weak so it is very important to select the correct region of the sample from where we can get the useful data. Once the sample region is selected, light is illuminated on it and the detector detects the scattered light and transform using computer software into desired spectrum. Usually Raman spectra provides us the data regarding the presence of several groups with their respective bending and vibrational modes. The schematic diagram of the main steps for a Raman spectra measurements are shown in Figure 2.5.

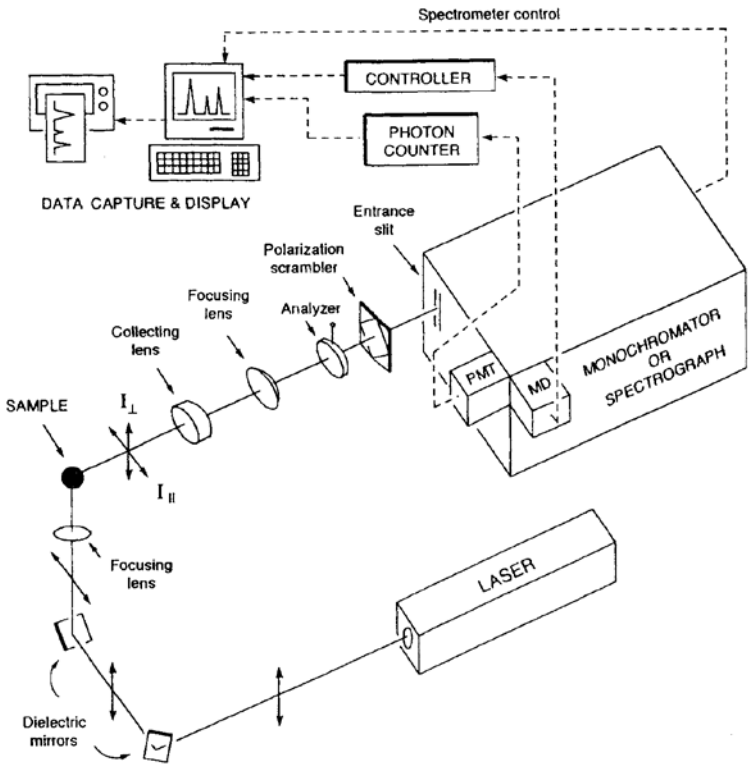

Figure 2.5 Schematic view of the Raman spectrometer showing key steps during data measurement. (Taken from Ref. 3)

2.1.3 Scanning electron microscopy (SEM)

This type of electron microscope is the most widely used in the materials science for examining the surface and cross sectional morphology, microscopic structure of the materials with very fine focal and high resolution arrangement. SEM creates an image of the sample under observation by using a focused beam of electrons which can scan all over the sample with most attractive feature elemental analysis using the equipped utility of X-ray energy dispersive spectrometer (EDS).

a) Theoretical background [1,4]

When high energy electrons form an electron source strikes with a sample, two types of electrons are generated i.e. secondary electrons (SE) by inelastic electron scattering and

backscattered electrons (BSE) by elastic electron scattering. Both the SE and BSE from the samples are used as information for creating the SEM images. For better understanding of SE and BSE, consider a pear shaped zone of sample shown in Figure 2.6 which interacts with the electron beam and in which it is considered that SE, BSE and other electromagnetic radiations are generated. It can be seen, the SE generated via inelastic scattering consists of a less sample volume with the depth within range of 5-50 nm whereas the BSE possess approximately similar energy as incident electron beam and because of high energy can escape from a deeper level of the sample i.e. within depth range of 50-300 nm. The trajectories of these SE and BSE are changed during the scanning of the samples, who are providing the topographical and compositional information respectively, regarding the sample under investigation.

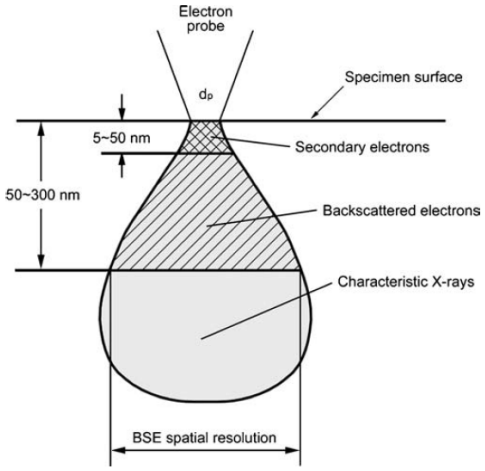

Figure 2.6 Schematic view of sample's interaction zone with incident electron beam below the sample surface. (Taken from Ref. 1)

b) Instrumentation

The instrumentation and construction of SEM machine is very complicated and sophisticated. A simple instrumental diagram for SEM machine is portrayed in Figure 2.7. The electron beam generated from electron gun (thermionic or field emission gun) have to pass through a series of electromagnetic lenses for proper alignment, focus and resolution of the

imaging. The simplest lens series consist of two condenser lenses and one objective lens. The purpose of the condenser lenses is to reduce the cross over diameter of the electron beam whereas the objective lens acts as a probe having diameter of nanometer scale. The scanning of the sample is done by a beam deflection system probing over the sample. The construction of image is done by collecting the electron signals form the sample at the detector.

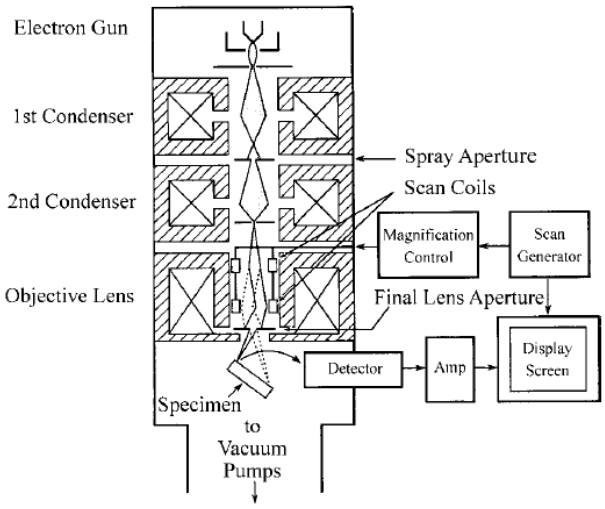

Figure 2.7 Structural diagram for a simple scanning electron microscope (SEM). (Taken from Ref.1)

2.1.4 Transmission electron microscopy (TEM)

Transmission electron microscopy (TEM) is another powerful tool for capturing the images of the materials. TEM usually uses a very high energy electron beam which can easily pass or diffract through the specimen hence providing useful information regarding the specimen topography and morphology.

a) Theoretical background [1,4]

In the case of the SEM, the electron gun operates between 0-40 kV accelerating potential, whereas for the TEM machine the accelerating voltages is raised to 50-300 kV. At such a high voltage the electron gun generates a very high energy electron beam (λ = 0.005 nm) which can penetrate to several microns of the sample and can provide information about

material morphology. If the material is highly crystalline or the electron beam cant penetrates the sample, then it is diffracted by the atomic planes. Thus based on the information from transmitted electrons and diffracted electrons the samples can be imaged with very fine and good resolution.

b) Instrumentation[1,4]

The structure of the TEM instrument is bit similar like the optical microscope with the main difference of light source is replaced with a high energy electron beam source. The TEM consist of electromagnetic lenses rather than the glass lenses as in optical microscope. The TEM machine requires a high vacuum environment to avoid the collisions of the air molecules with the electron beam. The prepared specimen is placed on TEM grid usually made of Cu or Ni mesh, the high energy electron beam after passing through the condenser lens passes the specimen. The electron beams are diffracted and transmitted through the specimen and are then magnified and captured on the fluorescent screen providing the images for the specimen under investigation. The simple structure of the TEM instrument is shown in Figure 2.8.

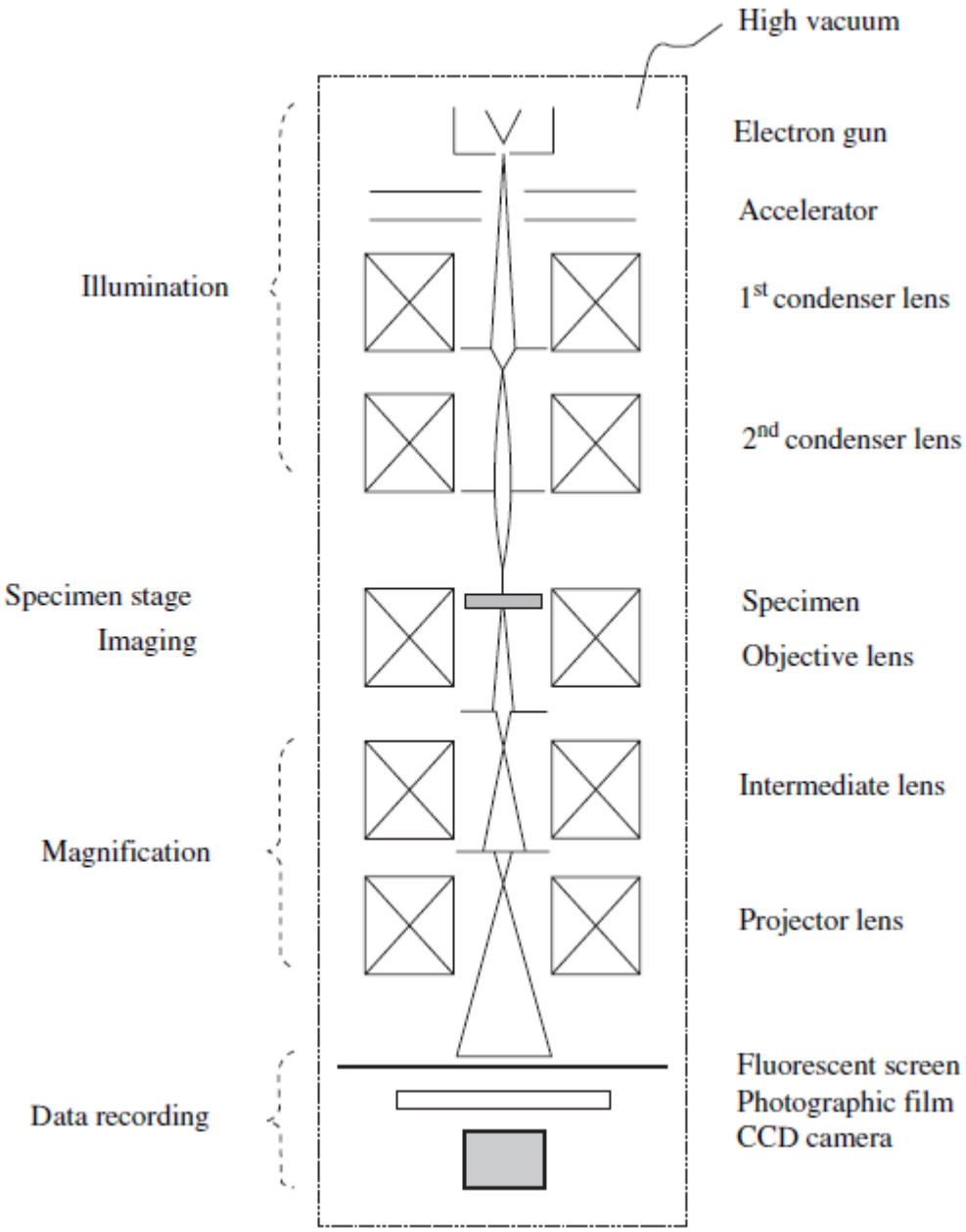

Figure 2.8 Structural diagram for a simple transmission electron microscope (TEM). (Taken from Ref. 1)

2.1.5 X-ray photoelectron spectroscopy (XPS)

X-ray photoelectron spectroscopy (XPS) is a very useful technique to determine mainly the chemical composition and electronic states of the elements in the specimen. XPS was previously known as ESCA (electron spectroscopy for chemical analysis) [1,5,6]. XPS was invented by Kai Seigbahn (Noble prize in 1981) and his research group at Uppsala University,

Sweden during mid-1960s [6]. XPS is considered an excellent surface analysis tool, as it uses soft X-rays from Alkα or Mgkα which strikes the sample and then emits the x-rays from the sample which are detected and a spectrum is plotted for each element detected. The spectrum of the sample is then analyzed which gives information regarding the presence, electronic state and quantity of the respective elements in the sample.

a) Theoretical background [1,5,6]

The XPS works on the basic principle of photoelectric emission effect. When a high energy X-ray photon interacts with the atom, due to its very high energy it can knock out the electron form the inner shell of the atom as a free electron and atom is ionized. As atom will be unstable in ionized state, so to relax to its normal state an electron from higher shell will fill that vacancy of the empty inner shell and in turn emits an X-ray photon. Another possible phenomenon which occurs is the emission of another electron by excess energy of outer shell electron when it fills the inner shell electron vacancy to achieve normal atomic state. This process is well known as Auger electron emission. Such emitted X-ray photons or photoelectron and Auger electrons can then be detected and investigated for elemental analysis. Schematic diagram showing the excitation and generation of photoelectron and Auger electron is well presented in Figure 2.9. The X-rays emitted are actually the energy difference between the two electrons in different shells where the energy of an electron in each shell for various elements are well defined, therefore from the X-rays emitted we can know the shells of specific elements and hence its presence, electronic states and composition as well.

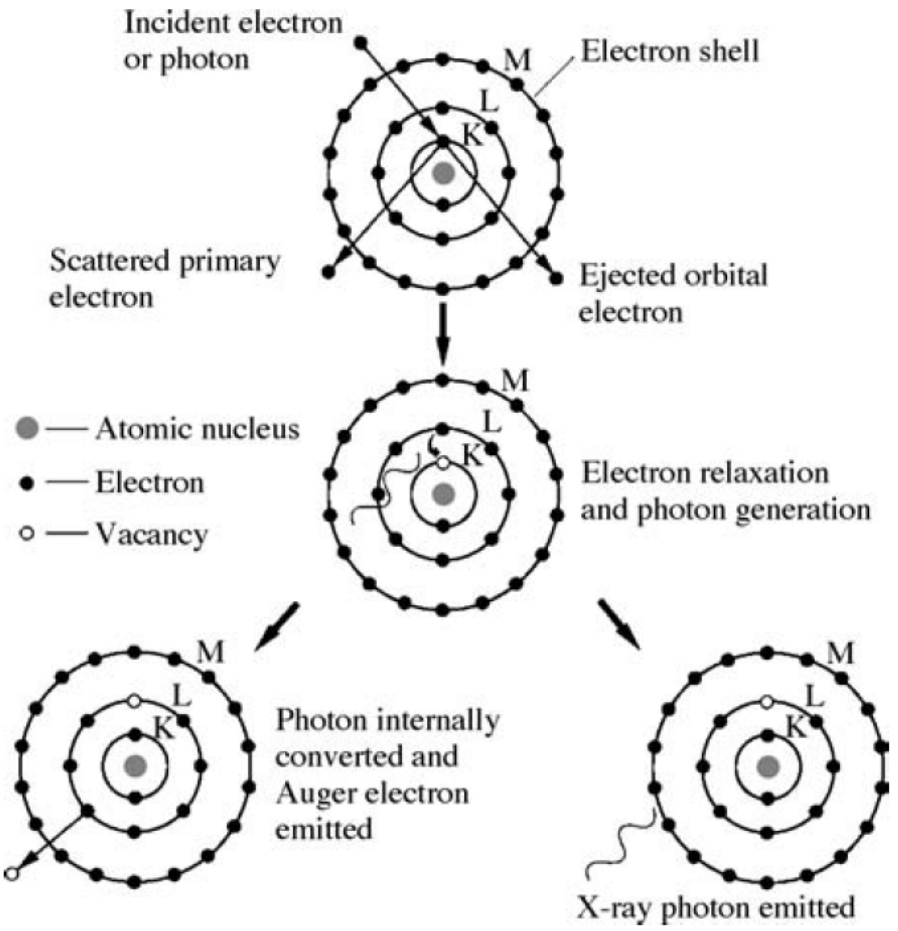

Figure 2.9 Schematic drawing of an atom with its shells excited by X-ray and then generating X-ray photon/photoelectron (Right side) and auger electron (left side). (Taken from Ref.1)

b) Instrumentation [5,6]

Simply, the main components of an XPS inurement includes

I. X-rays source

II. Sample holder placed in an appropriate vacuum chamber

III. An electron energy analyzer

IV. A detector

V. A data analysis system

As obvious from terminology, the X-ray source generates the X-rays of required energy which strikes the sample placed on sample holder in a vacuum chamber. The X-rays incident

on sample emits the photoelectrons from the sample which are then passed through an electron analyzer channel finally reaching the detector to produce the useful data. The simple diagram showing the structure of XPS instrument is shown in Figure 2.10.

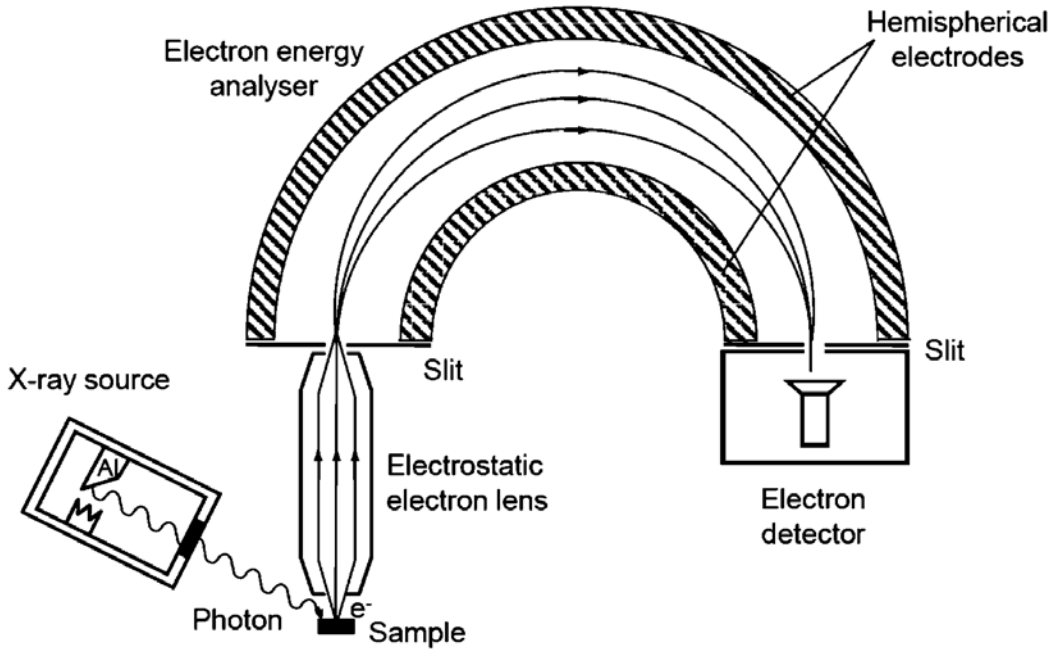

Figure 2.10 Simple structure of XPS instrument with its main components. (Taken from ref. 5)

2.1.6 UV-vis diffuse reflectance spectroscopy (UV-vis DRS)

UV-vis diffuse reflectance spectroscopy is a powerful tool to study the absorption and reflectance properties for solid samples such as powder materials and opaque thin films. It is an efficient way to measure the absorbance form reflectance by calculations for solid samples and time saving process as compared to other techniques used for absorption measurement of solid samples.

a) Theoretical background [7,8]

It is well known that when electromagnetic waves of the light come in contact with a certain material, specifically semiconductor material, four possible events can happen i.e. absorption, transmittance, scattering and reflectance of the light. Commonly used UV-vis spectroscopy is

employed mainly to investigate the absorption and transmittance for transparent liquid samples and thin films, colloidal solutions and porous thin films. However in the case of solid powder samples and compact thin films, normal UV-vis spectroscopy can't work and absorbance is therefore measured for solid samples by means of measuring the reflectance and scattering of the respective samples.

Reflectance can be generally defined as the ratio of the reflected light waves to the incident light waves and is mainly of two types, regular or specular reflectance and diffuse or volume (non-directional) reflectance. Specular reflectance is the reflectance form a sample surface in the same angle as that of the incident light whereas the diffuse reflectance represents the portion of the incident light which is reflected back in all directions as observed specifically in case of powdered samples. Hence depending upon the sample and equipment used, it is feasible to measure the specular and diffuse reflectance separately. Once the reflectance is measured, absorption of the samples can be obtained using the following equation

$$100\ \% = \%\ R + \%\ T + \%\ A \tag{2.2}$$

$$\%\ A = 100\ \% - (\%\ R + \%\ T) \tag{2.3}$$

b) Instrumentation [7,8]

The instrument used for the UV-vis DRS measurement is the same as used for UV-vis absorption spectroscopy with only difference of equipping the instrument with DRS accessory i.e. integrated sphere in which sample is placed. The integrated sphere have a variety of designs, most commonly used is the double beam sphere made of Spectralon (a polymer offering 100 % levels of diffuse reflectance up to spectral range of 2500 nm) having diameter of usually 150 mm. The sample is placed in a special designed sample holder fixed with the quartz lens at the front side. The sample holder is then attached at the specified place on the sphere and reflectance is being measured. The mechanism involved in the normal UV-vis absorption

spectrometer is show in in Figure 2.11a with the schematic of the integrated sphere in figure 2.11b.

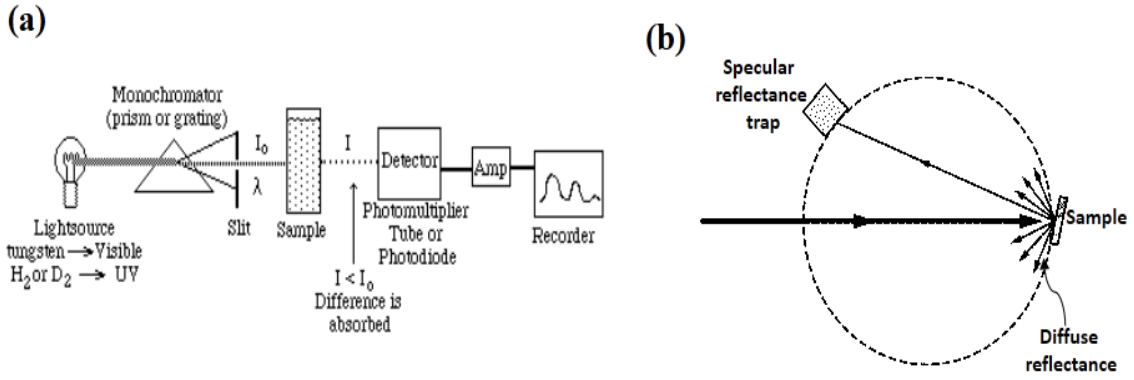

Figure 2.11 schematic diagram for **(a)** Simple UVis spectrometer and **(b)** an integrated sphere for measurement of diffuse reflectance.

2.1.7 Photoluminescence (PL) spectroscopy

Photoluminescence spectroscopy (PL) is another important non-destructive tool to analyze the optical properties of a material under investigation. The key purpose of employing PL in the field of photocatalysis is to investigate the emission properties, excited charge life time and effective separation of photoexcited charges for the given system.

a) Theoretical background [9,10]

When a photoactive material is excited by a light form respective light source, photo-excitation happens and electrons within a material are excited to permissible excited states. Generally there are two excited states considered in PL spectroscopy i.e. singlet excited states and triplet excited states. After staying a short time in the excited state the electron will come back again to its ground state with the emission of light wave, this phenomenon is known as photoluminescence. The energy released due to to such relaxation is equal to the energy difference of the two energy states that is

$$\Delta E = E_{excicted} - E_{ground} \quad (2.4)$$

PL is typically categorized into two forms based on its electron relaxation mechanism. When an electron is excited from a ground state to an excited state with same spin, this excited state is known as singlet excited state. The excited electron will stay for some time in the excited state and will then relax to the lower energy states or ground state with the emission of light wave termed as fluorescence. The fluorescence is the most familiar phenomenon happening with a short life time of 10^{-8} to 10^{-4} s. Second form of PL is phosphorescence, in which the electron is excited to a higher energy state with an alteration of spin i.e. triplet excited state. Such process takes a long time then fluorescence to relax the system to ground state, usually 10^{-4}-10^{-2} s. The triplet excited state lies at lower energy level than the singlet excited states so electron from a singlet excited can also relax and cross over to the triplet excited states within a molecule. Such phenomenon is commonly known as intersystem crossing. The schematic representation of the basic mechanism involved in the PL emission is depicted in Figure 2.12 as below.

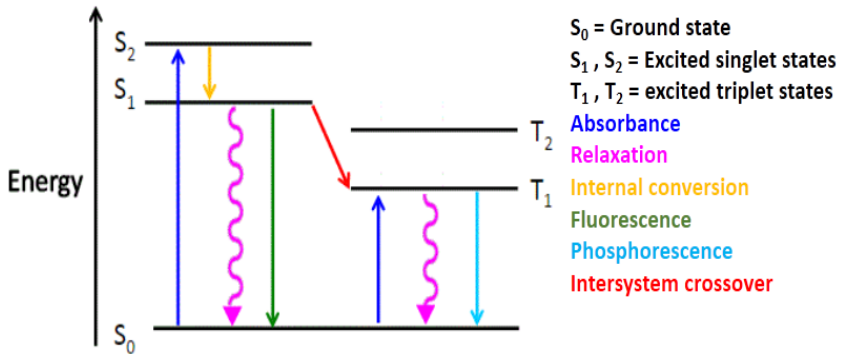

Figure 2.12 Energy level diagram displaying excitation of electron to singlet excited states and triplet excited states for generation of PL emissions.

b) Instrumentation [10]

The simple structure of the PL instrument is shown in Figure 2.13. The PL unit consists mainly of a laser source followed by tunable equipment to fine the monochromatic wavelength laser beam which then strikes the sample and excites it to higher energy state. After short time

of excitation, the energy waves from the sample due to relaxation to a lower energy state or a ground state gets emitted which are again passed through a grating monochromator to get a single wavelength emission peak as data of the sample which is processed and recorded by a computer control system linked to PL instrument.

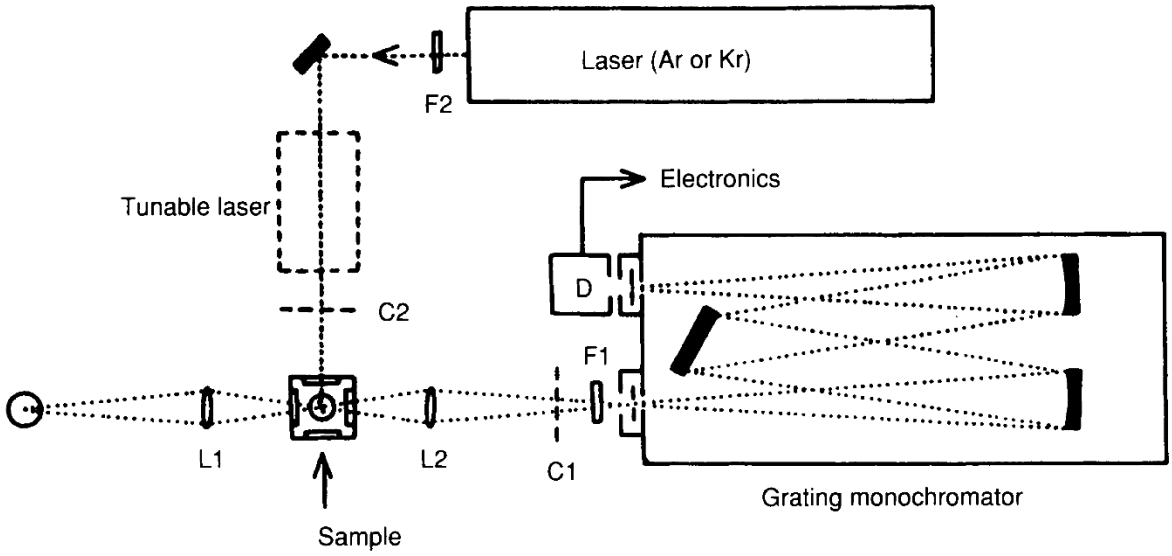

Figure 2.13 Schematic diagram showing a simple structure of Photoluminescence spectrometer. (Taken from Ref. 10)

2.1.8 Physisorption analysis

The physisorption analysis is an important technique providing a variety of textural information regarding the material by a simple phenomenon of physical adsorption of gas molecules on the material surface. The gas molecules are weakly adsorbed on the material surface and can be desorbed easily, the adsorption and desorption of the gas molecules can thus provide various important information. Some of the important properties for a material which are determined or calculated using the physisorption phenomenon are:

I. Surface area

II. Porosity

III. Pore size

IV. Pore volume

a) Theoretical background [11,12]

The adsorption of the gas molecules onto the solid surfaces is the key step in the physisorption analysis of materials. The type of the gas used, temperature, pressure all these parameters influence the adsorption phenomenon. The measurements in the physisorption analysis are usually done at a temperature less than the triple point of the gas, with the adsorption isotherms a principle of measurement. The adsorption isotherm can be defined as the curve obtained by measuring the amount of adsorbed gas molecules vs. adsorptive pressure of the gas at fixed temperature. The adsorptive pressure of the gas is presented as a ratio of the adsorptive pressure to its saturated vapor pressure over the materials surface. There are two methods mainly used for the measurement of adsorption isotherm, (i) volumetric method and (ii) gravimetric method. Most commonly used is the volumetric method in which the adsorption isotherm is plotted based on amount of the gas adsorbed *vs.* the adsorption pressure in a stepwise fashion at a constant temperature. Whereas the later method uses the mass gain data of adsorbed gas and provide the required information. In the volumetric method the amount of the gas adsorbed is measured by means of how much gas is being consumed for adsorption process form the reservoir.

The adsorption isotherms are classified into six types, according to international union for pure and applied chemistry (IUPAC) classification [12], as shown in the Figure 2.14. Each adsorption isotherm provides a specific information about the material surface properties. Type I isotherm indicates the micorporous nature of the material due to monolayer adsorption on its surface. However Type I isotherm can also appear for mesoporous materials with their pore size range close to micropores range. Type II and Type III isotherms appear for the macroporous materials due to multi-layer adsorption of the gas molecules leading to concision

of adsorption and desorption branches of the isotherms. Type IV and Type V isotherms appears due to multi-layer adsorption of gas molecules on macroporous solids followed by the capillary condensation.

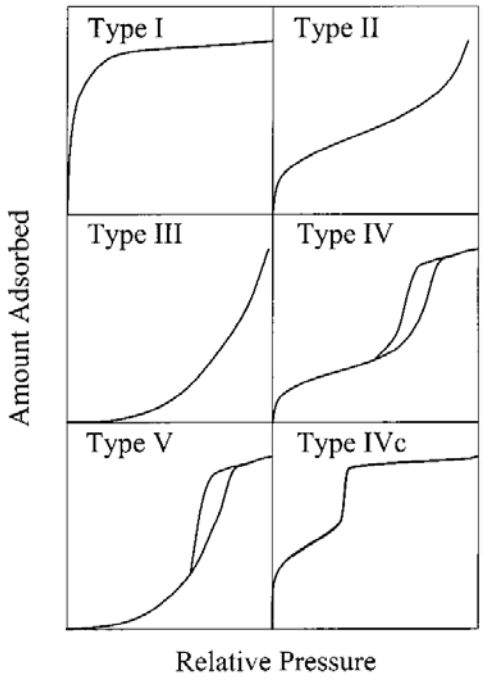

Figure 2.14 IUPAC classified adsorption isotherms for porous materials. (Taken from Ref. 12)

As it is well known, to investigate the mesoporous nature of the solids the adsorption process is analyzed using an adsorption-desorption hysteresis. Hysteresis loops are believed to appear because of thermodynamic effects of adsorption-desorption, pore interconnected networks or combination of both factors, however still this issue is not exactly clarified. Similar like the isotherms, hysteresis-loops are also classified into four main types according to IUPAC classifications and are shown in figure 2.15 [12]. Type H1 loop usually appears for the agglomerated materials with uniformly compact spherical type particles. These type of materials possess a high pore uniformity with fair pore connectivity. Type H2 hysteresis depicts a triangular and steep desorption branches which is due to presence of narrow mouths (ink-

bottle pores) and mainly observed for porous inorganic oxides. Type H3 hysteresis is commonly reported for the aggregated materials composing of plate like particles which forms slit like pores. The type H4 hysteresis loop shows parallel and almost horizontal branches which are associated to the mesoporous materials with narrow slit like pores.

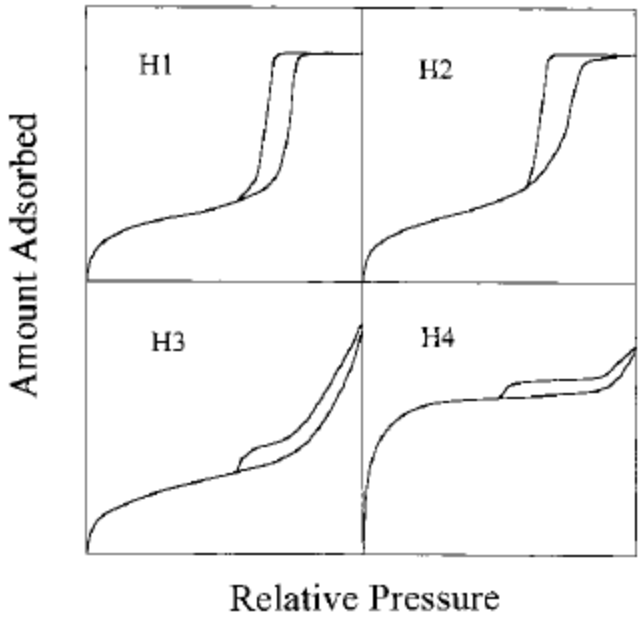

Figure 2.15 IUPAC classified adsorption isotherm hysteresis loops for mesoporous materials. (Taken from Ref. 12)

Based on the information obtained from the adsorption isotherms and hysteresis loops, one can find the various properties of the mesoporous material by applying various standard and recognized methods of calculation and estimation such as Barrett, Joyner and Halenda (BJH) method for the determination of pore size distribution and Brunauer-Emmet-Teller (BET) method to estimate the specific surface area of the material [12].

b) Instrumentation [11]

The basic structure of the equipment used in physisorption analysis using volumetric method is shown in Figure 2.16. The powder sample (P) is placed in a sample tube (H). The tubes are usually made of Pyrex glass and is immersed in liquid nitrogen bath (L) for temperature control. Nitrogen gas from the supply is opened using valve (G), which is equipped with pressure gauges and safety valve. Another valve (C) is linked to the sample tube and one can open when needed to adsorb the gas molecules on the sample surface. Before the measurement, the sample is degassed at high temperatures (around 200 °C) in a separate setup to desorb the impurities gas and evacuate them using a vacuum pump. A thermometer (T) and a temperature sensing couple (D) is introduced into the sample region to control the temperature of the sample region. Gas pressure changes from the gas supply as the adsorption continues which is measured by pressure sensors, based on pressure and temperature changes the calculations are made using gas equations.

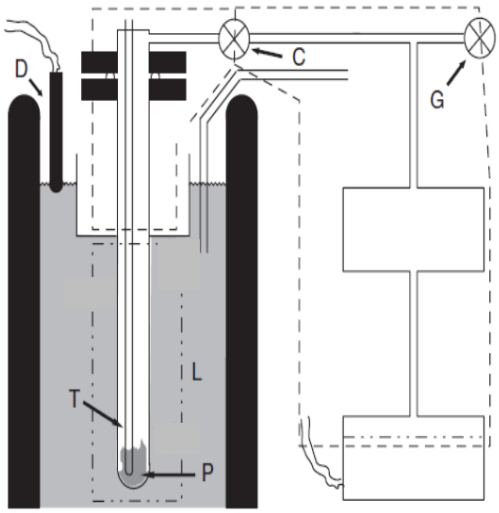

Figure 2.16 Illustration of simple physisorption analysis equipment using IUPAC classified adsorption isotherm hysteresis loops for porous materials. (Taken from Ref. 11)

2.2 Analysis techniques

Some of the important analysis techniques for the evaluation of the photocatalyst performance utilized during the research work with respect to basic fundamentals and principles are explained in the following sections.

2.2.1 Gas chromatographic (GC) analysis

Chromatography techniques are one of the powerful tools used for chemical analysis in which a number of distinct chemicals (analytes) can be identified and quantitatively measured. The chromatography techniques basically works on the principle of difference of vapor pressures for various components in mixture [13]. According to official definition by IUPAC chromatography can be defined as: “A physical method of separation in which the components needed to be separated from mixture are distributed between two phases, one of which is stationary (stationary phase) while the other moves in a definite direction (mobile phase)”. At present, certain number of chromatographic techniques are used for chemical analysis as shown in Figure 2.17. The name of each chromatography technique is based on the physical state of mobile phase.

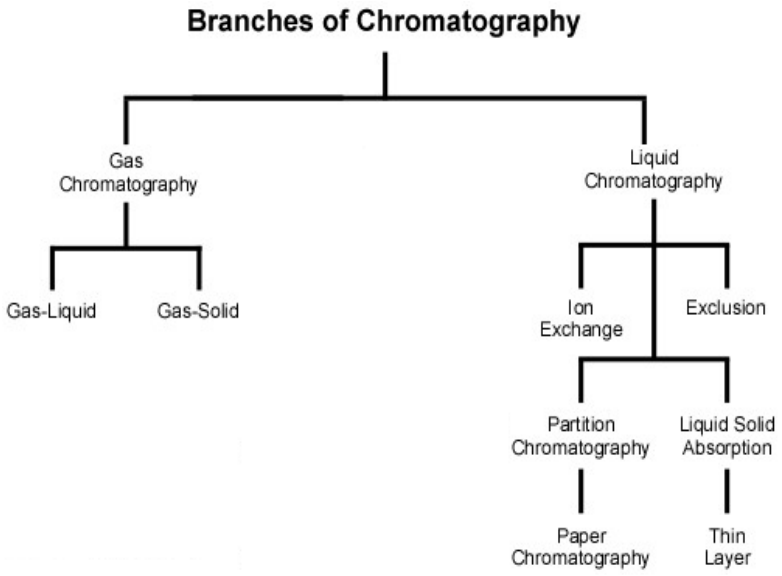

Figure 2.17 Various classes of chromatographic techniques.

a) Theoretical background [13]

The idea for the partition chromatography was given by British scientists J. P. Martin (Noble prize in chemistry 1941) and Anthony T. James. Later on Martin and his coworkers suggested and perform experiments regarding the separation of volatile compounds in forms of respective vapors as a mobile phase rather than liquid phase. In such chromatography, the sample mixture is injected into column and converted to respected vapors at higher injection temperatures, the vaporized components are carried by a carrier gas (mobile phase) through the column and are separated on the basis of their relative vapor pressures and affinities with the stationary phase. This type of chromatography is known as Gas chromatography (GC). GC have been received abundant attentions by industrial, research and development, and academic sectors as it seems an attractive and efficient manner to separate the volatile compounds. GC is further classified into two main types based on the stationary phase as:

I. Gas-solid chromatography (GSC) which uses solid as a stationary phase.

II. Gas-liquid chromatography (GLC) which uses liquid as a stationary phase.

The process involved in the chromatography can be well understood using the Figure 2.18. Consider a gaseous or vapor mixture of A+B which is injected to a GC through an injection port. The temperature at the injection port is kept high enough to vaporize all of the sample. As the sample is injected, it is carried by a carrier gas into the column (indicated by the line from left to right) where each component interacts with the packing or internal lining (solid stationary phase). Due to difference in the vapor pressures and chemical affinity with the stationary phase, a part of each component gets adsorbed onto stationary phase (lower peak) and some part flows through the column (upper peak). As it can be seen, the component A have more distribution in the flow gas so it will reach the detector earlier than the component B. The detector after detecting each separated component converts the signal in peaks form as shown on the chromatogram on the extreme right of the figure.

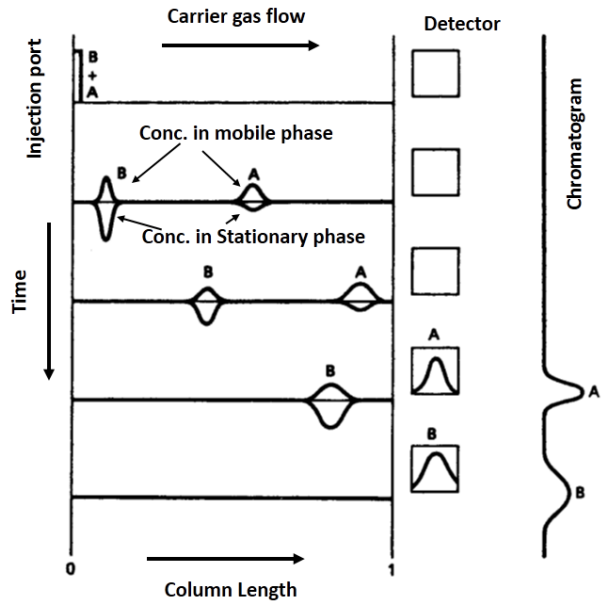

Figure 2.18 Illustration of basic process involved in the GC. (Taken from Ref. 13)

Each component of the mixture have its own tendency to interact with the stationary phase and is termed as equilibrium constant or distribution constant or partition coefficient. The component interaction to the stationary phase will be greater if the constant value is larger. Figure 2.19 shows the chromatogram for component A showing its peak appearing at retention time t_R and peak volume V_R. Both t_R and V_R are estimated with respect to the point of the injection. If the flow rate of the carrier gas (F_c) is fixed then the peak volume can be given by following equation:

$$V_R = t_R \times F_c \tag{2.6}$$

In GC sometimes a small peak is observed at early retention times. Such peak is attributed to the small amount of solute which does not interacts with the stationary phase and passes through to detector as it. Such behavior is usually observed in case of air or methane gases.

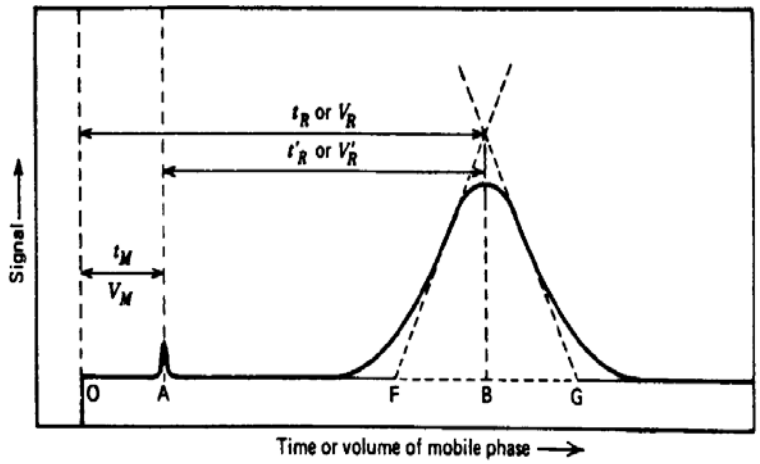

Figure 2.19 A typical example for a chromatogram illustration. (Taken from Ref. 13)

GC has several advantages, some of them are listed below:

- Quick analysis and high resolution.
- Sensitive to detect very small amounts of concentration i.e. up to ppb unit.
- Nondestructive process so can be coupled to another instrument such as mass spectroscopy (MS) for instance.
- Requires small amount of samples for injection, typically in micro liters.
- An inexpensive, simple and reliable technique.

Along with advantages it also bear some limitations such as:

- Analysis is limited to volatile samples.
- Can’t detect the fairly large amount of samples.
- For the confirmation of peak identity, linkage to another useful equipment is necessary such as MS.

b) Instrumentation [13]

A very basic schematic illustration of a simple GC unit is shown in Figure 2.20. A simple GC system is composed of following basic accessories:

I. **Carrier gas flow system:** A cylinder of carrier gas, mostly 99.9999 % pure He gas is used, gas regulator and flow controllers.

II. **Injection port:** The temperature of the injection port is commonly kept high enough (~200 °C) to readily vaporize the mixture sample but also low enough to avoid decomposition of the sample.

III. **Column:** Generally two types are used (i) packed column and (ii) capillary column.

IV. **GC oven:** To provide heat to the column for vaporizing the components and baking of the column. At higher oven temperature, the analysis time is less as in less time the components are separated but with the disadvantage of low resolution. However if the oven temperature is moderate enough, analysis time will be a bit long but the resolution is good enough.

V. **Detector:** Selection of detector depends upon the components to be detected, commonly used are thermal conductivity detector (TCD) and flame ionization detector (FID). The temperature of the detector are also kept high enough to avoid the condensation of the sample and water if it is a byproduct.

VI. **Data system:** A computer control linked to the GC instrument for its operation and analysis of the data in understandable form.

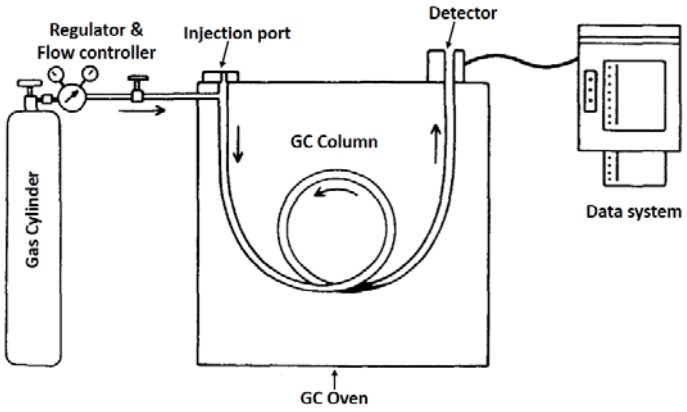

Figure 2.20 Schematic view of basic accessories equipped simple GC unit. (Taken from Ref. 13)

The most important part of the GC instrument is column, sometimes it is termed as "heart of the GC". For GC commonly two different types of columns are used i.e. packed and capillary column. The packed columns are packed with some good packing material like stainless steel and have lengths from 3, 6 or 12 feet. The outer diameter of the packed column is normally selected as 0.25 or 0.125 inch. On the other hand capillary columns are more simple with replacing the column packing by a thin film of solid phase usually silica, internally coated with the inside wall of the column. Another term usually used for capillary columns is "wall-coated open tubular" (WCOT) or simply OT columns. These columns offer very less resistance to gas flow and hence their lengths can be increased up to 100 meters. The cross sectional view for both types of column is shown in Figure 2.21.

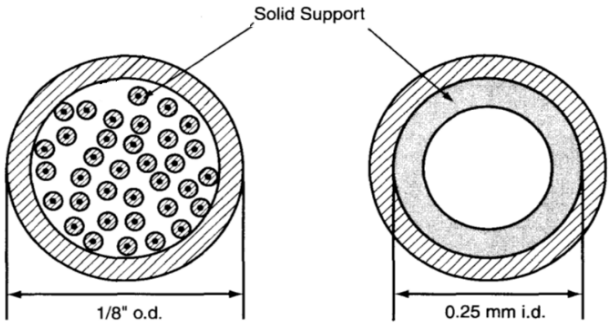

Figure 2.21 Schematic view of packed column (left) and capillary column (right). (Taken from Ref. 13)

Two very commonly used detectors consists of FID and TCD. FID is specifically invented for the GC which gives the signal to detector in forms of current after detecting the ions produced by burning the sample. A schematic for the FID is shown in Figure 2.22a. As the sample reaches the detector it is mixed with hydrogen gas and directed towards the burner tip where it is ignited using an igniter. The burner tip is surrounded by an air gas which is there to promote the combustion of the sample in an oxy-hydrogen flame. During the burning of the sample, ions are produced which are collected by the electrode biased at +300 V and collects the current generated by the ions.

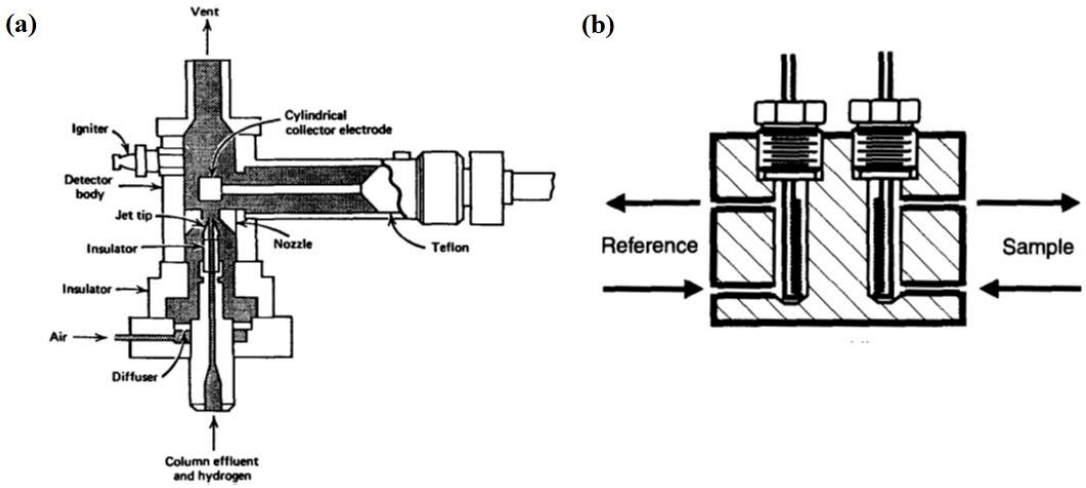

Figure 2.22 Schematic diagram of an (a) FID and (b) TCD detectors. (Taken from Ref. 13)

The TCD uses thermal conductivity data for producing the signals form the sample components. For the thermal conductivity measurements, a four cavity cell fabricated by drilling into a stainless steel block with each having a resistance wires or filaments (made of tungsten-rhenium alloy, WX filaments) is used. A Wheatstone bridge circuit is generally employed for measurement of TCD signal via resistance measurement. When pure carrier gas

(reference gas) flows through the all four cavities, the bridge is balanced. However, when the analyte gas passes through the cavities, the thermal conductivity of the gaseous mixture is decreased which leads to increase in the filament temperature and hence increase in resistance with an unbalanced bridge. The voltage is thus developed across opposite corners and is presented as an output signal. A schematic for the TCD-4 filament cell is shown in Figure 2.22b.

2.2.2 Gas chromatography-Mass spectroscopy (GC-MS) analysis

GC is one of very useful analysis technique, however shows a limitation and weakness in identity confirmation for separated components form a mixture sample. As in GC most of the components are identified on the basis of peak retention time and many components can have similar retention time under the similar conditions of GC testing. Therefore a doubtful situation can be created and the exact confirmation of the separated component can't be justified using the GC technique alone. To overcome such type of doubtful and confused situation, a common practice to identify appropriately the separated component is to couple the GC with another powerful and useful instrument i.e. mass spectrometer (MS). MS is a well-known analytical technique which ionizes the sample injected in a high vacuum, drive these ions to the ion detector through a magnetic mass analyzer and differentiate the components on the basis of the respective mass to charge (m/z) ratio. The MS data is presented in form of a mass spectrum, generated on the basis of ion signal vs. mass to charge (m/z) ratio which is well defined signature of the respective component [14–16].

MS was first developed by a physicist J. J. Thompson in 1910, in which he proved for the first time presence of ^{20}Ne and ^{22}Ne isotopes [14]. After his development, a large amount of investigation was done in the field of MS focused towards development of MS only. However with the idea of GC invented by Martin and coworkers, researches were directed towards the coupling of both GC and MS with the first commercial GC-MS system supplied by Finnigan Instruments Corporation for organic analysis in 1968. The combination of both tools i.e. GC and MS (GC-MS) makes the analysis system enough powerful and reliable to separate the components, identify and give qualitative and quantitate information. But GC-MS still bears some issues such as requirement of volatile samples, some limitation of molecular weight, high vacuum system and limitation of tuning and calibration before utilization.

In the following parts the basic principle, instrumentation and data acquisition are explained with respect to MS only as the GC related information is already explained well in section 2.2.1.

a) Theoretical background[14–16]

The basic principle for the MS can be defined on the basis of four main steps involved in MS which are: (i) Ionization, (ii) Acceleration, (iii) Deflection and (iv) Detection. As in GC-MS, MS is coupled with GC, the eluted components form the GC are injected into MS via an interface where the components are ionized using ionization source (electron ionization or chemical ionization). The ions of the respective components are then accelerated using a powerful electric field. The ions with high amount of electric charge moves faster as compared to the ions with the less electric charge. Thus the ions separated out on the basis of the amount of charge they possess. These separated ions are then passed through magnetic field, where they gets deflected on the basis of the masses they possess. Finally the ions are separated out on the basis of having different electrical charge to mass ratio (m/z), a finger print for specific ion, and are detected by an electrical detector and recorded in a spectrum form known as mass spectrograph. Different types of instruments are used for ionization process and electron/mass analysis which are explained in the instrumentation section.

b) Instrumentation [15]

A simple instrumentation diagram for GC-MS coupled system is shown in Figure 2.23. The instrumentation for GC system is explained in section 2.2.1. The key parts of MS system includes (i) interface, (ii) vacuum system, (iii) ionization source, (iv) mass analyzer, (v) detector and (vi) computer control for data processing. The brief explanation of all these parts are as follow:

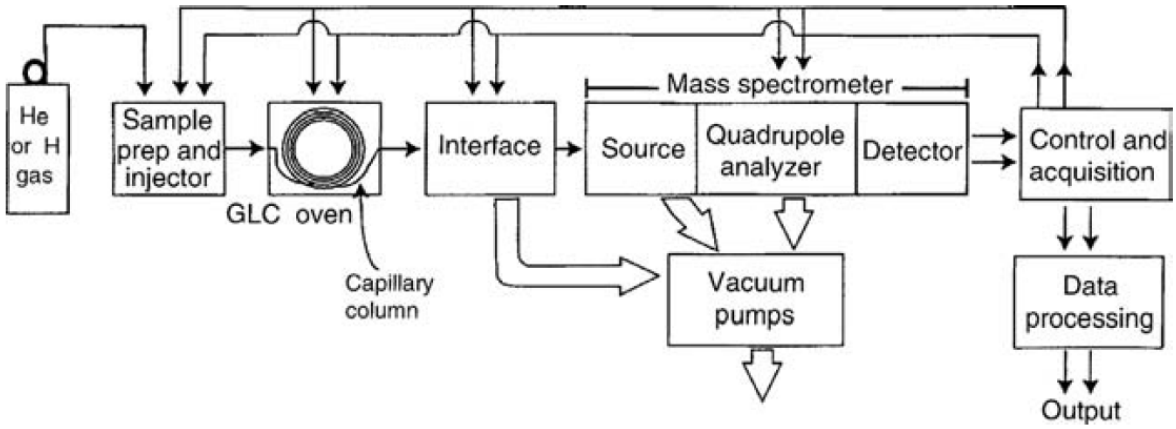

Figure 2.23 Schematic diagram of simple GC-MS instrumentation. (Taken from Ref. 15)

I. **Interface:** An interface between the GC and MS is very important part of the GC-MS system as it effects directly the performance of the GC-MS system. An interface transfers the sample from GC to MS, therefore it is very sensitive portion and should transfer the sample from GC in very accurate and undisturbed manner to avoid any ambiguity in the MS spectrum. Generally the leakage and components concentration are critical issues to be overcome during the sample transfer. Thus the interface can be designed in a variety of ways like designed with a separator to concentrate the sample or designed in a manner to provide carrier gas to aid the ionization process. As the separated gas components from GC enters the interface, the analyte components concentration can be increased by the removal of carrier gas jet separators or Bieman concenterators. The separated components by GC with moderate concentration travels to the MS by the aid of running carrier gas (He) if needed. A part of the gaseous component is also diverted to the secondary detector if used additionally or can also diverted to exhaust vacuum if exceeds the concentration limitation. A schematic view of the interface is shown in Figure 2.24.

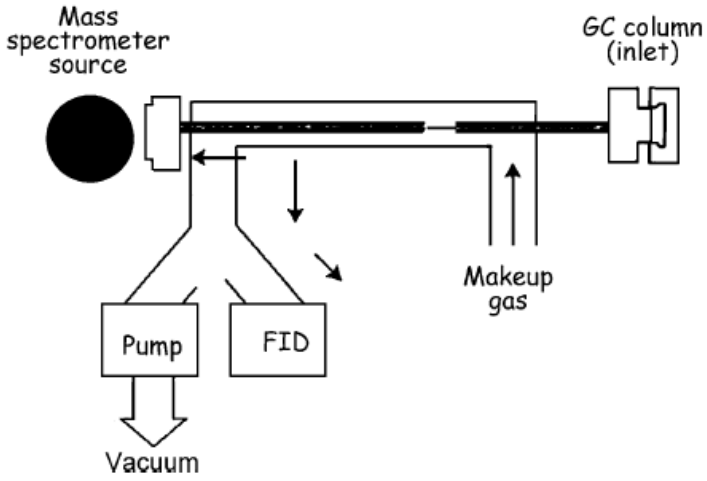

Figure 2.24 Schematic view of a simple interface for GC-MS system. (Taken from Ref. 15)

II. **Vacuum system providing high vacuum (10^{-5} Torr):** The MS coupled to a GC requires a high vacuum environment to have an accurate and undisturbed ionization from impurities. Generally for an MS system, vacuum is created in two stages. In the first stage the vacuum is generated by a fore pump down to 10^{-1} to 10^{-3} Torr. In the second stage oil diffusion or turbo pumps are employed to drop the vacuum down to 10^{-5} or 10^{-7} Torr.

III. **Ionization source:** At present there exists a number of ionization sources for employing in the MS. However, most commonly used ionization sources for the GC-MS system includes the electron impact (EI) and chemical ionization (CI) sources. The EI sources uses a high energy electron beam generated from heated filaments to knock out the electrons form the sample components leading to their ionization in the ionization chamber. The ions generated by the electron beam are then allowed to flow through a series of electrically charged focus lenses which accelerates the ions and finally enters the mass analyzer portion. Furthermore the analyzer vacuum (10^{-5} to 10^{-8} Torr) also supports the movement of the charge ions and avoidance of their collisions with themselves or with uncharged gas molecules. The high energy electron beam can also produce the fragments of the sample

thus providing the fragmentation pattern of the ions which is a fingerprint of each ionized molecule and hence can be easily identified. A simple schematic view of the EI is shown in Figure 2.25.

On the other hand the chemical ionization uses the mixture of already ionized gas samples with a fresh stream of sample. This mixture is then again bombarded by an electron beam, during which the ionized sample whose concentration are higher in the mixture is further ionized. These ionized molecules with high energy upon collision with the fresh sample molecules ionizes them with lower energy. Thus the fresh stream sample ions will be more stable without fragmentation and can provide the identity of the sample components.

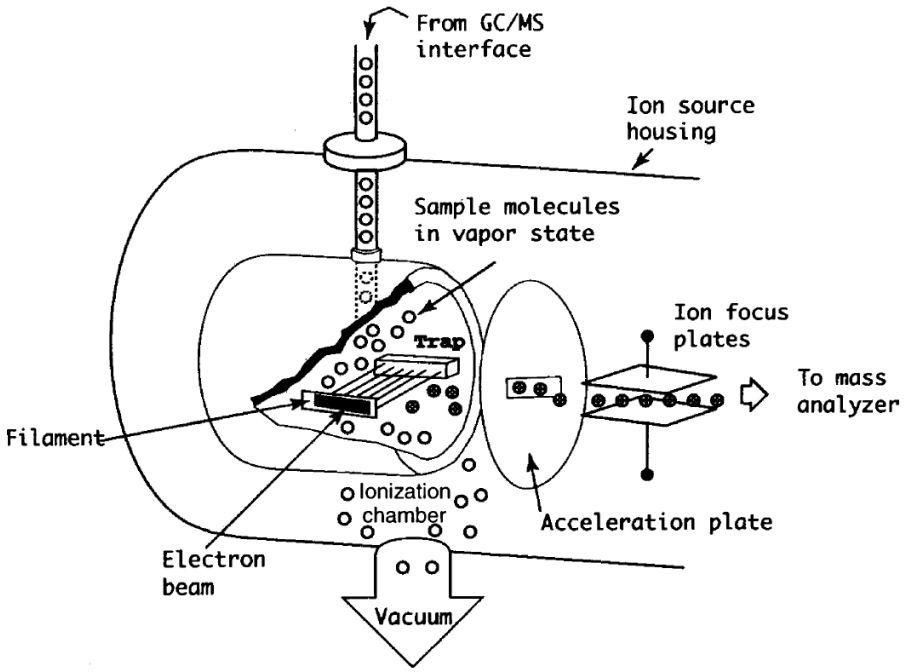

Figure 2.25 Schematic diagram showing the simple ionization source for a GC-MS.

(Taken from Ref. 15)

IV. Mass analyzer: Once the sample from GC column is ionized in the ionization chamber, the next step is to drive the fine stream of ion into mass analyzer. The commonly employed mass analyzer for a GC-MS system is quadrupole mass analyzer, structural and working

process diagram of which is shown in Figure 2.26. After the ionization step, the ions generated are accelerated towards the mass analyzer via electric field generated using electrically charged focusing lens. A voltage is applied to these lenses to attract, accelerate and streamline the charged ions of the sample. The ions with the same charge will definitely repel while passing through these lenses via columbic repulsion. After passing through the electrically charged focusing lenses the ions directly comes to the quadrupole mass analyzer.

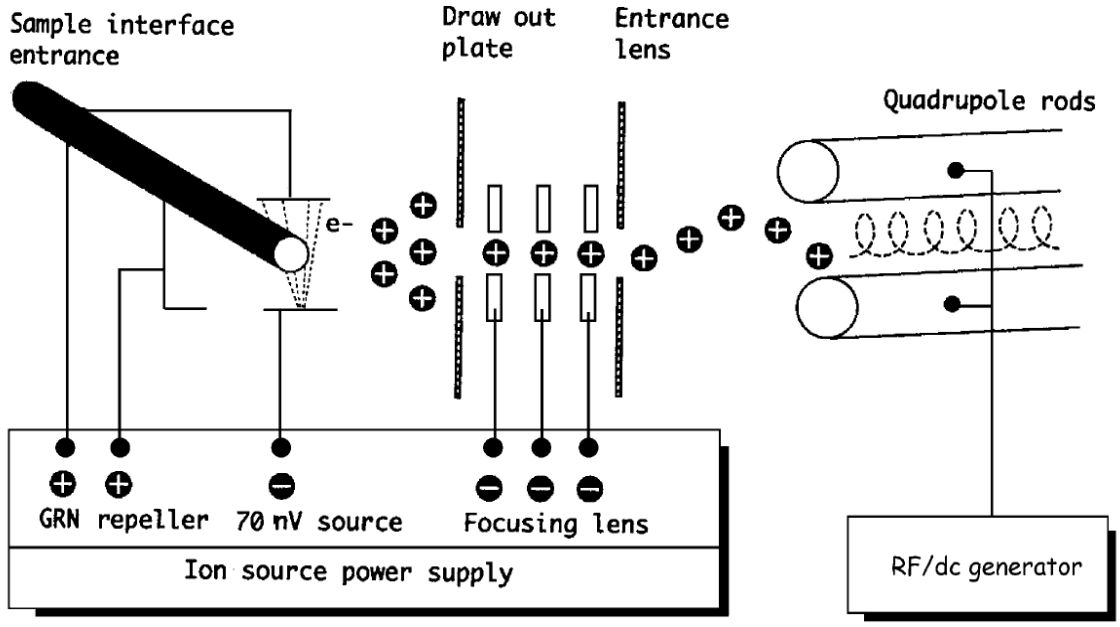

Figure 2.26 Schematic diagram showing the simple ionization source for a GC-MS.

(Taken from Ref. 15)

The quadrupole mass analyzer is termed as the “heart of the MS” and is fabricated by clamping four cylindrical quartz or metallic rods (10-20 cm long) in a pair of ceramic collars. It is considered as most inexpensive, simple and efficient for a GC-MS and is commonly used by the GC-MS sellers. When the accelerated beam enters the quadrupole electrodes or rods, it is forced by quadrupole electromagnetic field into three dimensional sine waves in a corkscrew

fashion. The electromagnetic field is generated across the quadrupole by applying a potential to the adjacent electrodes or rods of the quadrupole in opposite direction. The polarity of the potential across the pair of electrodes is reversed quickly in periodic and varying fashion leading to an oscillating trajectory for the ions. While passing through such an oscillating trajectory, a specified mass of ion (resonant ion) is deflected towards the ion detector surface and is detected. The potential applied across the quadrupole is swept to make field lower or high, the larger or smaller ions strike the ion detector, whereas the ions which fails to pass the trajectory smoothly (nonresonant ion) ends up after colliding with the walls of the quadrupole. A simple structure of the quadrupole with ion movement process for GC-MS is shown in Figure 2.27.

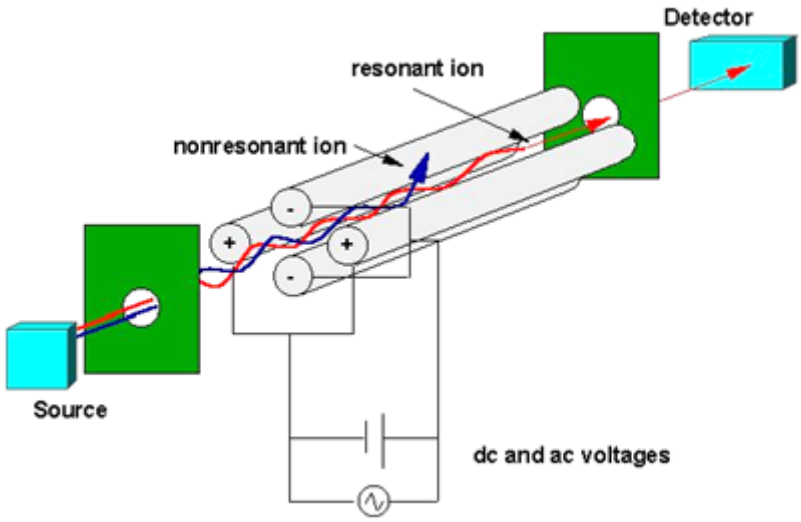

Figure 2.27 Structure and ion movement process in a quadrupole mass analyzer for GC-MS.

V. **Ion detector:** The ionized components and fragments passing through the electromagnetic field of quadrupole mass analyzer consist of two types of ions, the first type of ions are those which are unstable and follows a different path than the trajectory and ends up by colliding the rods. Second type of ions includes those ions which are stable through the path of the trajectory and are deflected towards the ionization detector. These ions before reaching the

detector are filtered by amu offset separating out the gamma rays which can false the data. The deflected ions from amu offset are then directed towards the conductive surface of the detector body inducing a cascade of ions with amplified signal to the data system. A schematic for the basic ion detection process is shown in Figure 2.28.

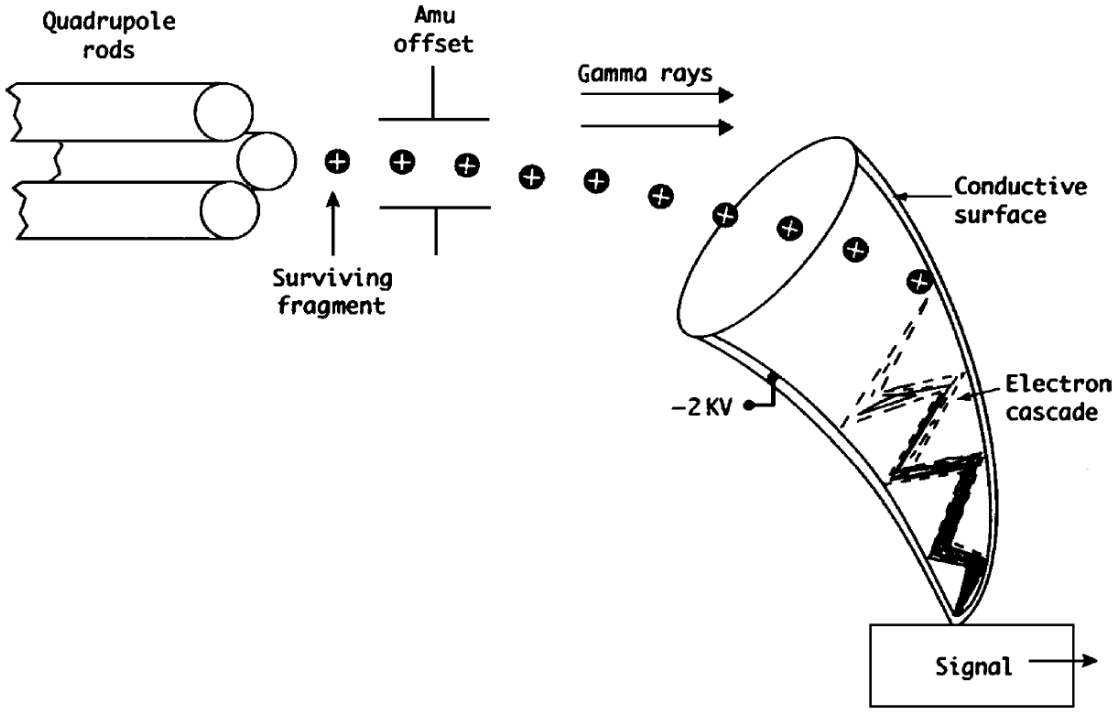

Figure 2.28 Process involved in the detection of the ionized streams from the quadrupole mass analyzer to the ion detector. (Taken from Ref. 15)

VI. Computer controls and data acquisition: As well defined by name, a computer control including software to control, operate GC-MS, generate and analyze the GC-MS data is linked with the GC-MS system. The spectrogram produced in the GC-MS is termed as total-ion current (TIC) chromatogram. A specified peak or spectrum range can be selected from the TIC and then can analyzed by using the similarity search option and confirming the data form the library source. Before running the GC-MS during the method preparation it is required to select the mode for the TIC analysis. Generally two types of modes are used for GC-MS, the SCAN mode and the single/selected ion monitoring (SIM) mode. The SCAN

mode offers to do a continuous scan over a range of masses and provides qualitative and quantitative both information. In contrary to SCAN mode, the SIM mode provides an opportunity to scan over only a discrete number of masses with high sensitivity and giving quantitative information. In general, MS-spectrogram is created in a three dimensional spectrum with time, intensity and m/z ratio as three axis, an example is shown in Figure 2.29.

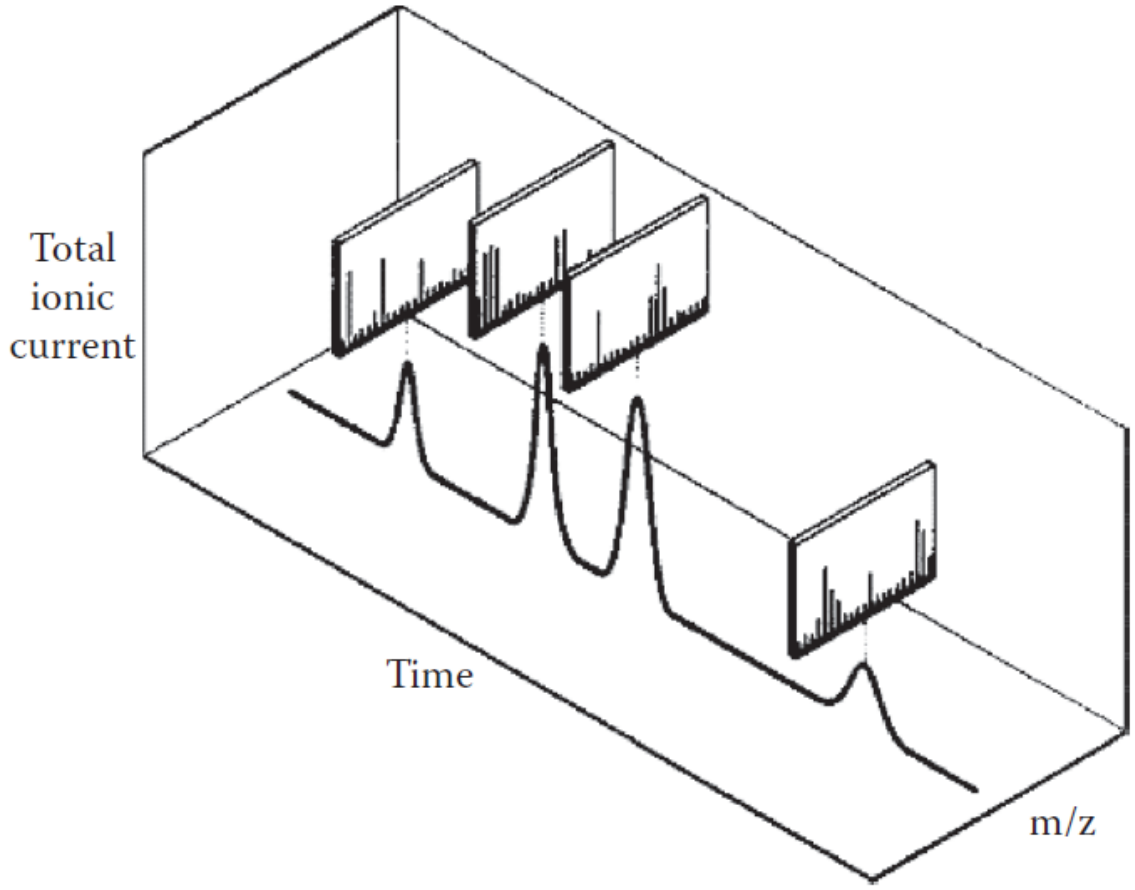

Figure 2.29 Typical three dimensional spectrogram generated by a GC-MS with TIC, time and m/z ratios as the three axis. (Taken from Ref. 16)

However, the spectrogram is usually presented in two dimensional form with the addition of all mass fragments intensities at a given time. In the case of the SIM mode, the spectrogram is known as single/selected ion current (SIC) chromatogram with the selected masses are being

analyzed. The corresponding m/z ratios can be determined for the selected peak in the two dimensional spectrogram (TIC or SIC) by selecting the peaks and similarity search from the available database of m/z ratios (library search). A real example for a standard hydrocarbon mixture (C1-C6) is shown in Figure 2.30 with m/z ratios determined for methane (CH_4) gas.

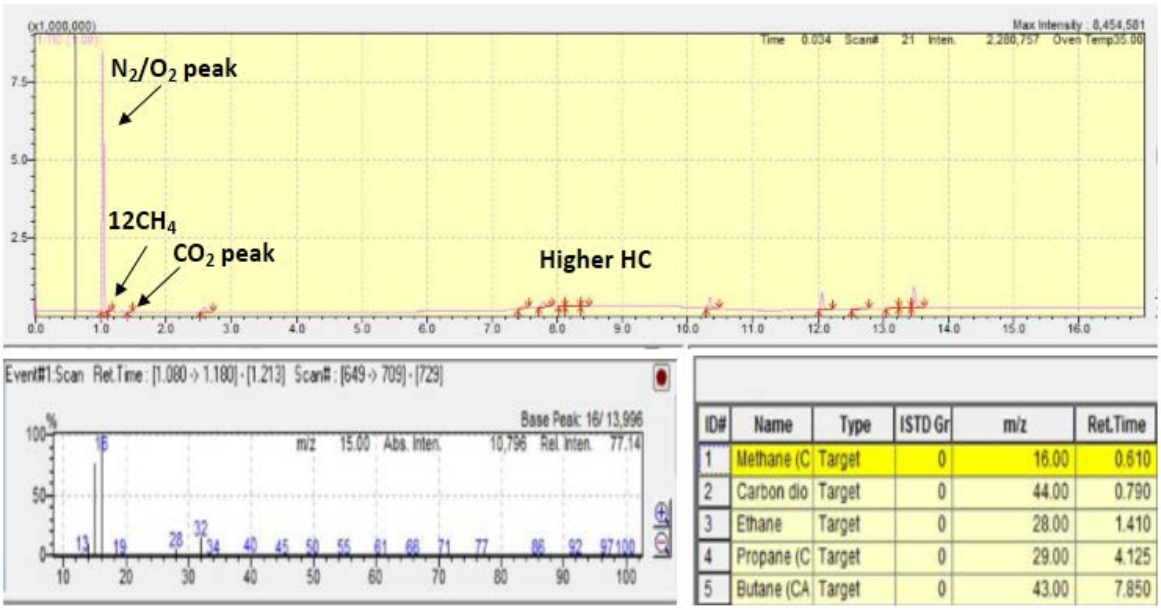

ID#	Name	Type	ISTD Gr	m/z	Ret.Time
1	Methane (C	Target	0	16.00	0.610
2	Carbon dio	Target	0	44.00	0.790
3	Ethane	Target	0	28.00	1.410
4	Propane (C	Target	0	29.00	4.125
5	Butane (CA	Target	0	43.00	7.850

Figure 2.30 TIC spectrogram for the CH_4 detected using lab GC-MS running in SIM mode.

2.2.3 Photocurrent measurements [17,18]

In the field of photocatalysis, photocurrent measurements for the respective photocatalyst is one of the efficient manner to investigate the photoresponsive properties such as photocurrent generation, charge separation at the interface or bulk volume, photoemission and photovoltaic effects of the photocatalysts. The definition of photocurrent can be made as electric current generated from a photocatalyst, semiconductor or any photosensitive device which exhibits photoelectric effect under the light irradiation. The photocurrent generated by a material during the light irradiation can be measured at open circuit potential (OCP) i.e. zero bias condition or at applied bias condition. The external bias applied is mostly required for the smooth flow of the electric current in the circuit by accelerating the photoelectrons generated in the material under investigtion.

The photocurrent measurements are presented mainly by two types of curves i.e. Current-Voltage (I-V) curves and Current-Time (I-t) curves. There are also several methods which can be used to determine the effect with voltage and time but the commonly used methods include analyzing the photocurrent response of photocatalyst with varied applied bias or with changing time under continuous or chopped light irradiation. The later I-V or I-t curves obtained under chopped light irradiation are well-known as transient photocurrent measurements.

a) Experimental arrangement

The experimental arrangement commonly used for the photocurrent measurements for a photocatalytic material includes

I. A light source (100/300 Watt Xe lamp)

II. Three electrode configuration setup consisting of working electrode (WE), reference electrode (Ag/AgCl) and counter electrode (CE, Pt electrode)

III. Electrolyte mainly composed of strong hole-scavengers such as NaOH, Na_2SO_4, $NaHPO_4$, $NaClO_4$.

IV. A potentiostat to measure the I-V or I-t curves with proper software installed.

A schematic illustration of the experimental arrangement is shown in Figure 2.31.

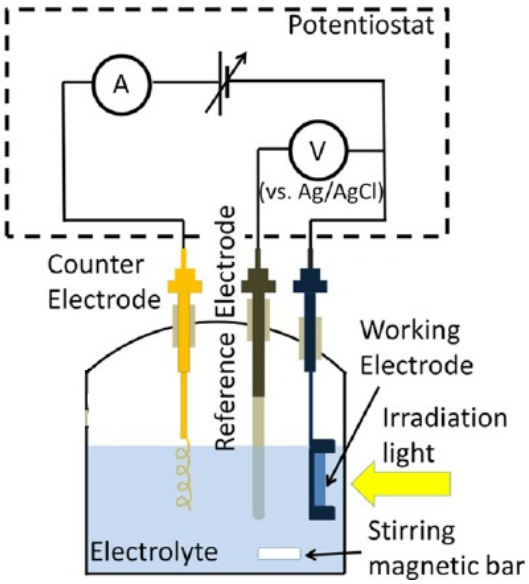

Figure 2.31 Illustration of simple electrochemical cell with three electrode electrochemical cell coupled with a potentiostat for photocurrent measurement of the interested material (WE).

b) Experimental procedure

For the measurements of photocurrents generated by photocatalytic materials, I-V curves and I-t curves are obtained via different methods. The commonly used experimental procedures for photocurrent measurement consists of:

(i) I-V curves measurement at zero bias, fixed bias or varying bias under continuous or chopped irradiation

(ii) I-t curves measurement at zero bias, fixed bias or varying bias under chopped irradiation

As obvious from the Figure 2.31, for the photocurrent measurements, the material of interest is attached as WE with Pt wire as a CE, and Ag/AgCl as a reference electrode in a three electrode configuration. The three electrode configuration is then dipped in an electrochemical

cell (made of glass, quartz or plastic material) filled with suitable electrolyte (in our research experiments we used Na_2SO_4 in deionized water) and quartz lens fixed at the front side of the cell body for light illumination. The light can be irradiated using an appropriated light source, in our case we used a simulated light from a 100 W Xe lamp. The external bias can be applied using the potentiostat and photocurrents generated as a result, are measured (using the same instrument). The data obtained can be plotted as I-V curves or I-t curves using the specified software in the computer control. The *chronoamperometry* and *linear scan voltammetry (LSV)* electrochemical techniques are generally used for continuous and transient photocurrent response respectively. An illustrative example of photocurrent measurements for a TiO_2 nanotube arrays is shown in Figure 2.32.

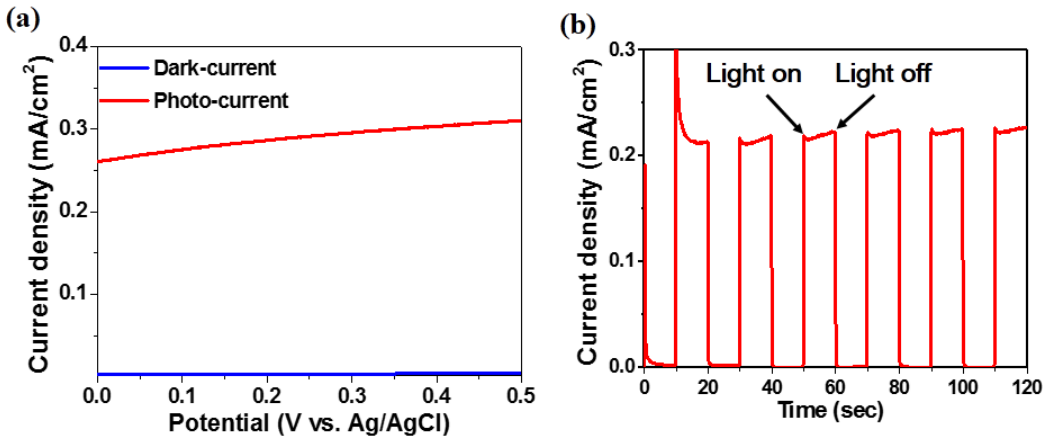

Figure 2.32 An illustrative example of photocurrent measurements for TiO_2 nanotubes arrays under 1 sun illumination showing (a) I-V curve with applied bias (0.5 V vs Ref.) and (b) transient photocurrent response under chopped light irradiation at zero bias.

2.3 Experimental setup for photocatalytic CO_2 conversion

2.3.1 Experimental assembly

The CO_2 photoreduction experiments throughout the research work are carried out in gaseous phase. The experimental setup used was designed in-house, the schematic of which is shown in Figure 2.33. The experimental setup mainly consists of the following components:

I. CO_2 gas cylinder providing 1000 ppm CO_2 in He to the reactor passing through a water bubbler to provide a saturated mixture of $CO_{2(g)}/H_2O$.

II. Mass flow controller (MFC) installed in the inlet line before the reactor to manipulate flow rate of $CO_{2(g)}/H_2O$ mixture to the photoreactor, which is normally 40 $cm^3 \cdot min^{-1}$.

III. A vacuum pump is installed at the outlet of the photoreactor to evacuate the air or any impurity gases before the experiments and gas tightening of the photoreactor.

IV. At both the inlet and outlet of the photoreactor, manual Swagelok valves are installed along with non-return valves (NRV) for the safe operation of the process. The locks are specifically designed to detach the photoreactor from the main experimental assembly in a safe manner and perform the required illumination. The photoreactor is a circular in shape (Volume =15.4 cm^3), with two side openings covered with rubber septums for sampling purposes. The quartz lens is placed at the top of the photoreactor with stainless steel made cover lid.

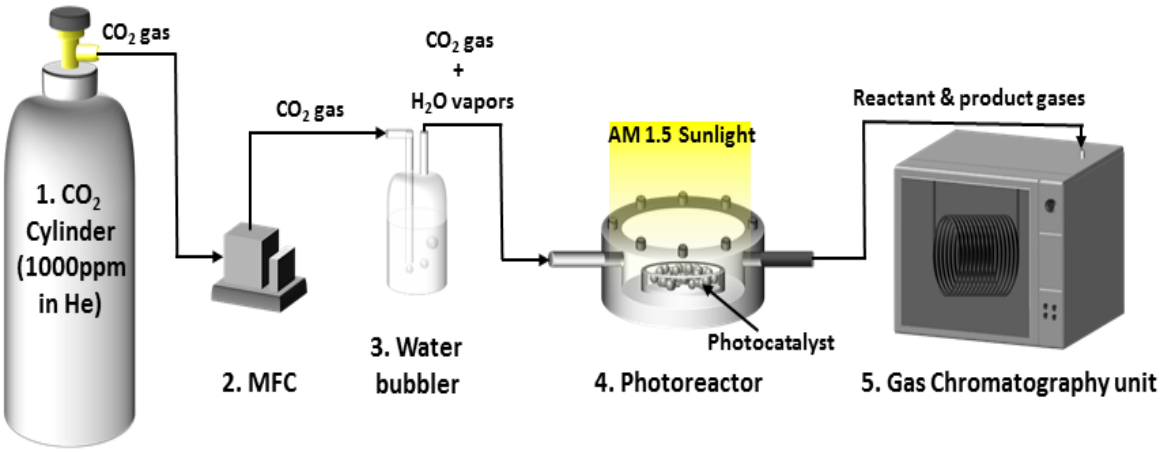

Figure 2.33 Schematic representation of experimental setup employed for CO_2 photoreduction involving (1) CO_2 gas cylinder (1000 ppm in He), (2) Mass flow controller, (3) Water bubbler for making CO_2 gas/H_2O vapors mixture, (4) Photoreactor (Stainless Steel, V=15.4 cm^3) loaded with photocatalyst material (70 mg of photocatalyst sample), irradiated by simulated solar light and (5) gas chromatography unit for analysis of product gases from photoreactor (equipped with FID).

2.3.2 Experiment preparation

The complete experimental procedure involves various important steps starting from purging of the line form CO_2 cylinder to reactor with the flow of CO_2 for enough time (30 minutes) to remove any air in the line if present. After satisfactory line flushing, the reactor inlet valve is then closed and the inlet line is saturated with the $CO_{2(g)}$/H_2O mixture. The photoreactor is then purged up to five cycles of purging before and after the catalyst loading in order to minimize the impurities effect and experimental errors. Each purging cycle consists of alternating steps of vacuum generation and filling of gaseous $CO_{2(g)}$/H_2O mixture. When the outlet valve of photoreactor is opened, the gaseous mixture inside it is evacuated and vacuum generation is continued until the vacuum display shows a value of 3.0 $x10^{-3}$ Torr. Upon

reaching the desired vacuum value the outlet valve of the reactor is closed gently while the inlet valve is opened and the CO_2 gas is passed to the reactor. The flow rate of the CO_2 gas is controlled by a mass flow controller (MFC). The CO_2 flows through the MFC and a water bubbler and finally reaches the reactor. While passing the bubbler CO_2 absorbs H_2O and form a mixture of H_2O and CO_2. The range of the MFC output is 0-40 cm^3/min. Just after opening the CO_2 cylinder valve, the MFC display shows a flow rate of 40 cm^3/min. As the CO_2 gas continues to flow, the flow rate value will decreases and eventually reaches 0 cm^3/min. This value is achieved due to the reason that the pressure difference within the reactor and the lines becomes zero. At this point it is considered that the photoreactor is completely filled with $CO_{2(g)}/H_2O$ mixture.

2.3.3 Experiment operation

After proper purging (five cycles) of the photoreactor loaded with specified amount of photocatalyst material (50-100 mg), it is allowed to completely filled with mixture of $CO_{2(g)}/H_2O$. The inlet and the outlet valves of the photoreactor are completely closed and the photoreactor is detached from experimental assembly. The photoreactor is then placed under solar light irradiation (UV lamp or solar simulator) for the required illumination time. After the required illumination and reaction time, the products samples is taken from the reactor via a glass syringe through the rubber septum covered opening at the side of photoreactor. The sample is then analyzed via injection into Gas Chromatography (GC) unit. Here it should be noted that before purging with $CO_{2(g)}/H_2O$, the photocatalyst loaded photoreactor is also purged with dry Argon gas for five cycles with similar purging procedure to remove any air contained inside the photoreactor or adsorbed contaminant species on photocatalyst surface which can contribute to hydrocarbon generation.

In general, three samples of each photocatalyst materials are tested under similar conditions of illumination and testing procedure. Then the average value (simple arithmetic mean) and standard deviation of these values is calculated using excel software. The standard deviation value is used to calculate the standard error value using formula

Standard error = Standard deviation/ (sum of all three values)$^{1/2}$

This standard error is illustrated as error bar in the bar graph showing the photocatalytic products obtained from photocatalytic CO_2 conversion.

2.3.4 Control test and carbon source investigation

Further to investigate the carbon source contribution to the generation of hydrocarbons, control tests with Ar(g)/H_2O mixture is done instead of using $CO_{2(g)}$/H_2O. The photocatalyst loaded photoreactor is filled with Ar(g)/H_2O mixture during the purging procedure, illuminated under similar irradiation conditions and the products are analyzed using GC. If the GC peaks related to hydrocarbons is significant, then this indicates the role of surface adsorbed carbon species on the photocatalyst surface for yielding hydrocarbon products. However if no significant amount of hydrocarbon fuels are generated under Ar(g)/H_2O environment, the results then confirms the negligible role of surface adsorbed carbon species to hydrocarbon generation and CO_2 is considered as a key carbon source which is getting converted into hydrocarbon fuels under illumination via photocatalytic reaction.

The more reliable and accurate test for confirming CO_2 and H_2O as a carbon and hydrogen sources for yielding hydrocarbon products is analysis using gas chromatography coupled mass spectrometer (GC-MS). For GC-MS tests, the carbon source is investigated by reacting the $^{13}CO_2$ isotope with H_2O on photocatalyst surface yielding $^{13}CH_4$, thus confirming the CO_2 as a carbon source and ensuring the photocatalytic conversion of CO_2 into hydrocarbon rather than

conversion of surface adsorbed carbon species. The possible reactions involved in $^{13}CO_2$ tests could be as follow (where MO = metal oxide photocatalyst)

$$MO + h\nu \text{ (sunlight)} \rightarrow MO (e^-_{CB}) + MO (h^+_{VB}) \quad (2.7)$$

$$MO (8h^+_{VB}) + 4H_2O \rightarrow 8H^+ + 2O_2 \quad (2.8)$$

$$^{13}CO_2 + 8H^+ + MO (8e^-_{CB}) \rightarrow {}^{13}CH_4 + H_2O \quad (2.9)$$

In above equations one can see when a photocatalyst material (MO) absorbs sunlight, electron and hole pairs are photogenerated. The holes generated in MO valence band are filled by water oxidation reactions resulting in protons (H^+ ions) and oxygen (O_2). The $^{13}CO_2$ can react with resulting H^+ ions and photogenerated electrons to yiled $^{13}CH_4$. If a photocatalyst is unactive and/or hydrocarbon prdouced is due to the surface adosrbed carbon species, then no peak (either realted to$^{12}CH_4$ or $^{13}CH_4$) is observed and/or only $^{12}CH_4$ peak (instead of $^{13}CH_4$) is observed in GC-MS spectrum respectively.

2.4 References

[1] Y. Leng, MATERIALS CHARACTERIZATION-Introduction to Microscopic and Spectroscopic Methods, John Wiley & Sons (Asia) Pte Ltd, 2008. www.wiley.com.

[2] W.E. Smith, G. Dent, Modern Raman Spectroscopy- A Practical Approach, John Wiley & Sons, Ltd, 2005. www.willey.com.

[3] J.R. Ferraro, K. Nakamoto, C.W. Brown, Introductory Raman Spectroscopy, Second Edition, Elsevier, 2003.

[4] R.F. Egerton, Physical Principles of Electron Microscopy An Introduction to TEM, SEM, and AEM, Springer Sciences+Buisness Media, Inc., 2005.

[5] J.F. Watts, J. Wolstenholme, An Introduction to Surface Analysis by XPS and AES, John Wiley & Sons, Ltd, 2003.

[6] J.F. Moulder, W.F. Stickle, P.E. Sobol, K.D. Bomben, Handbook of X-ray Photoelectron Spectroscopy, Physial Electronics, Inc., 1995.

[7] H.-H. Perkampus, UV-Vis Spectroscopy and Its Applications, WILEY-VCH Verlag GmbH, 1992.

[8] J. Torrent, V. Barron, Methods of Soil Analysis Part-5 Minerological Methods, Soil Society of America, Inc., 2008.

[9] An Introduction to Flourescence Spectroscopy, PerkinElmer, Inc., 2000.

[10] S. Perkowitz, Optical Characterization of Semiconductors: Infrared, Raman, and Phtoluminescence Spectroscopy, Academic Press Limited, 1993.

[11] J.B. Condon, Surfcae Area and Porosity Determinations by Physisorption Measurments and Theory, First Edition, Elsevier, 2006.

[12] M. Kruk, M. Jaroniec, Gas adsorption characterization of ordered organic-inorganic nanocomposite materials, Chem. Mater. 13 (2001) 3169–3183. doi:10.1021/cm0101069.

[13] H.M. McNair, J.M. Miller, Basic Gas Chromatography, John Wiley & Sons, Ltd, 1998.

[14] H.-J. Hubschmann, Handbook of GC/MS, WILEY-VCH Verlag GmbH, 2001.

[15] M.C. McMaster, GC/MS A Practical User's Guide, Second edition, Wiley-Interscience, 2008.

[16] S. Bouchonnet, Introduction to GC-MS Coupling, CRC Press Taylor & Francis Group, 2013.

[17] Y.-F. Su, T.-C. Chou, T.-R. Ling, C.-C. Sun, Photocurrent Performance and Nanostructure Analysis of TiO_2/ITO Electrodes Prepared Using Reactive Sputtering, J. Electrochem. Soc. 151 (2004) A1375. doi:10.1149/1.1775217.

[18] B. AlOtaibi, M. Harati, S. Fan, S. Zhao, H.P.T. Nguyen, M.G. Kibria, Z. Mi, High efficiency photoelectrochemical water splitting and hydrogen generation using GaN nanowire photoelectrode., Nanotechnology. 24 (2013) 175401. doi:10.1088/0957-4484/24/17/175401.

Chapter 3. Photocatalytic Conversion of CO_2 to Hydrocarbon fuel using Carbon and Nitrogen co-doped Sodium Titanate Nanotubes

3.1 Introduction

As is well documented, CO_2 is a thermodynamically stable molecule and requires a significant amount of energy for its conversion/reduction into useful chemicals and fuels. In case of solar-spectrum photocatalysis, such amount of energy is provided by sunlight which is absorbed by photocatalytic materials and then utilized for respective photocatalytic reactions. Thus in photocatalysis, the adequate and extensive absorbance of sunlight is one of the key requirements to make the process efficient. Until now, enormous researches have been conducted for the development of photocatalytic materials for photocatalytic CO_2 conversion such as ZnO [1], $ZnGe_2O_4$ [2], Ga_2O_3 [3], Co_3O_4 [4], TaO_3 [5], $BiVO_4$ [6], g-C_3N_4 [7], Si nanocrystals [8], GO [9] and TiO_2 [10]. Amongst various photocatalysts developed, Titanum dioxide/Titania (TiO_2) and/or TiO_2 based photocatalysts are still the prime choice due to its superb and outstanding properties as compared to various other photocatalytic materials such as abundant availability, nontoxicity, corrosion resistance, and chemical stability [11–13].

TiO_2 in nature mainly exists in three crystalline phases i.e. rutile, anatase and brookite. However further metastable phases are also reported in literature which are synthetically produced by various experimental methods [14,15]. The crystalline structure for these phases are depicted in Figure 3.1. Amongst the natural phases, rutile phase is considered as the most stable phase with 0.8 low $\Delta G_f°$ then the anatase. Anatase phase is also quite stable up to 600 °C annealing temperature, after 600 °C its conversion mainly to rutile is observed. In general, the anatase phase is believed to be more photocatalytic active then the other phases mainly due to its intrinsic properties of (i) longer charge carrier life time because of indirect band gap and, (ii) directional charge diffusion and low polaron effective mass leading to more efficient charge diffusion from the bulk to surface. Despite of the various benefits offered by TiO_2, the wider

band gap of TiO_2, approximately 3.2 eV, which is responsible for its excellent corrosion stability, limit its sunlight absorption to UV region, comprising only some 4-5 % of the terrestrial solar-spectrum energy [16]. Thus to apply for some energy demanding photocatalytic application like CO_2 photoreduction, modifications and developments are required to capture and harvest a broader light spectrum. In this regard, numerous approaches have been used for lowering the TiO_2 band gap such as metal ion implantation [17], non-metal doping [18–20], synthesis of low band gap hybrid nanomaterials [21], and dye-sensitization [22]. On contrary to loading of expensive metals, doping or co-doping of non-metals e.g. N, S, C, F etc. into TiO_2 lattice is an inexpensive way with significant narrowing of band gap resulting in improved light absorption [23].

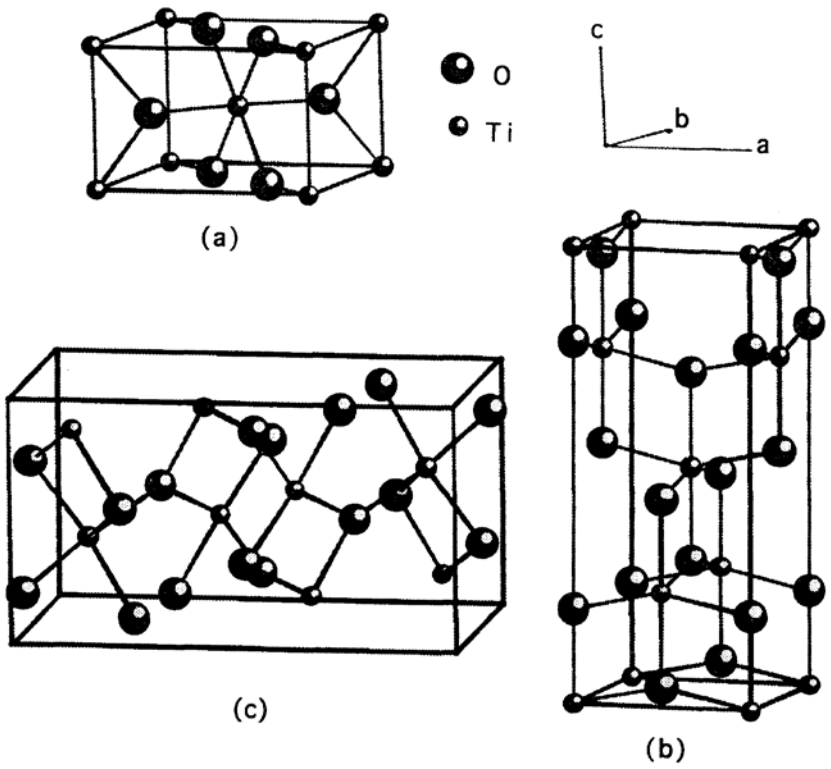

Figure 3.1 Crystal structures of naturally occurring phases for TiO_2: (a) rutile, (b) anatase and (c) brookite. (Taken from Ref#14)

Crystalline TiO_2 nanoparticles can also be converted to various nanostructures such as nanofibers, nanosheets and nanotubes [24–26], which offers large surface areas with improved adsorption capacity, moderate photocatalytic activity, and improved thermal and chemical stability. In this regard, an attempt was made by Kasuga *et. al.* [27] to convert the anatase TiO_2 powder into TiO_2 nanotubes, commonly known as titanate nanotubes, providing a high surface area of 400 m^2/g with almost similar band gap as that of anatase (~ 3.2 eV). He used a simple alkaline hydrothermal method i.e. treating the crystalline anatase TiO_2 nanoparticles with NaOH at high temperature and pressure in an autoclave. Since then, a large amount of experiments have been done for their investigations regarding the crystalline phase, activity and synthesis mechanism for such TiO_2 nanotubes and their application in a variety of research domains. The mechanism involved in the formation of TiO_2 nanotubes is still not clear, however it is generally considered that during hydrothermal treatment the metal cations (Na^+, Li^+ or K^+) interacts with the TiO_2 nanoparticles and got intercalated between the edge shared TiO_6 octahedral layers which hold it tight and appears in the form of nanosheets. On further hydrothermal treatment, some of the Na^+ ions can be replaced with larger size water molecules and are exfoliated forming curled shape nanosheets. As the nanosheets usually don't have inversion symmetry, finally forming the tubular structure via curling up with a release of strain energy [28]. Moreover, various nanostructures like nanosheets, nanodiscs, nanowires etc. have also been reported by such alkaline hydrothermal treatment by varying the reaction temperature, time, concentration of alkaline solution, post washing and annealing effects. A schematic for the process involved in the TiO_2/titanate nanotubes is shown in Figure 3.2.

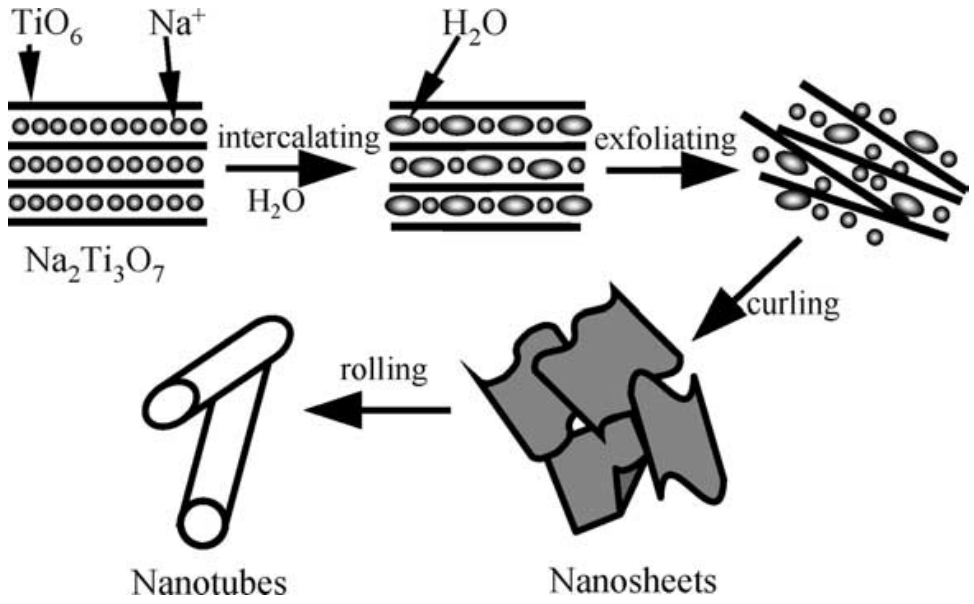

Figure 3.2 Proposed mechanism for the formation of Na^+-TNT by exfoliation-rolling model. (Taken from Ref. # 28)

Further, a lot of studies have also been done to investigate the crystalline structure of titanate nanotubes. It is commonly believed that, initially as synthesized titanate nanotubes are mainly consists of sodium trititanate ($Na_2Ti_3O_7$). However the acid washing and annealing have interesting effects on the phase of titanate nanotubes. During the acid washing the surface adsorbed and intercalated Na^+ ions can be removed and replaced by the protons thus interrupting the interlayer spacing and forming hydrogen titanate, $H_2Ti_3O_7$ [29]. The post annealing of the as-synthesized samples to achieve better crysatllinity for improved photocatalytic activity shows a variety of mixture of phases depending upon the duration and temperature of annealing. Mostly observed phases include sodium trititanate ($Na_2Ti_3O_7$), sodium hexatitanate ($Na_2Ti_6O_{13}$), TiO_2 (B) (a metastable monoclinic form of TiO_2) and anatase TiO_2 [30]. Usually the annealing temperature to achieve the crysatllinity for titanate nanotubes is kept in range of 400-500 °C. At this temperature a mixture of sodium trititanate ($Na_2Ti_3O_7$) and sodium hexatitanate ($Na_2Ti_6O_{13}$) is achieved [29]. The crystal structure of both is shown in Figure 3.3.

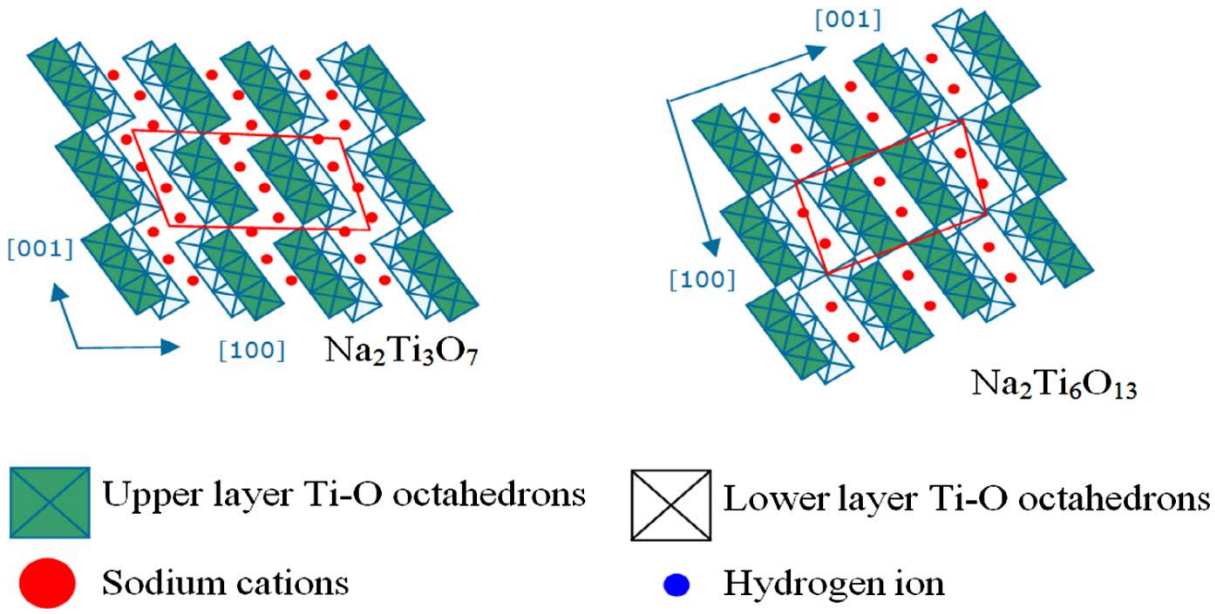

Figure 3.3 Crystal structures for sodium trititanate ($Na_2Ti_3O_7$) and sodium hexatitanate ($Na_2Ti_6O_{13}$). (Taken from Ref. # 31)

The titanate nanotubes (TNT) with a layered structure makes them ideally suitable with higher surface area for improved photocatalytic performance in CO_2 photoreduction. Furthermore, the Na^+ ions intercalated between the titanate layers probably acting as recombination centers thus decreasing photocatalytic activity [30–32], has recently been reported for improved CO_2 adsorption capacity that, in turn, will influence the rates of CO_2 photoconversion into hydrocarbons [33,34]. However, the limitation faced is still the same as faced by TiO_2, i.e. limited light absorption due to wider band gap.

Being inspired by the unique qualities, in the first experimental work of the Ph.D. research thesis, sodium titanate nanotubes (from now one represented as TNT) as a photocatalyst material is selected which can provide high surface area for CO_2 adsorption and reduction. To overcome the issue of limited light absorption, a co-doping strategy is designed rather than a single doping as a means to obtain broad light absorption resulting in improved photocatalytic properties of TNTs. Amongst various nonmetals, carbon and nitrogen are well known dopants

with admirable ability to improve the photocatalytic activity with enormous amount of investigations have been done for C and N doping in TiO_2 nanoparticles system. In this experimental work, a carbon and nitrogen co-doped sodium titanate nanotubes (C,N-TNTs) is the aim of the research, the photocatalytic activity of whose are tested mainly for photoconversion of CO_2 and water vapor into hydrocarbon fuel under simulated solar-light illumination.

The co-doping experimental procedure consists of two simple steps: (i) The first step involves the synthesis of sodium titanate nanotubes by a conventional alkaline hydrothermal treatment of available TiO_2 (anatase) followed by (ii) the mixing of produced TNT with desired amount of urea and calcining under air flow to achieve the final product i.e. C,N-TNT. It is reported, the most stable nanotube structure is obtained via alkaline hydrothermal treatment of TiO_2 (anatase) with NaOH as compared to nanotubes formed when other alkali metals are used [35,36], thus herein NaOH was used during alkaline hydrothermal treatment step. A series of the C,N-TNT is prepared by varying the composition of urea and its influence on photocatalytic activities of the materials is demonstrated.

3.2 Experimental section

3.2.1 Materials and Reagents

The chemical and reagents used in this experimental work includes, Sodium hydroxide (Reagents Duksan, 94 %), TiO_2 anatase (Daejung, > 98 %), Urea (Sigma-Aldrich, 98 %) and Deionized (DI) water.

3.2.2 Preparation of carbon and nitrogen co-doped sodium titanate nanotubes (C,N-TNT)

The synthesis strategy designed in this experimental work consists of two step experimental scheme for the preparation of carbon and nitrogen co-doped sodium titanate nanotubes (C,N-TNT). The schematic diagram for the designed process is shown in Figure 3.4.

The first step consist of synthesis of pure TNT by a typical alkaline hydrothermal method as reported earlier [49]. The process includes mixing of 2.0 g of commercially available TiO_2 powder (anatase) with 20 ml of 10 M NaOH solution in a beaker. The uniform suspension after stirring for 1h was transferred to a teflon lined autoclave (30 ml) and heated at 150 ºC for 24 hours. The reaction mixture was filtered after cooling and washed with deionized water to adjust the pH to 7.0. The obtained precipitate was dried at 70.0 ±10.0 ºC in an air oven, and calcined at 400 ºC in a muffle furnace (box furnace) for 6 hours in the presence of static air. This sample was labeled as TNT.

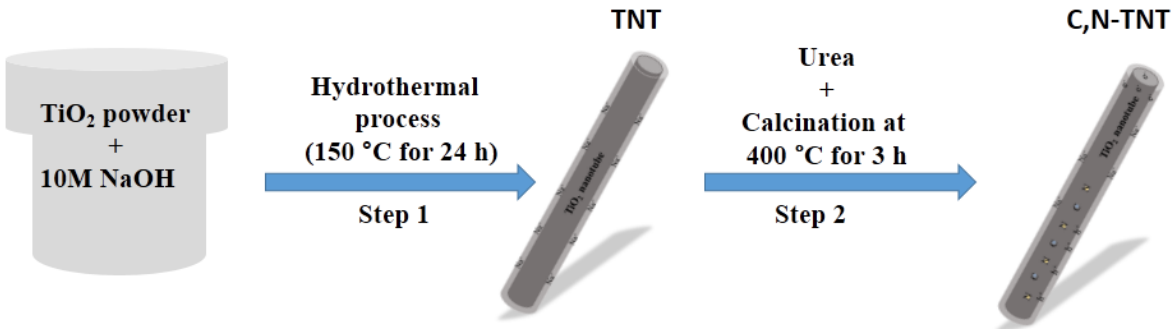

Figure 3.4 Schematic view of the experimental scheme designed for the synthesis of C,N-TNT.

In the second step, TNT was mixed with varied amount of urea in a mortar and ground well to obtain a homogeneous mixture. Typically 0.1 g of TNT was mixed with 0.1, 0.3, 0.6, and 1.0 g of urea to prepare a series of carbon and nitrogen co-doped sodium titanate (C,N-TNT). The powdered samples obtained after grinding were transferred to a crucible and calcined at 400 ºC for 3 hours in a tubular furnace under air flow (30 cm^3/min). The obtained materials were labeled as C,N-TNT01, C,N-TNT03, C,N-TNT06, and C,N-TNT1 for the sample obtained with 0.1, 0.3, 0.6, and 1.0 g of urea respectively.

3.2.3 Characterization

The crystalline structure of the materials were analyzed by powder X-ray diffraction (XRD) using X-ray diffractometer (Panalytical, Empyrean) operating at 40 kV and 30 mA with Cu Kα radiation (λ=1.54Å) as an X-ray source, scanned with a step degree of 0.02° and duration time of 0.05 s in the range of 2θ =5-70°. The phase transformation of the materials and the band assigned for titanate was studied by Raman spectroscopy using a NICOLET ALMECA XR Raman spectrometer equipped with a He-Ne laser (532 nm) as the light source. Morphological analysis of the materials were analyzed using field emission scanning electron microscopy (FE-SEM, Hitachi S-4800) and transmission electron microscopy (TEM) to know about the morphology and size of the materials. The TEM images were obtained by FE-TEM (Hitachi HF-3300) instrument operating at 300 kV. For TEM analysis, the samples were prepared by dispersing in ethanol followed by sonicating the mixture for 1 hour. One drop of the dilute suspension was dropped on a TEM grid and allowed to dry overnight. The UV-vis diffuse reflectance spectroscopy (UV-vis DRS) of the materials was measured using Cary series (CARY5000) UV-visible-near IR spectrophotometer (Agilent technologies) with a diffuse reflection accessory in the range of 200-700 nm. The N_2 physisorption measurements were carried out to know about the textural properties such as specific surface area, pore volume and

pore size distribution. For N_2 physisorption measurements, the samples were degassed extensively at 200 ºC at 20 mTorr for 300 minutes prior to the experiments. The N_2 sorption isotherms were measured at -196 ºC on a Micromeritics ASAP 2000 apparatus. The surface area was calculated by using the Brunauer–Emmett-Teller (BET) equation. The pore volume was determined from the amount of N_2 adsorbed at the highest relative pressure of (P/P_0) = 0.99. The BJH pore diameter was obtained by applying the Barrett-Joyner-Halenda (BJH) equation to the desorption isotherm. The surface composition and oxidation states of Ti, O, C and N in different materials were determined by X-ray photoelectron spectroscopy (XPS, Thermo Scientific, ESCALAB 250Xi) using Al Kα line (148606 eV) as the X-ray source. The XPS peaks calibration was done against the standard reference C 1s peak.

3.2.4 Photocatalytic CO_2 conversion

The prepared photocatalysts were employed for photocatalytic CO_2 conversion yielding CH_4 as a main product. The experimental procedure for photocatalytic CO_2 conversion test is explained in section 2.3 of chapter 2.0. Briefly, 100 mg of each photocatalyst prepared was loaded to the reactor and CO_2 gas (1000 ppm in He) was passed through a water bubbler, forming a mixture of CO_2 and H_2O vapors which then enters the reactor. A 100 W Xenon solar simulator (Oriel, LCS-100) with an AM 1.5 filter was used as a light source, the light spectrum of which is shown in Figure 3.5. The photoreactor products were analyzed using a gas chromatograph unit (Shimadzu GC-2014, Restek Rt-Q-Bond column, ID=0.53 mm, length=30 m) equipped with both thermal conductivity detector (TCD) and a flame ionization detector (FID).

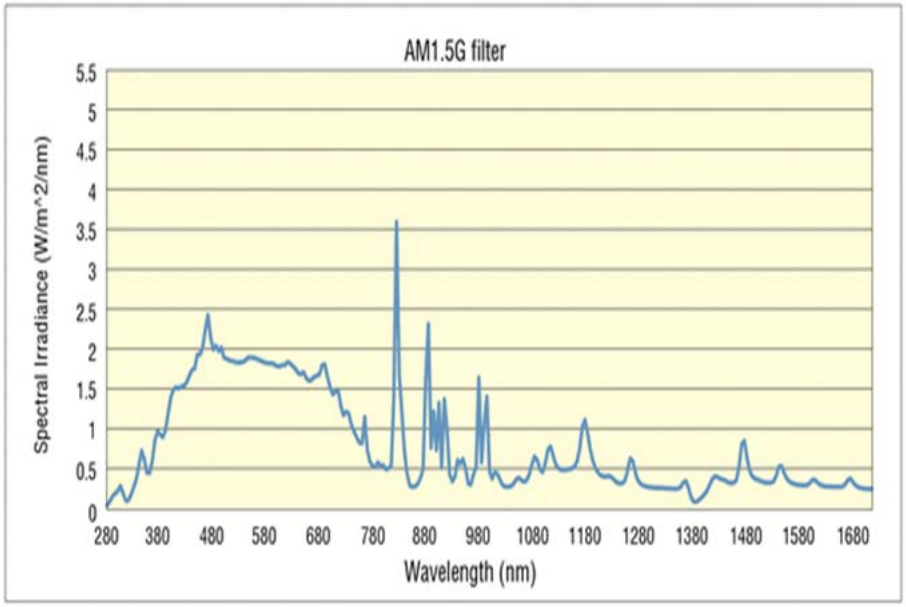

Figure 3.5 Spectral irradiance of 100 W Xe lamp passing through AM 1.5G filter.

After 1 h of irradiation, product samples from the reactor were manually taken with a 500 µL argon-purged syringe and injected into the gas-chromatography (GC) unit. Three measurements were performed for each sample; the average for the three readings is reported along with their standard error bar in the results and discussion part. The obtained values for the yielded product was in units of $ppm.g^{-1}.h^{-1}$, this unit was converted to $\mu mole.g^{-1}.h^{-1}$ on the basis of ideal gas equation with consideration of volume of evolved CH_4 gas as a basis. Control tests was also performed by illuminating C,N-TNT06 in an $Ar/H_2O(g)$ atmosphere rather than $CO_2/H_2O_{(g)}$ mixture to investigate the origin of the carbon intrinsic to the CH_4. The hour normalized CH_4 evolution rate was calculated using eq. 3.1 as:

$$\text{Rate of } CH_4 \text{ evolution} = \frac{\text{Amount of } CH_4 \text{ produced (ppm)}}{\text{Amount of photocatalyst used (g)}} \quad (3.1)$$

The yield in μmol of CH_4 gas produced can be determined from ppm on the volume basis equation as:

X ppm of CH_4= Y m^3 of CH_4 / Z m^3 of ideal gas in reactor (3.2)

Then using the ideal gas equation i.e. PV=nRT, the moles (n) of CH_4 gas yielded can be calculated by plugging the values of volume (V), pressure (P = 101.325 Pa), temperature (T = 303 K) and ideal gas constant (R = 8.314 $m^3 \cdot Pa \cdot K^{-1} \cdot mol^{-1}$).

3.3 Results and discussion

3.3.1 Crystallographic study

The crystalline structure of pure TNT and C,N-TNT samples are investigated using X-ray diffraction analysis and Raman spectroscopy. The XRD patterns for pure TNT and series of different C,N-TNT samples are shown in Figure 3.6a. It is observed that pure sample after proper annealing shows various diffraction peaks appearing at 2θ value of 10.2º, 24.2º, 28.6º, 33.8º, 38.6º and 61.6º. These peaks well matches to reported literature and are attributed to the interplanar spacing d_{200}, d_{110}, d_{310}, $d_{31\text{-}2}$, d_{004} and d_{020} respectively, indicating the presence of sodium titanate phase [37]. It can be noticed that the peaks appearing around 2θ values of 10.2º and 28.6º which are associated to TNT interlayer spacing in pure TNT [30,38], are shifted to higher angles in C,N-TNT samples with the peaks themselves becoming more diffuse. Such a peak-shifting after carbon and nitrogen doping [35], with the weakened intensities is an indication of a decreased interlayer spacing associated to TNT-protonation. The protonation can be possibly due to the doping induced by urea content and substitution of intercalated Na^+ ions with H^+ ions [30,38], suggesting TNT doping driven protonation in the second step of synthesis. For the sample C,N-TNT1with highest urea content, the protonation seems highest with the highly diffused interlayer peaks. In addition, another peak appearing at 25.6º is observed for samples C,N-TNT03, 06, and 1, which is not observed in the XRD patterns of

pure TNT and C,N-TNT01. This peak is associated to anatase phase, a result which suggest that protonation supporting the anatase phase formation while the higher Na^+ ions in pure and C,N-TNT01 inhibits the formation of anatase [39,40].

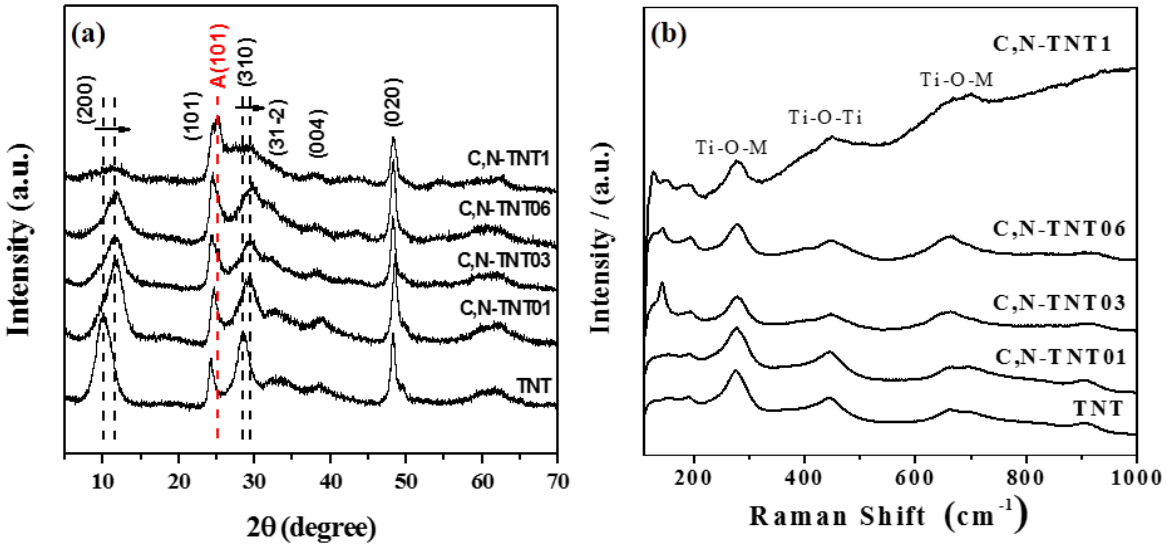

Figure 3.6 XRD patterns (a) and Raman spectra (b) of pure TNT and C,N-TNT samples with varied content of urea. (01, 03, 06 and 1 stands for 0.1, 0.3, 0.6, and 1.0 g of urea respectively for C,N-TNT)

Raman spectra for pure and all C,N-TNT samples are shown in Figure 3.6b. All samples exhibits broad Raman active bands at 280, 445, 675, and 908 cm^{-1}. Qamar *et al.* [29], suggested the bands appearing around 285 cm^{-1} and 675 cm^{-1} corresponds to Ti-O-Na stretching vibration of TNT whereas the bands appearing around 445 and 675 cm^{-1} of TNT can be attributed to Ti-O-Ti. The vibrational band at 908 cm^{-1} is associated to the stretching vibration of Ti-O indicating the presence of non-bridging oxygen atoms coordinated with sodium ions. However, the band intensity of vibration band at 908 cm^{-1} is decreased to a large extent upon co-doping but it can be observed for all the co-doped TNT samples thus indicating the partial exchange of sodium ions present in TNT with hydrogen ion. The bands at 141 cm^{-1} and 198 cm^{-1} observed specifically in the samples C,N-TNT03, C,N-TNT06, and C,N-TNT1 provides a clue regarding the presence of some amount of anatase TiO_2 in the respective materials [41].

3.3.2 Morphological analysis

The morphology for the pure TNT and C,N-TNT are studied using the field emission scanning electron microscopy (FE-SEM) and transmission electron microscopy (FE-TEM). Figure 3.7 shows the FE-SEM images for the pure TNT and C,N-TNT03. The FE-SEM images of pure TNT and C,N-TNT03 samples (Fig. 3.7) exhibits a fine tubular structure with several nanometer lengths.

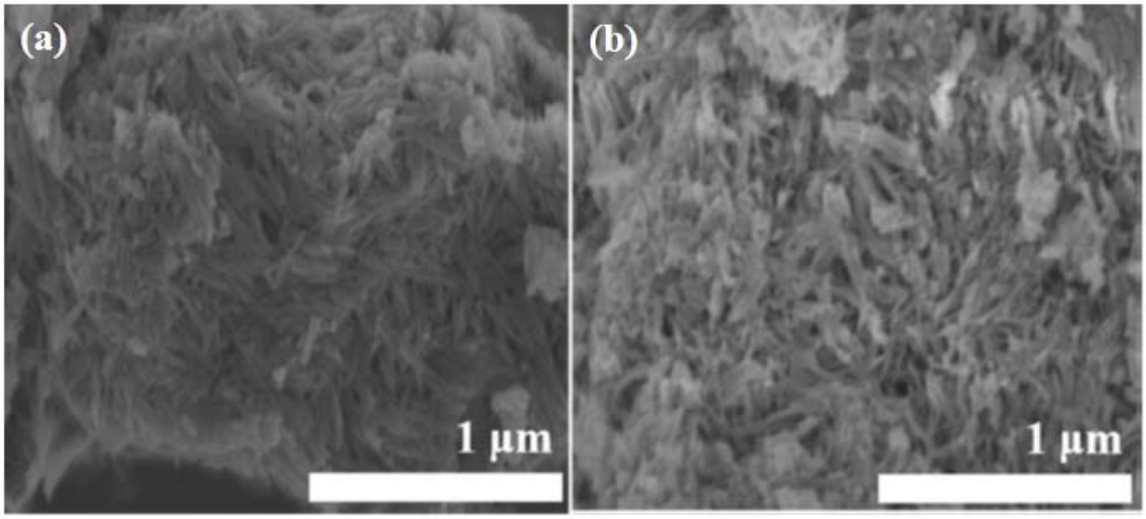

Figure 3.7 FE-SEM images of the pure TNT (a) and C,N-TNT03 (b).

Figure 3.8 displays the TEM images with low and high resolution for pure TNT and C,N-TNT03 sample as a representative sample for C,N-TNT. The TEM image for pure TNT exhibit its stable structure with well crystalline nature after the annealing step. Whereas for the C,N-TNT03 sample, a slight distortion of TNT walls is observed after the calcination with urea as a source of co-doping, possibly due to protonation effect induced by urea which destabilizes a little bit the nanotubes structure. However, besides a little distortion it is fair enough to suggest that the C,N-TNT03 sample retain almost similar tubular structure after C, N co-doping and calcination at 400 ˚C.

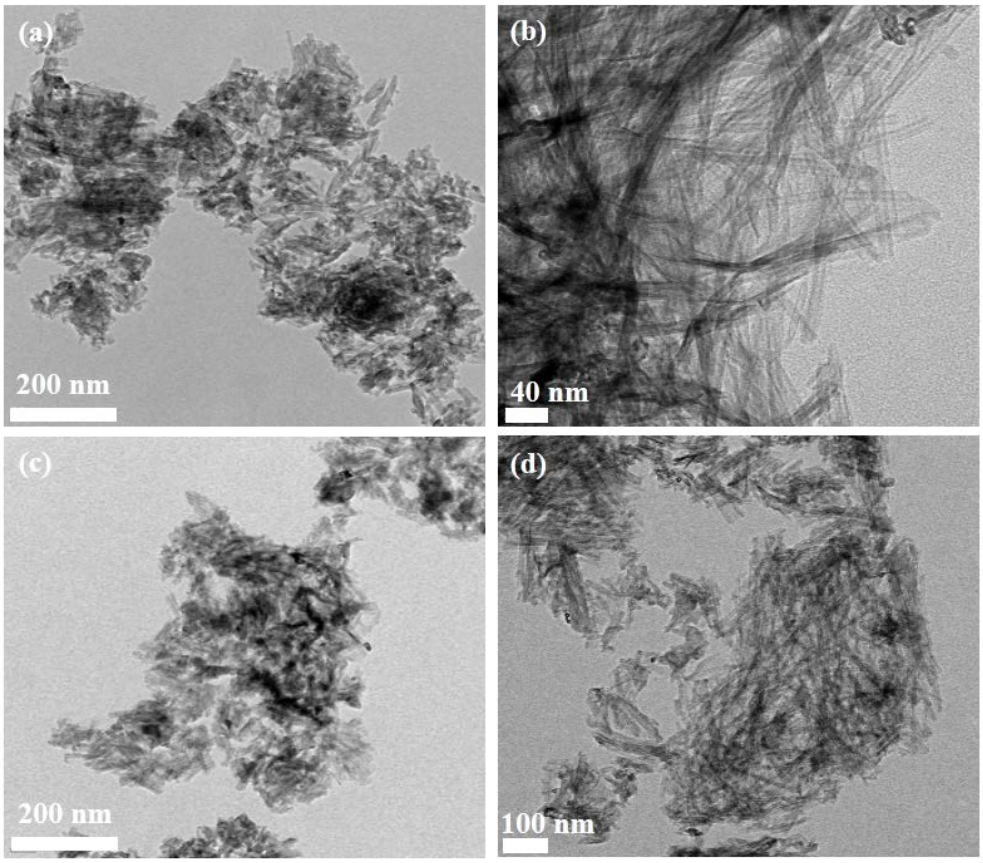

Figure 3.8 TEM images of the pure TNT (a & b) and C,N-TNT03 (c & d).

3.3.3 Light absorption and Band gap estimation

The light absorption properties are investigated using UV-vis DRS data obtained for pure TNT and all C,N-TNT samples is shown in Fig. 3.9a. It can be observed that the absorption of pure TNT is limited to UV range only ($\lambda < 400$ nm) due to wider band gap as typically observed for anatase TiO_2. However upon co-doping, a red shift of the absorption wavelength is observed which is extended to a portion of visible range and is increased with increased dopants level by increasing urea amount. The absorption below 400 nm is associated to the electron transitions from the valence to conduction band while the absorption above the 400 nm, extended up to 500 nm can be attributed to the synergistic effect of C and N co-doping, creating inter band gap states leading to narrowing down of the band gap and broadening of light absorption [42].

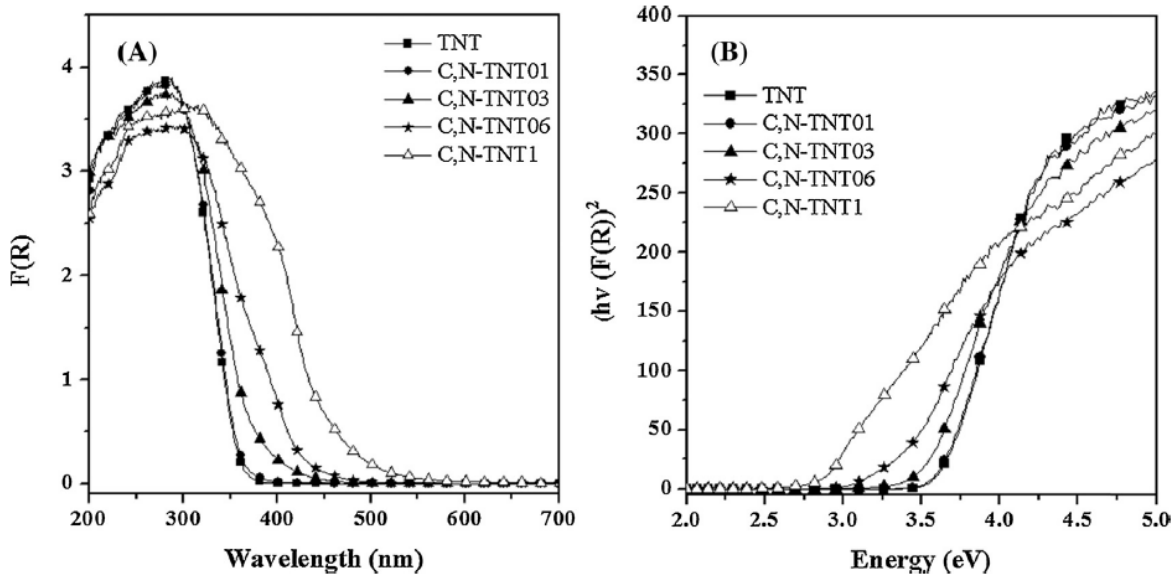

Figure 3.9 UV-vis DRS of pure TNT and C,N-TNT samples (a) and corresponding Tauc plot for band gap estimation (b). (01, 03, 06 and 1 stands for 0.1, 0.3, 0.6, and 1.0 g of urea respectively for C, N-TNT)

The band gap energies for all samples are estimated using a well-known Tauc relationship [43]. Tauc plots for all the samples are plotted using this relationship and shown in Figure 3.9b. The Tauc relationship is given as:

$$(\alpha h\nu) = \alpha_o(h\nu - E_g)^n \quad (3.3)$$

Where α_o is band tailing parameter constant, h is Planck constant, ν is frequency and Eg is the optical band gap of the material. The value of n for direct and indirect band gap is ½ and 2 respectively. The function $(\alpha h\nu)^n$ is plotted against energy hν and the linear portions of the curves are extrapolated to zero (y-axis) to determine the estimated band gap values. The band gap estimated for each material is shown in Table 3.1. It is obvious that all C,N-TNT samples possess lower band gap as compared to the pure TNT. The variation in band gap is attributed to the difference in amount of carbon and nitrogen dopants in these materials.

3.3.4 N_2-physisorption analysis

The textural properties of the prepared samples are investigated via N_2-physisorption analysis of respective samples. The N_2-sorption isotherms of pure TNT and all C,N-TNT samples are displayed in Figure 3.10a. According to IUPAC classification [44], the isotherms of TNT and C,N-TNT samples are classified as type IV with initial depiction of a monolayer adsorption at low relative pressures, followed by a steep rise. Such behavior depicts a multilayer adsorption of gas molecules which is eventually followed by capillary condensation occurring in the mesopores at high relative pressure. Due to the differences in pressures at which capillary evaporation and condensation take place, the isotherms display H3 hysteresis loops revealing the existence of aggregated plate-like particles with slit-like pores [44].

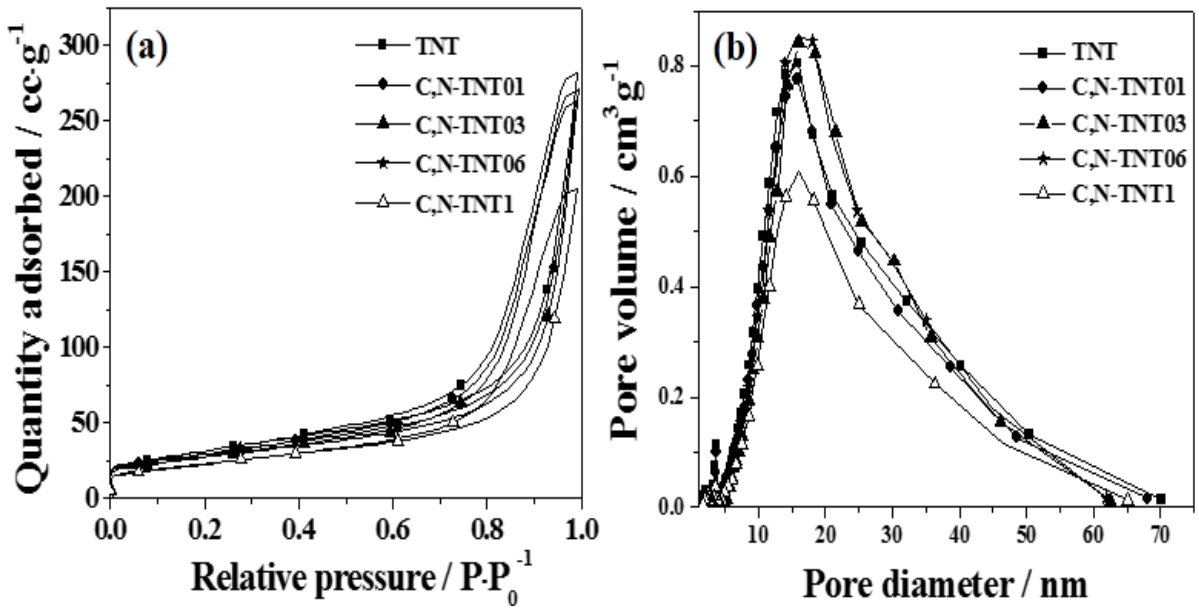

Figure 3.10 Nitrogen physisorption isotherms (a) and pore size distribution (b) of pure TNT and C,N-TNT samples. (01, 03, 06 and 1 stands for 0.1, 0.3, 0.6, and 1.0 g of urea respectively for C,N-TNT)

It is observed that all co-doped samples exhibit a bit lower surface area than the pure TNT. This might be due to the protonation effect rupturing somewhat the tubular morphology and slightly decreasing the surface area. However the variation amongst the surface areas is not as significant to influence the photocatalytic performance of materials. Amongst all co-doped samples, the material C,N-TNT1 shows lowest surface area and pore volume compared to pure TNT indicating that C, N co-doping making significant variation in this material. The pore volume of C,N-TNT1 is 0.32 nm, while pure TNT shows slightly higher pore volume, 0.42 nm. The BJH pore size distributions of pure TNT demonstrate relatively wide spread mesoporosity and macroporosity ranging from 5 to 70 nm with the majority of pores centered around 16 nm as shown in the Figure 3.10b. The macroporosity seems to arise from the pores formed between various TNT particles, *i.e.* intra-particle pores. The BJH pore size distributions of C,N-TNT01, C,N-TNT03, C,N-TNT06, and C,N-TNT1 indicate the presence of relatively

similar mesoporosity and same macroporosity as that of pure TNT. The textural properties, including specific surface area, pore volume and average pore diameters obtained from nitrogen adsorption-desorption analysis, are listed in Table 3.1.

Table 3.1 Textural properties and photocatalytic CH_4 evolution rate for TNT and C,N-TNT samples.

Materials	**S_{BET} ($m^2 \cdot g^{-1}$)**[a]	**Pore volume ($cm^3 \cdot g^{-1}$)**[b]	**Band gap energy (eV)** [c]	**Amount of CH_4 ($ppm.g^{-1}.h^{-1}$)**	**Amount of CH_4 ($\mu mol\ .g^{-1}.h^{-1}$)**
Pure TNT	114	0.44	3.46	90.62	3.7
C,N-TNT01	105	0.40	3.44	153.08	6.25
C,N-TNT03	98	0.42	3.3	111.53	4.6
C,N-TNT06	100	0.43	2.8	230.80	9.75
C,N-TNT1	83	0.32	2.4	165.33	6.75

[a] Surface area determined by applying Brunauer-Emmett-Teller (BET) equation to a relative pressure (P/P0) range of 0.05-0.35 of the adsorption isotherm.

[b] Pore diameter is calculated from the Barrett-Joyner-Halenda (BJH) equation using the desorption isotherm.

[c] Band gap energies estimated from Tauc plots.

3.3.5 X-ray photoelectron spectroscopy (XPS) analysis

To investigate the surface elemental composition and their electronic states, XPS analysis for all the samples are performed and is shown in Figure 3.11. The survey scan XPS spectra of all samples i.e. pure TNT and all C,N-TNT samples (Figure 3.11a) clearly indicate the presence of Ti, O, N, and C elements in them with no trace of unwanted impurities. Figure 3.11b displays a high-resolution XPS spectra of the N 1s. It is observed that the pure TNT and lowest urea treated sample C,N-TNT-01 do not show any peak corresponding to N 1s. Such information indicates that low amount of urea treatment does not make any significant variation in the TNT composition. However with increased urea content, the N 1s spectra of C,N-TNT03 and C,N-TNT06 shows the peaks which can be best fitted as a combination of two peaks appearing around at 397.8 eV and in the range of 399.8 eV-400.1 eV. The later peak at 400.1 eV can be assigned to N atoms from chemisorbed N-containing compounds [45], while the first peak can be attributed to N atoms that replace O atoms in TNT and form Ti-N bonds [46]. Furthermore, sample C,N-TNT1 with the highest amount of urea treated TNT material, shows an additional shoulder peak at 394.7 eV along with these two peaks appearing around 397.8 eV and 400.1 eV. The additional shoulder peak might be possibly due to atomic nitrogen formed by dissociation of a small fraction of the adsorbing molecules [47].

XPS spectra of C 1s for all samples is shown in Figure 3.11c. For C 1s region, various peaks observed can be deconvoluted mainly to three peaks appearing at 284.6 eV, 286.1 eV and 288.3 eV. The first peak can be ascribed to the elemental carbon [48], while the other two peaks appearing at 286.1 eV and 288.3 eV are attributed to C–O and C=O bonds, respectively, which indicates the formation of carbonated species and a probable substitution of lattice titanium or oxygen ions to form Ti–O–C bonding [48].

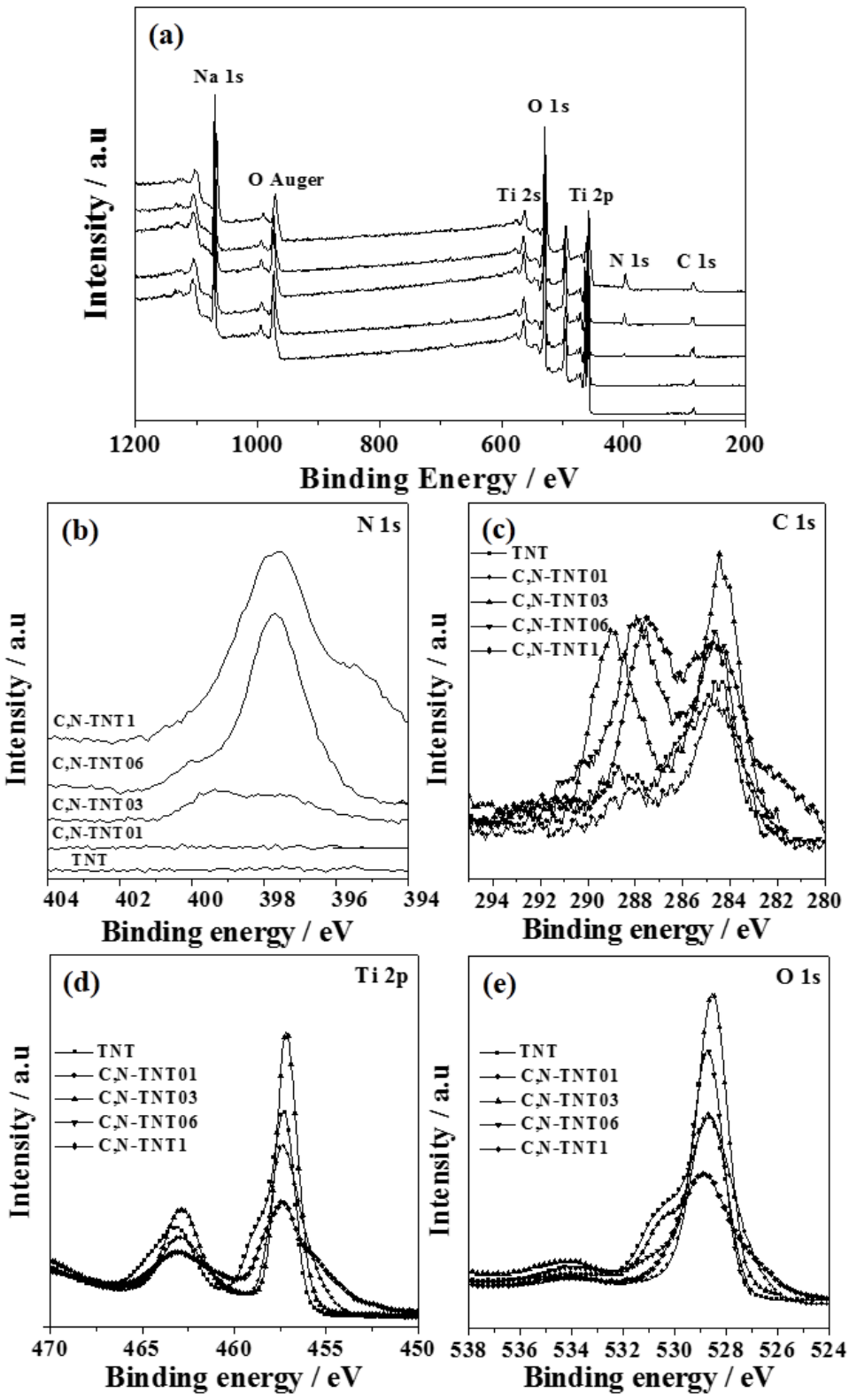

Figure 3.11 XPS spectra of pure TNT and C,N-TNT samples: survey scan (a), N 1s (b), C 1s (c), Ti 2p (d), and O 1s (e). (01, 03, 06 and 1 stands for 0.1, 0.3, 0.6, and 1.0 g of urea respectively for C, N-TNT)

Figure 3.11d shows the high resolution XPS spectra of Ti 2p region with appearance of two intense peaks at 458.7 eV and 464.5 eV, observed for pure TNT and all C,N-TNT samples. These peaks are attributed to the Ti $2p_{3/2}$ and Ti $2p_{1/2}$ binding energy region, which indicates the presence of Ti^{4+} ions in TNT. O 1s region for pure TNT and all C,N-TNT samples is shown in Figure 3.11e. The O 1s spectra reveals the presence of three peaks corresponding to Ti-O bond (529.0 eV), O-H bond (531.4 eV), and C-O bond (533.5 eV) respectively [49].

The atomic % for C, N, Ti, and O elements present in all the samples are also determined using the XPS-EDS (Energy dispersive X-ray spectroscopy) and is displayed in Table 3.2. It can be observed that no nitrogen content is found in pure TNT and C,N-TNT01 samples, the data well matching with the XPS data. On increasing the urea content for samples C,N-TNT03, C,N-TNT06 and C,N-TNT1, the nitrogen and carbon elemental composition is increased with the sample C,N-TNT1 having the highest C and N content.

Table 3.2 C, N, Ti and O atomic composition for pure TNT and different C,N-TNT samples.

Material	**C 1s (Atomic %)**	**N 1s (Atomic %)**	**Ti 2p (Atomic %)**	**O 1s (Atomic %)**
TNT	7.59	-	20.12	52.47
C,N-TNT01	7.97	-	20.14	52.89
C,N-TNT03	11.15	1.37	16.52	49.93
C,N-TNT06	14.59	5.8	15.56	43.86
C,N-TNT1	15.59	11.95	14.5	40.33

3.3.6 Photocatalytic CO_2 conversion

Photocatalytic CO_2 conversion tests with water vapors (as a reducing agent) into hydrocarbon fuels in gas phase are conducted to evaluate the photocatalytic activities of pure TiO_2 (used for synthesis of TNT, purchased from Daejung chemicals South Korea), pure TNT and all C,N-TNT samples. It was observed that all samples under simulated light illumination yielded methane, CH_4 as a primary product with no other products being detected. This might be due to absence of any co-catalysts (Pt, Cu, Pd etc.) for production of other products. The photocatalytic CH_4 evolution rates for anatase TiO_2, pure TNT, and a series of C,N-TNT samples are shown in Figure 3.12. It can be clearly seen, pure TiO_2 used as a reference material exhibits a negligible amount of CH_4 evolution. Sample C,N-TNT06 shows the highest CH_4 evolution (392.14 $ppm.g^{-1}.h^{-1}$ **or** 9.75 $\mu mol.g^{-1}.h^{-1}$), 2.7 times higher than pure TNT (148.81 $ppm.g^{-1}.h^{-1}$ **or** 3.7 $\mu mol.g^{-1}.h^{-1}$). To investigate the origin of the carbon intrinsic to the CH_4, control tests were performed by illuminating C,N-TNT06 in an $Ar/H_2O_{(g)}$ atmosphere, which shows a negligible amount of CH_4, suggesting an insignificant effect from any organic impurities contamination.

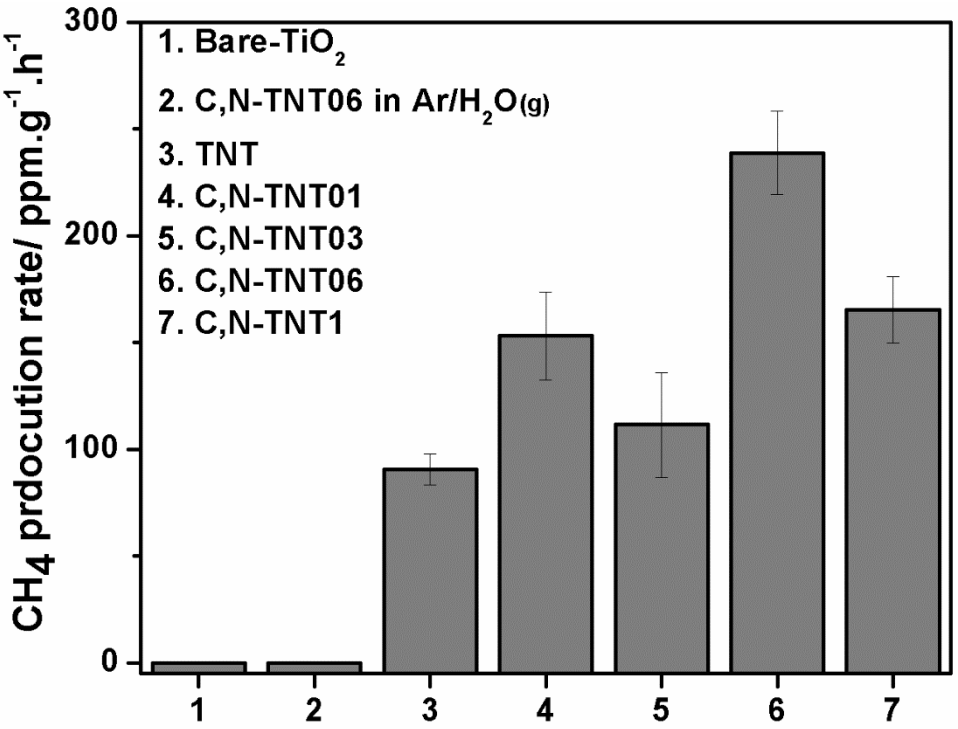

Figure 3.12 Photocatalytic conversion of CO_2 into CH_4 employing TiO_2, pure TNT and C,N-TNT samples (after 1 h irradiation).

It can be clearly seen that C,N-TNT samples exhibits a significant improvement in photocatalytic CO_2 conversion rate as compared to pure TNT and anatase TiO_2 with the order: C,N-TNT06 > 1 > 01 > 03 > pure TNT. Such a trend of results seems interesting and on the basis of reported literature we presume no less than five factors that are intrinsic to understanding the photocatalytic activities of TNT and C,N-TNT samples: (i) Sample crystallinity; (ii) Sample surface area; (iii) The presence of Na^+ ions that act to improve CO_2 adsorption; (iv) The presence of Na^+ ions acting as recombination centers for photogenerated electron-hole pairs; (v) Light absorption properties of the sample. All five of these rate-determining properties are dependent of sample C,N-doping concentrations.

For the pure TNT, C,N-TNT01 and C,N-TNT03, we consider Na^+ ions as a CO_2 adsorption sites [31] and recombination centers [34] might be the key parameters influencing the

performance of respective samples. As previously explained in relation to our XRD analysis, the C,N co-doping induces a protonation effect by substitution of Na^+ ions with H^+ ions, which we suggest are coming from dissociation of the urea (dopant source), with the appearance of the anatase phase for the more highly-doped samples. The band gaps estimated for TNT (3.46 eV), C,N-TNT01 (3.44 eV), and C,N-TNT03 (3.33 eV) do not show a significant variation, with all three samples absorbing little of the solar spectrum energy, so the effect of co-doping is not considered a prominent factor influencing their performance. With respect to sample C,N-TNT01, a small amount of dopant can induce mild protonation which decreases the Na^+ ion content, perhaps offering enhanced CO_2 adsorption without a corresponding increase in charge recombination, with the end result a superior performance than that of TNT. While for the samples C, N-TNT06 and C,N-TNT1 we consider the extended light absorption and small amount of anatase phase might be possible reasons for their relative improved photocatalytic performance. As it is well reported that C and N co-doping of TNT induces C 2p and N 2p isolated states above the valence band maximum [42]. These isolated states are considered to be responsible for significant red shift in light absorption of C, N-TNT06 and C,N-TNT1 samples. The enhanced light absorption increases the sub-band gap excitations and photoexcited electrons. The maximum photocatalytic activity in terms of CH_4 evolution rate exhibited by C,N-TNT06 can be interpreted as optimum level of dopant concentrations balancing well all factors which influences the photocatalyst performance. However, on increasing the dopant concentration beyond that of C,N-TNT06, the photocatalytic activity decreases. While we do not yet understand the role of Na^+ ions in helping to determine photocatalytic properties, for both samples C,N-TNT06 and 1, we hypothesize that their improved performance is due to increased light absorption and improved crystallinity associated with the C,N-doping, and presumably some optimal point on the trade-off of Na^+ effects.

The proposed mechanism for photocatalytic CO_2 conversion into hydrocarbon fuels is suggested on the basis of well reported and most agreed proton assisted multi-electrons reduction process via carbene pathway [50,51]. It is considered that upon illumination a photocatalyst material (M) which is pure TNT or C,N-TNT samples in this experimental work, pairs of electron (e^-) and hole (h^+) are created at the photocatalyst (M) active sites (Eq. 3.4). The holes are assumed to be filled by water oxidation reaction with release of hydroxyl radicals (·OH) and protons (H^+) (Eq. 3.5). Simultaneously, the adsorbed CO_2 on photocatalyst get reacted with the electron and proton and reduces into carbon radicals (·C) through an intermediate product of CO (Eq. 3.6 & 3.7). Carbon radicals finally react with multiple H^+ and e^- yielding hydrocarbon fuel as a product (Eq. 3.8).

$$M\ (e^-\text{-}h^+) + h\nu \rightarrow e^-_{CB} + h^+_{VB} \quad (3.4)$$

$$H_2O + h^+ \rightarrow H^+ + \cdot OH \quad (3.5)$$

$$CO_2 \rightarrow CO + \tfrac{1}{2}\ O_2 \quad (3.6)$$

$$CO \rightarrow \cdot C + \tfrac{1}{2}\ O_2 \quad (3.7)$$

$$\cdot C + 4H^+ + 4e^- \rightarrow CH_4 \quad (3.8)$$

The proposed mechanism for photocatalytic CO_2 conversion to CH_4 employing C,N-TNT samples is schematically illustrated in Figure 3.13.

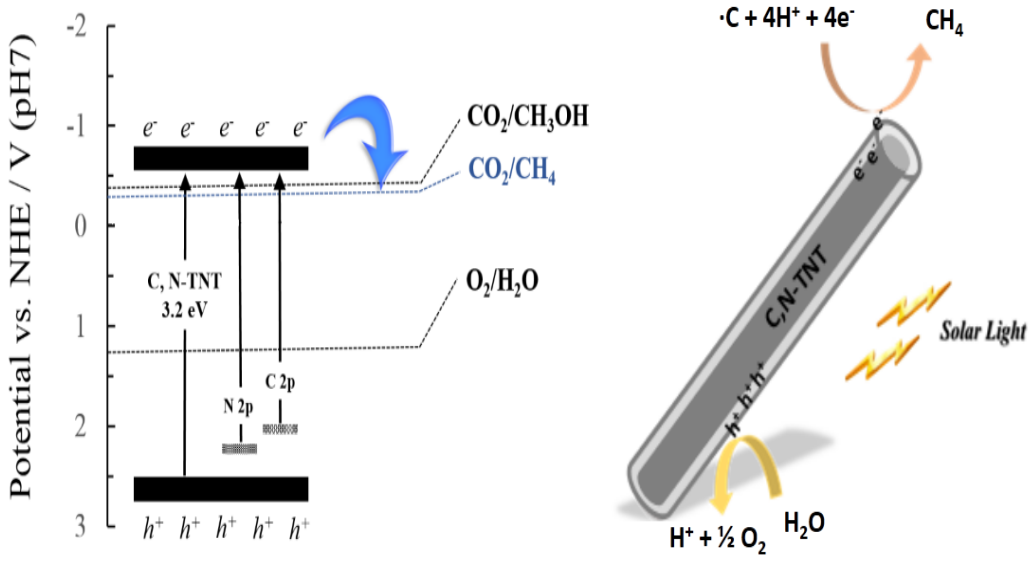

Figure 3.13 Schematic illustration of photocatalytic conversion of CO_2 into CH_4 by C,N co-doped TNT.

3.4 Conclusions

A solar light active C,N co-doped sodium titanate nanotubes photocatalyst was synthesized by a simple two step synthesis strategy. The photocatalytic performance of the synthesized materials were evaluated by photocatalytic CO_2 conversion into CH_4. Different samples of C,N-TNT were prepared by varying the amounts of urea content which acted as C and N doping source. The optimum sample yielded enhanced CH_4 production rate which was 2.7 times higher than undoped / pure TNT sample. Such improved performance can be attributed to the extended light absorption as a result of isolated C and N 2p states above the valence band maximum of TNT, moderate surface areas, anatase phase formation and favorable competition between the dual roles of Na^+ ions concentration present in the photocatalyst.

3.5 References

[1] G. Mahmodi, S. Sharifnia, F. Rahimpour, S.N. Hosseini, Photocatalytic conversion of CO_2 and CH_4 using ZnO coated mesh: Effect of operational parameters and optimization, Sol. Energy Mater. Sol. Cells. 111 (2013) 31–40. doi:10.1016/j.solmat.2012.12.017.

[2] S.C. Yan, S.X. Ouyang, J. Gao, M. Yang, J.Y. Feng, X.X. Fan, L.J. Wan, Z.S. Li, J.H. Ye, Y. Zhou, Z.G. Zou, A room-temperature reactive-template route to mesoporous $ZnGa_2O_4$ with improved photocatalytic activity in reduction of CO_2, Angew. Chemie - Int. Ed. 49 (2010) 6400–6404. doi:10.1002/anie.201003270.

[3] H. Tsuneoka, K. Teramura, T. Shishido, T. Tanaka, Adsorbed Species of CO_2 and H_2 on Ga_2O_3 for the Photocatalytic Reduction of CO_2, J. Phys. Chem. C. 114 (2010) 8892–8898. doi:10.1021/jp910835k.

[4] J.A. Mendoza, H.K. Kim, H.K. Park, K.Y. Park, Photocatalytic reduction of carbon dioxide using Co_3O_4 nanoparticles under visible light irradiation, Korean J. Chem. Eng. 29 (2012) 1483–1486. doi:10.1007/s11814-012-0115-z.

[5] K. Teramura, S.I. Okuoka, H. Tsuneoka, T. Shishido, T. Tanaka, Photocatalytic reduction of CO_2 using H_2 as reductant over $ATaO_3$ photocatalysts (A = Li, Na, K), Appl. Catal. B Environ. 96 (2010) 565–568. doi:10.1016/j.apcatb.2010.03.021.

[6] J. Mao, T. Peng, X. Zhang, K. Li, L. Zan, Selective methanol production from photocatalytic reduction of CO_2 on $BiVO_4$ under visible light irradiation, Catal. Commun. 28 (2012) 38–41. doi:10.1016/j.catcom.2012.08.008.

[7] J. Mao, T. Peng, X. Zhang, K. Li, L. Ye, L. Zan, Effect of graphitic carbon nitride microstructures on the activity and selectivity of photocatalytic CO_2 reduction under visible light, Catal. Sci. Technol. 3 (2013) 1253. doi:10.1039/c3cy20822b.

[8] F. Peng, J. Wang, G. Ge, T. He, L. Cao, Y. He, H. Ma, S. Sun, Photochemical reduction

of CO_2 catalyzed by silicon nanocrystals produced by high energy ball milling, Mater. Lett. 92 (2013) 65–67. doi:10.1016/j.matlet.2012.10.059.

[9] H.C. Hsu, I. Shown, H.Y. Wei, Y.C. Chang, H.-Y. Du, Y.-G. Lin, C.-A. Tseng, C.-H. Wang, L.C. Chen, Y.-C. Lin, K.H. Chen, Graphene Oxide as a Promising Photocatalyst for CO_2 to Methanol Conversion, Nanoscale. (2013) 262–268. doi:10.1039/c2nr31718d.

[10] Y. Liu, L. Zhao, H. Andino, J. M. Li, Photocatalytic CO_2 Reduction with H_2O on TiO_2 Nanocrystals: Comparison of Anatase, Rutile, and Brookite Polymorphs and Exploration of Surface Chemistry, ACS Catal. 2 (2012) 1817–1828. doi:10.1016/j.apcatb.2010.08.015.

[11] M. Anpo, H. Yamashita, Y. Ichihashi, S. Ehara, Photocatalytic reduction of CO_2 with H_2O on various titanium oxide catalysts, J. Electroanal. Chem. 396 (1995) 21–26. doi:10.1016/0022-0728(95)04141-A.

[12] M. Tahir, N.S. Amin, Advances in visible light responsive titanium oxide-based photocatalysts for CO_2 conversion to hydrocarbon fuels, Energy Convers. Manag. 76 (2013) 194–214. doi:10.1016/j.enconman.2013.07.046.

[13] G. Liu, N. Hoivik, K. Wang, H. Jakobsen, Engineering TiO_2 nanomaterials for CO_2 conversion/solar fuels, Sol. Energy Mater. Sol. Cells. 105 (2012) 53–68. doi:10.1016/j.solmat.2012.05.037.

[14] Z. Yang, D. Choi, S. Kerisit, K.M. Rosso, D. Wang, J. Zhang, G. Graff, J. Liu, Nanostructures and lithium electrochemical reactivity of lithium titanites and titanium oxides: A review, J. Power Sources. 192 (2009) 588–598. doi:10.1016/j.jpowsour.2009.02.038.

[15] S. Di Mo, W.Y. Ching, Electronic and optical properties of three phases of titanium dioxide: Rutile, anatase, and brookite, Phys. Rev. B. 51 (1995) 13023–13032. doi:10.1103/PhysRevB.51.13023.

[16] O.K. Dalrymple, E. Stefanakos, M.A. Trotz, D.Y. Goswami, A review of the mechanisms and modeling of photocatalytic disinfection, Appl. Catal. B Environ. 98 (2010) 27–38. doi:10.1016/j.apcatb.2010.05.001.

[17] J.S. M. Fuerte, A.J. Maira, A. Martinez-Arias, M. Fernadez-Garcia, J.C. Conesa, Visible light-activated nanosized doped-TiO_2 photocatalysts, Chem. Commun. vol. 24 (2001) 2718–2719. doi:10.1039/b107314a.

[18] C. Jimmy, L. Zhang, Z. Zheng, J. Zhao, Synthesis and characterization of phosphated mesoporous titanium dioxide with high photocatalytic activity, Chem. Mater. (2003) 15 2280–2286. doi:0.1021/cm0340781.

[19] T. Ohno, M. Akiyoshi, T. Umebayashi, K. Asai, T. Mitsui, M. Matsumura, Preparation of S-doped TiO_2 photocatalysts and their photocatalytic activities under visible light, Appl. Catal. A: Gen. 265 (2004) 115–121. doi:10.1016/j.apcata.2004.01.007.

[20] Y. Liu, X. Chen, J. Li, C. Burda, Photocatalytic degradation of azo dyes by nitrogen-doped TiO_2 nanocatalysts, Chemosphere. 61 (2005) 11–18. doi:10.1016/j.chemosphere.2005.03.069.

[21] T. Hirai, K. Suzuki, I. Komasawa, Preparation and Photocatalytic Properties of Composite CdS Nanoparticles–Titanium Dioxide Particles, J. Colloid Interface Sci. 244 (2001) 262–265. doi:10.1006/jcis.2001.7982.

[22] D. Chatterjee, A. Mahata, Demineralization of organic pollutants on the dye modified TiO_2 semiconductor particulate system using visible light, Appl. Catal. B Environ. 33 (2001) 119–125. doi:10.1016/S0926-3373(01)00170-9.

[23] R. Asahi, Visible-Light Photocatalysis in Nitrogen-Doped Titanium Oxides, Science. 293 (2001) 269–271. doi:10.1126/science.1061051.

[24] A. Nakahira, T. Kubo, C. Numako, TiO_2-derived titanate nanotubes by hydrothermal process with acid treatments and their microstructural evaluation, ACS Appl. Mater.

Interfaces. 2 (2010) 2611–2616. doi:10.1021/am1004442.

[25] N. Li, L. Zhang, Y. Chen, M. Fang, J. Zhang, H. Wang, Highly efficient, irreversible and selective ion exchange property of layered titanate nanostructures, Adv. Funct. Mater. 22 (2012) 835–841. doi:10.1002/adfm.201102272.

[26] H. Yu, B. Tian, J. Zhang, Layered TiO_2 composed of anatase nanosheets with exposed {001} facets: Facile synthesis and enhanced photocatalytic activity, Chem. - A Eur. J. 17 (2011) 5499–5502. doi:10.1002/chem.201003437.

[27] T. Kasuga, M. Hiramatsu, A. Hoson, T. Sekino, K. Niihara, Formation of Titanium Oxide Nanotube, Langmuir. 14 (1998) 3160–3163. doi:10.1021/la9713816.

[28] M. Wei, Y. Konishi, H. Zhou, H. Sugihara, H. Arakawa, Formation of nanotubes TiO_2 from layered titanate particles by a soft chemical process, Solid State Commun. 133 (2005) 493–497. doi:10.1016/j.ssc.2004.12.026.

[29] M. Qamar, C.R. Yoon, H.J. Oh, N.H. Lee, K. Park, D.H. Kim, K.S. Lee, W.J. Lee, S.J. Kim, Preparation and photocatalytic activity of nanotubes obtained from titanium dioxide, Catal. Today. 131 (2008) 3–14. doi:10.1016/j.cattod.2007.10.015.

[30] M. Qamar, C.R. Yoon, H.J. Oh, D.H. Kim, J.H. Jho, K.S. Lee, W.J. Lee, H.G. Lee, S.J. Kim, Effect of post treatments on the structure and thermal stability of titanate nanotubes, Nanotechnology. 17 (2006) 5922–5929. doi:10.1088/0957-4484/17/24/004.

[31] C.K. Lee, C.C. Wang, M. Du Lyu, L.C. Juang, S.S. Liu, S.H. Hung, Effects of sodium content and calcination temperature on the morphology, structure and photocatalytic activity of nanotubular titanates, J. Colloid Interface Sci. 316 (2007) 562–569. doi:10.1016/j.jcis.2007.08.008.

[32] H. Liu, D. Yang, Z. Zheng, X. Ke, E. Waclawik, H. Zhu, R.L. Frost, A Raman spectroscopic and TEM study on the structural evolution of $Na_2Ti_3O_7$ during the the adsorption of Sr^{2+} and Ba^{2+} cations, J. Raman Spectrosc. 41 (2010) 1792–1796.

doi:10.1002/jrs.2561.

[33] H. Park, H.H. Ou, A.J. Colussi, M.R. Hoffmann, Artificial photosynthesis of C1-C3 hydrocarbons from water and CO_2 on titanate nanotubes decorated with nanoparticle elemental copper and CdS quantum dots, J. Phys. Chem. A. 119 (2015) 4658–4666. doi:10.1021/jp511329d.

[34] K. Upendar, A. Sri Hari Kumar, N. Lingaiah, K.S. Rama Rao, P.S. Sai Prasad, Low-temperature CO_2 adsorption on alkali metal titanate nanotubes, Int. J. Greenh. Gas Control. 10 (2012) 191–198. doi:10.1016/j.ijggc.2012.06.008.

[35] Q. Chen, W. Zhou, G.H. Du, L.M. Peng, Trititanate nanotubes made via a single alkali treatment, Adv. Mater. 14 (2002) 2000–2003. doi:10.1002/1521-4095(20020903)14:17<1208::AID-ADMA1208>3.0.CO;2-0.

[36] Z.Y. Yuan, B.L. Su, Titanium oxide nanotubes, nanofibers and nanowires, Colloids Surfaces A Physicochem. Eng. Asp. 241 (2004) 173–183. doi:10.1016/j.colsurfa.2004.04.030.

[37] Y. Mao, S.S. Wong, Size- and shape-dependent transformation of nanosized titanate into analogous anatase titania nanostructures, J. Am. Chem. Soc. 128 (2006) 8217–8226. doi:10.1021/ja0607483.

[38] E. Morgado, M.A.S. de Abreu, G.T. Moure, B.A. Marinkovic, P.M. Jardim, A.S. Araujo, Effects of thermal treatment of nanostructured trititanates on their crystallographic and textural properties, Mater. Res. Bull. 42 (2007) 1748–1760. doi:10.1016/j.materresbull.2006.11.020.

[39] L. Shi, L. Cao, W. Liu, G. Su, R. Gao, Y. Zhao, A study on partially protonated titanate nanotubes: Enhanced thermal stability and improved photocatalytic activity, Ceram. Int. 40 (2014) 4717–4723. doi:10.1016/j.ceramint.2013.09.013.

[40] C.K. Lee, M. Du Lyu, S.S. Liu, H.C. Chen, The synthetic parameters for the preparation

of nanotubular titanate with highly photocatalytic activity, J. Taiwan Inst. Chem. Eng. 40 (2009) 463–470. doi:10.1016/j.jtice.2008.12.007.

[41] L. Qian, Z.L. Du, S.Y. Yang, Z.S. Jin, Raman study of titania nanotube by soft chemical process, J. Mol. Struct. 749 (2005) 103–107. doi:10.1016/j.molstruc.2005.04.002.

[42] D. Chen, Z. Jiang, J. Geng, Q. Wang, D. Yang, Carbon and nitrogen co-doped TiO_2 with enhanced visible-light photocatalytic activity, Ind. Eng. Chem. Res. 46 (2007) 2741–2746. doi:10.1021/ie061491k.

[43] J. Tauc, R. Grigorovici, A. Vancu, Optical Properties and Electronic Structure of Amorphous Germanium, Phys. Status Solidi. 15 (1966) 627–637. doi:10.1002/pssb.19660150224.

[44] M. Kruk, M. Jaroniec, Gas adsorption characterization of ordered organic-inorganic nanocomposite materials, Chem. Mater. 13 (2001) 3169–3183. doi:10.1021/cm0101069.

[45] G.B. Soares, B. Bravin, C.M.P. Vaz, C. Ribeiro, Facile synthesis of N-doped TiO_2 nanoparticles by a modified polymeric precursor method and its photocatalytic properties, Appl. Catal. B Environ. 106 (2011) 287–294. doi:10.1016/j.apcatb.2011.05.018.

[46] E.D.L. Rienks, J.W. Bakker, A. Baraldi, S. A. C. Carabineiro, S. Lizzit, C.J. Weststrate, B.E. Nieuwenhuys, Interaction of nitric oxide with Pt(100). A fast X-ray photoelectron spectroscopy study, Surf. Sci. 516 (2002) 109–117. doi:10.1016/S0039-6028(02)01910-6.

[47] Z. Wu, F. Dong, W. Zhao, H. Wang, Y. Liu, B. Guan, The fabrication and characterization of novel carbon doped TiO_2 nanotubes, nanowires and nanorods with high visible light photocatalytic activity, Nanotechnology. 20 (2009) 235701. doi:10.1088/0957-4484/20/23/235701.

[48] H. Xu, L. Zhang, Selective nonaqueous synthesis of C-Cl-codoped TiO_2 with visible-light photocatalytic activity, J. Phys. Chem. C. 114 (2010) 11534–11541.

[49] K. Lalitha, G. Sadanandam, V.D. Kumari, M. Subrahmanyam, B. Sreedhar, N.Y. Hebalkar, Highly stabilized and finely dispersed Cu_2O/TiO_2: A promising visible sensitive photocatalyst for continuous production of hydrogen from glycerol:water mixtures, J. Phys. Chem. C. 114 (2010) 22181–22189. doi:10.1021/jp107405u.

[50] W. Fan, Q. Zhang, Y. Wang, Semiconductor-based nanocomposites for photocatalytic H_2 production and CO_2 conversion., Phys. Chem. Chem. Phys. 15 (2013) 2632–49. doi:10.1039/c2cp43524a.

[51] S.N. Habisreutinger, L. Schmidt-Mende, J.K. Stolarczyk, Photocatalytic reduction of CO_2 on TiO_2 and other semiconductors, Angew. Chemie - Int. Ed. 52 (2013) 7372–7408. doi:10.1002/anie.201207199.

Chapter 4. TiO_2 Nanotube Arrays Covered with Reduced Graphene Oxide: A Facile Fabrication approach towards a Noble Metal-Free Photocatalyst and its application in photocatalytic CO_2 conversion to methane.

4.1 Introduction

During past few years, TiO_2 nanotube arrays (TNT) [1,2] have become an attractive and interesting research domain with its application in a variety of fields such as photocatalysis [3], chemical sensors [4], biomedical applications [5], environmental cleaning [6], solar cells and solar fuels [7,8]. As mentioned previously in chapter 3, the TNT provides a higher surface area as compared to TiO_2 nanoparticles powder. However the TNT in powder form also bears a drawback of its recyclability and reusability. In this regard the well oriented and directionally grown TiO_2 nanotubes on a Ti foil substrate can provide a better mean to resolve the issues of recyclability and reusability without sample loss. In addition, TNT arrays also provide a higher surface area and directional/vectorial charge flow which leads to improved surface active sites and decreased charge recombination, respectively.

Generally, TNT arrays are synthesized using a simple, easy and low cost electrochemical method in which titanium foil is subjected to electrochemical anodization [9,10] resulting in a photocatalytic material platform with intriguing prospects for solar cells and solar fuel applications. However the relatively high band gap of TiO_2 (~3.2 eV), as is well known can significantly limits the absorption of solar spectrum energy [11,12]. Thus in order to utilize the excellent photo-corrosion stability and charge transport properties of TNT arrays while extending its light absorption spectrum, various investigators have tried approaches such as noble metals loading, e.g., with Pt, Au or Pd [13], elemental doping, e.g., with B, N or S [14], and coupling of TNT arrays with low band gap semiconductors [15]. Amongst these approaches, loading of noble metals on TNT arrays as a co-catalyst is an effective but expensive

way of improving electron-hole separation, whereas doping increases the solar spectrum absorption. Both these methods quite improves the photocatalytic performance but beyond a few non-repeatable results, to always degrade its charge transport properties. To avoid the high cost and short life of noble metal loading, in recent years coupling of TiO_2 nanostructured materials with carbon materials such as C60, CNT, graphene [16,17] have been investigated and become an attractive research domain offering improved charge transfer dynamics and photocatalytic activity. A major drawback of using carbon materials is their potential to weaken the light absorption. However, Graphene a carbon allotrope since its invention by Geim and Novoselov in 2004 [18,19], have received an enormous amount of attention because of its superb properties along with good transparency to the sunlight. The important and extraordinary properties of this wonder material are tabulated in Table 4.1.

Typically high electron mobility, high surface area (~2600 $m^2 \cdot g$) and light transparency [20] have motivated the photocatalysis researchers to employ and investigate the graphene based photocatalytic materials for a wide variety of applications.

Being inspired from such excellent properties, in this experimental work we designed a systematic fabrication approach is designed which resulted in a novel nanostructure material that does not requires the use of expensive noble metal loading. The nanostructured material is comprised of TiO_2 nanotube arrays with a surface coating of reduced graphene oxide (rGO) platelets embedded with TiO_2 nanoparticles (rGO-TNTNP). The experimental strategy adopted for synthesis of rGO-TNTNP consists of two steps i.e. simultaneous electrophoretic deposition and reduction of GO on Ti foil followed by second step of electrochemical anodization of rGO-Ti foil. The electrochemical anodization step is performed with a specific electrolyte concentration in order to obtain the porous surface morphology and avoid debris formation. The photocatalytic properties of the resulting novel nanostructured photocatalyst architecture

are investigated using photocurrent measurements and its application for photocatalytic CO_2 conversion primarily to methane as a product.

Table 4.1 Some specific properties of graphene

Property	**Value**
Specific surface area	2630 $m^2 \cdot g$
Optical transmittance	~97.7 %
Thermal conductivity	5000 $W \cdot m^{-1} \cdot K^{-1}$
Young's modulus	1 TPA
Thermal resistance	~ 4 x 10^{-8} $K \cdot m^2 \cdot W^{-1}$
Electron mobility	200000 $cm^2 \cdot V^{-1} \cdot S^{-1}$
Fermi velocity	300-500 nm
Current density	1000000 ms^{-1}

4.2 Experimental section

4.2.1 Materials and reagents

The chemical and reagents used in the synthesis of graphene oxide include graphite powder (Lab grade, 99.0 %), potassium permanganate ($KMnO_4$, 93.5 %), hydrogen peroxide (H_2O_2, 28.0 %), concentrated sulfuric acid (H_2SO_4, 95.0 %) all purchased from Duksan Chemicals and sodium nitrate ($NaNO_3$, 99.0 %) purchased from Sigma-Aldrich. Ammonium fluoride (NH_4F, 98.0 %) and ethylene glycol (C_2H_6O, 99.0 %) used in electrochemical anodization were purchased from Alfa Aesar. Titanium foil (0.1 mm in thickness, 99.5 %) from Nilaco Corporation, Japan was used in this investigation. Sodium sulfate (Na_2SO_4, 99.0 %) was purchased from Sigma-Aldrich and was used in its present form as an electrolyte for the photocurrent measurements.

4.2.2 Synthesis of graphene oxide (GO)

The graphene oxide (GO) was synthesized using modified hummers method in two steps. Firstly, graphite oxide (G-O) was synthesized by modified Hummers method [21]. The procedure starts with mixing of 3.0 g (1 wt. equiv.) of graphite powder and 1.5 g (0.5 wt. equiv.) of $NaNO_3$ with 69 ml of concentrated H_2SO_4 in a flask. Then, 9.0 g (3 wt. equiv.) of $KMnO_4$ was slowly added into the mixture placed in ice bath to keep the reaction temperature below 20 °C. After addition of $KMnO_4$, the reaction temperature was warmed to 35 °C and kept under vigorous stirring for 7 h followed by addition of more 9.0 g (3 wt. equiv.) of $KMnO_4$ and finally stirred for 12 h. Then 400 ml of ice water was added to the reaction mixture followed by drop wise addition of H_2O_2 (6 ml) under stirring. The mixture was then filtered, washed and centrifuged for multiple times until the pH of the mixture become neutral (pH 6 ~ 7). The final centrifuged product was vacuum dried to get a solid product of graphite oxide (G-O). In the second step, the obtained graphite oxide (G-O) with concentration of 1.0 mg/ml was sonicated

well for 3 hours. The sonication was done at room temperature i.e. 30 °C and finally a well dispersed suspension of graphene oxide (GO) was obtained which was used as it without further processing.

4.2.3 Synthesis of reduced graphene oxide-TiO_2 nanotubes covered with TiO_2 nanoparticles (rGO-TNTNP)

The synthesis of the novel nanostructure i.e. TNT arrays coated with platelets of rGO and TiO_2 NPs was done by specifically designed two steps synthesis procedure, the schematic representation of which is shown in Figure 4.1. During the first step, the GO platelets were deposited on titanium (Ti) foils by electrophoretic deposition. The Ti foil was cleaned by sonicating for 10 min each in acetone, ethanol and DI water. The titanium foil (2.0 cm × 2.0 cm) acts as anode with a stainless steel wire as a cathode. The electrodes were vertically dipped in the GO suspension and separated by a distance of 1.0 cm. A voltage of 10 V was applied using a power supply for 10 s. During the electrophoretic deposition of the GO onto Ti foil, it was observed the GO also gets reduced and the resulting substrate was termed as rGO-Ti foil. The rGO deposited titanium foil (rGO-Ti) was then air dried at room temperature followed by heating at 100 °C (1 h) to vaporize the residual water molecules.

The second step includes the electrochemical anodization of above prepared rGO-Ti foil resulting in a novel nanostructure comprising of TiO_2 nanotube arrays covered with the rGO-TiO_2 nanoparticles composite (rGO-TNTNP). The electrochemical anodization was carried out in a two-electrode electrochemical cell comprised of rGO-Ti as a working electrode (anode) and a carbon paper as a counter electrode (cathode). The electrolyte bath consists of 0.25 wt. % NH_4F and 2 vol. % DI water in ethylene glycol. The anodization was performed at 55 V for 30 min. with a distance of 2.0 cm between the two electrodes. After anodization the porous rGO-TNTNP composite was washed with DI water several times and air dried. The resulting rGO-

TNTNP composite was annealed at 400 °C for 1 h in argon. For comparison, pure TiO_2 nanotube (TNT) arrays annealed under argon atmosphere were also prepared with similar electrolyte and anodization conditions.

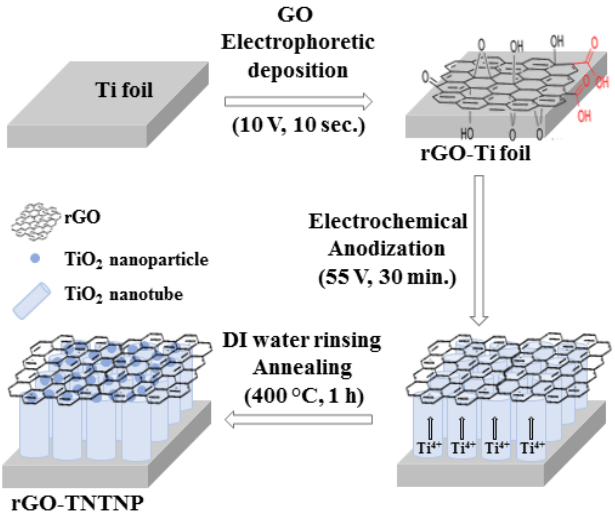

Figure 4.1 Schematic representation for synthesis of rGO-TNTNP.

4.2.4 Characterization

The crystalline structure of the pure Ti foil, pure TNT arrays and rGO-TNTNP were analyzed by powder X-ray diffraction (XRD) using X-ray diffractometer (Panalytical, Empyrean) operating at 40 kV and 30 mA with Cu Kα radiation (λ=1.54Å) as an X-ray source, scanned with a step degree of 0.02° and duration time of 0.05 s in the range of 2θ =20-80°. To confirm the presence of rGO content in the rGO-Ti foil and rGO-TNTNP, Raman spectroscopy was performed for respective samples using a NICOLET ALMECA XR Raman spectrometer equipped with a He-Ne laser (532 nm) as a light source. Morphological analysis of the materials was performed using field emission scanning electron microscopy (FE-SEM, Hitachi S-4800). The TiO_2 nanoparticles composition embedded within the rGO-TNTNP surface was investigated using the energy dispersive x-rays spectroscopy (EDS) using FE-SEM and also EDS using X-ray photoelectron spectroscopy (XPS). The UV-vis diffuse reflectance spectra (UV-vis DRS) for pure Ti foil, rGO-Ti foil, bare TNT arrays and rGO-TNTNP were measured

using Cary series (CARY5000) UV-visible-near IR spectrophotometer (Agilent technologies) with a diffuse reflection accessory in the range of 300-700 nm. Photoluminescence (PL) spectra were measured using Cary Eclipse Fluorescence Spectrophotometer (Agilent Technologies) with an excitation wavelength of λ_{ex} = 300 nm. The samples with area 2.0 cm × 2.0 cm were selected for both UV-vis DRS and PL measurements. The surface composition, oxidation states of Ti, O, and C in different materials were determined by X-ray photoelectron spectroscopy (XPS, Thermo Scientific, ESCALAB 250Xi) using Al Kα line (148606 eV) as the X-ray source. The XPS peaks calibration was done against the standard reference C1s peak and peak fitting done using Levenberg-Marquardt's method via "Fitt" software.

4.2.5 Photocurrent measurements

The Photocurrent measurements for pure TNT arrays and rGO-TNTNP were taken to investigate their photocatalytic properties and charge separation improvement. The measurements were carried out in a homemade cell (20 ml) with a three electrode configuration. A quartz lens was fitted at the front side of the cell body for photo-illumination purpose. Pure TNT and rGO-TNTNP samples, having an exposed area of 1.0 cm^2, were connected to three electrode configuration system as a working electrode, a Pt wire was attached as a counter electrode, and an Ag/AgCl as a reference electrode. All electrodes were then immersed in 0.1 M Na_2SO_4 (20 ml, pH adjusted to 7.0) aqueous solution in the cell. The cell assembly was illuminated using a 100 W Xenon solar simulator (Oriel, LCS-100) with an AM 1.5 filter. Photocurrent measurements were taken in a chopped fashion with zero bias applied relative to an Ag/AgCl reference electrode.

4.2.6 Photocatalytic CO_2 conversion

The photocatalytic activity performance of the prepared samples were tested by employing in photocatalytic CO_2 conversion yielding methane (CH_4) as a main product. The experimental procedure for photocatalytic CO_2 conversion test is explained in detail in section 2.3 of chapter 2.0. Briefly, 2.0 cm × 2.0 cm of respective photocatalyst substrate was placed in the reactor and CO_2 gas (1000 ppm in He) passing through a water bubbler, forming a mixture of CO_2 and H_2O vapors which then enters the reactor. A 100 W Xenon solar simulator (Oriel, LCS-100) with an AM 1.5 filter was used as a light source and the products were analyzed using a gas chromatograph unit (Shimadzu GC-2014, Restek Rt-Q-Bond column, ID=0.53 mm, length=30 m) equipped with both thermal conductivity detector (TCD) and a flame ionization detector (FID). Control tests was also performed by illuminating rGO-TNTNP sample in an $Ar/H_2O(g)$ atmosphere rather than $CO_2/H_2O(g)$ mixture to investigate the origin of the carbon intrinsic to the CH_4.

After 1 h irradiation product samples from the reactor were manually taken with a 500 µL argon-purged syringe and injected into the gas-chromatograph. Three measurements were performed for each sample; the average for the three readings was reported along with their standard error bar in the results and discussion part. The obtained values for the yielded product was calculated using following equation:

$$\text{Rate of } CH_4 \text{ evolution} = \frac{\text{Amount of } CH_4 \text{ produced (ppm)}}{\text{Area of photocatalyst exposed } (cm^2)} \quad (4.1)$$

The stability and reusability testing of the rGO-TNTNP sample was performed by irradiating the same sample for four cycles of CO_2 photoreduction. Each cycle is illuminated for 1 h under simulated solar light. After every cycle the photoreactor was purged with CO_2 gas (1000 ppm in He) and vacuum (five cycles), then re-filled with CO_2 gas (1000 ppm in He) and illuminated (1 h) for the next testing cycle.

4.3 Results and discussion

4.3.1 Morphological analysis

The surface morphology and cross sectional investigation for pure TNT arrays and novel nanostructured rGO-TNTNP are studied by field emission scanning electron microscopy (FE-SEM). It can be seen from Figure 4.2a, the surface of the pure TNT arrays show uniform porous morphology with a precipitated TiO_2 layer on its surface. Such a layer is associated to the low dissolution rate (U_{dis}) than the anodization rate (U_{anod}) as explained by the *Wang et al.* [22]. It is well known that during the electrochemical anodization, when strong positive bias is applied to Ti foil, it withdraws electrons from Ti foil and pushes the Ti^{4+} outwards to Ti foil/electrolyte interface reacting with O^{2-} and F^- ions in electrolyte forming $Ti(OH)_4$ or TiF^{6-} water soluble complexes. These complexes can also stick on the Ti foil surface which are then chemical etched by fluoride ions in electrolyte. If the concentration of the fluoride ions in the electrolyte is less, the dissolution rate of these complexes is slow then their formation rate on the surface (the formation rate determined by anodization rate) and finally they precipitate as a uniform porous layer of $Ti(OH)_2$ or TiF^{6-} on the surface. In general, the uniform porous layer is mainly composed of precipitated $Ti(OH)_2$ whereas sdebris is observed plugged in the TiO_2 nanotubes in case of TiF^{6-} complex sticks on the TNT surface. In the present study, a uniform layer is observed onto the TNT arrays surface which is considered herein as TiO_2 layer after annealing. However a small amount of fluoride content is also observed in the elemental analysis done using FE-SEM energy dispersive spectroscopy (EDS). The atomic ratio of fluoride content is very less and can be associated to the surface adsorbed fluoride contents.

Similarly, when the rGO-Ti foil is anodized using a similar electrolyte concentration (0.25 wt. % NH_4F in Ethylene glycol with 2.0 vol. % H_2O), an interesting surface morphology is observed comprising of rGO platelets embedded with small nanoparticles (which are confirmed as TiO_2) on the surface of well oriented TNT arrays as shown in Figure 4.2b. The cross

sectional images of the both samples show vertically aligned nanotubes of 6.6-6.9 µm length (Figure 4.2c & d). High resolution FE-SEM images of rGO-TNTNP surface clearly displays a transparent layer of rGO (Figure 4.2e) and TiO_2 nanoparticles (Figure 4.2f).

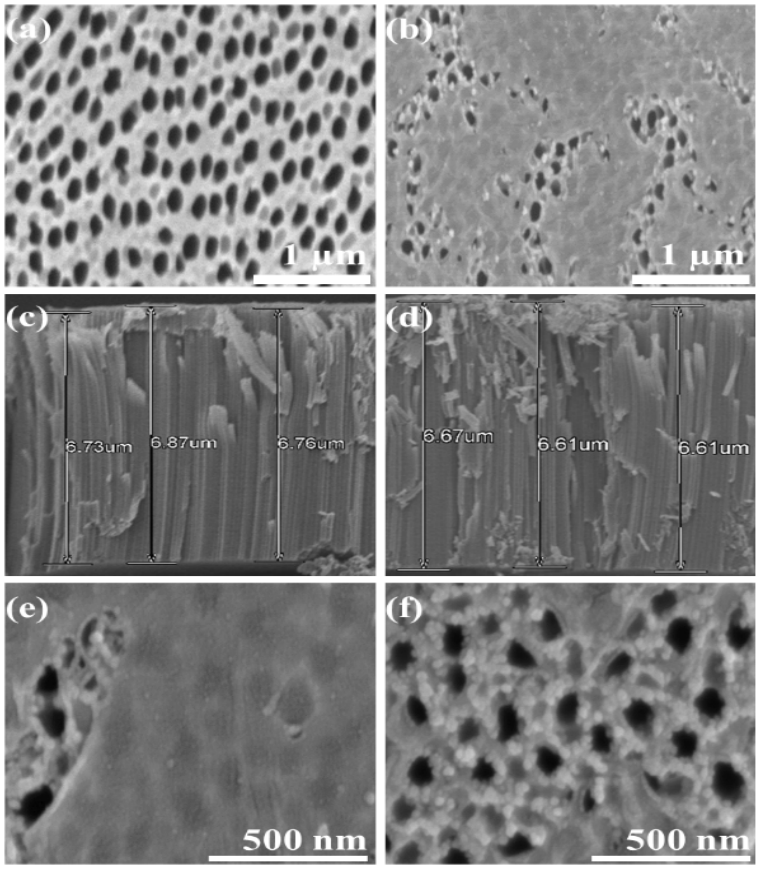

Figure 4.2 Surface morphology and cross sectional view for pure TNT (a & c) and for rGO-TNTNP (b & d). High resolution surface image of rGO-TNTNP showing transparent rGO platelets (e) and TiO_2 nanoparticles (f).

To further confirm the elemental composition of the surface nanoparticles, FE-SEM EDS was performed of the selected surface of rGO-TNTNP, shown in Figure 4.3. The EDS result of the surface shows that it is mainly composed of Ti, O, C with small contents of Pt and F. Pt is present due to Pt coating of rGO-TNTNP to make its surface conductive for better FE-SEM

imaging while the fluoride content might be associated to the surface adsorbed fluoride during the electrochemical anodization.

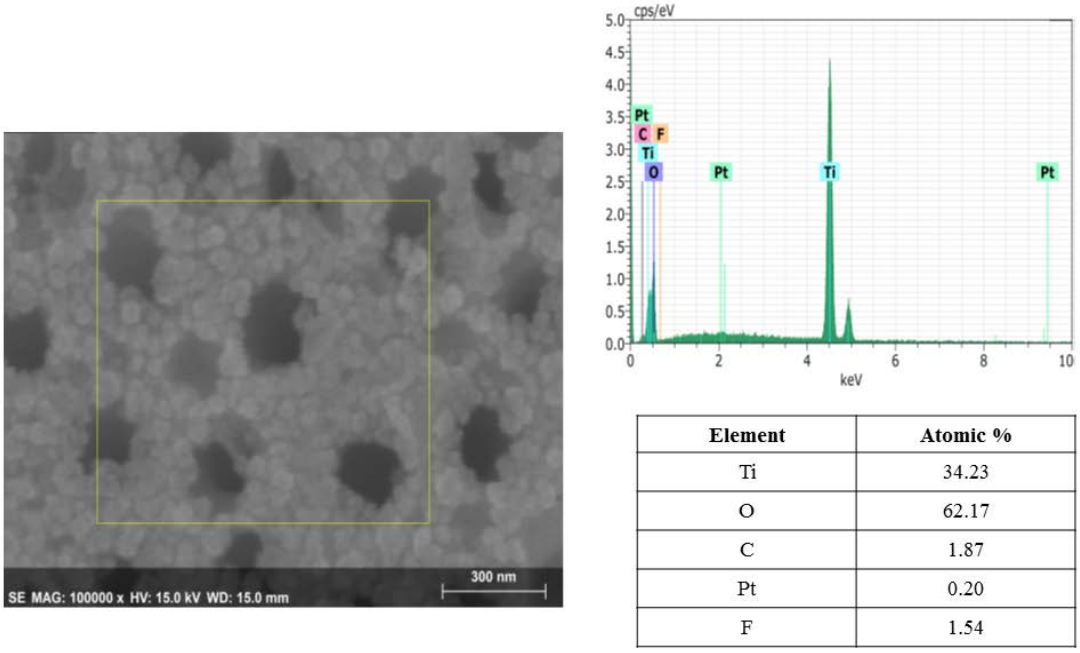

Element	Atomic %
Ti	34.23
O	62.17
C	1.87
Pt	0.20
F	1.54

Figure 4.3 FE-SEM-EDS for TiO_2 nanoparticles grown on surface of rGO-TNTNP.

4.3.2 Crystallographic study

The crystalline properties of the pure TNT and rGO-TNTNP are investigated using the X-ray diffractometry (XRD) patterns of both samples and is shown in Figure 4.4a. It can be observed clearly that both pure TNT and rGO-TNTNP shows the appearance of anatase phase confirming the proper crystallization of TiO_2 during annealing process [23]. However the rGO-TNTNP doesn't shows a peak of rGO which might be possibly due to lower rGO content as compared to peaks of titanium (T) and anatase TiO_2 (A) or dispersed rGO platelets on the rGO-TNTNP surface. Hence to confirm the rGO presence on the surface of Ti foil and rGO-TNTNP, Raman spectra of the respective samples are performed and investigated as shown in Figure 4.4b. Raman spectroscopy is considered a powerful technique to investigate the sp^2 and sp^3 hybridized carbon atoms [24]. Raman spectra of as synthesized GO shows two prominent peaks

around 1365 cm^{-1} and 1594 cm^{-1} corresponding to well establish D and G bands. These bands are well reported to the graphitic layer defects and Raman-active E_{2g} mode, respectively [25]. For the rGO-Ti foil, a clear shift of D band peak is observed towards lower wavenumber, 1345 cm^{-1} presumably due to reduction of GO platelets being deposited onto Ti foil. During the electrophoretic deposition of GO on Ti foil, a Kolbe-like decarboxylation is considered a possible reason for reduction of GO platelets by electrophoretic deposition as suggested by *An et al.* [26]. The anodization of the rGO-Ti foil finally results in rGO-TNTNP which show Raman peaks at 1345 cm^{-1} and 1590 cm^{-1} for D and G bands respectively, with decreased D peak intensity and asymmetric shape. This further shift in G band and decreased D band intensity of rGO-TNTNP can possibly be attributed to passivation of the surface functional groups by TiO_2 nanoparticles thus lowering the concentration of sp^3 hybridized defects as compared to rGO-Ti foil [27]. It is also observed that the D band to G band intensity ratio (I_D/I_G), a measure of disorders, for rGO-Ti foil (0.93) shows an increase in value as compared to GO (0.81) which also supports the reduction of GO platelets being electrically deposited on Ti foil. However after electrochemical anodization, a decrease in D band to G band intensity ratio value (I_D/I_G = 0.89) is observed as compared to rGO-Ti foil (I_D/I_G = 0.93). This again decrease can be postulated here due to the possible passivation of rGO surface oxygen functional groups by Ti^{4+} ions coming from core Ti foil resulting in the embedment of TiO_2 nanoparticles into rGO layers which are electrophoretically deposited on Ti foil [28]. The peaks appearing around 148 cm^{-1}, 400 cm^{-1}, 515 cm^{-1} and 640 cm^{-1} corresponds to E_g, B_{1g}, A_{1g} and E_g modes of anatase TiO_2, respectively [29].

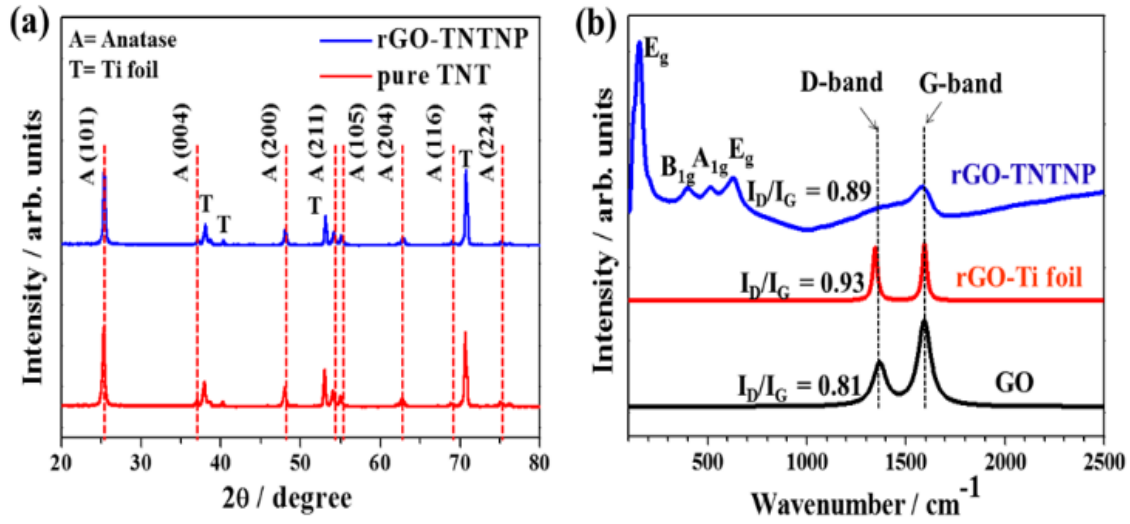

Figure 4.4 (a) XRD patterns of pure TNT and rGO-TNTNP. **(b)** Raman spectra of GO, rGO-Ti foil and rGO-TNTNP.

4.3.3 X-ray photoelectron spectroscopy (XPS) analysis

The surface elemental composition and their electronic states are investigated using X-ray photoelectron spectroscopy (XPS). Figure 4.5 shows the high resolution C 1s and O 1s XPS for rGO-Ti foil and GO-Ti foil (used as a comparative reference sample). The reference GO-Ti foil is prepared by drop-casting GO solution (1 mg/ml) on Ti foil and drying at ambient temperature. Figure 4.5a and 4.5c shows C 1s deconvoluted XPS spectra for GO-Ti foil and rGO-Ti foil respectively. The deconvolution of C 1s XPS spectra for both samples show three peaks within range of 284.5-285.0 eV, 286.5-287.0 eV and 288.3-288.6 eV, that can be associated to C-C, C-O-C and O-C=O, respectively [30]. For the electrophoretically prepared rGO-Ti foil (Figure 4.5c), a significant decrease of intensity is observed for XPS peaks located at 287.0 eV and 288.6 eV. While no prominent change in the intensity of sp^2 carbon (C-C) peak at 284.5 eV is observed. Such a decrease in intensity corresponds mainly to the reduction of GO by removal of surface oxygen functional groups [30,31]. Further, the O 1s spectra for GO-Ti and rGO-Ti foils (Figure 4.5b and 4.5d) are also deconvoluted and fitted into two peaks located at 530-531 eV and 531-532 eV and can be related to C=O/O=C-OH and C-OH groups

respectively [30]. For rGO-Ti foil the peak intensity for the peak appearing around 530-531 eV decreases and can be attributed to the loss of oxygen groups. The oxygen to carbon (O/C) atomic ratio for reference GO-Ti foil (prepared by drop casting) and electrophoretically deposited rGO-Ti foil are obtained using their C 1s and O 1s XPS data. The O/C atomic ratio shows a decreased value for rGO-Ti foil (0.56) as compared to that for GO-Ti foil (0.89). Such a decrease of O/C atomic ratio indicates the reduction of GO, in agreement with our Raman spectra results and consistent with reported literature [32].

The XPS spectra for pure TNT and rGO-TNTNP is shown in Figure 4.6. The XPS peaks of Ti 2p region for pure TNT and rGO-TNTNP are exhibited in Figure 4.6a. The pure TNT exhibits two main peaks located at 458.68 eV and 464.48 eV assigned to Ti $2p_{3/2}$ and Ti $2p_{1/2}$ respectively, corresponding to Ti^{4+} in pure anatase [33]. The Ti 2p peak of the rGO-TNTNP shows a shift to higher binding energies as compared to pure TNT which suggests the drainage of electrons from Ti to rGO and formation of bonds between TiO_2 nanotubes or TiO_2 nanoparticles with rGO at surface [34]. This shift also supports the passivation of rGO surface with TiO_2 nanoparticles as indicated by Raman spectra. The O 1s spectra of both pure TNT and rGO-TNTNP is shown in Figure 4.6b. It is observed that the O 1s peak also exhibits a shift towards higher energy as compared to pure TNT (Figure 4.6b) and can be suggested due to the possible bonding with graphene contents in the rGO-TNTNP [35]. The raw XPS data (solid line) and deconvoluted peaks (dashed lines) of O 1s region for rGO-TNTNP are shown in Figure 4.6c. The main peaks located between 530-531 eV are attributed to the Ti-O-Ti from lattice [35] whereas the shoulder peaks appearing around 531-532 eV can be assigned to non-lattice peaks such as Ti-OH and Ti-O-C respectively [35]. The other peaks centered at 533-534 eV corresponds to the C-O groups related to the presence of organic compounds from ambient chemical environment [36].

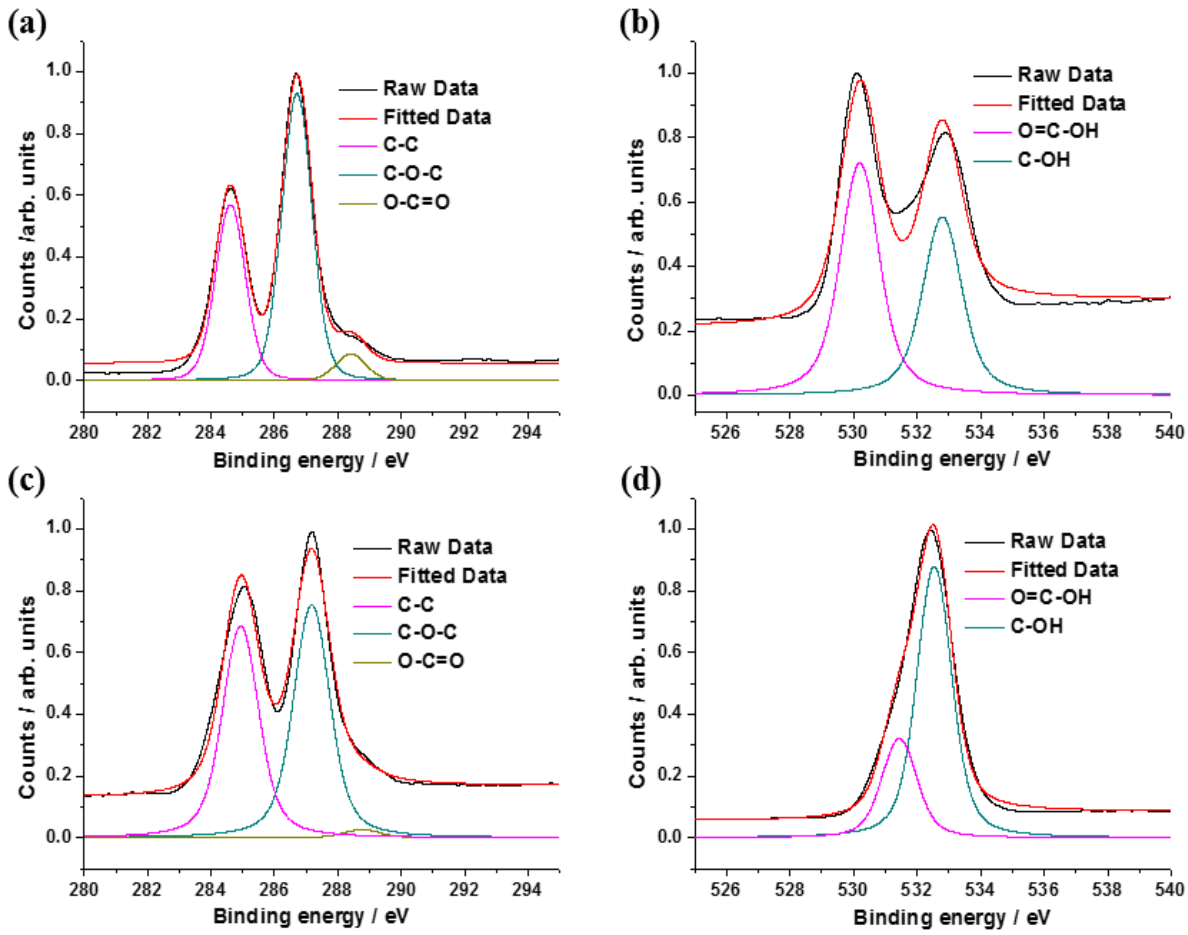

Figure 4.5 High resolution XPS spectra of: (a) C 1s, and (b) O 1 s for GO-Ti foil (reference foil prepared by GO solution drop casting on pure Ti foil). High resolution XPS spectra of: (c) C 1s, and (d) O 1s for rGO-Ti foil.

All these peaks of Ti, O and C confirms the presence of these elements in both samples, however a prominent decrease in the peak intensities of Ti 2p and O 1s is observed in case of rGO-TNTNP. The probable reason might be less TiO_2 content at rGO-TNTNP surface as compared to the porous TiO_2 layer on pure TNT surface. Figure 4.6d shows the deconvoluted peaks with raw XPS data (solid line) of C 1s region for rGO-TNTNP respectively. The C 1s XPS signals are also deconvoluted into three peaks appearing at 284.98 eV, 286.58 eV and 289.18 eV. The peak at 284.98 eV corresponds to C-C bond due to sp^2 carbon atoms of rGO

[33]. The peak appearing at 286.58 eV can be assigned to oxygenated carbon species such as C-O-R or O=C-OH [37]. The peak appearing at 289.18 eV can be attributed to Ti-O-C bond formed by the $Ti(OH)_2$ and carboxyl group of rGO thus confirming the presence of rGO in rGO-TNTNP [38].

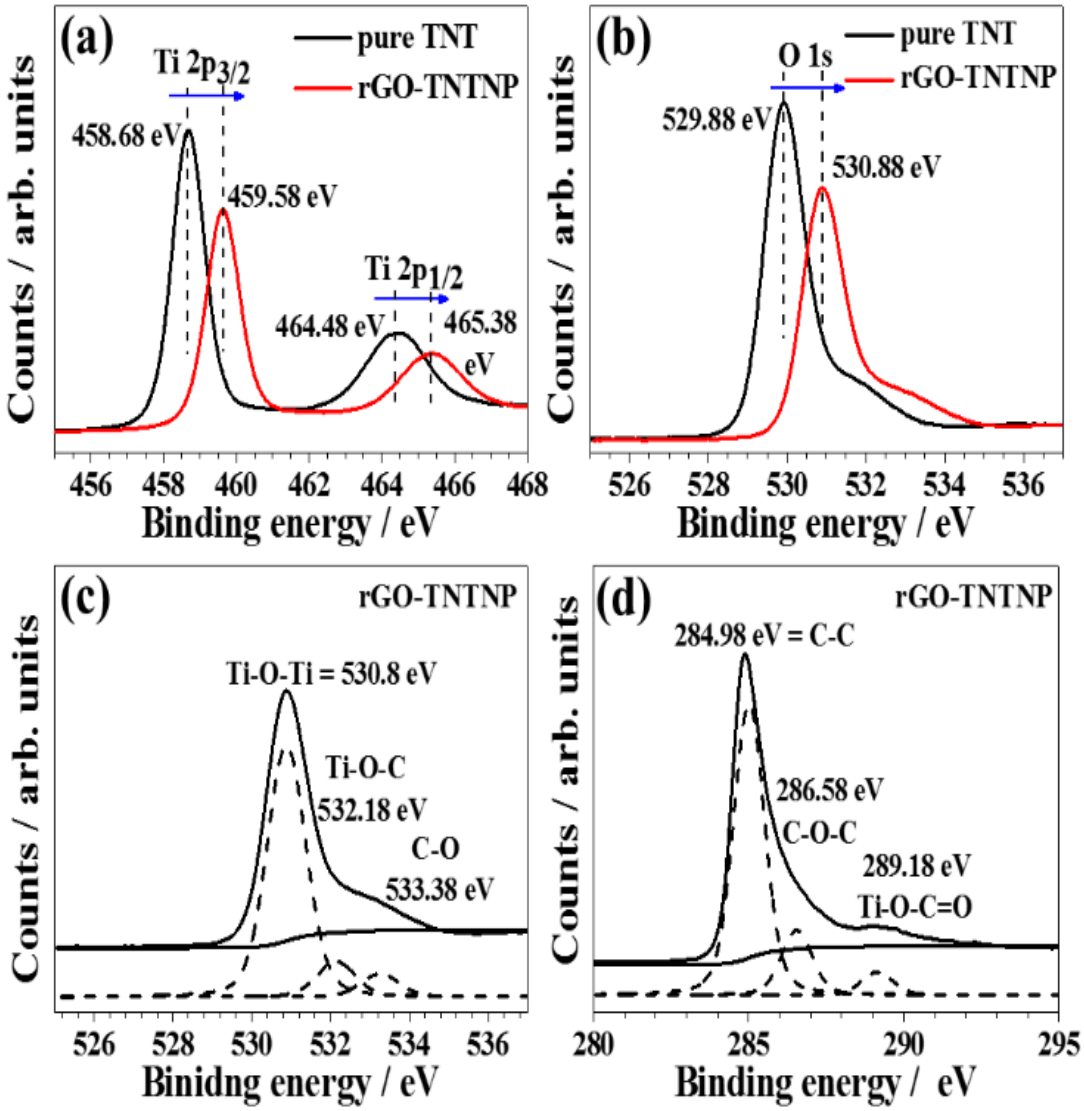

Figure 4.6 High resolution XPS spectra of (a) Ti 2p and (b) O 1 s for pure TNT and rGO-TNTNP. Core level XPS spectra of rGO-TNTNP (c) O 1s and (d) C 1s.

Furthermore the atomic % of elements is also obtained using XPS-EDS (Table 4.2). It can be seen that the carbon atomic % is higher in rGO-TNTNP sample as compared to pure TNT,

ensuring the presence of graphene contents. While the atomic % of Ti and O is lower as compared to pure TNT sample. The possible reason as explained above is the lesser TiO_2 contents on rGO-TNTNP surface.

Table 4.2 C, Ti and O atomic composition for pure TNT and rGO-TNTNP.

Material	C 1s (Atomic %)	Ti 2p (Atomic %)	O 1s (Atomic %)
Pure TNT	19.11	21.64	58.59
rGO-TNTNP	41.16	14.84	42.7

4.3.4 rGO-TNTNP formation mechanism

The mechanism involved in the formation of rGO-TNTNP acting as a photocatalyst substrate is not fully understood. However based on the reported literature and the experimental results specifically Raman spectra, XPS analysis and FE-SEM images, a possible mechanism is proposed and presented herein. The mechanism for the formation of rGO-TNTNP can be mainly divided into two parts: (i) The simultaneous deposition and reduction of GO platelets on Ti foil during electrophoretic deposition and (ii) formation of TiO_2 nanoparticles embedded in the rGO platelets at rGO-TNTNP surface during electrochemical anodization.

As is well known the graphene oxide (GO) produced using Hummers method have abundant functional groups on its edges and basal planes. The edges usually contains the carboxylate and carbonyl functional groups while the oxygen based functional groups like hydroxyl and epoxides are present on the edges of the GO. The GO platelets well dispersed in aqueous solution have negative surface charge, due to abundant deprotonated carboxylate groups. Hence the GO platelets in the aqueous suspension with negatively charged surface can be easily drawn towards the positive electrode or anode on applying bias. It is also well known

that at anode the oxidation reactions occurs, however in the current experiments the reduction and deposition of GO is happening at the Ti foil (anode) as confirmed using the Raman spectra and XPS data of rGO-Ti foil which is contrary to the realistic understanding of anode reactions. Such reduction and deposition of GO at anode is well explained by *An et al.* [26] in their findings, where they suggested the reduction of GO platelets during the electrophoretic deposition process. They suggested a Kolbe like reactions are occurring during the electrophoretic deposition which promotes the reduction of GO platelets.

The Kolbe reaction named on the German Chemist Herman Kolbe, for electrochemical prcoess is generally defined as the anodic oxidation of a carboxylate structure on the metal surface with subsequent decarboxylative dimerization of two carboxylic ions to yield a hydrocarbon or a substituted derivative corresponding to the alkyl function in the carboxylate reactant [39]. Unlike the conventional electrochemical process, Kolbe reaction involves two carboxylic ions, undergoing a sequence of consecutive reactions of decarboxylation, coupling and transfer of two electrons to complete the overall reaction as a single step reaction. The overall reaction with consecutive elementary steps involved in the Kolbe reactions for an electrochemical process are mentioned as under [39]:

Overall reaction:

$$2RCOO^- \rightarrow R\text{-}R + CO_2 + e^- \quad (4.2)$$

Elementary reactions:

$$RCOO^- \rightarrow RCOO^\bullet(M) + e^- \quad \text{(oxidation of carboxylate ion)} \quad (4.3)$$

$$RCOO^\bullet(M) \rightarrow R^\bullet(M) + CO_2 \quad \text{(oxidative decarboxylation)} \quad (4.4)$$

$$R^\bullet(M) + R^\bullet(M) \rightarrow R\text{-}R \quad \text{(dimerization of radicals)} \quad (4.5)$$

Thus based on Kolbe reactions and mechanism as reported by *An et al.* [26], it is considered herein that when the electrical contact is made to the Ti foil dipped in the GO aqueous

suspension, a series of reactions occur during the electrophoretic process proceeding the reduction of GO platelets while at the same time negatively charged surface of the GO platelets lead the deposition of rGO platelets at the Ti foil (anode) surface forming rGO-Ti foil. As soon as the electrical current is made, the oxidative decarboxylation of the carboxylate groups at edges can happen due to movement of electrons away from the platelets forming unpaired electrons within the graphene platelets and CO_2. The unpaired electrons are free to couple with another pair of electrons to make the covalent bond. Such Kolbe like oxidative decarboxylation process might can address the reduction of GO during electrophoretic process, however the process for basal hydroxyl or epoxides groups are not understood clearly based on Kolbe reactions. The possible reactions involved in the reduction of GO by Kolbe like oxidative decarboxylation as reported by *An et al.* [26] include equations 4.2-4.5 of Kolbe reactions.

Whereas during the second step of electrochemical anodization of rGO-Ti foil, the formation of rGO-TNTNP can be proposed based on the understanding of the conventional anodization process happening for pure TNT. When strong positive bias is applied to Ti foil during the anodization process, it withdraws electrons from Ti foil and pushes the Ti^{4+} outwards to Ti foil/electrolyte interface where it reacts with O^{2-} and F^{-} ions in electrolyte forming $Ti(OH)_4$ or TiF^{6-} water soluble complexes. For the pure TNT with specific electrolyte concentration we observed a TiO_2 porous layer on its surface due to low dissolution rate as compared to anodization rate (as mentioned previously in section 4.3.1) [22]. In a similar manner we suggest the reason of TiO_2 nanoparticles embedded in rGO layer might be due to precipitation of TiO_2 on the rGO-Ti foil surface. During electrochemical anodization of rGO-Ti foil, the Ti^{4+} ions migrating towards the rGO-Ti foil surface can be partially captured by surface functional oxygen groups at rGO surface which are left behind and are not subjected to Kolbe like oxidative decarboxylation during electrophoretic deposition. These left behind

surface functional groups acts as nucleation sites for the growth of TiO_2 nanoparticles resulting in the formation of TiO_2 nanoparticles embedded in rGO layers on surface.

4.3.5 Optical properties and photocurrent measurements

The optical properties are investigated by UV-vis diffuse reflectance spectra (UV-vis DRS) and photoluminescence (PL) spectroscopy investigations. The UV-vis DRS of pure Ti foil, rGO-Ti foil, pure TNT, and rGO-TNTNP are shown in Figure 4.7a. It can be observed that the rGO-TNTNP sample exhibits enhanced absorption in the visible range (400-700 nm) as compared to pure TNT sample. Whereas the control samples i.e. rGO-Ti foil shows absorbance in the visible region along with absorption peak appearing around wavelength of 300 nm supporting for rGO-TNTNP sample, the absorption in UV region (300-400 nm) is mainly due to the TiO_2, while the rGO platelets are largely responsible for absorption in the visible range.

To analyze the charge separation efficiency of the photogenerated electron and hole (e^-/h^+) pairs in pure TNT and rGO-TNTNP, PL spectra and transient photocurrent response of pure TNT and rGO-TNTNP are measured and shown in Figure 4.7b and 4.7c respectively. It can be clearly seen that the PL emission peak for rGO-TNTNP is significantly quenched as compared to pure TNT (Figure 4.7b). As is well known, the PL peak intensity is proportional to the e^-/h^+ recombination rate with higher peak intensity indicating higher recombination rate. Hence the low peak intensity for rGO-TNTNP indicates the effective transfer or trapping of photoexcited electrons ensuring the decreased recombination rate of e^-/h^+ pairs. Such peak quenching behavior supports the effective charge separation possibly due to electrons extraction by graphene domains acting as efficient pathways for electron transfer.

Further confirmation of effective charge separation hypothesis suggested by PL data is investigated by photocurrent measurements. The transient photocurrent response for both pure TNT and rGO-TNTNP is shown in Figure 4.7c. It can be observed under the simulated light

illumination, the photocurrent density of rGO-TNTNP is above 0.15 mA·cm^{-2}, whereas that of pure TNT is approximately 0.04 mA·cm^{-2}. The photocurrent response of rGO-TNTNP is around 3.75 times higher than pure TNT synthesized under similar experimental conditions. Such increased photocurrent supports the PL data and confirms the effective separation of the photogenerated electrons in the rGO-TNTNP due to efficient photogenerated charge extraction by rGO platelets.

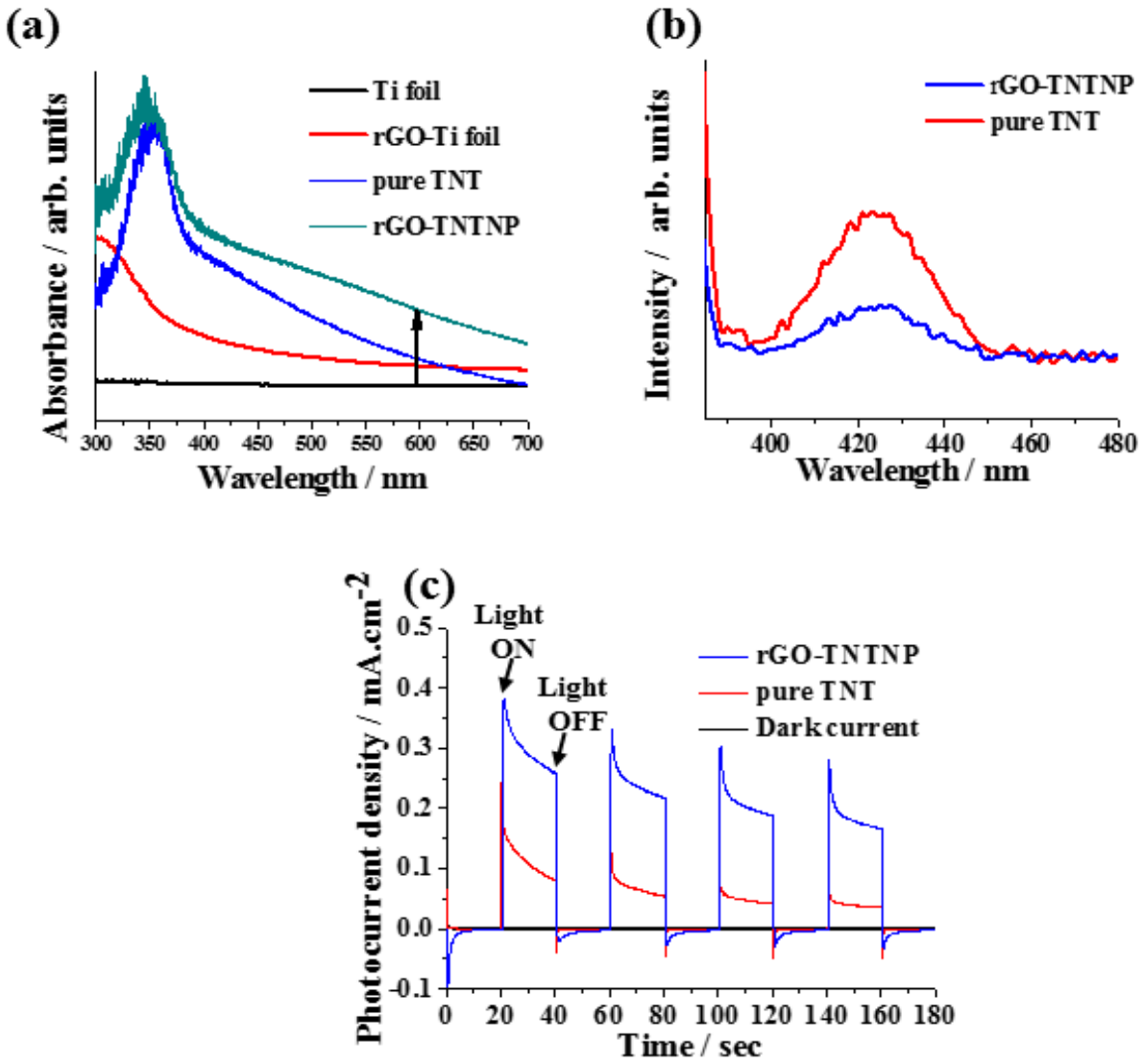

Figure 4.7 (a) UV-vis DRS spectra of pure Ti foil, rGO-Ti foil, pure TNT, and rGO-TNTNP samples. (b) Photoluminescence (PL) emission spectra and (c) Transient photocurrent response of pure TNT and rGO-TNTNP.

4.3.6 Photocatalytic CO_2 conversion

The photocatalytic activity and performance of both pure TNT and rGO-TNTNP are tested with respect to utility in photocatalytic CO_2 conversion to hydrocarbon products mainly CH_4, under simulated solar light irradiation (AM 1.5 G). The photocatalytic conversion of CO_2 with water vapor as a reducing agent is carried out in a gas phase ($CO_2/H_2O_{(g)}$) reactor. The complete experimental setup employed for CO_2 conversion is explained in detail in section 2.3.

The photocatalytic CH_4 evolution rate for pure TNT and rGO-TNTNP is shown in Figure 4.8. It can be clearly seen that the rGO-TNTNP sample exhibits a CH_4 evolution rate (5.67 $ppm.cm^{-2}.h^{-1}$) which is about 4.4 times higher than the pure TNT samples (1.28 $ppm.cm^{-2}.h^{-1}$). To investigate the carbon source for the CH_4 evolution, control experiments employing rGO-Ti foil and rGO-TNTNP in $Ar/H_2O_{(g)}$ instead of $CO_2/H_2O_{(g)}$ are performed. Both samples shows a negligible amount of CH_4 evolution besides the background measurement noise suggesting negligible involvement of any organic impurities on the surface of the samples.

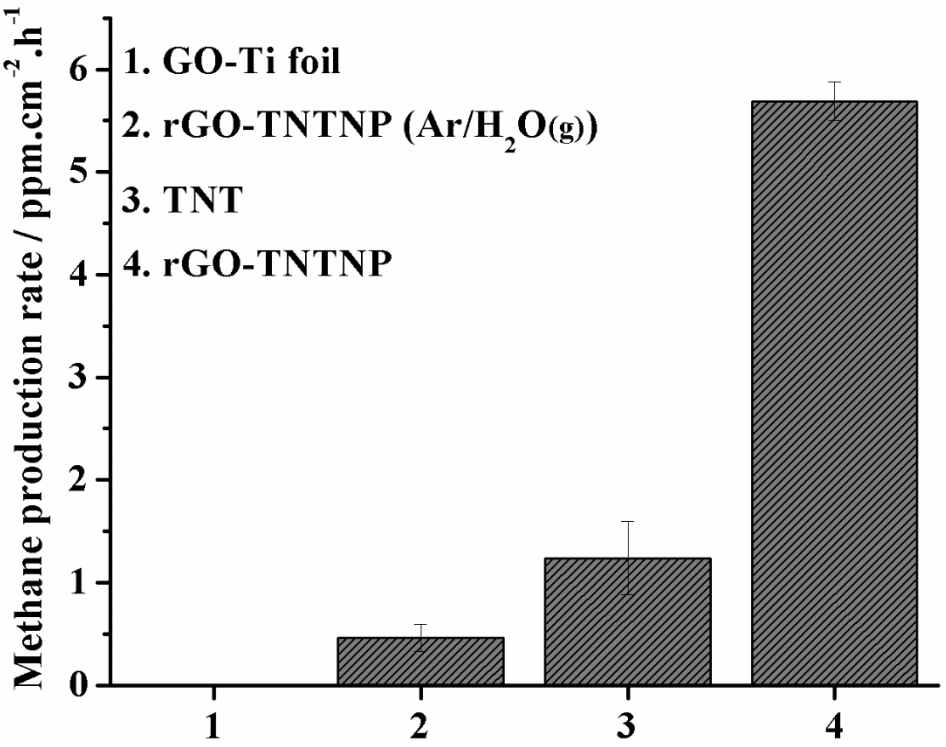

Figure 4.8 Photocatalytic methane evolution rates employing rGO-TNTNP under simulated solar light irradiation.

The Sample stability is investigated by repeated testing of rGO-TNTNP samples up to four cycles for CO_2 photoreduction (Figure 4.9). It is observed that that the CH_4 production rate during the second cycle is not as much as first cycle, with subsequent tests providing comparable results: in general, the rate of CO_2 reduction on the fourth test is approximately 75% that of the first.

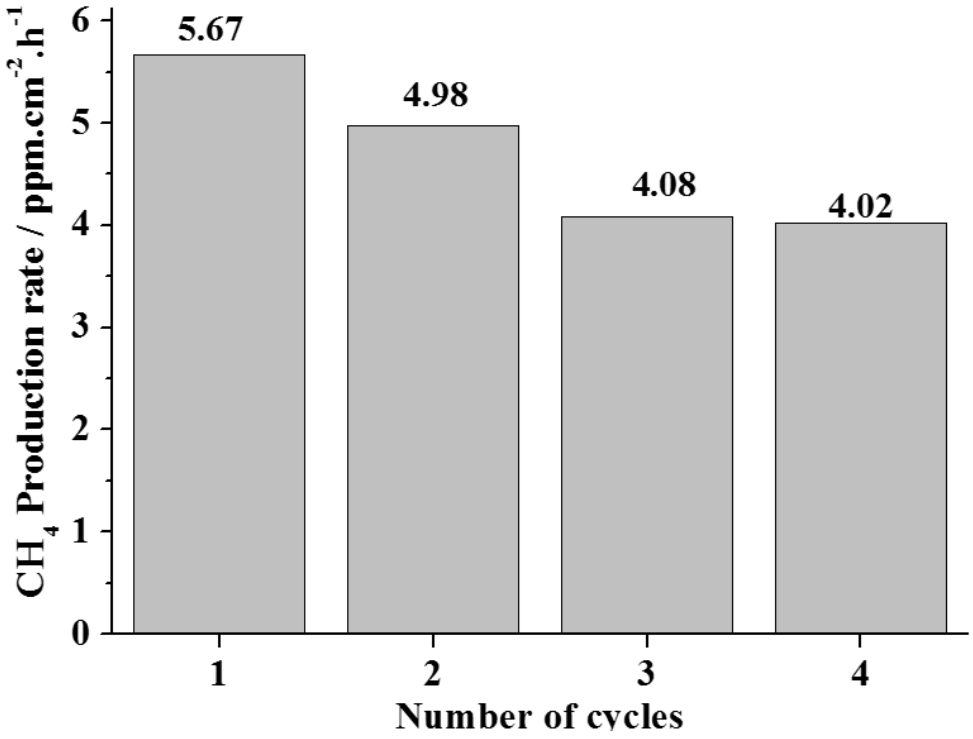

Figure 4.9 Stability test employing rGO-TNTNP sample for four cycles of CO_2 photoreduction under simulated solar light irradiation.

The possible mechanism involved in the photocatalytic CO_2 conversion is proposed for the present work based on reported literature and our experimental data. A proton assisted multi-electron process via carbene pathway [40,41] is proposed for photocatalytic CO_2 conversion to CH_4 and is shown in Figure 4.10a. It is proposed that under light illumination, pairs of photogenerated e^-/h^+ are created at various active sites on the TiO_2 nanotubes and surface TiO_2 nanoparticles embedded within the rGO platelets. The 1-D TiO_2 nanotubes can promote unidirectional vectorial charge flow as mentioned previously [42], to the rGO platelets on rGO-

TNTNP. In addition the surface TiO_2 nanoparticles embedded in rGO platelets can also generate the photoexcited electrons. Both the electrons photogenerated from the TiO_2 nanotubes and surface TiO_2 nanoparticles can be efficiently extracted by rGO platelets and can react with adsorbed CO_2 species and protons (H^+) provided by water oxidation to produce CH_4, whereas the holes migrate in the opposite direction to oxidize adsorbed H_2O.

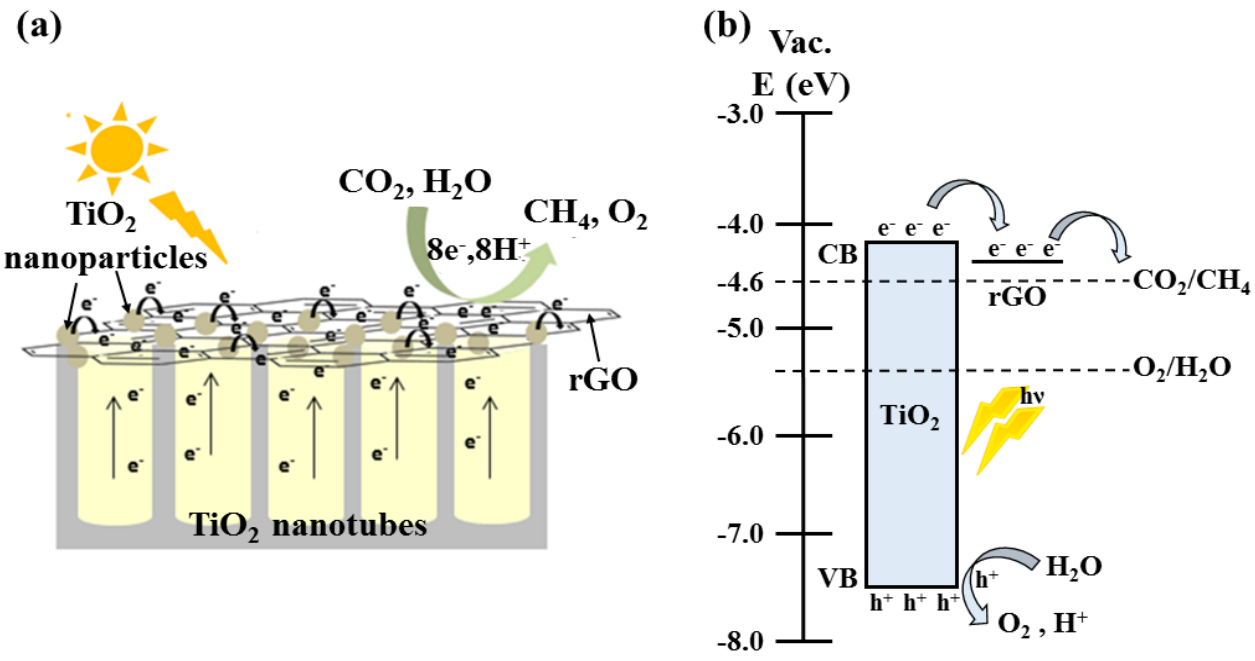

Figure 4.10 (a) Schematic illustration of photocatalytic CO_2 conversion into CH_4 and (b) Energy level diagram for rGO-TNTNP under simulated solar light.

Based on the well reported and documented relative positions of CB, VB, and redox potential for TiO_2 and rGO, an energy level diagram for rGO-TNTNP is proposed and diplayed in Figure 4.10b. The CB of anatase TiO_2 and work function of rGO lies at -4.2 eV and -4.4 eV *vs.* vacuum respectively [43], whereas the redox potential of CO_2/CH_4 lies around -4.6 eV [40]. Hence, under illumination, the photoexcited electrons in TiO_2, efficiently extracted by rGO platelets, are transferred to surface adsorbed CO_2 evolving CH_4 with enhanced yield. On contrary, the valence band of TiO_2 is below the water redox potential, 5.3 eV *vs.* vacuum [40],

hence holes in TiO_2 valence band can be filled through the water oxidation reaction producing, in turn possibly O_2 and H^+ protons. The possible reactions involved in the photocatalytic conversion of CO_2 into CH_4 are summarized in the following equations.

$$rGO\text{-}TNTNP \rightarrow rGO\ (e^-) + TNTNP\ (h^+_{VB}) \quad (4.4)$$

$$TNTNP\ (8h^+_{VB}) + 4H_2O \rightarrow 8H^+ + 2O_2 \quad (4.5)$$

$$CO_2 + 8H^+ + 8e^- \rightarrow CH_4 + 2H_2O \quad (4.6)$$

4.4 Conclusions

A facile synthesis approach was developed aimed towards fabrication of a noble metal free novel photocatalyst architecture. The simply designed synthesis strategy resulted in TiO_2 nanotube arrays covered with rGO platelets embedded with TiO_2 nanoparticles. The photocatalyst characterization was investigated by various analytical tools and instruments such as XRD, FE-SEM, Raman spectra, XPS, UV-vis DRS and PL spectroscopy. The photocatalytic and photoelectrochemical performance of the rGO-TNTNP photocatalyst was investigated by photocurrent measurements and photocatalytic CO_2 conversion into CH_4. The respective photocatalyst showed an increased photocurrent (3.75 times) and improved CH_4 production yield (4.4 times) as compared to pure TNT, reference sample. Such an increased performance observed for rGO-TNTNP sample can be attributed mainly to the improved light absorption and enhanced charge separation induced by rGO platelets.

4.5 References

[1] S.-I. In, Y. Hou, B.L. Abrams, P.C.K. Vesborg, I. Chorkendorff, Controlled Directional Growth of TiO_2 Nanotubes, J. Electrochem. Soc. 157 (2010) E69. doi:10.1149/1.3308599.

[2] S. Yoriya, C.A. Grimes, Self-assembled anodic TiO_2 nanotube arrays: electrolyte properties and their effect on resulting morphologies, J. Mater. Chem. 21 (2011) 102. doi:10.1039/c0jm02421j.

[3] S. Karthik, K.M. Gopal, E.P. Haripriya, Y. Sorachon, P. Maggie, K.V. Oomman, A.G. Craig, Highly-ordered TiO_2 nanotube arrays up to 220 μm in length: use in water photoelectrolysis and dye-sensitized solar cells, Nanotechnology. 18 (2007) 65707. doi:10.1088/0957-4484/18/6/065707.

[4] O.K. Varghese, D. Gong, M. Paulose, K.G. Ong, C.A. Grimes, Hydrogen sensing using titania nanotubes, Sensors Actuators B Chem. 93 (2003) 338–344. doi:10.1016/S0925-4005(03)00222-3.

[5] K.C. Popat, M. Eltgroth, T.J. LaTempa, C.A. Grimes, T.A. Desai, Titania nanotubes: A novel platform for drug-eluting coatings for medical implants?**, Small. 3 (2007) 1878–1881. doi:10.1002/smll.200700412.

[6] S. In, M.G. Nielsen, P.C.K. Vesborg, Y. Hou, B.L. Abrams, T.R. Henriksen, O. Hansen, I. Chorkendorff, Photocatalytic methane decomposition over vertically aligned transparent TiO_2 nanotube arrays., Chem. Commun. 47 (2011) 2613–2615. doi:10.1039/c0cc02570d.

[7] O.K. Varghese, M. Paulose, T.J. LaTempa, C.A. Grimes, High-Rate Solar Photocatalytic Conversion of CO_2 and Water Vapor to Hydrocarbon Fuels, Nano Lett. 9 (2009) 731–737. http://pubs.acs.org/doi/abs/10.1021/nl803258p.

[8] O.K. Varghese, M. Paulose, C.A Grimes, Long vertically aligned titania nanotubes on

transparent conducting oxide for highly efficient solar cells., Nat. Nanotechnol. 4 (2009) 592–597. doi:10.1038/nnano.2009.226.

[9] N.K. Allam, K. Shankar, C.A. Grimes, Photoelectrochemical and water photoelectrolysis properties of ordered TiO_2 nanotubes fabricated by Ti anodization in fluoride-free HCl electrolytes, J. Mater. Chem. 18 (2008) 2341. doi:10.1039/b718580d.

[10] S. Yoriya, N. Bao, C.A. Grimes, Titania nanoporous/tubular structures via electrochemical anodization of titanium: effect of electrolyte conductivity and anodization voltage on structural order and porosity, J. Mater. Chem. 21 (2011) 13909. doi:10.1039/c1jm12759d.

[11] X. Cheng, H. Liu, Q. Chen, J. Li, P. Wang, Preparation of graphene film decorated TiO_2 nano-tube array photoelectrode and its enhanced visible light photocatalytic mechanism, Carbon. 66 (2014) 450–458. doi:10.1016/j.carbon.2013.09.021.

[12] K. Eufinger, D. Poelman, H. Poelman, R. De Gryse, G.B. Marin, Photocatalytic activity of dc magnetron sputter deposited amorphous TiO_2 thin films, Appl. Surf. Sci. 254 (2007) 148–152. doi:10.1016/j.apsusc.2007.07.009.

[13] S.C. Roy, O.K. Varghese, M. Paulose, C.A. Grimes, Toward Solar Fuels : Photocatalytic Hydrocarbons, ACS Nano. 4 (2010) 1259–1278. doi:10.1021/nn9015423.

[14] S. In, A. Orlov, R. Berg, F. García, S. Pedrosa-Jimenez, M.S. Tikhov, D.S. Wright, R.M. Lambert, Effective visible light-activated B-doped and B,N-codoped TiO_2 photocatalysts, J. Am. Chem. Soc. 129 (2007) 13790–13791. doi:10.1021/ja0749237.

[15] J.C. Cardoso, C. a. Grimes, X. Feng, X. Zhang, S. Komarneni, M.V.B. Zanoni, N. Bao, Fabrication of coaxial TiO_2/Sb_2S_3 nanowire hybrids for efficient nanostructured organic–inorganic thin film photovoltaics, Chem. Commun. 48 (2012) 2818. doi:10.1039/c2cc17573h.

[16] A. Kongkanand, P. V. Kamat, Electron Storage in Single Wall Carbon nanotubes. Fermi

level equilibration in Semiconductor–SWCNT Suspensions, ACS Nano. 1 (2007) 13–21. doi:10.1021/nn700036f.

[17] J. Lin, R. Zong, M. Zhou, Y. Zhu, Photoelectric catalytic degradation of methylene blue by C_{60}-modified TiO_2 nanotube array, Appl. Catal. B Environ. 89 (2009) 425–431. doi:10.1016/j.apcatb.2008.12.025.

[18] A.K. Geim, Graphene : Status and Prospects, Science. 320 (2009) 1530–1534. doi:10.1126/science.1158877.

[19] K. S. Novoselov, A.K. Geim, S. V. Morozov, D. Jiang, Y. Zhang, S. V. Dubonos, I. V. Grigorieva, A.A. Firsov, Electric Field Effect in Atomically Thin Carbon Films, Science. 306 (2004) 666–669.

[20] X. Zhang, B.R.S. Rajaraman, H. Liu, S. Ramakrishna, Graphene's potential in materials science and engineering, RSC Adv. 4 (2014) 28987–29011. doi:10.1039/C4RA02817A.

[21] D.C. Marcano, D. V. Kosynkin, J.M. Berlin, A. Sinitskii, Z. Sun, A. Slesarev, L.B. Alemany, W. Lu, J.M. Tour, Improved synthesis of graphene oxide, ACS Nano. 4 (2010) 4806–4814. doi:10.1021/nn1006368.

[22] D. Wang, Y. Liu, B. Yu, F. Zhou, W. Liu, TiO_2 Nanotubes with Tunable Morphology , Diameter , and Length : Synthesis and Photo-Electrical / Catalytic Performance TiO_2 Nanotubes with Tunable Morphology , Diameter , and Length : Synthesis and Photo-Electrical/Catalytic Performance, Chem. Mater. (2009) 1198–1206. doi:10.1021/cm802384y.

[23] G. Ali, H.J. Kim, J.J. Kim, S.O. Cho, Controlled fabrication of porous double-walled TiO_2 nanotubes via ultraviolet-assisted anodization., Nanoscale. 6 (2014) 3632–3637. doi:10.1039/c3nr05894h.

[24] D. Luo, G. Zhang, J. Liu, X. Sun, Evaluation criteria for reduced graphene oxide, J. Phys. Chem. C. 115 (2011) 11327–11335. doi:10.1021/jp110001y.

[25] T. Xu, L. Zhang, H. Cheng, Y. Zhu, Significantly enhanced photocatalytic performance of ZnO via graphene hybridization and the mechanism study, Appl. Catal. B Environ. 101 (2011) 382–387. doi:10.1016/j.apcatb.2010.10.007.

[26] S.J. An, Y. Zhu, S.H. Lee, M.D. Stoller, T. Emilsson, S. Park, A. Velamakanni, J. An, R.S. Ruoff, Thin film fabrication and simultaneous anodic reduction of deposited graphene oxide platelets by electrophoretic deposition, J. Phys. Chem. Lett. 1 (2010) 1259–1263. doi:10.1021/jz100080c.

[27] Y.T. Liang, B.K. Vijayan, K.A. Gray, M.C. Hersam, Minimizing graphene defects enhances titania nanocomposite-based photocatalytic reduction of CO_2 for improved solar fuel production, Nano Lett. 11 (2011) 2865–2870. doi:10.1021/nl2012906.

[28] A. Das, S. Pisana, B. Chakraborty, S. Piscanec, S.K. Saha, U.V. Waghmare, K.S. Novoselov, H.R. Krishnamurthy, A.K. Geim, A.C. Ferrari, A.K. Sood, Monitoring dopants by Raman scattering in an electrochemically top-gated graphene transistor., Nat. Nanotechnol. 3 (2008) 210–5. doi:10.1038/nnano.2008.67.

[29] W.F. Zhang, Y.L. He, M.S. Zhang, Z. Yin, Q. Chen, Raman scattering study on anatase TiO_2 nanocrystals, J. Phys. D. Appl. Phys. 33 (2000) 912–916. doi:10.1088/0022-3727/33/8/305.

[30] D. Yang, A. Velamakanni, G. Bozoklu, S. Park, M. Stoller, R.D. Piner, S. Stankovich, I. Jung, D.A. Field, C.A. Ventrice, R.S. Ruoff, Chemical analysis of graphene oxide films after heat and chemical treatments by X-ray photoelectron and Micro-Raman spectroscopy, Carbon. 47 (2009) 145–152. doi:10.1016/j.carbon.2008.09.045.

[31] S. Park, J. An, J.R. Potts, A. Velamakanni, S. Murali, R.S. Ruoff, Hydrazine-reduction of graphite- and graphene oxide, Carbon. 49 (2011) 3019–3023. doi:10.1016/j.carbon.2011.02.071.

[32] J. Kim, S. Ganorkar, Y.H. Kim, S. Il Kim, Graphene oxide hole injection layer for high-

efficiency polymer light-emitting diodes by using electrophoretic deposition and electrical reduction, Carbon. 94 (2015) 633–640. doi:10.1016/j.carbon.2015.07.049.

[33] L.C. Sim, K.H. Leong, S. Ibrahim, P. Saravanan, Graphene oxide and Ag engulfed TiO_2 nanotube arrays for enhanced electron mobility and visible-light-driven photocatalytic performance, J. Mater. Chem. A. 2 (2014) 5315–5322. doi:10.1039/c3ta14857b.

[34] X.R. Cao, G.H. Tian, Y.J. Chen, J. Zhou, W. Zhou, C.G. Tian, H.G. Fu, Hierarchical composites of TiO_2 nanowire arrays on reduced graphene oxide nanosheets with enhanced photocatalytic hydrogen evolution performance, J. Mater. Chem. A. 2 (2014) 4366–4374. doi:10.1039/c3ta14272h.

[35] T. Lu, R. Zhang, C. Hu, F. Chen, S. Duo, Q. Hu, TiO_2-graphene composites with exposed {001} facets produced by a one-pot solvothermal approach for high performance photocatalyst, Phys. Chem. Chem. Phys. 15 (2013) 12963–70. doi:10.1039/c3cp50942g.

[36] S. Sreekantan, K.A. Saharudin, Z. Lockman, T.W. Tzu, Fast-rate formation of TiO_2 nanotube arrays in an organic bath and their applications in photocatalysis., Nanotechnology. 21 (2010) 365603. doi:10.1088/0957-4484/21/36/365603.

[37] M.S. Arif Sher Shah, K. Zhang, A.R. Park, K.S. Kim, N.-G. Park, J.H. Park, P.J. Yoo, Single-step solvothermal synthesis of mesoporous Ag-TiO_2-reduced graphene oxide ternary composites with enhanced photocatalytic activity., Nanoscale. 5 (2013) 5093–101. doi:10.1039/c3nr00579h.

[38] O. Akhavan, M. Abdolahad, Y. Abdi, S. Mohajerzadeh, Synthesis of titania/carbon nanotube heterojunction arrays for photoinactivation of E. coli in visible light irradiation, Carbon. 47 (2009) 3280–3287. doi:10.1016/j.carbon.2009.07.046.

[39] A. K. Vijh, B.E. Conway, Electrode Kinetic Aspects of the Kolbe Reaction, Chem. Rev. 67 (1967) 623–664. doi:10.1021/cr60250a003.

[40] W. Fan, Q. Zhang, Y. Wang, Semiconductor-based nanocomposites for photocatalytic H_2 production and CO_2 conversion., Phys. Chem. Chem. Phys. 15 (2013) 2632–49. doi:10.1039/c2cp43524a.

[41] S.N. Habisreutinger, L. Schmidt-Mende, J.K. Stolarczyk, Photocatalytic reduction of CO_2 on TiO_2 and other semiconductors, Angew. Chemie - Int. Ed. 52 (2013) 7372–7408. doi:10.1002/anie.201207199.

[42] X. Feng, K. Zhu, A.J. Frank, C.A. Grimes, T.E. Mallouk, Rapid Charge Transport in Dye-Sensitized Solar Cells Made from Vertically Aligned Single-Crystal Rutile TiO_2 Nanowires., Angew. Chem. (2012) 2781–2784. doi:10.1002/ange.201108076.

[43] Y.-K. Kim, D.-H. Min, UV protection of reduced graphene oxide films by TiO_2 nanoparticle incorporation., Nanoscale. 5 (2013) 3638–42. doi:10.1039/c3nr00321c.

Chapter 5. Reduced TiO_2 (TiO_{2-x}) Photocatalyst prepared by a New Approach for Efficient Solar Light CO_2 Conversion to Hydrocarbon fuels.

5.1 Introduction

Development of efficient solar-spectrum activated photocatalytic material is one of the most effective and favorable ways for enhanced photocatalytic CO_2 conversion to useable chemicals. In this regard, enormous amount of research and development have been done and still under progress to achieve a stable and efficient photocatalytic material with extended light absorption in an efficient manner to enhance the yield of solar fuels generated by CO_2 photoreduction such as methane, ethane, methanol, carbon monoxide [1–3]. As mentioned previously, amongst various photocatalytic materials, Titania (TiO_2) is considered as one of the champion material bearing superb properties of chemical stability, nontoxicity, corrosion resistance, abundant availability and low cost [4]. However, the photocatalytic performance of TiO_2 is limited due to higher recombination rate of photoexcited electron and hole (e^-/h^+) pairs and wider band gap (~3.2 eV for anatase), resulting in low quantum efficiency and limited light absorption mainly to UV wavelengths which is composed of only 4-5 % of the terrestrial sunlight [4].

In general, for an efficient photocatalytic CO_2 reduction, photocatalysts should fulfill the following three key requirements of (i) broader light absorption, (ii) effective separation of photogenerated charge along with the fundamental condition of (iii) its band edges position well matching the redox potential of the selective product. To achieve such requirements, various strategies have been developed and adopted for enhancing the photocatalytic performance such as metal and non-metal doping [5,6], coupling of low band gap materials [7,8], and dye-sensitization [9]. These strategies to a large extent are focused towards the narrowing of the band gap of TiO_2 as a means of enhancing light absorption and approaching the ideal utilization of solar spectrum energy. Furthermore, for an efficient separation of

photoexcited charges, deposition of noble metals (e.g Pt, Ag, Cu etc.) as a co-catalysts and coupling of electron carriers with TiO_2 surface, enhances the photocatalytic performance via providing a direct pathway for photogenerated charge extraction [10].

In the above mentioned strategies, metals and non-metals doping of TiO_2 have been adopted frequently to extend its light absorption to visible range leading to improved performance. Usually in metal doping, metal ions replace the Ti^{4+} ions and non-metal ions replaces O^{2-} ions in the TiO_2 lattice [11]. In addition metal and non-metals are also combined to replace partially both Ti^{4+} and O^{2-} ions. Both doping strategies no doubt improve the photocatalytic performance to a moderate extent, the dopants also mainly acts as recombination centers and again limits the material performance [12]. In contrary to foreign elements doping, it has been revealed that various photocatalytic properties such as light absorption, charge transport, electronic structure and surface adsorption of various chemical species are largely related to the oxygen vacancies (V_O) in TiO_2 or TiO_2 based metal oxides [13]. Schematic representation of various defects within the TiO_2 lattice is portrayed in Figure 5.1 [14].

The creation of V_O is considered responsible for broadening of TiO_2 light absorption to visible and near infrared (NIR) regions with vacancies acting as electron and hole traps rather than recombination centers, thus can improve the photocatalytic performance and charge separation. In addition it has also been reported V_O plays an important role for various species to get adsorbed on the surface, improving the reaction rates. For these reasons, there have been a great interest for the development of TiO_2 with tuned oxygen vacancies (V_O) (commonly known as hydrogenated/reduced TiO_2 and represented as TiO_{2-x}) and exploring their superb photocatalytic properties in a variety of photocatalytic applications.

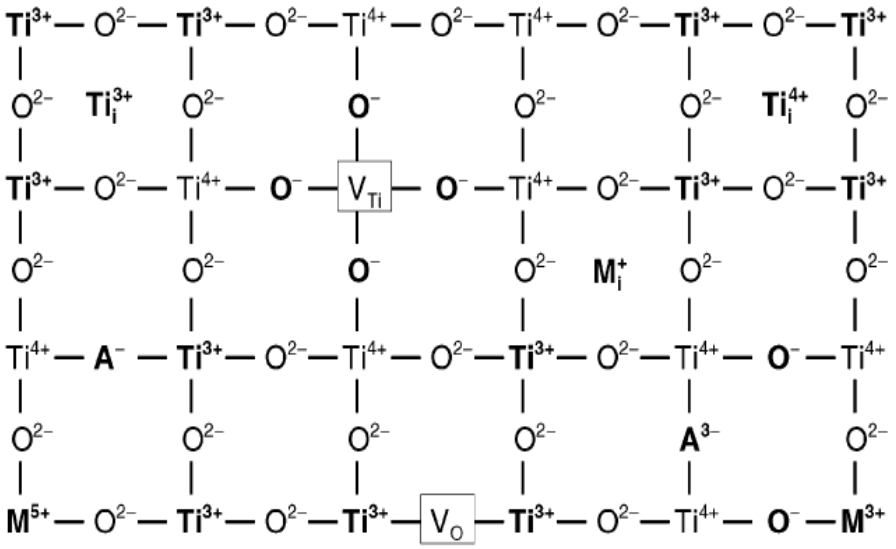

Figure 5.1 Schematic representation of a TiO_2 lattice with a variety of defects. Where V_O= oxygen vacancy, V_{Ti} =Ti metal vacancy, M^{3+} and M^{5+} = Foreign metals doped, Ti_i^{4+}, Ti_i^{3+} and M_i^+ = metal interstitials. (Taken from Ref. #14)

It is commonly accepted that the V_O in the TiO_2 are created by thermal treatment of TiO_2 under vacuum and/or reducing environment resulting in Ti^{3+} self-doped and/or reduced TiO_2 (RT) photocatalyst. On the basis of experimental evidence and theoretical calculations [11,13], it is generally believed that at high thermal conditions (> 450 °C) with reducing environment, H_2 gas for instance, hydrogen atom interacts with the oxygen atom of the lattice, transfer the electrons to oxygen atom and oxygen atom leaves the lattice as a water leaving behind V_O and an electron rich Ti^{3+} ion. Moreover at extremely high temperature, H_2 treatment not only creates the V_O but also can form the Ti interstitial defects in the TiO_2 lattice and large degree of lattice disorder [13]. Such vacancies, defects and lattice disorders induce the shallow donor and accepter states below and above the conduction band and valence band edges respectively, resulting in the downward shift of the conduction band and upward shift of the valence band. Depending upon the concentration of V_O or defects, the reduced TiO_2 or TiO_{2-x} shows different color, starting form yellow, blue, gray, black-grey to fully black. It has been observed with the

increase in V_O, specifically in anatase TiO_2, these generated donor and acceptor states can overlap the conduction and valence band with a tailing towards the mid-gap energy states. Such defects induced tailing of the shallow energy levels towards the mid-gap energy states narrows down the band gap of the TiO_2 and transfer the charge from O 2p orbitals to the Ti 3d orbitals in similar manner as transferred from the valence band to conduction band in the bulk TiO_2 under illumination [11,12]. Such reduction induces shallow and deep states which acts as an electron and hole traps resulting in the localization of photoexcited electrons and holes, minimizing the effect of charge recombination centers as observed in foreign elements doped TiO_2. A pictorial view of the reduced TiO_2 or TiO_{2-x} with respective to their energy states is depicted in Figure 5.2.

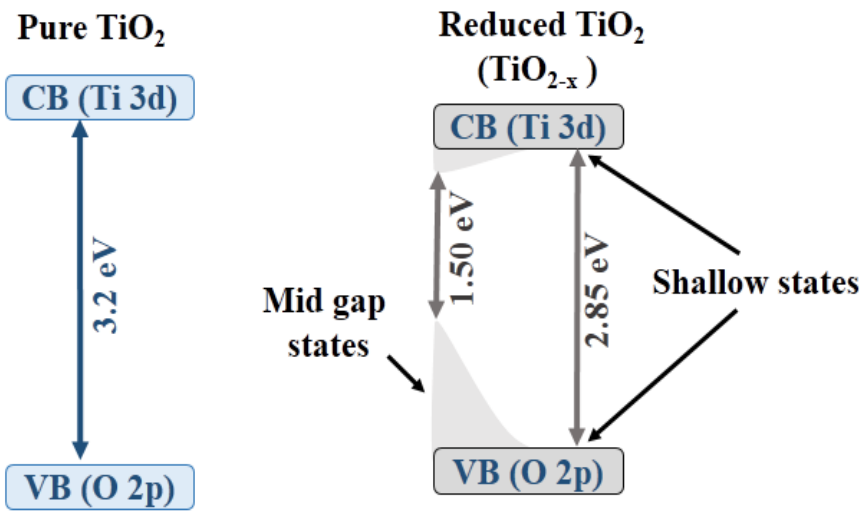

Figure 5.2 Band energy diagram for anatase TiO_2 and reduced TiO_2 (TiO_{2-x}). The band gap is decreased from 3.2 eV to 2.85 eV by creation of shallow states below and above conduction band minimum and valence band maximum respectively, with tailing up to mid gap deep states induced by V_O or Ti^{3+} ions and surface defects.

In 2011, *Chen et al.* [15] reported the synthesis of black hydrogenated TiO_2 nanocrystals with a highly disordered surface layer resulting in enhanced light absorption (extended to

visible and NIR regions), henceforth improving photocatalytic activity for methylene blue degradation and hydrogen production via water splitting. Since then several studies have been done for the development of hydrogenated or reduced TiO_2 with different strategies to achieve efficient TiO_{2-X} such as via manipulation and influence of various reaction parameters (temperature, pressure, gas composition etc.), synthesis methodologies, and different initial TiO_2 precursors [16–19]. All such approaches are designed for achieving significantly enhanced photocatalytic activity in diverse range of applications [20,21].

Focused towards the development of new synthesis methodology, a new approach for synthesis of reduced TiO_2 (RT) is developed in this experimental work and its photocatalytic activity is tested for photocatalytic CO_2 conversion to hydrocarbon fuels. The new synthesis strategy involves the reduction of anatase white TiO_2 with dual reducing agents that is magnesium (Mg) powder at high thermal temperature under 5% H_2/Ar gas environment followed by acid washing. The acid washing is done to remove the unreacted Mg or probable MgO produced during the process and finally providing a Mg free reduced TiO_2. Mg at high temperature had been used for reduction of $TiCl_4$ to achieve a high purity Ti metal, the process commonly known as Kroll process [22]. Thus being inspired from such favorable opportunity offered by Mg we designed a process with dual reducing agents i.e Mg powder and H_2 gas to obtain an efficient RT photocatalyst. Such process is termed as magnesiothermic reduction in 5% H_2/Ar [23,24].

As mentioned previously that it is generally accepted the reduction of TiO_2 generates large number of surface defects and Ti^{3+} ions /oxygen vacancies, which are mainly responsible for the improved light absorption as well as higher photocatalytic performance [16–19]. In terms of CO_2 photoreduction, until now there exists few studies employing hydrogenated/reduced TiO_2 systems demonstrating enhanced activity which suggests the oxygen vacancies and surface defects acts as electron donors which can promote charge transportation and CO_2

activation [11–13]. Being motivated form superb properties offered by hydrogenated/reduced TiO_2, more importantly, improved visible light activity, herein, we investigate the simulated solar light-driven CO_2 photoreduction with H_2O vapors on RT nanoparticles synthesized by controlled magnesiothermic reduction of commercial nano-TiO_2 (CT) in 5% H_2/Ar gas. Interestingly, the band edge positions of RT are found in good alignment with CO_2/CH_4 redox potential, hence possessing a favorable band gap producing CH_4 as the dominant product with ethane (C_2H_6) and higher alkanes (C_xH_y) as minor products. Further, platinum (Pt), a well-known electron transferring co-catalyst is photodeposited onto RT surface for efficient separation of photogenerated charges. Optimization of Pt deposition is done by preparing a series of Pt deposited RT with varied weight percent (theoretically calculated) of platinum precursor and employing for CO_2 photoreduction. Thus, aforementioned requirements of broad light absorption, efficient charge transfer and well-aligned band edges, all are achieved for the developed photocatalyst system. The optimized Pt loaded RT sample demonstrated a significant enhancement of the CO_2 photoreduction superior to that of commercial Degussa P25 and CT (Aldrich, USA) and competitive to those of previously reported reduced TiO_2 materials for CO_2 photoreduction.

5.2 Experimental section

5.2.1 Materials and reagents

The chemicals used in the synthesis of reduced TiO_2 (RT) includes commercial nano-Titanium (IV) oxide (anatase TiO_2 nanopowder, < 25 nm particle size, 99.7 % trace metals basis) and Magnesium powder (≥ 99 %). Both chemicals were purchased from SIGMA-ALDRICH and were annealed under H_2 gas environment from a 5% H_2/Ar cylinder. Concentrated hydrochloric acid (HCl, ACS reagent, 37.0 %) from SIGMA-ALDRICH was used for washing the unreacted Mg and MgO in the RT sample. Chloroplatinic acid hexahydrate ($H_2PtCl_6.6H_2O$, ACS reagent, ≥ 37.50 %) also purchased from SIGMA-ALDRICH was used as a Platinum (Pt) precursor. Pt precursor solution was made in Deionized (DI) water and methanol (CH_3OH, 99.8 %, DUKSAN REAGENTS, Korea) acting as a hole scavenger.

5.2.2 Synthesis of reduced TiO_2 (RT)

Typical procedure for the synthesis of RT by a newly developed approach includes mixing of 1.6 g (20 mmol) of commercial nano-TiO_2 (CT) with 240 mg (10 mmol) of Mg powder. The well mixed powder of both Mg and TiO_2 was then heated at 650 °C (ramp 2 °C/min) for 5 h under 5% H_2/Ar in a tube furnace. After cool down, the sample was collected and washed with dilute HCl (1.0 M) to remove the Mg Species. The Mg and Cl^- free RT was obtained after washing with plenty of water and dried in a hot air oven for overnight at 80 °C. The 1:0.5 molar ratio of TiO_2 and Mg was selected, as such ratio was previously optimized resulting in the best photocatalyst for photoinduced hydrogen production [23]. The detail optimization process is not included in this experimental work. For the purpose of comparison and to investigate the synergetic effect of our synthesis approach, different control samples were also prepared such as (i) CT with Mg only annealed under Ar gas named as RT(Mg), (ii)

CT annealed under Ar only named as CT(Ar) and (iii) CT annealed under 5% Ar/H_2 named as RT(H_2).

5.2.3 Synthesis of Pt deposited reduced TiO_2 (Pt-x-RT)

Pt nanoparticles as a co-catalyst were deposited by a photodeposition method on the desired amount of RT [25]. A series of Pt photodeposited RT samples were prepared and termed as Pt-x-RT, where x = 0.5, 0.9, 1.0, 1.2 and 2.0, represents calculated weight percent (wt. %) of Pt with respect to fixed amount of RT (100 mg). Based on calculation, required amount of $H_2PtCl_6.6H_2O$ is added to 25 ml of DI water containing 20 vol. % methanol and 100 mg of RT. The mixture was well stirred for 1 h (500 rpm) in a closed system to obtain a well-dispersed solution which was then irradiated using a 300 W Xe arc lamp (Newport) with a 6.0 cm long IR water filter. The irradiation was done for 2 h under mild stirring (300 rpm). Finally, the Pt photodeposited RT samples were thoroughly washed with deionized (DI) water, using centrifugation (15000 rpm, 10 min.) and kept for drying under vacuum at 90 °C for 12 h. Pt (1.0 wt. %) was also photodeposited on all control samples with similar procedure and tested for CO_2 photoconversion experiments.

5.2.4 Characterization

X-ray diffraction (XRD) patterns of the samples were taken to analyze the crystallinity of the samples using an X-ray diffractometer (Panalytical, Empyrean) operated at 40 kV and 30 mA with Cu Kα radiation (λ=1.54 Å) as an X-ray source, scanned with a step degree of 0.02° and duration time of 0.05 s in the range of 2θ = 20-80°. UV-visible diffuse reflectance spectroscopy (UV-vis DRS) was used to determine the light absorption of powder samples using a Cary series (CARY5000) UV-visible-near IR spectrophotometer (Agilent Technologies) with a diffuse reflection accessory in the range of 300-700 nm. Photoexcited

charge separation was analyzed using Photoluminescence (PL) spectroscopy. PL spectra of the samples were measured using Cary Eclipse Fluorescence Spectrophotometer (Agilent Technologies) with an excitation wavelength of λ_{ex} = 300 nm. The samples for PL measurement were prepared by dispersing powder samples in ethanol with a concentration of 0.5 mg/ml. To confirm the crystallinity of the pure anatase CT and RT samples, transmission electron microscopy (TEM) images of samples were obtained using FE-TEM (Hitachi HF-3300). Size of the Pt nanoparticles on the RT samples was also analyzed by TEM images and estimated using ImageJ software. The samples for TEM analysis were prepared by dispersing powder samples (0.05 mg/ml) in ethanol followed by sonication of the mixture for few minutes (5-10 minutes), then one drop of the suspension was dropped onto a Ni TEM grid and allowed to dry overnight at 70 °C temperature in an oven. X-ray photoelectron spectroscopy (XPS) was used to investigate the surface composition and oxidation states for pure commercial nano-TiO_2 (CT), RT and Pt (1 wt. %) deposited RT (Pt-1.0-RT). XPS data was obtained by X-ray photoelectron spectroscopy (XPS, Thermo Scientific, ESCALAB 250Xi) using Al Kα line (148606 eV) as the X-ray source. The curve fitting of respective XPS spectra was performed using the Gaussian method. Valence band XPS for pure commercial nano-TiO_2 (CT) and RT samples were also measured to investigate the upshifting of the valence band for RT sample induced by V_O or Ti^{3+} ions. Further confirmation of CT reduction was done using electron paramagnetic resonance (EPR) spectroscopy at -163.5 °C with a continuous wave X-band spectrometer (JEOL, JES-FA200) using microwaves with power of 0.998 mW and frequency of 9185.041 MHz. The textural properties of pure CT, RT and Pt-x-RT (where x = 0.5, 0.9, 1.0, 1.2 and 2.0, represents theoretically calculated wt. % of Pt for photodeposition) samples such as surface area, pore size, and pore volume were investigated by N_2 physisorption measurements. Micromeritics ASAP 2000 apparatus was used to measure the N_2 sorption isotherms at -196 ^oC. Prior to measurement, all the samples were extensively degassed at 200

^{o}C to 20 mTorr for 300 minutes. The Brunauer-Emmett-Teller (BET) equation was used to calculate the surface area for all samples in the relative pressure (P/P_0) range of 0.05 to 0.30. The pore size and pore volume were obtained by applying the Barrett-Joyner-Halenda (BJH) equation to desorption isotherms.

5.2.5 Band gap estimation

Tauc plots for pure CT and RT samples were plotted to estimate the respective band gaps (Eg) [26]. The function $(\alpha hv)^2$ (where α is the absorption coefficient, h is Planck constant and v is frequency) was plotted against band gap energy ($E=hv=hc/\lambda$). The band gaps were determined by extrapolating the linear portions of the curves to zero of the y-axis. The valence band top positions were obtained from valence band XPS which was aligned *vs.* NHE. The conduction band bottom was then obtained by subtracting the band gap value from valence band maximum value. The proposed band structure of CT and RT along with CO_2/CH_4 redox potential is illustrated in potential (E) *vs.* NHE.

5.2.6 Photocatalytic CO_2 conversion

The photocatalytic performance of the prepared materials were investigated for photocatalytic CO_2 conversion with water (H_2O) vapors into CH_4 using gaseous phase reactor arrangement. The details of the experimental setup and procedure is explained in section 2.3 of chapter 2. In this experiment, 70 mg of the photocatalyst was loaded in stainless steel made photoreactor (Volume = 15.4 cm^3) with a quartz window. The CO_2 (1000 ppm in He) was allowed to pass through the water bubbler forming a mixture of CO_2 /$H_2O_{(g)}$ filling the reactor. Prior to photoreduction tests, the reactor was purged with CO_2 gas (1000 ppm in He) and vacuum repeatedly up to five times in order to remove any air or other gaseous impurities which may present in the photoreactor. The photoreactor was illuminated with 1 sun simulated sunlight using a 100 W xenon solar simulator (Oriel, LCS-100) equipped with an AM 1.5G

filter. After 1 h of continuous illumination, a volume of 500 µL of sample was taken from photoreactor using an argon-purged syringe and manually injected to gas chromatography (GC) unit (Shimadzu GC-2014, Restek RT-Q-Bond column, ID = 0.53 mm, length = 30m) equipped with flame ionization detector (FID). The hour normalized rate of CH_4 formation is calculated by:

$$\text{Rate of } CH_4 \text{ evolution} = \frac{\text{Amount of } CH_4 \text{ produced (ppm)}}{\text{Amount of photocatalyst used (g)}} \quad (5.1)$$

In general three tests for each sample were done under similar experimental conditions with each time employing freshly prepared sample. The average of the three measurements (for each sample) with their standard measurement error indicated by error bar was reported as CH_4 evolution rate. The control and photocatalytic stability tests were also conducted using Pt-1.0-RT sample. The control test was performed by illuminating Pt-1.0-RT sample in an $Ar/H_2O_{(g)}$ atmosphere rather than $CO_2/H_2O_{(g)}$ mixture to investigate the origin of the carbon intrinsic to the CH_4 evolution. Pt (1.0 wt. %) was also photodeposited on all control samples and they were employed for CO_2 photoconversion experiments.

The stability test was performed by illuminating the same spent Pt-1.0-RT sample up to four cycles of CO_2 photoreduction. After each cycle of CO_2 photoreduction, the photoreactor was properly purged with Ar and vacuum (five times) followed by purging with CO_2 gas (1000 ppm in He) and vacuum (three times), then refilled finally with CO_2 gas /H_2O vapor mixture and illuminated for 1 h.

The conversion of initial units of the CH_4 evolution from $ppm \cdot g^{-1} \cdot h^{-1}$ to $\mu mol \cdot g^{-1} \cdot h^{-1}$ with the basis of 1 hour illumination and 1 g of photocatalyst is calculated as follow:

CH_4 evolution from Pt-1.0-RT = 1640.58 ppm = 1640.58 µmol / mole of gaseous mixture

Considering the ideal gas molar volume for gaseous mixture in the photoreactor, the µmol of CH_4 evolved is obtained as:

$$\frac{1640.58\ \mu mol}{1\ mol\ of\ gaseous\ mixture} \times \frac{1\ mol\ of\ gaseous\ mixture}{22.4\ L\ of\ gas} \times 0.0154\ L\ (Volume\ of\ photoreactor)$$

= 1.13 µmol of CH_4 evolved for 1 hr illumination with basis of 1 g of photocatalyst.

5.2.7 $^{13}CO_2$ isotopic experiment

To further investigate CO_2 as the main source of carbon, $^{13}CO_2$ isotope tracer experiment was done employing Pt-1.0-RT sample. $^{13}CO_2$ (^{13}C 99.0 %, 1000 ppm in He) was purchased from ALDIRCH and a mixture of $^{13}CO_2/H_2O_{(g)}$ ($^{13}CO_2$ after passing through water bubbler) is filled into argon purged photoreactor loaded with respective photocatalyst (70 mg). The photoreactor is then illuminated using 1 sun simulated sunlight by a 100 W xenon solar simulator (Oriel, LCS-100) equipped with an AM 1.5G filter. The products were analyzed using gas chromatography-mass spectrometry (GC-MS) unit (Shimadzu, GCMS-QP2010 model) equipped with Restek RT Q-Bond column (ID = 0.32 mm, length = 30m).

5.3 Results and discussion

5.3.1 Crystallographic studies

The crystallinity for pure CT, RT and Pt-x-RT samples are investigated using powder X-ray diffraction (XRD) patterns and transmission electron microscopy (TEM). The XRD patterns for all the samples is shown in Figure 5.3. It can be clearly observed that all samples exhibits significantly the main diffraction peak of anatase (A) appearing at 2θ value of 25.2° corresponding to d_{101} along with other respective minor peaks [27].

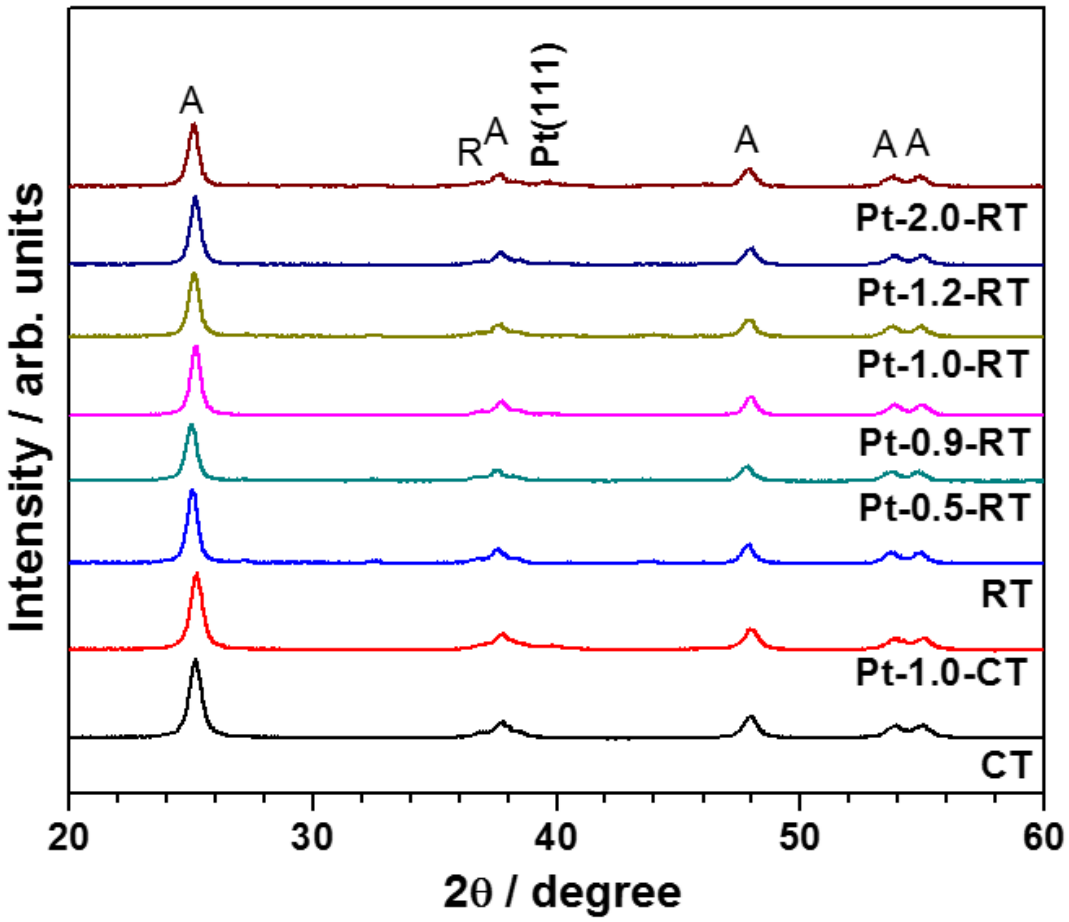

Figure 5.3 X-ray diffraction pattern for pure CT, RT and various Pt-x-RT samples (where x = 0.5, 0.9, 1.0, 1.2 and 2.0 corresponds to theoretically calculated wt. % of Pt for photodeposition). All the samples display the corresponding peaks of anatase TiO_2. Pt-2.0-RT sample also shows characteristic Pt peak with increased Pt content.

Such data ensures that no transformation or appearance of any new phase happens during the reduction process of pure CT and also during the Pt photodeposition. It is also obvious that the Pt-x-RT samples show anatase (A) phase of TiO_2 in their respective XRD patterns. However the XRD peaks corresponding to Pt are not observed in all the Pt-x-RT samples. This might be due to the high dispersion of Pt nanoparticles or due to low level of Pt concentration which is beyond the XRD detection limit. But with the increased Pt concentration for sample Pt-2.0-RT, a Pt peak corresponding to d_{111} is observed at 2θ value of 39.67° [28]. Hence, further analysis like XPS and STEM are also conducted to confirm the presence of Pt in these samples.

The high-resolution transmission electron microscopy (HR-TEM) images for CT and RT are shown in Figure 5.4. The HR-TEM images for CT and RT indicate the particle size which is in the range of 20-25 nm with an interplanar spacing of 0.35 nm corresponding to the d_{101} plane of anatase TiO_2 [27].

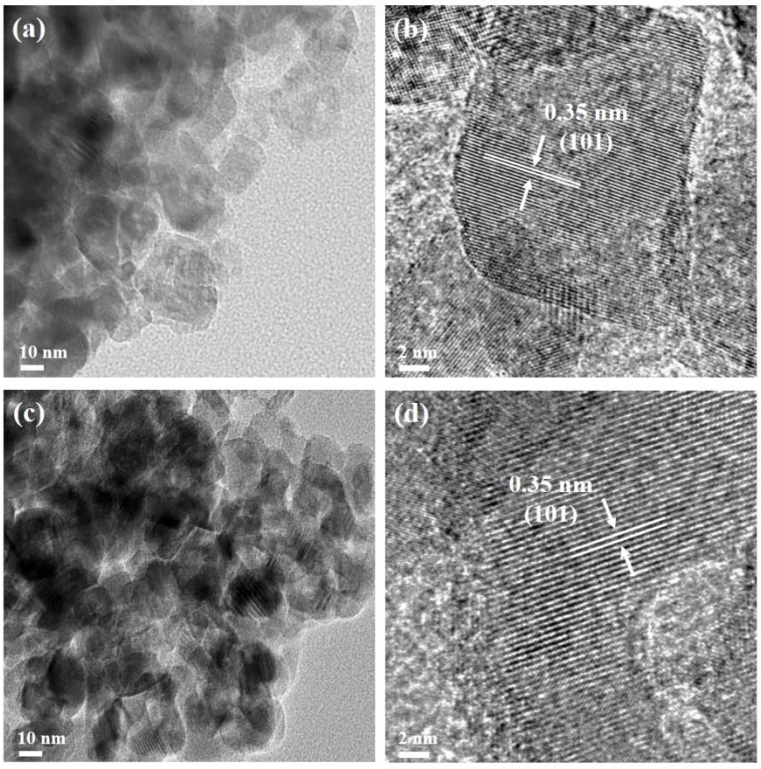

Figure 5.4 HR-TEM images of CT (a and b) and RT (c and d)**.**

To support the Pt photodeposition on the RT samples, elemental mapping for Pt-1.0-RT sample (representative sample) is conducted using scanning TEM-energy dispersive spectroscopy (STEM-EDS) and is shown in Figure 5.5. It can be seen the same sample, the XRD of which doesn't shows any Pt peak reveals a clear indication of Pt presence in it with Ti and O (Figure 5.5a-d). Thus SETM-EDS confirms the successful Pt photodeposition on the RT samples. Further the HR-TEM image of the Pt-1.0-RT sample clearly demonstrates the interplanar spacing of 0.35 nm corresponding to the d_{101} plane of anatase TiO_2 and well-defined Pt nanoparticles (~ 2-3 nm) on the surface of RT with an interplanar spacing of 0.22 nm corresponding to the d_{111} (Figure 5.5e and f) [29].

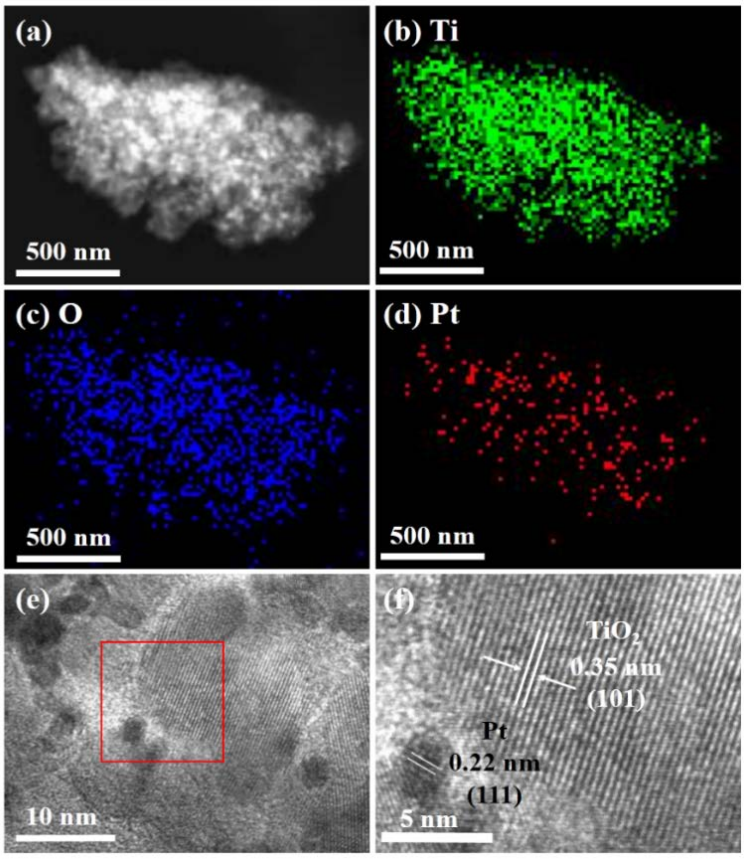

Figure 5.5 STEM image (a) and STEM elemental mapping (b-d) for Pt-1.0-RT sample showing the presence of Ti (b), O (c), and Pt (d) in the representative sample. HRTEM image (e) for Pt-1.0-RT sample with selected portion (red square) showing (f) lattice fringes corresponding to Pt (111) and TiO_2 (101).

5.3.2 Light absorbance and photoluminescence (PL) spectroscopy

The light absorption properties of all the samples are investigated by UV-Visible diffuse reflectance spectroscopy (UV-vis DRS) and charge separation properties by photoluminescence (PL) spectroscopy. The data for both UV-vis DRS and PL is shown in Figure 5.6. The UV-vis DRS spectra (Figure 5.6a) clearly exhibits a slight red shift in absorption peak with increased light absorption in the visible region (λ = 400-700 nm) for RT sample as compared to pure CT. Such extended light absorption for RT sample suggests the narrowing of the band gap due to formation of new energy states near VB top and CB bottom corresponding to oxygen vacancies or Ti^{3+} ions and surface defects produced during reduction of CT and can be expected to enhance photocatalytic performance [16–19]. The UV-vis DRS for Pt-x-RT samples exhibits a further increase in absorption mainly in the visible region. This increased visible light absorption for Pt-x-RT samples can be attributed to a well-known local surface plasmon resonance (LSPR) effect of Pt nanoparticles loaded on RT [30]. The LSPR effect is observed for all the Pt-x-RT samples increases with the increment of Pt loading (up to 1 %) but after that diluted gradually, and no significant difference is observed in the UV-vis DRS spectra for Pt-1.2-RT and Pt-2.0-RT. Therefore, the Pt loading was bound to Pt-2.0-RT sample.

To investigate the charge separation ability of the pure RT and Pt-x-RT samples, photoluminescence (PL) measurements were recorded for all the samples in the wavelength range of 350-700 nm (Figure 5.6b) and compared to the pure CT sample. It can be seen that the PL spectrum of CT displays an intense emission peak around a wavelength of 390 nm, which can be associated to the band to band transition of photogenerated charge (electron) in anatase TiO_2. However PL spectrum for RT sample exhibits a significant quenching of this peak with the appearance of another broader peak cantered at the wavelength of 620 nm associated to the surface defects of RT, an

evidence for the presence of defects on RT surface. As the spectral intensity of PL emission peak is proportional to photogenerated electron and hole (e^-/h^+) recombination rate, the higher intensity implying for higher recombination rate and decreased intensity for decreased charge recombination rate. Compared to pure CT, the decreased intensity of first peak (λ = 390 nm) for RT indicates a low e^-/h^+ band to band transitions and recombination. This can be explained probably because of the reason of Ti^{3+} states and oxygen vacancy states acting as a traps for photogenerated electrons and holes, which can increase the charge lifetime in localized states and hence favor its higher photocatalytic activity. Moreover, The PL spectra for the Pt-x-RT samples show a further decrease in intensity of the main emission peak (λ = 390 nm) as compared to initial parent RT. Such peak quenching can be associated to the effective transfer/separation of photoexcited electrons by Pt nanoparticles which acts as an electron sinks, providing an efficient pathway for electron transfer [31,32]. Amongst all the Pt-x-RT samples, the Pt-1.0-RT sample shows the lowest PL intensity, implying the optimal Pt content photodeposited on RT which might lead to the most efficient separation of photoexcited electrons.

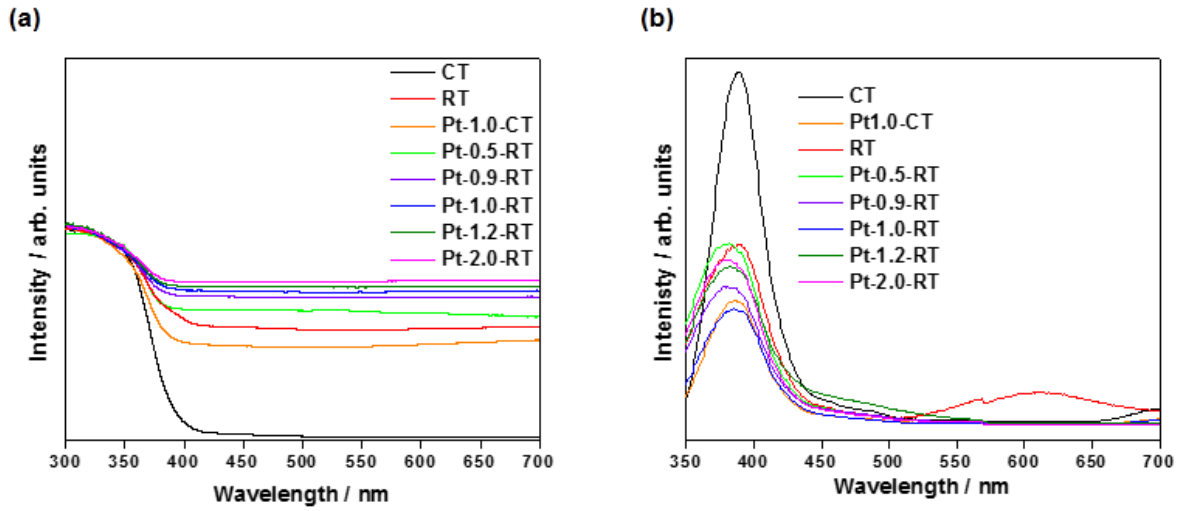

Figure 5.6 UV-vis DRS (a) and Photoluminescence (PL) spectra (b) for pure CT, RT and various Pt-x-RT samples (where x = 0.5, 0.9, 1.0, 1.2 and 2.0 corresponds to theoretically calculated wt. % of Pt for photodeposition).

5.3.3 X-ray photoelectron spectroscopy (XPS) analysis

The electronic states and surface composition of the pure CT, RT and Pt-x-RT samples are investigated by X-ray photoelectron spectroscopy (XPS) analysis tool. Figure 5.7a displays HR-XPS of Ti 2p region for CT and RT samples. It can be seen that both samples exhibit the corresponding peaks for Ti $2p_{3/2}$ and Ti $2p_{1/2}$. The pure CT exhibits the respective Ti 2p peaks located at 458.38 and 464.07 eV [33]. As compared to CT, a slight peak shifting (~ 0.13 eV) towards lower binding energy was observed for RT with peak broadening which indicates the presence of Ti^{3+} in RT [16]. Further, Ti $2p_{3/2}$ peak of RT sample shows a peak tail at lower binding energy as shown in Fig. 5.7b, with increased area (~ 6 % of $2p_{3/2}$ peak area) as compared to CT (~ 2 % of $2p_{3/2}$ peak area). Such an increase in peak tail area can be attributed to Ti^{3+} that formed in RT sample. It can also be noticed that the O 1s HR-XPS spectrum (Figure 5.7c) of CT shows the main peak located at 529.59 eV corresponding to Ti-O-Ti from lattice with the shoulder peak appearing at 530.68 eV associated to non-lattice oxygen [15,23]. The O 1s HR-XPS spectrum of RT also shows a shift of O 1s peak to lower binding energy which again supports the presence of Ti^{3+} [15]. For the RT, the peak appearing at higher binding energy (for non-lattice oxygen) have large area as compared to pure CT. This increase of area can be associated to more oxygen vacancies in RT as compared to CT.

The XPS spectrum for Pt photodeposited representative sample i.e. Pt-1.0-RT sample was also taken and is shown in Figure 5.8. It can be observed that the Pt-1.0-RT exhibits more or less similar XPS peaks for Ti 2p and O 1s as RT sample. The appearance of the Pt 4f ensures the photodeposition of Pt nanoparticles on RT surface. The Pt 4f spectrum can be fitted into four peaks with the main peaks appearing at 70.22 eV and 73.55 eV corresponding to metallic Pt(0) state [32]. The rest shoulder peaks appearing at higher binding energy values can be attributed to the Pt(II)O and Pt(IV)O_2 species respectively [32].

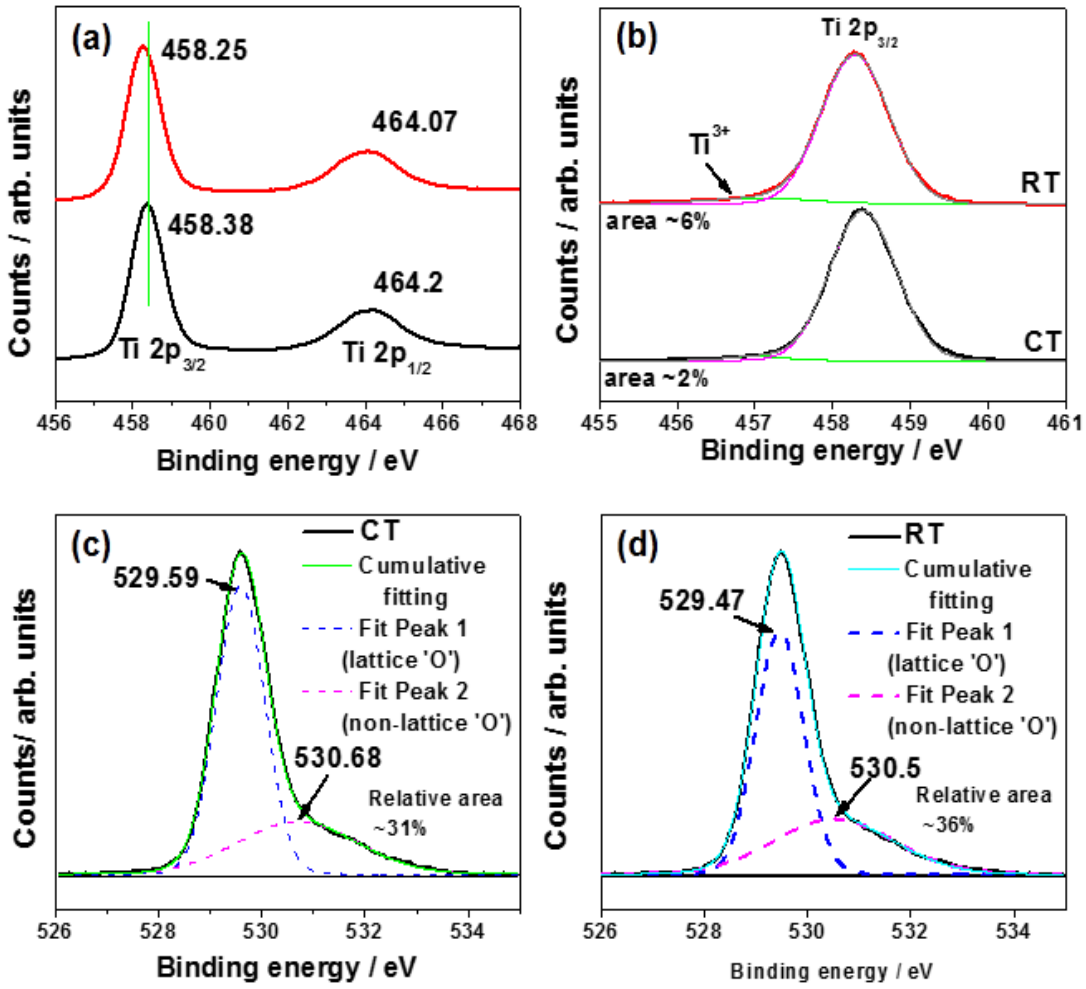

Figure 5.7 X-ray photoelectron spectroscopy (XPS) of pure CT and RT samples with regions of Ti 2p (a), enlarged view of Ti $2p_{3/2}$ region (b). Oxygen region for pure CT (c) and RT (d).

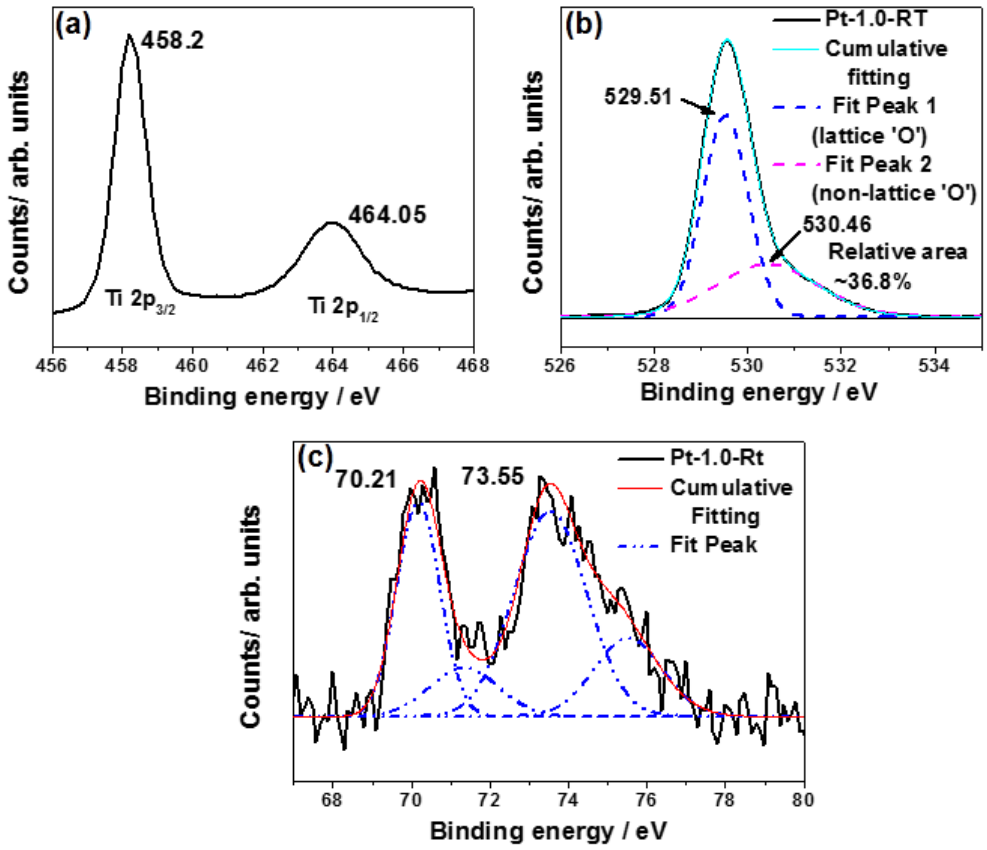

Figure 5.8 X-ray photoelectron spectroscopy (XPS) of Pt-1.0-RT sample with regions of: **(a)** Ti, **(b)** O, and **(c)** Pt.

The Pt 4f XPS spectra for all Pt-x-RT samples were also taken and presented in Figure 5.9 which confirms the successful photodeposition of Pt on all RT samples. The XPS signals are also increased with the increase of Pt content. The elemental analysis obtained using XPS is also tabulated in Table 5.1. The elemental analysis also supports firmly the increased Pt atomic ratio with increased Pt precursor concentration for photodeposition

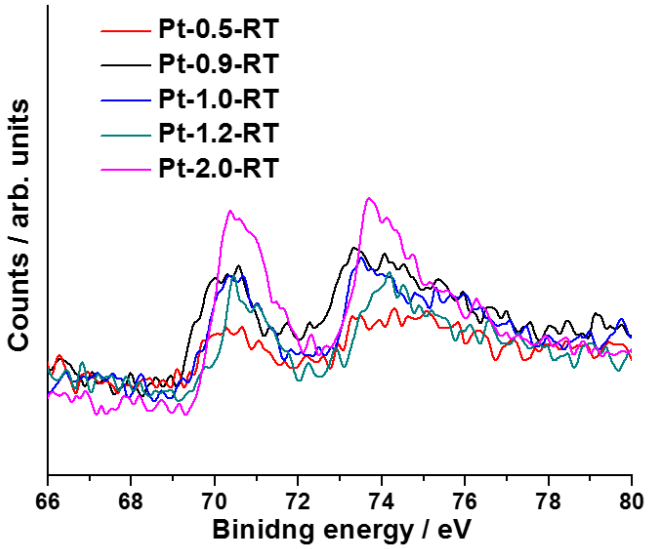

Figure 5.9 X-ray photoelectron spectroscopy (XPS) for Pt region of various Pt-x-RT samples (where x = 0.5, 0.9, 1.0, 1.2 and 2.0 corresponds to theoretically calculated wt. % of Pt for photodeposition).

Table 5.1 Pt atomic % determined by X-ray photoelectron spectroscopy (XPS) for various Pt-x-RT samples (where x = 0.5, 0.9, 1.0, 1.2 and 2.0 corresponds to theoretically calculated wt. % of Pt for photodeposition).

Sample	Pt atomic %
Pt-0.5-RT	0.05
Pt-0.9-RT	0.07
Pt-1.0-RT	0.09
Pt-1.2-RT	0.12
Pt-2.0-RT	0.27

5.3.4 Electron paramagnetic resonance (EPR) analysis

Further confirmation of the Ti^{3+} ions and oxygen vacancies and formation of RT is confirmed by electron paramagnetic resonance spectroscopy analysis. EPR spectroscopy is considered as a highly sensitive technique for the detection of unpaired electrons from paramagnetic species, thus providing firm information regarding the presence of Ti^{3+} species and oxygen vacancies. Figure 5.10 shows the EPR spectra for CT and RT. It is obvious that CT doesn't show any noticeable absorption EPR peak. However, RT sample exhibits an intense absorption EPR signal at g = 1.975 with small shoulder peak at g = 1.99, both peaks can be assigned to the Ti^{3+} ions paramagnetic center [34, 35]. Another small shoulder peak appearing around g = 2.002 can be attributed to the O^- species, possibly generated by the interaction of O_2 with surface Ti^{3+} ions [36] indicating the presence of both surface and bulk Ti^{3+}.

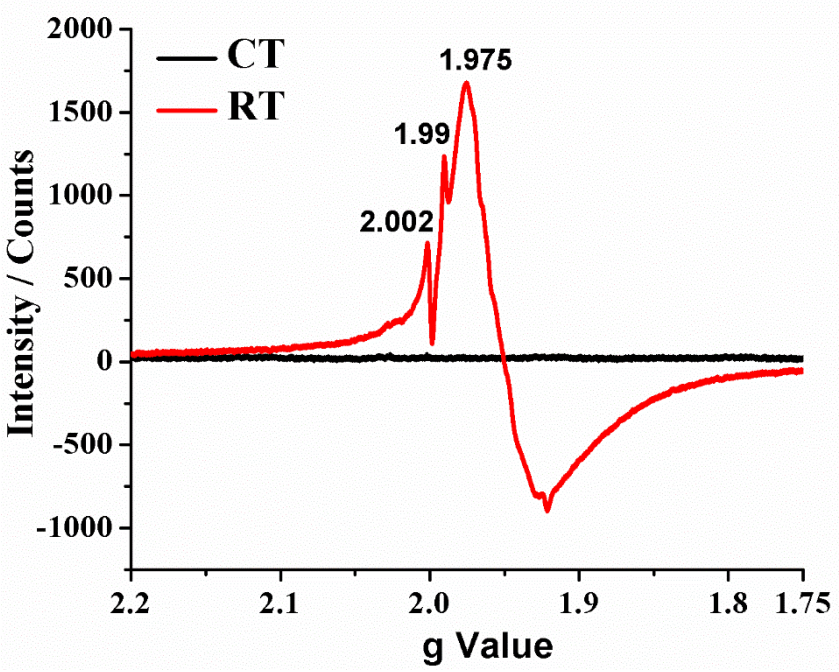

Figure 5.10 EPR spectra of CT and RT samples, recorded at -163.5 °C.

5.3.5 N_2-phyisisorption analysis

The textural properties such as Brunauer-Emmet-Teller (BET) surface area and Barrett-Joyner-Halenda (BJH) pore size distribution were determined for pure CT, RT and Pt-x-RT samples. The N_2-sorption results demonstrate the isotherms to be of type IV with H3 hysteresis loops according to the IUPAC classification [37] and are shown in Figure 5.11. The pore size within range of 2-50 nm demonstrate their mesoporous nature for all samples. BET Surface area along with pore size decreases for RT after Mg treatment from 82.3 $m^2 \cdot g^{-1}$ for parent CT to 40.6 $m^2 \cdot g^{-1}$, probably due to the heating at 650 °C during magnesiothermic reduction. Interestingly, the surface area and pore size then increases for Pt-x-RT samples after Pt loading compared to that of parent RT (as shown in Table 5.2). Anyway, all Pt-x-RT samples show more or less similar surface area and is hard to consider as a prominent factor for increased CH_4 production rate.

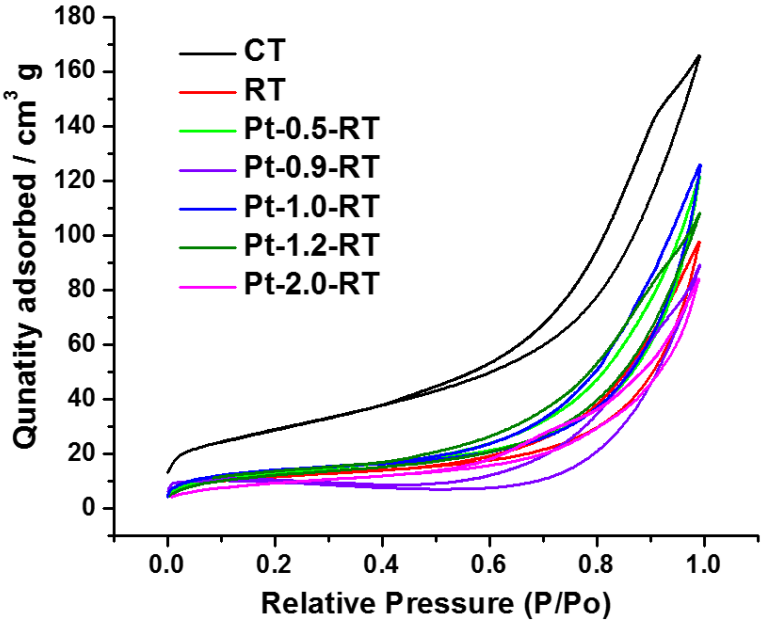

Figure 5.11 Nitrogen physiosorption isotherms of Brunauer-Emmet-Teller (BET) surface area measurement and for pure CT, RT and various Pt-x-RT samples (where x = 0.5, 0.9, 1.0, 1.2 and 2.0 corresponds to theoretically calculated wt. % of Pt for photodeposition).

Table 5.2 Brunauer-Emmet-Teller (BET) surface areas and Barrett-Joyner-Halenda (BJH) pore size for pure CT, RT and various Pt-x-RT samples (where x = 0.5, 0.9, 1.0, 1.2 and 2.0 corresponds to theoretically calculated wt. % of Pt for photodeposition).

Sample	Surface area ($m^2 \cdot g^{-1}$) [a]	Pore diameter [b] (nm)
CT	82.23	8.39
RT	40.62	13.52
Pt-0.5-RT	43.96	12.34
Pt-0.9-RT	42.93	12.84
Pt-1.0-RT	43.24	11.46
Pt-1.2-RT	45.03	10.59
Pt-2.0-RT	53.10	12.09

[a] Surface area determined by applying Brunauer-Emmett-Teller (BET) equation to a relative pressure (P/P_0) of the adsorption isotherm.

[b,] Average Pore diameter are calculated from the Barrett-Joyner-Halenda (BJH) equation using the desorption isotherm.

5.3.6 Band gap estimation

As mentioned in experimental section, section 5.2.5, the band gaps for pure CT and RT are estimated using Tauc plot [26]. The linear portions of these curves are then extrapolated to zero (y-axis) and band gap values are determined as shown in Figure 5.12a. It can be clearly seen that CT sample shows a band gap of 3.15 eV while RT sample shows a band gap of 2.85 eV with another lower band gap of 1.50 eV obtained by extrapolation of the additional slope (in the range of 2.5-3.0 eV), suggesting a new density of states (DOS) by tailing of conduction band (CB) and valence band (VB) [36]. To determine the valence band (VB) positions for both

CT and RT samples, valence band (VB) XPS for both samples are obtained and shown in Figure 5.12b-d. The VB XPS for CT show its VB top at 2.05 eV (Figure 5.12b) and for RT at 1.95 eV (Figure 5.12c) and 0.76 eV (Figure 5.12d). It is believed that the reduction of CT for synthesis of RT, narrows the band gap of CT via induction of O vacancies or Ti^{3+} ions and surface defects corresponding to downward (0.20 eV) and upward (0.10 eV) shifts of CB bottom and VB top [15,36]. Moreover, a further narrowing of band gap is observed probably because of shallows states (near CB and VB) tailing up to deep mid-gap states as predicted by band gap estimation possibly because of new DOS.

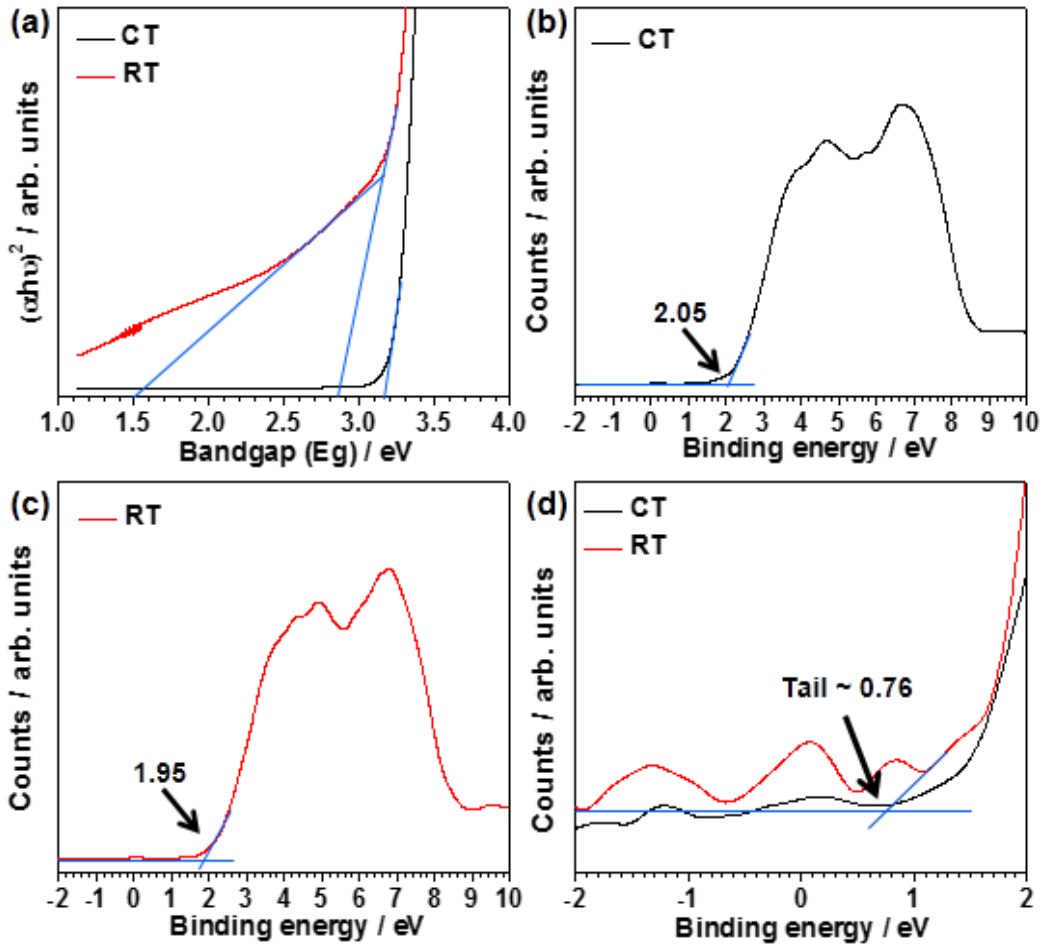

Figure 5.12 Band gap estimation using Tauc plot (a) and valence band XPS (b-d) for pure CT and RT. The RT shows a VB band tail up to 0.76 eV hence further shifting VB upward.

Based on the band gap estimation and VB XPS data, a schematic illustration for the energy level diagram (potential *vs.* NHE) showing the band gap narrowing by creation of new DOS is proposed and shown in Figure 5.13. It is evident form the proposed band gap diagram that RT sample possess a narrow band gap as compared to pure CT with well aligned CB and VB edges versus desired redox reactions and hence can appear as a more efficient photocatalyst.

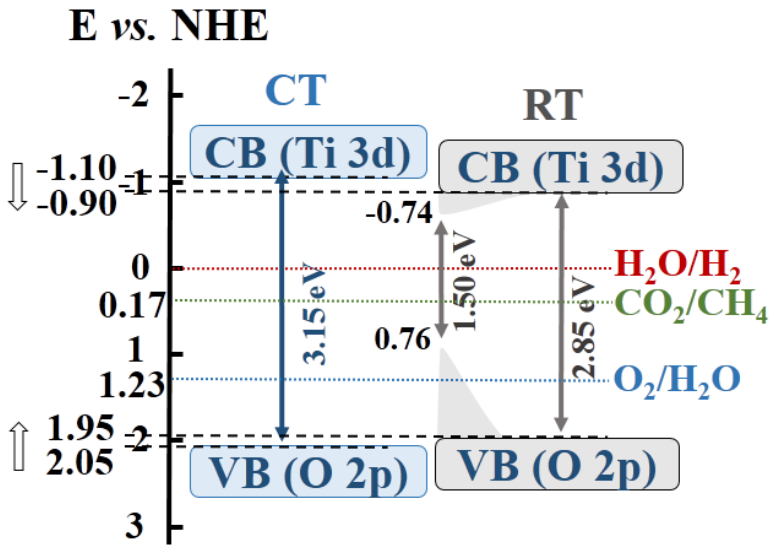

Figure 5.13 Energy level diagram for pure CT and RT samples with respective CB and VB edges positions.

5.3.7 Photocatalytic CO_2 conversion

The photocatalytic performance of the CT, RT and Pt-x-RT samples is evaluated by testing them for photocatalytic CO_2 conversion into hydrocarbons primarily methane (CH_4) with other minor products such as ethane (C_2H_6) and higher alkanes (C_xH_y). The photocatalytic experiments were carried out in a gas phase reactor setup (the details of the experimental setup are well explained in section 2.3) under simulated solar light irradiation (1 sun, AM 1.5G). The bar diagram showing photocatalytic performance of

the respective samples is shown in Figure 5.14. It can be seen that without Pt co-catalyst, pure CT produced a negligible amount of CH_4 whereas RT exhibits low yield of CH_4. However, when Pt nanoparticles are photodeposited on the respective samples as a co-catalyst, the CH_4 production rate is significantly improved. Amongst all samples, Pt-1.0-RT yields CH_4 with a rate of 1640.58 ppm·g^{-1}·h^{-1} (1.13 µmol·g^{-1}·h^{-1}), which is around 82 times higher than that of pure RT (18.31 ppm·g^{-1}·h^{-1}, 0.013 µmol·g^{-1}·h^{-1}) and >3 times higher than that of Pt-1.0-CT sample (546 ppm·g^{-1}·h^{-1}, 0.38 µmol·g^{-1}·h^{-1}). The production rate and selectivity of CH_4 are detected highest for all the samples employed for CO_2 photoreduction with H_2O vapor into hydrocarbons as compared to the other products i.e. C_2H_6 and higher alkanes. The photocatalytic hydrocarbons yield with selectivity is shown in Table 5.3 whereas the turn over number (TON) and turn over frequency (TOF) for all the tested samples are presented in Table 5.4.

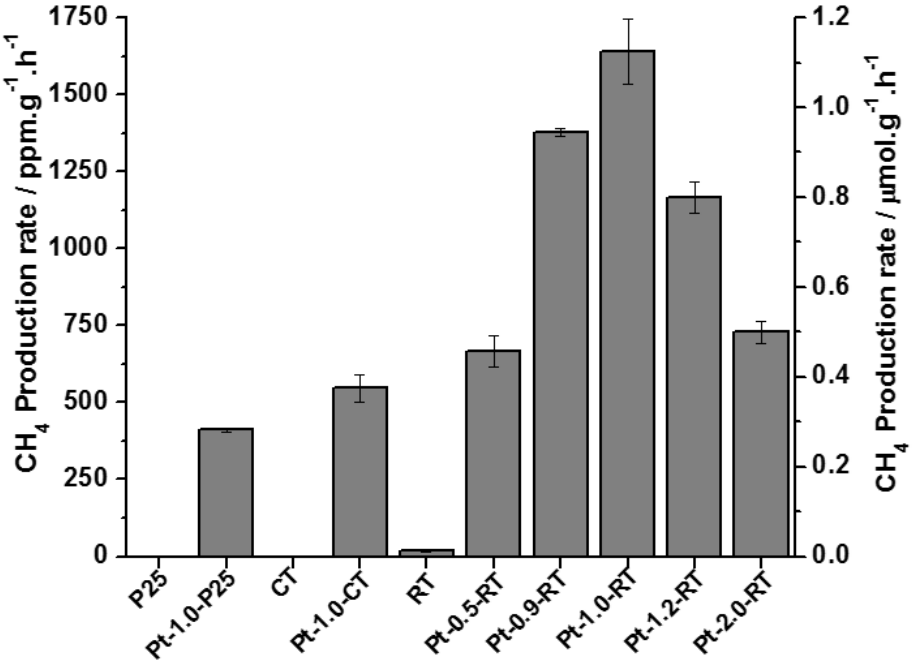

Figure 5.14 Methane production rate from P25 (Degussa), pure CT, RT and various Pt-x-RT samples (where x = 0.5, 0.9, 1.0, 1.2 and 2.0 corresponds to theoretically calculated wt. % of Pt for photodeposition).

Table 5.3 Photocatalytic hydrocarbons production rate and selectivity, by P25 (Degussa), pure CT, RT and various Pt-x-RT samples (where x = 0.5, 0.9, 1.0, 1.2 and 2.0 corresponds to theoretically calculated wt. % of Pt for photodeposition).

Sample	Hydrocarbons production rate ($ppm \cdot g^{-1} \cdot h^{-1}$)			Selectivity (%)		
	CH_4	C_2H_6	C_xH_y	CH_4	C_2H_6	C_xH_y
P25	0	0	0	0	0	0
Pt-1.0-P25	411.02	49.59	37.31	82.54	9.95	7.51
CT	0	0	0	0	0	0
Pt-1.0-CT	546.98	55.26	127.41	74.96	7.62	17.42
Pt-1.0-CT(Ar)	468.57	64.66	45.58	80.95	11.17	7.88
RT	18.31	0	0	100	0	0
Pt-0.5-RT	668.13	22.17	14.48	89.94	6.08	3.98
Pt-0.9-RT	1373.66	138.62	110.05	84.67	8.54	6.79
Pt-1.0-RT	1640.58	160.14	164.65	83.47	8.14	8.39
Pt-1.2-RT	1166.52	55.28	132.29	86.14	4.08	9.78
Pt-2.0-RT	729.52	51.38	105.32	82.32	5.79	11.89

Selectivity of the samples is calculated using:

$$\text{Selectivity (\%)} = \frac{\text{Concenteration of the desired product } (C_i)}{\text{Concentration of total products } (C_T)} \times 100$$

Table 5.4 Turnover number (TON) and turnover frequency (TOF) for Pt-1.0-CT and various Pt-x-RT samples (where x = 0.5, 0.9, 1.0, 1.2 and 2.0 corresponds to theoretically calculated wt. % of Pt for photodeposition).

Sample name	[a]TON	[b]TOF (h^{-1})
Pt-1.0-CT	0.65	0.65
Pt-0.5-RT	1.02	1.02
Pt-0.9-RT	1.25	1.25
Pt-1.0-RT	1.41	1.41
Pt1.2-RT	0.83	0.83
Pt-2.0-RT	0.41	0.41

The turnover number (TON) and turnover frequency (TOF) were calculated by using the following equations:[38,39]

$$^{a}\text{TON} = \frac{\mu\text{moles of } CH_4 \text{ produced}}{\mu\text{moles of Pt content present on the photocatalyst}}$$

$$^{b}\text{TOF} = \frac{\text{TON}}{\text{Reaction time (hours)}}$$

These results ensures a clear enhancement of photoactivity of RT compared to CT which is further improved after Pt photodeposition and can be associated mainly to (i) the improved light absorption in visible light of RT due to the lowering of band gap and reduced recombination; (ii) the more effective charge separation by Pt and also the enhanced absorption due to LSPR effect of Pt. The influence of Pt content photodeposited on RT samples is further studied for CH_4 production. It is observed that when the Pt loading is increased from 0.5 wt. % to 1.0 wt. %, the CH_4 production also increases, which can be realized as a result of the increased light absorption and enhanced charge separation. However when the Pt wt. % is increased above 1.0 wt. % i.e. 1.2 wt. % and 2.0 wt. %, the CH_4 yield is decreased instead of increasing and such photocatalytic behaviour can be ascribed to some limitation of Pt functioning as a co-catalyst. As explained above in section 5.3.4, the samples show more or less similar surface area so it is hard to consider surface area and pore size as prominent factors for increased CH_4 production rate. On the basis of reported literature [36], the combination of Pt nanoparticles dispersion and size is presumed here as a key factor influencing the photocatalytic performance of Pt-x-RT samples. The detailed investigation is done by taking HR-TEM images with Pt nanoparticles size histograms generated using ImageJ software and is shown in Figure 5.15. It can be considered herein that as the Pt loading is increased from 0.5 wt. % to 1.0 wt. %, the amount of Pt nanoparticles is also increased with good dispersion, while on further increasing the Pt loading above 1.0 wt. %, the size of Pt nanoparticles increases which might limits well dispersion and also increase the diffusion length of the separated electrons as well as recombination of the photogenerated e^-/h^+ pairs [40]. Such phenomenon is also supported by PL spectra (Figure 5.6), where Pt-1.2-RT and Pt-2.0-RT show higher emission peaks as compared to Pt-1.0-RT sample. These results suggests that high Pt loading is unfavourable for

photogenerated electron-hole pair separation with 1.0 wt. % Pt loading as an optimal loading concentration.

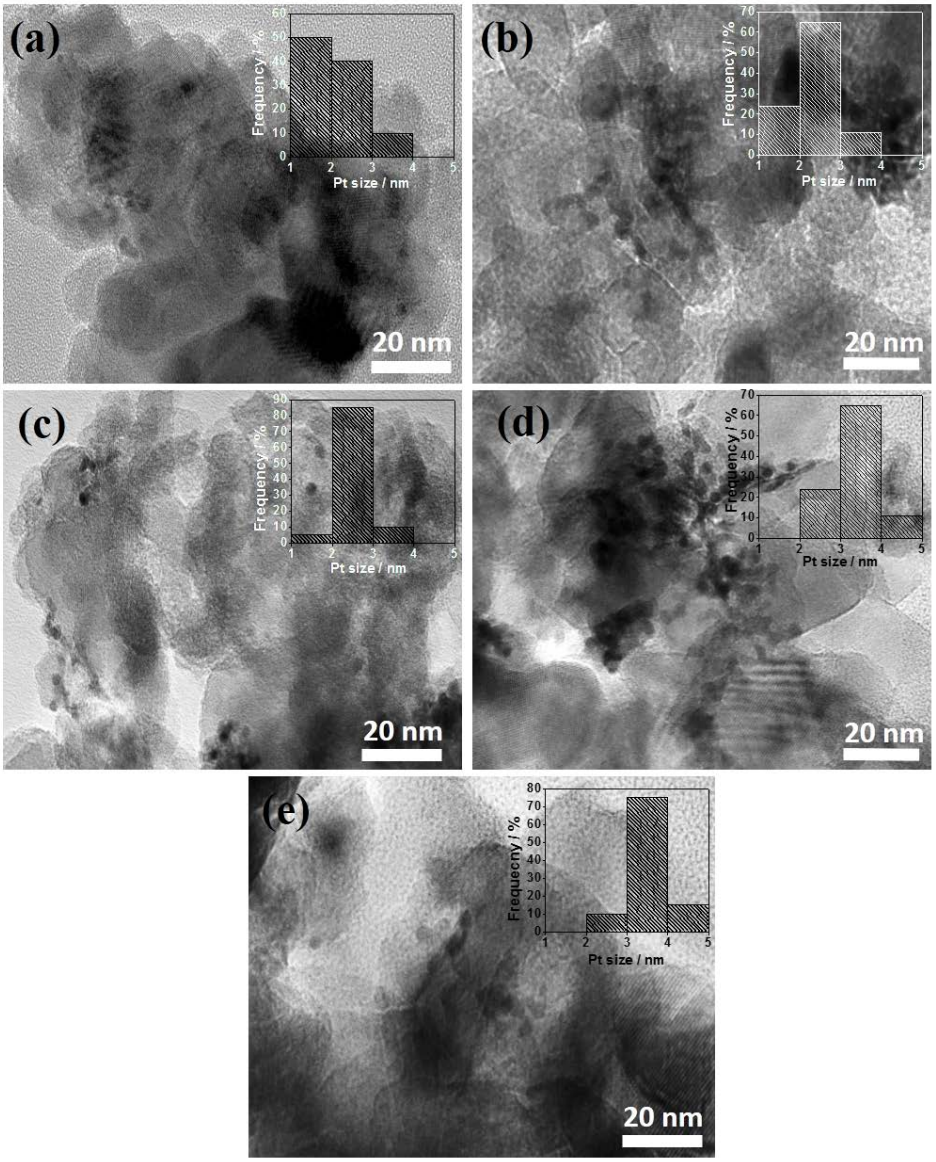

Figure 5.15 HR-TEM images for various Pt-x-RT samples with corresponding Pt particle size distribution (where x = 0.5, 0.9, 1.0, 1.2 and 2.0 corresponds to theoretically calculated wt. % of Pt for photodeposition) : (a) Pt-0.5-RT, (b) Pt-0.9-RT, (c) Pt-1.0-RT, (d) Pt-1.2-RT and (d) Pt-3.0-RT.

To investigate the original source of carbon for CH_4 formation, $^{13}CO_2$ isotopic experiment is done. Figure 5.16 shows the gas chromatogram of $^{13}CO_2$ isotopic experiment employing Pt-1.0-RT sample under similar conditions of irradiation. It can be observed that peaks at m/z = 45 and m/z = 17 are observed which are associated to the $^{13}CO_2$ and $^{13}CH_4$ respectively. Hence the GC-MS analysis shows the formation $^{13}CH_4$ from $^{13}CO_2$, confirming the CH_4 produced during the photochemical reaction is mainly originated from CO_2.

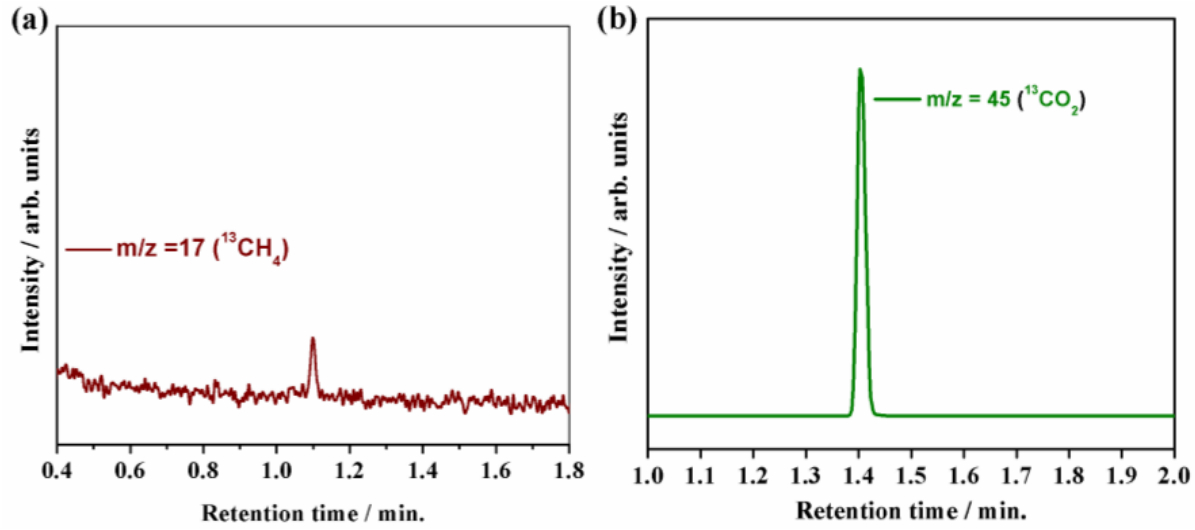

Figure 5.16 GC-MS chromatogram of (a) $^{13}CH_4$ (m/z = 17) and (b) $^{13}CO_2$ (m/z = 45) for CO_2 photoreduction products obtained over Pt-1.0-RT sample under $^{13}CO_2$ atmosphere with 3 h irradiation.

The photocatalytic stability of the Pt-1.0-RT is also investigated by cycling the same sample upto four cycles of photocatalytic CO_2 conversion and is shown in Figure 5.17. The stability test studied using Pt-1.0-RT demonstrated almost similar amount of CH_4 evolution for 1st and 2nd cycle. The activity was decreased sharply for the 3rd cycle. Then, the Pt-1.0-RT was reactivated by heating at 90 °C under vacuum for 3 h, and photocatalytic activity is almost recovered for 4th and 5th cycles of the stability test. The mechanism for photocatalyst deactivation is not exactly known. However, possible reason reported in literature is the coverage of active sites on photocatalyst by intermediate products [41–43] which can be supported by the regeneration of the photocatalytic activity after thermo-vacuum treatment.

Further, control experiment employing Pt-1.0-RT sample under similar irradiation conditions with the absence of CO_2(g) and in the presence of Ar/H_2O(g) mixture produced negligible hydrocarbon suggesting no involvement of any organic impurities on the surface of the samples for CO_2 photoreduction. For purpose of comparison and to investigate the synergetic effect of our synthesis approach for synthesis of RT, a series of control samples were synthesized by changing the synthesis condition as mentioned in experimental section 5.2.2. The CH_4 evolution rate yielded by various control samples is shown in Figure 5.18. It is obvious that the RT sample with dual reduction approach shows a superior performance as compared to all control samples. Henceforth, the solar light activated RT synthesized using magnesiothermic reduction approach herein, exhibits a superior and competitive performance with respect to control samples and previously reported reduced TiO_2 samples categorically for CO_2 photoreduction into CH_4 with gaseous (vapor) reaction setup (Table 5.5).

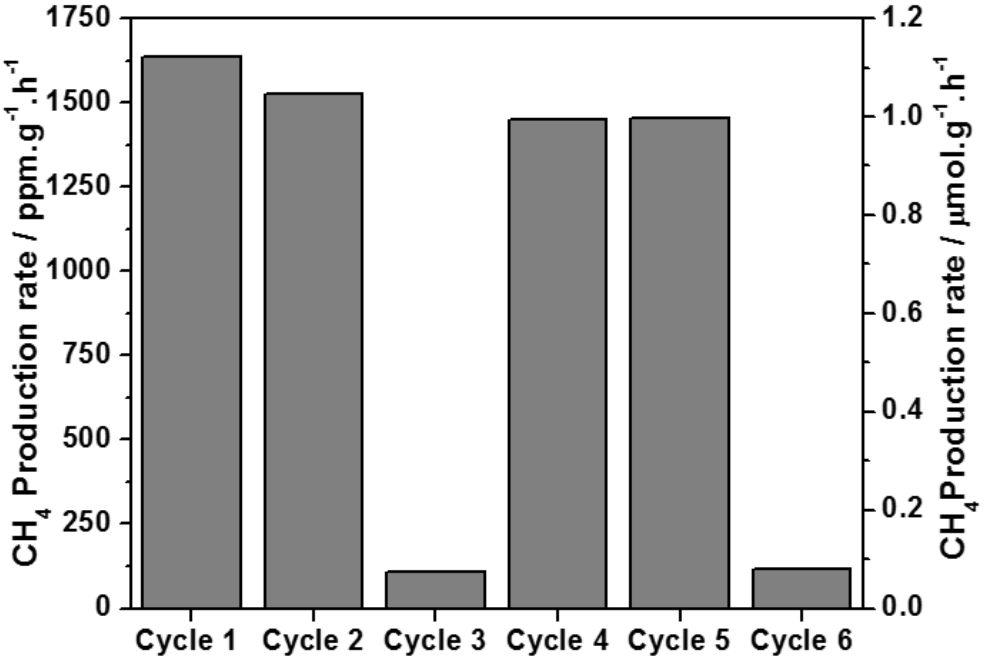

Figure 5.17 Methane production rate from Pt-1.0-RT sample for four cycles of CO_2 photoreduction test.

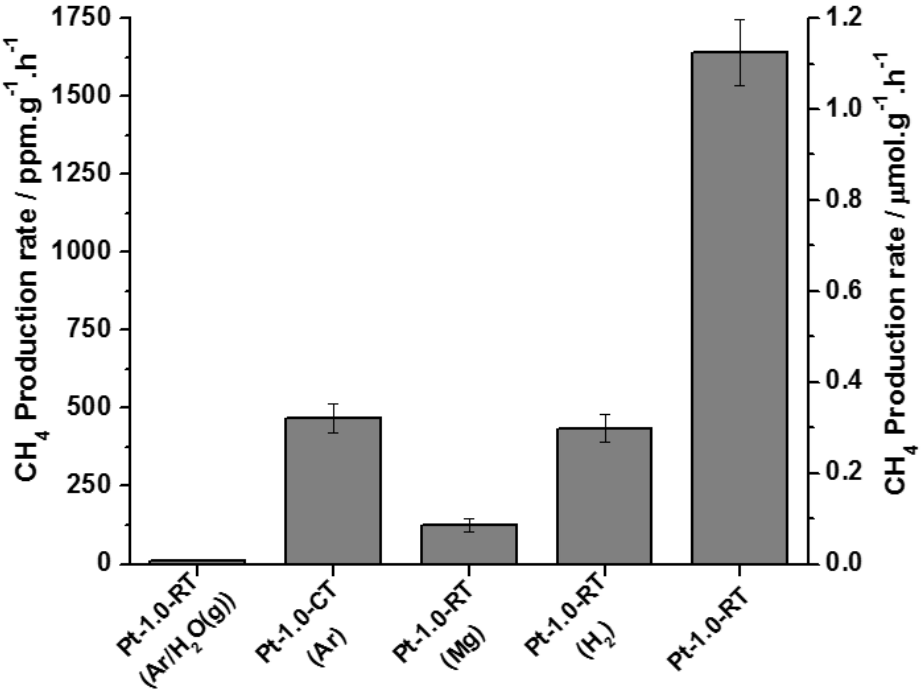

Figure 5.18 Methane production rate from different Pt (1.0 wt. %) photodeposited control samples and Pt-1.0-RT (original sample).

Table 5.5 Comparison of different reduced/hydrogenated TiO_2 photocatalysts employed for CO_2 photoreduction (gaseous/vapor reaction mode) with respective reaction conditions and products amount.

Photocatalyst	**Reaction conditions**	**Products amount**
Reduced TiO_2 Nanoparticles [44]	Photocatalyst (100 mg) illuminated using 300 W Xe lamp (AM 1.0 solar spectral irradiance).	**After 6 h illumination** CO; 1818 $ppm \cdot g^{-1}$ CH_4; 477 $ppm \cdot g^{-1}$
$Cu(I)/TiO_{2-x}$ Nanoparticles [45]	Photocatalyst (50 mg) preheated using 250 W infrared lamp followed by illumination by 150 W solar simulator (Oriel).	CO; 4.3 $\mu mol \cdot g^{-1} \cdot h^{-1}$
TiO_{2-x}{001}-{101} Nanocrystals [46]	Photocatalyst (40 mg) preheated using a 250 W infrared lamp to a temperature of 150 °C. Illumination done using: <u>UV-Vis light:</u> 100 W mercury vapor lamp <u>Visible light:</u> 450 W Xe lamp with UV filter	**After 5 h illumination** <u>UV-Vis light:</u> CO; 54.5 $\mu mol \cdot g^{-1}$ <u>Visible light:</u> CO; 26.5 $\mu mol \cdot g^{-1}$
H_2-pretreated Cu/TiO_2 Nanoparticles [47]	Photocatalyst (50 mg) preheated with H_2 using a 250 W infrared lamp to a temperature of 220 °C. Illuminated using 150 W solar simulator (Oriel).	**After 6.5 h illumination** CO; 25 $\mu mol \cdot g^{-1}$ CH_4; 4.4 $\mu mol \cdot g^{-1}$
Slightly hydrogenated TiO_2 Nanoparticles by H_2 plasma treatment [20]	Photocatalyst (90 mg) loaded onto photoreactor. Illuminated using 550 W Xe-lamp with AM 1.5G filter for **3 h**.	CO; 7.22 $nmol \cdot g^{-1} \cdot h^{-1}$ CH_4; 4.67 $nmol \cdot g^{-1} \cdot h^{-1}$
Current work Pt Photodeposited magnesiothermally reduced TiO_2	Photocatalyst (70 mg) loaded onto photoreactor. No pretreatment or preheating done and illuminated using 100 W Xe solar simulator (Oriel, LCS-100 with AM1.5G filter)	<u>Pt1.0 wt. % RT sample</u>: CH_4; 1.13 $\mu mol \cdot g^{-1} \cdot h^{-1}$ C_2H_6;0.13 $\mu mol \cdot g^{-1} \cdot h^{-1}$ C_xH_y;0.11 $\mu mol \cdot g^{-1} \cdot h^{-1}$ <u>Bare RT sample:</u> CH_4;12.59 $nmol \cdot g^{-1} \cdot h^{-1}$

5.3.8 CO_2 conversion mechanism

A schematic illustration for the energy level diagram (potential *vs.* NHE) and CO_2 photoreduction is proposed using reported literature and the experimental information obtained from the band gap estimation via UV-vis DRS measurement and VB XPS data. The energy level diagram displaying the narrowing of the band gap for RT, relative positions of CB and VB for CT and RT, and redox potentials for CO_2/CH_4 and H_2O/O_2 is portrayed in Figure 5.19a. It can be seen that after magnesiothermic reduction, the RT sample offers its CB minimum at -0.90 eV with CB tail up to -0.74 eV while the VB maximum at 1.95 eV with VB tail up to 0.76 eV. Even after reduction of pure CT, the downward shifted CB bottom lies above the redox potential of CO_2/CH_4 (0.17 eV) whereas the VB top lies above the H_2O/O_2 redox potential (1.23 eV) [48] and thus can proceed the CO_2 photoreduction reactions in an efficient manner. The possible reactions happening on the RT surface under simulated solar light illumination are portrayed in Figure 5.19b. When simulated solar light is illuminated on the Pt-x-RT sample, the photogenerated electron-hole pairs are generated via band to band and sub-band gap excitations and are efficiently extracted by Pt nanoparticles. With the consideration of proton assisted multi-electron process via carbene pathway for CO_2 photoreduction [3,49], these photoexcited electrons can react with surface adsorbed CO_2 in the presence of protons (H^+, provided by water oxidation) to evolve CH_4 as a primary product with enhanced yield. On the other hand, the holes generated in the valence band can be filled by water oxidation reaction which can in turn produce O_2 and protons (H^+). The possible reactions involved in the CO_2 photoreduction to CH_4 can be summarized by following equations:

$$\text{Pt-RT} + h\nu\ (\text{sunlight}) \rightarrow \text{Pt-RT}(e^-_{CB}) + \text{Pt-RT}(h^+_{VB}) \quad (5.2)$$

$$\text{Pt-RT}(8h^+_{VB}) + 4H_2O \rightarrow 8H^+ + 2O_2 \quad (5.3)$$

$$CO_2 + 8H^+ + \text{Pt-RT}(8e^-_{CB}) \rightarrow CH_4 + 2H_2O \quad (5.4)$$

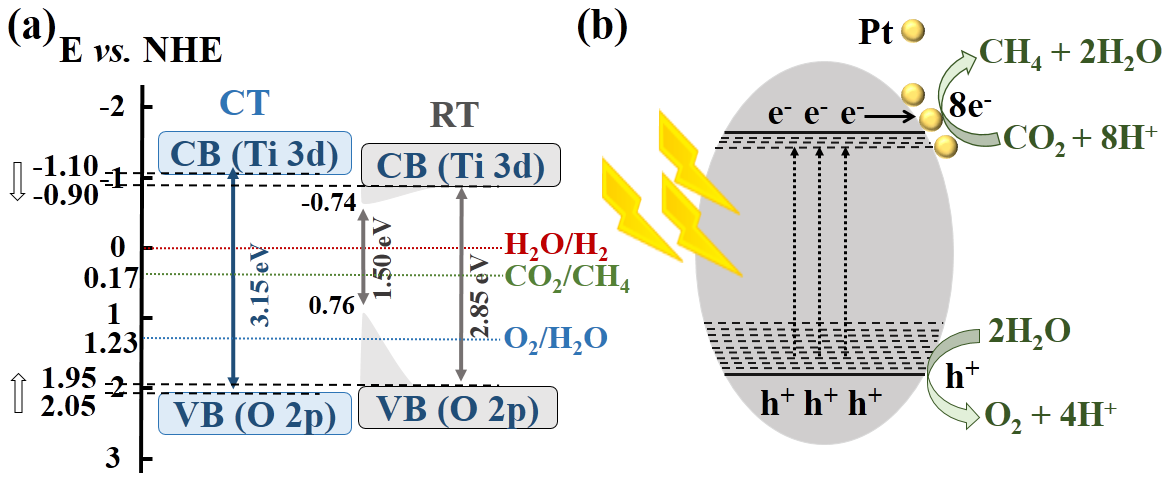

Figure 5.19 Energy level diagram (potential *vs.* NHE) (a) and proposed mechanism for CO_2 photoreduction (b).

5.4 Conclusions

Highly efficient reduced TiO_2 (RT) was successfully prepared by a newly developed two-step method termed as magnesiothermic reduction in 5% H_2/Ar gaseous environment. Pt nanoparticles were photodeposited on RT acting as a co-catalyst. A variety of Pt photodeposited RT samples were prepared by varying the amount of Pt precursor and their performance was evaluated by employing in photocatalytic CO_2 conversion to hydrocarbon fuels under simulated solar light irradiation. Pt (1.0 wt. %) photodeposited RT was found to the optimum sample with CH_4 yield three times higher than pure commercial nano TiO_2 and four times higher than P25 with similar loading of Pt co-catalyst. Such results revealed that the photocatalytic activity was dependent on the Pt nanoparticle size. The synergetic effect of newly developed synthesis approach was investigated by preparing different control samples under Mg reduction with Ar gas environment, pure Ar gas environment and 5% H_2/Ar gas environment with similar conditions of annealing. It was observed that the RT prepared by magnesiothermic reduction method yielded maximum CH_4 comparatively, suggesting optimal

reduction of CT resulting with favorable band edges position leading to enhanced photocatalytic CO_2 conversion. Overall improvement in the photocatalytic performance can be attributed to (i) effective separation of photogenerated charges by Pt nanoparticles with controlled size and a (ii) favorable combination of various factors like Ti^{3+} and oxygen vacancies/surface defects driving toward (iii) optimal band gap with well-aligned band position during the synthesis of reduced TiO_2

5.5 References

[1] A. Dhakshinamoorthy, S. Navalon, A. Corma, H. Garcia, Photocatalytic CO_2 reduction by TiO_2 and related titanium containing solids, Energy Environ. Sci. 5 (2012) 9217. doi:10.1039/c2ee21948d.

[2] S. Xie, Q. Zhang, G. Liu, Y. Wang, Photoctalytic and photoelectrocatalytic reduction of CO_2 using heterogeneous catalysts with controlled nanostructures, Chem. Commun. 52 (2015) 35–59. doi:10.1039/C5CC07613G.

[3] J.L. White, M.F. Baruch, J.E. Pander, Y. Hu, I.C. Fortmeyer, J.E. Park, T. Zhang, K. Liao, J. Gu, Y. Yan, T.W. Shaw, E. Abelev, A.B. Bocarsly, Light-Driven Heterogeneous Reduction of Carbon Dioxide: Photocatalysts and Photoelectrodes, Chem. Rev. 115 (2015) 12888–12935. doi:10.1021/acs.chemrev.5b00370.

[4] M.D. Hernández-Alonso, F. Fresno, S. Suárez, J.M. Coronado, Development of alternative photocatalysts to TiO_2: Challenges and opportunities, Energy Environ. Sci. 2 (2009) 1231. doi:10.1039/b907933e.

[5] S.K. Parayil, A. Razzaq, S.M. Park, H.R. Kim, C.A. Grimes, S. Il In, Photocatalytic conversion of CO_2 to hydrocarbon fuel using carbon and nitrogen co-doped sodium titanate nanotubes, Appl. Catal. A Gen. 498 (2015) 205–213. doi:10.1016/j.apcata.2015.03.044.

[6] O.K. Varghese, M. Paulose, T.J. LaTempa, C.A. Grimes, High-Rate Solar Photocatalytic Conversion of CO_2 and Water Vapor to Hydrocarbon Fuels, Nano Lett. 9 (2009) 731–737. http://pubs.acs.org/doi/abs/10.1021/nl803258p.

[7] S. Il In, D.D. Vaughn, R.E. Schaak, Hybrid CuO-$TiO_{2-x}N_x$ hollow nanocubes for photocatalytic conversion of CO_2 into methane under solar irradiation, Angew. Chemie - Int. Ed. 51 (2012) 3915–3918. doi:10.1002/anie.201108936.

[8] K. Kim, A. Razzaq, S. Sorcar, Y. Park, C.A. Grimes, S.-I. In, Hybrid mesoporous Cu_2

$ZnSnS_4$ (CZTS)–TiO_2 photocatalyst for efficient photocatalytic conversion of CO_2 into CH_4 under solar irradiation, RSC Adv. 6 (2016) 38964–38971. doi:10.1039/C6RA02763F.

[9] D. Chatterjee, A. Mahata, Demineralization of organic pollutants on the dye modified TiO_2 semiconductor particulate system using visible light, Appl. Catal. B Environ. 33 (2001) 119–125. doi:10.1016/S0926-3373(01)00170-9.

[10] S.C. Roy, O.K. Varghese, M. Paulose, C.A. Grimes, Toward Solar Fuels : Photocatalytic Hydrocarbons, ACS Nano. 4 (2010) 1259–1278. doi:10.1021/nn9015423.

[11] X. Chen, L. Liu, F. Huang, Black titanium dioxide (TiO_2) nanomaterials., Chem. Soc. Rev. 44 (2015) 1861–1885. doi:10.1039/c4cs00330f.

[12] H. Xu, S. Ouyang, L. Liu, P. Reunchan, N. Umezawa, J. Ye, Recent advances in TiO_2 -based photocatalysis, J. Mater. Chem. A. 2 (2014) 12642. doi:10.1039/C4TA00941J.

[13] X. Pan, M.-Q. Yang, X. Fu, N. Zhang, Y.-J. Xu, Defective TiO_2 with oxygen vacancies: synthesis, properties and photocatalytic applications., Nanoscale. 5 (2013) 3601–14. doi:10.1039/c3nr00476g.

[14] T. Bak, J. Nowotny, M.K. Nowotny, L.R. Sheppard, Defect Chemistry of Titanium Dioxide. Application of Defect Engineering In Processing of TiO_2-Based Photocatalysts. J. Phys. Chem. C. 112 (2008) 5275-5300. doi:10.1179/1743676111Y.0000000027.

[15] X. Chen, L. Liu, P.Y. Yu, S.S. Mao, Increasing solar absorption for photocatalysis with black hydrogenated titanium dioxide nanocrystals., Science. 331 (2011) 746–50. doi:10.1126/science.1200448.

[16] S. Hoang, S.P. Berglund, N.T. Hahn, A.J. Bard, C.B. Mullins, Enhancing visible light photo-oxidation of water with TiO_2 nanowire arrays via cotreatment with H_2 and NH_3: synergistic effects between Ti^{3+} and N., J. Am. Chem. Soc. 134 (2012) 3659–62.

doi:10.1021/ja211369s.

[17] A. Danon, K. Bhattacharyya, B. Vijayan, J. Lu, D. Sauter, K. Gray, P. Stair, E. Weitz, Effect of Reactor Materials on Properties of Titanium Oxide Nanotubes, ACS Catal. 2 (2012) 45–49. doi:10.1021/cs200392m.

[18] H. Lu, B. Zhao, R. Pan, J. Yao, J. Qiu, L. Luo, Y. Liu, Safe and facile hydrogenation of commercial Degussa P25 at room temperature with enhanced photocatalytic activity, RSC Adv. 4 (2014) 1128–1132. doi:10.1039/C3RA44493G.

[19] X. Yu, B. Kim, Y.K. Kim, Highly enhanced photoactivity of anatase TiO_2 nanocrystals by controlled hydrogenation-induced surface defects, ACS Catal. 3 (2013) 2479–2486. doi:10.1021/cs4005776.

[20] Y. Yan, M. Han, A. Konkin, T. Koppe, D. Wang, T. Andreu, G. Chen, U. Vetter, J.R. Morante, P. Schaaf, Slightly hydrogenated TiO_2 with enhanced photocatalytic performance, J. Mater. Chem. A. 2 (2014) 12708. doi:10.1039/C4TA02192D.

[21] K. Sasan, F. Zuo, Y. Wang, P. Feng, Self-doped Ti^{3+}–TiO_2 as a photocatalyst for the reduction of CO_2 into a hydrocarbon fuel under visible light irradiation, Nanoscale. 7 (2015) 13369–13372. doi:10.1039/C5NR02974K.

[22] F. Habashi, Handbook of Extractive Metallurgy, Wiley-VCH, Wienheim, Germany, 1197.

[23] A. Sinhamahapatra, J.-P. Jeon, J.-S. Yu, A new approach to prepare highly active and stable black titania for visible light-assisted hydrogen production, Energy Environ. Sci. 8 (2015) 3539–3544. doi:10.1039/C5EE02443A.

[24] A. Sinhamahapatra, J.-P. Jeon, J. Kang, B. Han, J.-S. Yu, Oxygen-Deficient Zirconia (ZrO_{2-x}): A New Material for Solar Light Absorption, Sci. Rep. 6 (2016) 27218. doi:10.1038/srep27218.

[25] Z. Jiang, Z. Zhang, W. Shangguan, M.A. Isaacs, L.J. Durndell, C.M.A. Parlett, A.F. Lee,

Photodeposition as a facile route to tunable Pt photocatalysts for hydrogen production: on the role of methanol, Catal. Sci. Technol. 6 (2016) 81–88. doi:10.1039/C5CY01364J.

[26] J. Tauc, R. Grigorovici, A. Vancu, Optical Properties and Electronic Structure of Amorphous Germanium, Phys. Status Solidi. 15 (1966) 627–637. doi:10.1002/pssb.19660150224.

[27] P.A. Sedach, T.J. Gordon, S.Y. Sayed, T. Fürstenhaupt, R. Sui, T. Baumgartner, C.P. Berlinguette, Solution growth of anatase TiO_2 nanowires from transparent conducting glass substrates, J. Mater. Chem. 20 (2010) 5063. doi:10.1039/c0jm00266f.

[28] D. Wang, H.L. Xin, R. Hovden, H. Wang, Y. Yu, D. a. Muller, F.J. DiSalvo, H.D. Abruña, Structurally ordered intermetallic platinum–cobalt core–shell nanoparticles with enhanced activity and stability as oxygen reduction electrocatalysts, Nat. Mater. 12 (2012) 81–87. doi:10.1038/nmat3458.

[29] B. Zhang, D. Wang, Y. Hou, S. Yang, X.H. Yang, J.H. Zhong, J. Liu, H.F. Wang, P. Hu, H.J. Zhao, H.G. Yang, Facet-dependent catalytic activity of platinum nanocrystals for triiodide reduction in dye-sensitized solar cells., Sci. Rep. 3 (2013) 1836 1–7. doi:10.1038/srep01836.

[30] D. Manchon, J. Lermé, T. Zhang, A. Mosset, C. Jamois, C. Bonnet, J.-M. Rye, A. Belarouci, M. Broyer, M. Pellarin, E. Cottancin, Plasmonic coupling with most of the transition metals: a new family of broad band and near infrared nanoantennas, Nanoscale. 7 (2015) 1181–1192. doi:10.1039/C4NR05383D.

[31] Q. Gu, J. Long, H. Zhuang, C. Zhang, Y. Zhou, X. Wang, Ternary $Pt/SnO_x/TiO_2$ photocatalysts for hydrogen production: consequence of Pt sites for synergy of dual co-catalysts, Phys. Chem. Chem. Phys. 16 (2014) 12521–12534. doi:10.1039/c4cp01496k.

[32] J.S. Jang, S.H. Choi, H.G. Kim, J.S. Lee, Location and State of Pt in Platinized CdS/TiO_2 Photocatalysts for Hydrogen Production from Water under Visible Light, J. Phys. Chem.

C. 112 (2008) 17200–17205.

[33] M.C. Biesinger, B.P. Payne, A.P. Grosvenor, L.W.M. Lau, A.R. Gerson, R.S.C. Smart, Resolving surface chemical states in XPS analysis of first row transition metals, oxides and hydroxides: Sc, Ti, V, Cu and Zn, Appl. Surf. Sci. 257 (2010) 887–898. doi:10.1016/j.apsusc.2010.10.051.

[34] C.P. Kumar, N.O. Gopal, T.C. Wang, M.-S. wong, S.C. Ke, EPR investigation of TiO_2 nanoparticles with Temperature-Dependent Properties., J. Phys. Chem. B 110 (2006) 5223–5229. doi: 10.1021/jp057053t.

[35] F. Zuo, L. Wang, T. Wu, Z. Zhang, D. Borchardt, P. feng, Self-Doped Ti^{3+} Enhanced Photocatalyst for Hydrogen Production under Visible light., J. Am. Chem. Soc. 132 (2010) 11856–11857. doi: 10.1021/ja103843d.

[36] A. Naldoni, M. Allieta, S. Santangelo, M. Marelli, F. Fabbri, S. Cappelli, C.L. Bianchi, R. Psaro, V. Dal Santo, Effect of nature and location of defects on bandgap narrowing in black TiO_2 nanoparticles, J. Am. Chem. Soc. 134 (2012) 7600–7603. doi:10.1021/ja3012676.

[37] M. Kruk, M. Jaroniec, Gas Adsorption Characterization of Ordered Organic - Inorganic Nanocomposite Materials, Chem. Mater. 13 (2001) 3169–3183. doi:10.1021/cm0101069.

[38] A.J. Morris, G.J. Meyer, E. Fujita, Molecular Approaches to the Photocatalytic Reduction of Carbon Dioxide for Solar Fuels, Acc. Chem. Res. 42 (2009) 1983–1994. doi:10.1021/ar9001679.

[39] Z. Sun, H. Zheng, J. Li, P. Du, Extraordinarily efficient photocatalytic hydrogen evolution in water using semiconductor nanorods integrated with crystalline Ni_2P cocatalysts, Energy Environ. Sci. 8 (2015) 2668–2676. doi:10.1039/C5EE01310K.

[40] W.N. Wang, W.J. An, B. Ramalingam, S. Mukherjee, D.M. Niedzwiedzki, S.

Gangopadhyay, P. Biswas, Size and Structure Matter: Enhanced CO_2 Photoreduction Efficiency by Size-Resolved ultrafine Pt Nanoparticles on TiO_2 Single Crystals, J Am Chem Soc. 134 (2012) 11276–11281. doi:10.1021/ja304075b.

[41] F. Saladin, I. Alxneit, Temperature dependence of the photochemical reduction of CO_2 in the presence of H_2O at the solid/gas interface of TiO_2, J. Chem. Soc. Faraday Trans. 93 (1997) 4159–4163. doi:10.1039/a704801g.

[42] Y. Ji, Y. Luo, Theoretical Study on the Mechanism of Photoreduction of CO_2 to CH_4 on the Anatase TiO_2(101) Surface, ACS Catal. 6 (2016) 2018–2025. doi:10.1021/acscatal.5b02694.

[43] M. Li, L. Zhang, M. Wu, Y. Du, X. Fan, M. Wang, L. Zhang, Q. Kong, J. Shi, Mesostructured CeO_2/g-C_3N_4 nanocomposites: Remarkably enhanced photocatalytic activity for CO_2 reduction by mutual component activations, Nano Energy. 19 (2016) 145–155. doi:10.1016/j.nanoen.2015.11.010.

[44] H. Yaghoubi, Z. Li, Y. Chen, H.T. Ngo, V.R. Bhethanabotla, B. Joseph, S. Ma, R. Schlaf, A. Takshi, Toward a Visible Light-Driven Photocatalyst : The Effect of Midgap-States-Induced Energy Gap of Undoped TiO_2 Nanoparticles, ACS Catal. 5 (2015) 327–335. doi:10.1021/cs501539q.

[45] L. Liu, C. Zhao, Y. Li, Spontaneous Dissociation of CO_2 to CO on Defective Surface of Cu(I)/TiO_{2-x} Nanoparticles at Room Temperature, J. Phys. Chem. C. 116 (2012) 7904–7912. doi:10.1021/jp300932b.

[46] L. Liu, Y. Jiang, H. Zhao, J. Chen, J. Cheng, K. Yang, Y. Li, Engineering Coexposed {001} and {101} Facets in Oxygen-Deficient TiO_2 Nanocrystals for Enhanced CO_2 Photoreduction under Visible Light, ACS Catal. 6 (2016) 1097–1108. doi:10.1021/acscatal.5b02098.

[47] L. Liu, F. Gao, H. Zhao, Y. Li, Tailoring Cu valence and oxygen vacancy in Cu/TiO_2

catalysts for enhanced CO_2 photoreduction efficiency, Appl. Catal. B Environ. 134-135 (2013) 349–358. doi:10.1016/j.apcatb.2013.01.040.

[48] X. Chang, T. Wang, J. Gong, CO_2 Photo-reduction: Insights into CO_2 Activation and Reaction on Surfaces of Photocatalysts, Energy Environ. Sci. (2016) doi:10.1039/C6EE00383D.

Chapter 6. Concluding remarks

The primary goal of the research done during the Ph.D. research span was to develop efficient photocatalytic materials with the key focus of their utility in photocatalytic CO_2 conversion to hydrocarbon fuels. On the basis of detailed literature survey and superb intrinsic properties, titanium dioxide or titania (TiO_2) was selected as a base semiconductor material which act as a key photocatalyst and three different TiO_2 based photocatalysts were developed. The key strategies adopted for the photocatalyst performance enhancement of TiO_2 based photocatalysts include: (i) doping of TiO_2 nanostructure i.e. nanotubes with foreign elements such as carbon and nitrogen, (ii) coupling of TiO_2 nanotube arrays with rGO contents to get a novel heterostructured photocatalyst with improved photocatalytic performance and (iii) synthesis of reduced TiO_2 with a newly developed reduction approach and investigating the Pt nanoparticles deposition effect acting as co-catalysts on reduced TiO_2 photocatalysts. Hence the experimental works can be categorized into two main types, the first type exhibits a noble metal free approaches for improved photocatalytic performance while the second type demonstrates a high performance Pt loaded reduced TiO_2 photocatalyst by a newly developed approach.

In the first experimental approach, carbon and nitrogen co-doped sodium titanate nanotubes (C,N-TNT) samples were successfully prepared by simply designed two-step process of alkaline hydrothermal treatment of anatase TiO_2 powder followed by calcination process with urea content. The alkaline hydrothermal method yields sodium titanate nanotubes (TNT) with well-developed tubular morphology which was then mixed with varied contents of urea and calcined under air flow yielding C,N-TNT. The doping was confirmed using XRD, Raman spectroscopy, UV-vis DRS and XPS analysis. The surface morphology and textural properties were investigated using SEM/TEM images and N_2 physisoprtion analysis respectively. The photocatalytic performance of the various C,N-TNT samples prepared with varied content of

urea were investigated for photocatalytic conversion of CO_2 into CH_4 without any use of noble metals as a co-catalyst. The photocatalytic conversion of CO_2 employing C,N-TNT samples exhibited higher CH_4 evolution rate as compared to bare TNT. The improved rates of CH_4 formation are mainly attributed to enhanced light absorption, formation of the anatase phase, significant surface area, and favorable competition between the dual role Na^+ ions play in (desired) CO_2 adsorption and (unwanted) charge recombination. It can be concluded that, the light absorption enhancement is due to the isolated N and C 2p states above the valence band maximum of the TNT. The Na^+ ions in the C,N-TNT can also serve to promote CO_2 adsorption as reported earlier while also can act as electron-hole recombination centers. The amount of C,N-doping affects sample crystallinity, surface area, and band gap energy, all of which, in turn, influence overall photocatalytic performance.

The second research work presented a unique experimental design which resulted in a novel nanostructured noble metal-free material architecture, TiO_2 nanotube (TNT) arrays covered with reduced graphene oxide (rGO) platelets containing embedded TiO_2 nanoparticles. The GO was successfully electrophoretically deposited and reduced simultaneously on cleaned Ti foil. This rGO-Ti foil was then electrochemically anodized by a conventional electrochemical approach using fluoride based electrolyte to give a nanostructured TNT arrays covered with rGO and TiO_2 nanoparticles. Powerful investigative tools such as Raman spectroscopy and XPS confirmed the reduction and presence of graphene content onto rGO-TNTNP surface. The rGO-TNTNP showed an increased light absorption, mainly in visible light range and improved charge separation as measured by UV-vis DRS and photoluminescence (PL) spectroscopy, respectively. Such increased light absorption can be attributed to the absorption by the graphene contents on the rGO-TNTNP surface whereas the improved charge separation indicated by quenched PL emission peak confirms the role of graphene contents acting as a direct pathway for efficient photogenerated charge extraction.

The photoelectrochemical and photocatalytic performance of the rGO-TNTNP was investigated by photocurrent measurements and photocatalytic CO_2 conversion. rGO-TNTNP showed a significantly enhanced photocurrent and methane yield as compared to pure TNT sample which can be attributed to the graphene and additional TiO_2 nanoparticles on its surface providing enhanced light absorption and effective separation of the photogenerated charges. We believe the synthesis strategy in this work can provide new inroads for a wide variety of design-specific hybrid metal-oxide graphene-based materials helping to lead to sustainable photocatalytic systems.

The third experimental approach is focused towards the synthesis of reduced TiO_2 (RT) by a newly developed approach and its application in photocatalytic CO_2 conversion to hydrocarbon fuels. RT was prepared from commercial nano-TiO_2 (CT), by a two-step method involving magnesiothermic reduction in 5% H_2/Ar followed by acid washing and investigated with respect to its utility in CO_2 photoreduction to CH_4 under simulated solar light irradiation (1 sun, AM 1.5G). The crystallinity of the samples i.e. pure CT and RT were investigated using XRD and HR-TEM which ensures the retaining of similar crystalline structure for RT sample with no appearance of any other phase or impurities in it. The UV-vis DRS of RT showed an improved light absorption which suggests the successful formation of surface defects and Ti^{3+} ions/oxygen vacancies. The photoluminescence (PL) spectrum also showed a decreased emission peak for RT as compared to pure CT indicating the defects acting as charge traps rather than recombination centers. The band gap estimation using light absorption data and valence band XPS suggest the suitable band edge positions of RT for proceeding the CO_2 photoreduction experiments. Pt as a co-catalyst, was photodeposited onto pure CT and RT samples and its presence confirmed using STEM elemental mapping, HR-TEM and XPS analysis. The Pt photodeposition was optimized by varying the theoretically calculated Pt wt. % with respect to its performance in CO_2 photoreduction experiments. A significant

enhancement of CH_4 evolution with Pt nanoparticles as a co-catalyst is observed for CO_2 photoreduction experiments. The activity was also depended on the size and amount of Pt nanoparticles as revealed by HR-TEM images of Pt-x-RT samples (where x corresponds to theoretically calculated wt. % of Pt). The reduced TiO_2 sample with 1.0 wt. % of Pt yielded the maximum photocatalytic CH_4 yield of 1640.58 $ppm \cdot g^{-1} \cdot h^{-1}$ (1.13 $\mu mol \cdot g^{-1} \cdot h^{-1}$), which is three times higher than pure commercial nano-TiO_2 and four times higher than commercial P25 with the similar loading of Pt as a co-catalyst. Such an improvement in the photocatalytic performance can be attributed to effective separation of photogenerated charges by Pt nanoparticles with controlled size and a favorable combination of various factors like Ti^{3+} and oxygen vacancies/surface defects driving toward optimal band gap with well-aligned bands position during the synthesis of reduced TiO_2.

Appendix 1) Abstract in Korean language

요 약 문

인위적으로 발생하는 CO_2가 방대하고 끊임없이 방출되면서 대기 중의 CO_2의 규모가 과도하게 증가하고 있다. 따라서 지구 온난화, 기후 변화, 환경오염이 진행되고 자연적인 탄소 순환이 방해받고 있다. CO_2는 온실가스 중 온난화 효과에 가장 큰 기여도가 높은 물질로 알려져 있다. 따라서 대기 중의 CO_2의 농도가 상승되는 것을 막기 위해서는 산업 공정에서 활용을 위해 CO_2를 포집하거나, 다른 화합물이나 사용 가능한 연료로 전환하는 방법이 있다. 열역학적 연구에서 알 수 있듯이, CO_2는 안정한 분자로, 사용 가능한 화합물로 전환되기 위해서는 큰 장벽을 넘을 수 있는 추가적인 에너지를 필요로 한다. 이 에너지를 넘기 위한 다양한 기술들에는 화학적 변환, 열적 변환, 생물학적인 변환, 전기학적인 변환, 광전기화학적인 변화, 광촉매적인 변환이 있다. 이러한 방법 중에서 빛을 이용하여 CO_2를 탄화수소 화합물로 전환하는 광촉매적 전환이 가장 매력적인 방법이다. 왜냐하면, 지속가능한 측면에서 볼 때, 재생에너지와 환경과 에너지 인프라구축하는 목적에 가장 잘 부합하는 방법이기 때문이다. 광범위한 연구와 개발에도 불구하고, 각 분야는 아직 초창기 단계에 있으며, 효율적인 촉매반응과 생성물 선택적 반응 부분에서 아직은 많은 노력이 요구되고 있다. CO_2 광화학적 환원반응 촉매제에는 다양한 물

질들이 개발되고 있고 그 중에서 TiO_2가 가장 널리 알려져 있다. TiO_2는 부식에 대한 안정성이 높으며, 풍부하고 값싼 가격 등의 이점이 있지만 넓은 밴드 갭(~3.2 eV)로 인해 빛 흡수가 적고, 표면과 큰 부피에서의 전하 재결합으로 햇빛에서 낮은 양자 수득률을 나타내어 사용하기에는 한계가 있다. 그러나 이러한 결함이 있음에도 불구하고, TiO_2는 뛰어난 안정성으로 광촉매 분야에서 으뜸으로 여겨지고 있다. 따라서 제한적인 빛 흡수와 효과적인 전하분리를 극복하기 위해서, 비금속이나 백금과 같이 귀금속을 조촉매로 도핑하거나 낮은 밴드 갭을 갖고 있는 반도체를 연결하거나 탄소를 기본으로 한 TiO_2 를 합성하는 등의 다양한 방법을 연구를 진행하고 있다. 그러므로 본 논문에서 연구한 내용은 TiO_2 물질과 이를 기본으로 한 물질의 광촉매적인 활동을 증가하기 위한 것으로 빛 흡수를 증가하고 전하 분리를 향상 하는 것을 포함하고 있다. 따라서, Ph. D 과정 동안에 진행된 실험은 총 세 가지이다. 먼저, TiO_2 나노 튜브에 다른 원소를 도핑시키고, 두 번째로는 환원된 그래핀 산화물(rGO)을 새로운 헤테로 구조로 된 TiO_2 나노 튜브와 합성하고, 마지막으로 새로운 접근을 통해 환원된 TiO_2 개발에 대한 연구를 진행하였

.

지난 몇 년 동안에, 1차원적인 TiO_2 나노튜브는 많은 활성부위를 갖고 있으며, 넓은 표면적과 방향성이 있는 전자 이동에 의하여 전하 분리가 잘 이뤄진다는 점에서 광촉매 연구 분야에서 큰 관심을 얻었다. 논문의 첫 번째 실험적인 접근은, 다른 원소를 조요소로

도핑하여 티탄산나트륨 나노튜브의 촉매 작용을 증가하도록 하였다. 탄소와 질소가 도핑 되어있는 티탄산나트륨 나노튜브는 다양한 양의 요소 (질소와 탄소의 근원)와 잘 섞여 있는 나트륨 이온의 결합된 티탄산나트륨 나노튜브 (알카라인 열처리방법을 통해 얻어짐)를 열처리하는 방법으로 합성된다. 광촉매는 많은 실험 기술에 따라서 그 특성이 정해진다. 그 중에 인공 태양 빛을 사용하여 CO_2와 수증기를 촉매제를 통해 반응시켜 메탄으로 전환하는 실험 진행하였다. 탄소와 질소가 최적의 농도로 도핑된 티탄산나트륨의 경우 메탄 230.80 $ppm \cdot g^{-1} \cdot h^{-1}$최대로 생산하였고, 이는 도핑 되지 않은 티탄산나트륨을 사용했을 때보다 메탄 생산량이 2.63배에 증가하였다. 광촉매 활성을 증가하는데 필요한 요소는 빛 흡수, 표면적, CO_2 흡착 위치이며 광전자들의 재결합 중심인 TiO_2 나노튜브 물질의 나트륨 이온의 농도이다. 도핑 비율이 높은 TiO_2 나노튜브는 특정 표면적이 줄어들거나, 재결할 부분이 증가하여 낮은 광촉매 활성이 나타낸다. 따라서 조요소로 도핑된 나노구조의 광촉매는 조직적이나 광촉매의 특성을 향상 시키는 특성이 있어 각각 분야에 적용할 수 있는 좋은 방법이라 생각한다.

그래핀을 기본으로 한 TiO_2 나노구조는 그래핀의 특성인 빠른 전하전달뿐만 아니라 향상된 빛 흡수로 인해 높은 광전기화학적 특성 갖고 있다고 알려져 있다. 향상된 광흡수와 효과적인 전하분리를 통한 개선된 광촉매 효과를 위해 그래핀 산화물(rGO)와 1차원 TiO_2 나노튜브를 사용한 새로운 헤테로 구조 합성을 두 번째 실험으로 진행하였다. 환원

된 산화그래핀-TiO_2 나노입자들로 뒤덮인 티탄산염 나노튜브의 1차원적 배열로 이루어져 있고 귀금속을 포함하지 않는 새로운 나노구조 광촉매물질의 손쉬운 합성법이 만들어졌다. 새로운 나노구조의 광촉매 제조와 관련된 가능성 있는 메커니즘은 보고된 문헌과 라만 스펙트럼, XPS 결과, SEM 사진의 실험결과를 바탕으로 다루고 있다. 새로운 나노구조는 상당히 향상된 광전류 밀도와 인공 태양 아래에서 CO_2를 메탄으로 전환하는 광화학적인 활동을 보여준다. rGO-TNTNP는 5.67 $ppm \cdot cm^{-2} \cdot h^{-1}$ 생산하며, 순수한 TiO_2 나노튜브에 비해 4.4배 증가한 양에 해당한다. 이러한 향상된 결과는 빛 흡수 증가와 rGO의 특성으로 인해서 효과적인 전자 분리를 통해 얻었다는 것을 알 수 있다.

넓은 빛 흡수와 적절한 밴드 구조를 가진 black TiO_2 또는 환원된 TiO_2는 높은 광촉매 특성을 갖고 있다. 현재까지 환원된 TiO_2 (RT)의 합성법은 다양한 방법으로 알려져 있으며, 많은 공정 변수에 의해서 물질의 특성들이 달라진다. 세 번째이자 마지막 실험에서는 인공 태양광을 이용하여 CO_2과 수증기를 환원된 TiO_2와 반응시켜 탄화수소, 특히, 메탄이 발생하는지를 확인 하였다. 이 실험에서 사용한 환원된 TiO_2는 5% H_2/Ar에 Mg 같은 이중의 환원제를 사용하는 새로운 방법으로 합성하였다. 또한, 전자 분리 효율을 증가하기 위해서, 백금 나노입자를 조촉매로써 사용했고 최적화된 농도를 환원된 TiO_2 위에 광증착 방법으로 처리하였다. 환원된 TiO_2 표면에 최적화된 백금 나노입자를 빛을 통해 적층시켰을 때, 메탄의 생산량 (1640.58 $ppm \cdot g^{-1} \cdot h^{-1}$, 1.13 $\mu mol \cdot g^{-1} \cdot h^{-1}$)이 상용화된 나노

크기의 TiO_2를 사용 (546.98 $ppm \cdot g^{-1} \cdot h^{-1}$, 0.38 $\mu mol \cdot g^{-1} \cdot h^{-1}$)했을 때 보다 세 배 증가한 것을 알 수 있다. 향상된 광촉매 효과는 빛 흡수를 향상시킨 적절한 밴드갭, CO_2/CH_4 산화환원 전위에 대한 띠 끝의 잘 정렬된 위치와 최적의 크기와 농도로 잘 분산되어 있는 Pt 나노입자 조촉매를 통한 효과적인 광전하 분리가 기인한다고 볼 수 있다.

핵심어: 광촉매적 CO_2 전환, 태양광 활성 광촉매, TiO_2 나노튜브, 동반도핑, 환원된 산화그래핀, 환원된 TiO_2

ACKNOWLEDGEMENTS

All praises are for the creator of the whole universe, almighty ALLAH (God), who from his countless blessings and bounties bestowed me the patience and wisdom to encounter the challenging and tough task of Ph.D. degree.

I would like to express my deepest gratitude towards my adviser professor, Professor Su-Il In for his excellent guidance, caring, patience, and motivation to enhance, advance and nurture and my personal, academic and research affairs. I am grateful to him for his extensive efforts to create a friendly workplace which allows me to spotlight my study and research in an effective manner. I am also thankful and grateful to my co-adviser Dr. Soo-Keun Lee for guidance, caring, and kindness which definitely motivates me to pursue my efforts in an efficient manner for the accomplishments achieved during the Ph.D. degree research work.

It's a rule of nature and my belief that nothing can be gained without losing. In this regard, I give my deepest love and dedicate all hard work to my parents, my lovely wife and kids without whose inspirations, motivations, encouragement and moral support I have never been successful in such a difficult task. In true sense, I am lack of words to express their endurance toward hardships they faced during my Ph.D. degree.

I am thankful to all of my lab members, both Korean and foreigners, who helped me to a great extent in the moments of need. Their coordination in each aspect of lab life, creates a friendly environment for research resulting in fruitful results. I wish all the lab members the best and successful future ahead. I would like to express my profound thanks toward DGIST for the award of Ph.D. scholarship and technical facilities which enabled me to pursue my higher education in a technological challenging atmosphere of a reputed university of South Korea. I am also thankful to all funding sources, without whose financial and technical support, the research wouldn't have been accomplished.